Study of Fatigue Crack Propagation in Metallic Structures

Roberto Manuel Canito Miranda

Master in Mechanical Engineering

Supervisors:

Professors Paulo M. S. Tavares de Castro and Miguel A. V. de Figueiredo



Faculdade de Engenharia da Universidade do Porto

Mestrado Integrado em Engenharia Mecânica

July 2010

Aos meus pais e avós

Estudo de Propagação de Fendas de Fadiga em Estruturas Metálicas

Resumo

A presente dissertação tem como tema principal a caracterização de leis de propagação de fendas de fadiga de um aço usado na ponte de Alcácer do Sal em vias de construção para a REFER.

Foram realizadas simulações numéricas 2D e 3D (bi- e tri-dimensionais) por elementos finitos com vista ao estudo do factor de intensidade de tensões em função do comprimento da fenda e da posição ao longo da espessura, para os provetes CT (*compact tension*) utilizados.

Foram medidas durezas em amostras de soldaduras extraídas de uma placa soldada com preparação em X de onde foram também extraídos os provetes CT. Foram realizados ensaios de propagação de fendas de fadiga em provetes de metal base com razão de tensão (R = carga mínima/carga máxima) R=0.1, 0.4 e 0.7, e também da zona afectada pelo calor de ligações soldadas topo a topo, com R=0.1, seguindo a norma ASTM E647. Foi obtida a relação comprimento de fenda *vs*. número de ciclos e seguidamente procedeu-se à determinação das respectivas leis de propagação.

Foi realizada uma avaliação aproximada do efeito de *crack closure* no provete de zona afectada pelo calor testado com R=0.1, e com base nessa avaliação determinada a relação da/dN *vs.* ΔK_{eff} para esse provete.

Abstract

The main subject of the present dissertation is the characterization of fatigue crack propagation laws for the steel used in the Alcácer do Sal bridge being built for REFER.

The stress intensity factor calibration of CT (compact tension) specimens was carried out using 2D and 3D finite element analyses, as a function of crack length and of position through the thickness.

Hardness values were measured in samples of double V joints. These samples and the CT specimens tested were extracted from the same plate. Fatigue crack propagation tests were carried out in base metal (BM) specimens under load ratios (R=minimum load / maximum load) of 0.1, 0.4 and 0.7, and also of the heat affected zone (HAZ) of butt welds under R=0.1, according to the ASTM standard E647. The relationship crack length *vs*. number of cycles was obtained, and afterwards the crack propagation laws were determined.

An approximate assessment of the crack closure effect found in the HAZ CT specimen tested at R=0.1 was carried out, and on the basis of that assessment the relationship da/dN *vs.* ΔK_{eff} was determined for that specimen.

Acknowledgements

After concluding the present master thesis I would like to express my acknowledgements to those involved, directly or indirectly, in its realization.
So, I would like to thank particularly:

- Professor Paulo Tavares de Castro of the Department of Mechanical Engineering, Faculty of Engineering, University of Porto, not only for the orientation, but also for the means put at my disposal, for his commitment and professionalism during the development of this project and for the careful revision of this thesis;
- Professor Miguel Vigário Figueiredo of the Department of Mechanical Engineering, Faculty of Engineering, University of Porto, not only for the co-orientation, but also for the valuable suggestions;
- Professor Rui Calçada, of the Department of Civil Engineering, Faculty of Engineering, University of Porto, for giving me the opportunity to participate in the PTDC/ECM/ 69697/2006 project of FCT (Fundação para a Ciência e Tecnologia – Portuguese Foundation for Science and Technology) ;
- Valentin Richter-Trummer and Daniel Peixoto for their friendship and support during this work, for informal conversations and also for the support in the experimental activity;
- Pedro Moreira for the suggestions made during this project and for his support.
- Emília de Rosário Soares for her support during the realization of this project;
- Rui Silva for the support given in the installation of the equipment used in experimental work;
- Carlos Albuquerque for informal conversations, support and for the documentation provided.
- Sérgio Oliveira Tavares, for the informal conversations and support.
- Departments of Mechanical and Civil Engineering, Faculty of Engineering, University of Porto, for the opportunity given to me for the realization of this project;
- Teixeira Duarte SA, who kindly provided the materials used in the present thesis;
- Fundação para a Ciência e Tecnologia, that partially funded this work through the project PTDC/ECM/ 69697/2006.

Contents

Resumo v
Abstract vii
Acknowledgements ix
Contents xi
List of Figures xiii
List of Tables xix
List of Acronyms xxi
List of Symbols xxiii
1. Introduction 2
1.1. Generalities 2
1.2. Aims of the Present Thesis 4
2. Fatigue 8
2.1. Fatigue Life Prediction Models 9
2.1.1. The S-N curve 9
2.1.2. Damage Tolerance 10
2.2. Factors Affecting Fatigue Performance 12
2.2.1. Fatigue Loading 12
2.3. Fracture Behavior Regions or Regimes 13
2.4. Stress Intensity Factor (SIF) 14
2.5. Crack Propagation Laws 15
2.5.1. The Compact Tension Specimen (CTS) 18
3. Experimental 22
3.1. Material 22
3.1.1. Metallographic Study 23
3.1.1.1. Samples 23
First Sample 24
Second Sample 28
Vickers Hardness Test 35
3.2. Calculation of the CT specimen dimensions 40
3.2.1. Specimen dimensions 40
3.2.2. Test loads and plastically deformed region ahead the crack 42
3.3. Study of the notch geometry 44
3.3.1. Determination of the Stress Concentration Factor (SCF) 48
3.3.2. Stress Intensity Factor values as a function of crack length 56
3.3.3. Stress intensity factor through thickness (a/W=0,23) 59
3.3.3.1. Notch angle of 30^{o} 60
3.3.3.2. Notch angle of 60^{o} 64
3.3.3.3. EDM notch 68
3.4. Fatigue crack growth testing 71
3.4.1. Specimen Preparation 71
3.5. Results 73
3.5.1. BM specimen tested with R=0,1 74
3.5.2. BM specimen tested with R=0,4 79
3.5.3. BM specimen tested with R=0,7 86
3.5.4. HAZ specimen tested with R=0,1 91
3.5.5. Fatigue crack propagation threshold values 101
3.5.6. Summary of FCP laws abtained 102
4. Discussion. Crack Closure Effects 104
4.1. Crack Closure Assessment for HAZ Specimen 104

4.2. Crack Closure Assessment for Base Metal 113
Conclusions 120
Suggestion for Future Works 122
References 124
Annex A 126
Clevis design 126
Annex B 127
Resources used 127
Annex C 128
Spider 8 dynamic measurements 128

List of Figures

Figure 1 - Survey of the various aspects of fatigue of structures [1].....2
Figure 2 - Photograph of St. Mary's Bridge similar to the Point Pleasant Bridge [2]. 3
Figure 3 - Photograph of Point Pleasant Bridge after collapse [2].....3
Figure 4 - Photograph showing origin of failure in Point Pleasant Bridge [2].....4
Figure 5 - Photograph of I.O.S. 3301 barge failure in 1972 [2].....4
Figure 6 - Image of the three arches of the Alcácer do Sal Bridge. 5
Figure 7- Alcácer do Sal Bridge: detail of the technical passageway under the viaduct. 5
Figure 8 - Metallic box girder used in the 3-span Alcácer do Sal Bridge.....6
Figure 9 - Double V weld: detail A of Figure 8. 6
Figure 10 - Fatigue test results of unnotched specimens of a low alloy steel (SAE 4130) [1].....9
Figure 11 - Principle of safe life crack growth by periodic inspections [1].....11
Figure 12 - Terminology in Constant-amplitude fatigue [2].....13
Figure 13 - Random-stress loading [2].....13
Figure 14 - General regions of fracture behavior for structural steels [2].....14
Figure 15 - K_I values for different crack geometries [2].....15
Figure 16 - Typical fatigue crack propagation behavior (A533B steel) [4].....17
Figure 17 - Values of the CT specimen dimensions for K_{Ic} measurements, e.g. ASTM E399 [5].....19
Figure 18 - Zone of the welded plate where the first sample was taken. 24
Figure 19 - Representation of the zone of the welded plate where the second sample was taken. 24
Figure 20 - Macrostructure of the welding (first sample). 25
Figure 21 - Microstructure of two cracked zones ;above interface between weld metal (right) and base metal (left); below, inter-run zone.....26
Figure 23 - Macrostructure of the steel weld with the respective hardness points measured (first sample). 27
Figure 22 - Microstructure of cracked zone. 27
Figure 24 - Macrostructure of the welding (second sample).....28
Figure 25 - Macrostructure of the welding (second sample), with reference to the welded zones from where the microstructures pictures were acquired.....29
Figure 26 - Macrostructure of the steel weld with the respective hardness points measured (second sample).....30
Figure 27 - Microstructure ferritic-perlitic of the Base Metal, zone 2 of Figure 25. 31
Figure 28 - Microstructure ferritic-perlitic of the Base Metal (DIC), zone 2 of Figure 25.....31
Figure 29 - Microstructure of the Heat Affected Zone material; zone 5 of Figure 25. ...32
Figure 30 - Microstructure of the Heat Affected Zone material coarse grain zone, essentially bainitic; zone 1 of Figure 25.....32
Figure 31 - Microstructure of the Welded material composed of acicular ferrite and proeuctectoid ferrite (boundary ferrite); zone 3 of Figure 25.....33

Figure 32 - Microstructure of the melded material: detail of Figure 30 showing acicular ferrite. 33
Figure 33 - Microstructure of the welded material: inter-run zone. Zone 4 of Figure 25. 34
Figure 34 - Representation of the zones where the hardness measurements were carried out. 35
Figure 35 - Line 1 hardness measurements. 36
Figure 36 - Line 2 hardness measurements. 37
Figure 37 - Line 3 hardness measurements. 38
Figure 38 - Line 1, 2, 3 hardness measurements 40
Figure 39 - Initially intended CT specimen dimensions. 40
Figure 40 - Dimensional relationships given by the ASTM E647 standard [9]. 41
Figure 41 - Plastically deformed region ahead of the crack for $\Delta K_{th} = 2$ MPam. 43
Figure 42 - Plastically deformed region ahead of the crack for $\Delta K_{th} = 8$ MPam. 44
Figure 43 - Notch details and minimum fatigue precracking requirements, from [9]. 45
Figure 44 - Fractured 30^o milling tool. The tool was firstly supplied as a disk finished with the 30^o cutting tool. 46
Figure 45 - Specimen dimensions with a 30^o notch angle. 46
Figure 46 - CT Specimen dimensions with a 60^o notch angle 47
Figure 47 – a) CT Specimen dimensions with a straight EDM notch angle. b) Detail of the EDM notch. 48
Figure 48 – Detail of the specimen with EDM notch. Meshed model using 53930 C3D8R elements (half model). 49
Figure 49 – Detail of the specimen with 30^o . Meshed model using 68864 C3D8R elements (half model). 49
Figure 50 - σ_x values for a Compact Tension Specimen with an EDM notch. 50
Figure 51 - σ_y values for a Compact Tension Specimen with an EDM notch. 51
Figure 52 - σ_z values for a Compact Tension Specimen with an EDM notch. 51
Figure 53 - σ_x values for a Compact Tension Specimen with a 30^o notch angle. 52
Figure 54 - σ_y values for a Compact Tension Specimen with a 30^o notch angle. 52
Figure 55 - σ_z values for a Compact Tension Specimen with a 30^o notch angle. 53
Figure 56 - Forces and moments applied in the specimen for the nominal stress calculation. 54
Figure 57 - Stress intensity factor values for different values of a/W using FEM 2D. 56
Figure 58 – K values along the thickness for different values of a/W. 57
Figure 59 - Stress intensity factor maximum, minimum and average values for different values of a/W using FEM 3D. 58
Figure 60 - Comparison of stress intensity factor values for different values of a/W. 58
Figure 61 - Error committed using FEM compared with the ASTM E647 standard. 59
Figure 62 - Detail of less refined mesh for 30^o notch angle for a/W=0,23. 60
Figure 63 - Comparative plot of the % differences between ASTM E647 and FEM as a function of the coordinate z/t for both meshes for a/W=0,23. 62

Figure 64 - Nodes for calculating the average stress intensity factor for an element.....62
Figure 65- Detail of meshed model using C3D8R elements (half model). 64
Figure 66 - Detail of the less refined mesh for a 60^{o} notch angle for a/W=0,23 65
Figure 67 - Comparative plot of the % differences between ASTM E647 and FEM as a function of the coordinate z/t for both meshes for a/W=0,23. 67
Figure 68 - Detail of less refined mesh for an EDM notch for a/W=0,23.....68
Figure 69 - Comparative plot of the % differences between ASTM E647 and FEM as a function of the coordinate z/t for both meshes for a/W=0,23. 70
Figure 70- Representation of the position of the weld in the tested specimens. 71
Figure 71 - Precracking sequence used in the first test specimen (MB, R=0,1, precrack measured from the tip of the EDM notch);a measured from EDM notch. 72
Figure 72 - PEAK microscope, to be mounted on a travelling device incorporating a Mitutoyo digital ruler. 73
Figure 73 - MTS machine used for the tests and traveling microscopes (one on each side of the specimen). 74
Figure 74- a vs. N data results obtained from measurements of the test specimen fatigue crack (BM, R=0,1).....75
Figure 75 - da/dN vs. K data results using the Excel (SM, BM, R=0,1).....76
Figure 76 - da/dN vs. Δ K data results using the Matlab (SM, BM, R=0,1). 76
Figure 77 - da/dN vs. Δ K data results using the Matlab (PM, BM, R=0,1). 77
Figure 78 - Comparative plot of the experimental results with the calculated Paris laws (BM R=0,1). 78
Figure 79 - Specimen Picture in the end of the test (BM R=0,1). 79
Figure 80 - Precracking sequence used in the MB R=0,4 test specimen; a measured from the EDM notch. 80
Figure 81 - N vs. a data results obtained from measurements of the test specimen fatigue crack (BM, R=0,4).....81
Figure 82 - da/dN vs. Δ K data results using the Excel (SM, BM R=0,4). 82
Figure 83 - da/dN vs. Δ K data results using the Matlab (SM, BM R=0,4). 82
Figure 84 - da/dN vs. Δ K data results using the Matlab (PM, BM R=0,4). 83
Figure 85 - Comparative plot of the experimental results with the calculated Paris laws (BM R=0,4). 84
Figure 86 – Fracture surfaces in the end of the test (BM R=0,4). 85
Figure 87 - Precracking sequence used in the BM R=0,7 test specimen; a measured from EDM notch. 86
Figure 88- N vs. a data results obtained from measurements of the test specimen fatigue crack (BM R=0,7).....87
Figure 89 - da/dN vs. Δ K data results using the Excel (SM, BM R=0,7). 88
Figure 90 - da/dN vs. Δ K data results using the Matlab (SM, BM R=0,7). 88
Figure 91 - da/dN vs. Δ K data results using the Matlab (PM, BM R=0,7). 89
Figure 92- Comparative plot of the experimental results with the calculated Paris laws (BM R=0,7). 90
Figure 93 - Fracture surfaces in the end of the test (BM R=0,7).....91

Figure 94 - Precracking sequence used in the HAZ R=0,1 test specimen; a measured from EDM notch. 92
Figure 95....94
Figure - 96 da/dN vs. K data results (SM, HAZ R=0,1). 95
Figure 97 - da/dN vs. Δ K data results using the Excel (SM, HAZ R=0,1). 96
Figure 98 - da/dN vs. Δ K data results using the Matlab (SM, HAZ R=0,1). 96
Figure 99 - da/dN vs. Δ K data results using the Matlab (PM, HAZ R=0,1). 97
Figure 100 - Specimen Picture in the end of the test (HAZ R=0,1). 98
Figure 101 - Representation of the two cases in study (a_1=a_2=15 mm and a_1=a_2=25 mm)....99
Figure 102 - σ_y values for a_1=a_2=15 mm (using 22938 elements of type C3D8R)....100
Figure 103 - σ_y values for a_1=a_2=25 mm (using 27558 elements of type C3D8R)....101
Figure 104 - da/dN vs. ΔK summary of FCP laws obtained in the tests. 102
Figure 105 - Back face strain gauge used. 104
Figure 106 - Data acquisition system used to obtain the Force vs strain graphic. 105
Figure 107 - Redistribution of residual stress with crack length [13]. 105
Figure 108 - Back face strain vs. force applied in the HAZ test specimen for a=58,46 mm. 106
Figure 109 - Back face strain vs. force applied in the HAZ test specimen for a=64,19 mm. 107
Figure 110 - Back face strain vs. force applied in the HAZ test specimen for a=69,43 mm. 107
Figure 111 - Back face strain vs. force applied in the HAZ test specimen for a=76,58 mm. 108
Figure 112 - Crack opening loads infection points (HAZ R=0,1). 109
Figure 113 - Back face strain vs. force applied in the HAZ test specimen for a=64,19 mm, under cyclic load. 110
Figure 114 - da/dN vs. ΔK_{eff} data results using the Matlab with MB, HAZ and HAZ effective R=0,1 (SM). 111
Figure 115 – Fatigue crack growth results correlated using the effective stress intensity factor range.[14]....112
Figure 116 - Fatigue crack growth rates as a function of external and effective SIF [12]. 112
Figure 117 - Back face strain vs. force applied in the test specimen for a=47,91 mm (BM specimen R=0,4). 113
Figure 118 - Back face strain vs. force applied in the test specimen for a=51,27 mm (BM specimen R=0,4). 114
Figure 119 - Back face strain vs. force applied in the test specimen for a=52,69 mm (BM specimen R=0,4). 114
Figure 120 - Back face strain vs. force applied in the test specimen for a=65,43 mm (BM specimen R=0,4). 115
Figure 121 - Back face strain vs. force applied in the test specimen for a=74,37 mm (BM specimen R=0,4). 115

Figure 122 - Back face strain vs. force applied in the test specimen for a=84,39 mm (BM specimen R=0,4). 116
Figure 123 - Back face strain vs. force applied in the test specimen for a=87,55 mm (BM specimen R=0,4). 116
Figure 124 - Crack opening loads inflection points (MB R=0,4).....117
Figure 125 - Back face strain vs. force applied in the test specimen for a=47,91 mm (BM specimen R=0,4, under cyclic load).....118
Figure 126 - da/dN vs. ΔK_{eff} data results using the Matlab with MB and MB effective R=0,4 (SM).....119
Figure 127 – Clevis design. 126
Figure 128 – Force vs. strain plot under dynamic load with a=64,19 mm with 1HZ frequency (HAZ R=0,1). 128
Figure 129- Force vs. strain plot under dynamic load with a=69,43 mm with 16 HZ frequency (HAZ R=0,1). 129
Figure 130 - Back face strain vs. force applied in the test specimen for a=51,27 mm (BM specimen R=0,4, under cyclic load).....129
Figure 131 - Back face strain vs. force applied in the test specimen for a=52,69 mm (BM specimen R=0,4, under cyclic load).....130
Figure 132 - Back face strain vs. force applied in the test specimen for a=65,43 mm (BM specimen R=0,4, under cyclic load).....130
Figure 133 - Back face strain vs. force applied in the test specimen for a=74,37 mm (BM specimen R=0,4, under cyclic load).....131
Figure 134- Back face strain vs. force applied in the test specimen for a=84,39 mm (BM specimen R=0,4, under cyclic load).....132
Figure 135 - Back face strain vs. force applied in the test specimen for a=87,55 mm (BM specimen R=0,4, under cyclic load).....132

List of Tables

Table 1 - Chemical composition of the S355NLZ15 steel (base material). 22
Table 2 - Some mechanical proprieties of the base material. 22
Table 3 - S355NL steel: welding process 136 WQP according to EN ISO 15614-1:2004. 23
Table 4 - Fatigue threshold values [5] 42
Table 5 - Typical Fatigue threshold for modern steels [10]. 42
Table 6 - Maximum fatigue crack loads [10]. 44
Table 7 - Non-dimensional 3D FEM SIF along the thickness, 45942 elements mesh for a/W=0,23. 61
Table 8 - Non-dimensional 3D FEM SIF along the thickness, 68704 elements mesh a/W=0,23. 61
Table 9 - 3D FEM$K/\sigma\sqrt{\pi a}$, 68704 elements mesh for a/W=0,23. 63
Table 10 - Non-dimensional 3D FEM SIF along the thickness, 78946 elements mesh for a/W=0,23. 66
Table 11 - Non-dimensional 3D FEM SIF along the thickness, 44608 elements mesh for a/W=0,23. 66
Table 12 - 3D FEM $K/\sigma\sqrt{\pi a}$, 78496 elements mesh for a/W=0,23. 67
Table 13 - Non-dimensional 3D FEM SIF along the thickness, 29988 elements mesh for a/W=0,23. 69
Table 14 - Non-dimensional 3D FEM SIF along the thickness, 53930 elements mesh for a/W=0,23. 69
Table 15 - 3D FEM $K/\sigma\sqrt{\pi a}$, 53730 elements mesh for a/W=0,23. 70
Table 16 - Load variation during the test. 92
Table 17 - Stress values in the y direction for points A and B. 101
Table 18 – Fatigue crack propagation threshold values obtained from the experimental tests. 102
Table 19 - - Crack closure load values at the fatigue crack front (HAZ R=0,1). 108
Table 20 - Crack closure load values at the fatigue crack front (BM R=0,4). 117

List of Acronyms

ASTM - American Society for Testing and Materials;

BM - base metal;

CA - constant amplitude;

COD - crack opening displacement;

CTOD - crack tip opening displacement;

CTS - compact tension specimen;

DIC - Differential interference contrast microscopy;

EDM - electrical discharge machining;

FCP - fatigue crack propagation;

FEM - Finite Element Method;

HAZ - heat affected zone;

PM - polynomial method;

SCF - stress concentration factor;

SIF - stress intensity factor;

SM - secant method;

VA - variable amplitude;

WM - welded metal;

List of Symbols

A - Area;

a - crack length;

a_c - critical crack size;

a_0 - initial crack length;

a_1 - crack length in the side 1;

a_2 - crack length in the side 2;

B,t - CT specimen thickness;

C - Paris law constant;

$\frac{da}{dN}$ - crack propagation rate;

E - Young modulus;

F - Force;

H - CT specimen height;

h - Maximum height of the machined notch;

J - integral J;

K_c - critical stress intensity factor;

K_I - stress intensity factor mode I;

K_{Ic} - critical stress intensity factor in mode I;

K_{max} - maximum stress intensity factor;

K_{min} - minimum stress intensity factor;

L - CT specimen length;

m - Paris Law exponent;

N - number of cycles;

N_i - number of cycles necessary to initiate a fatigue crack;

N_p - number of cycles necessary to propagate a fatigue crack to a critical size;

N_t - total fatigue life;

P_{max} - maximum load

P_{min} - minimum load;

R - Stress ratio;

R_{eh} - Material yield strength;

R_m - Material ultimate tensile strength (also called S_U , see below);

R^2 - determination ratio;

S_a - stress amplitude;

S_f - fatigue life stress;

S_m - mean stress;

S_{max} - maximum stress;

S_{min} - minimum strees;

S_U - tensile strength of the material (also called R_m , see above);

W - CT specimen width;

Y - geometric factor;

Greek Symbols

δ - crack tip opening displacement;

ΔK - stress intensity factor variation;

ΔK_{th} - fatigue crack propagation threshold;

ΔP - fatigue load range;

Δσ - stress variation;

σ_{amp} - stress amplitude;

σ_{mean} - mean stress;

σ_{max} - maximum stress;

σ_{min} - minimum stresss;

σ_{nom} - nominal stress;

σ_{xx} - stress in the x direction;

σ_{yy} - stress in the y direction;

σ_{ys} - material yield stress;

σ_{zz} - stress in the z direction;

ν - Poisson ratio;

1. Introduction

1.1. Generalities

A single application of a load substantially lower than the static strength of a structure does not create damage, but if that load is repeated many times it could lead to a complete failure. Fatigue failures are a well known phenomenon in metallic structures. In the 19th century the first fatigue investigations were carried out. In Figure 1 [1] some of the fatigue most important fatigue design aspects are shown.

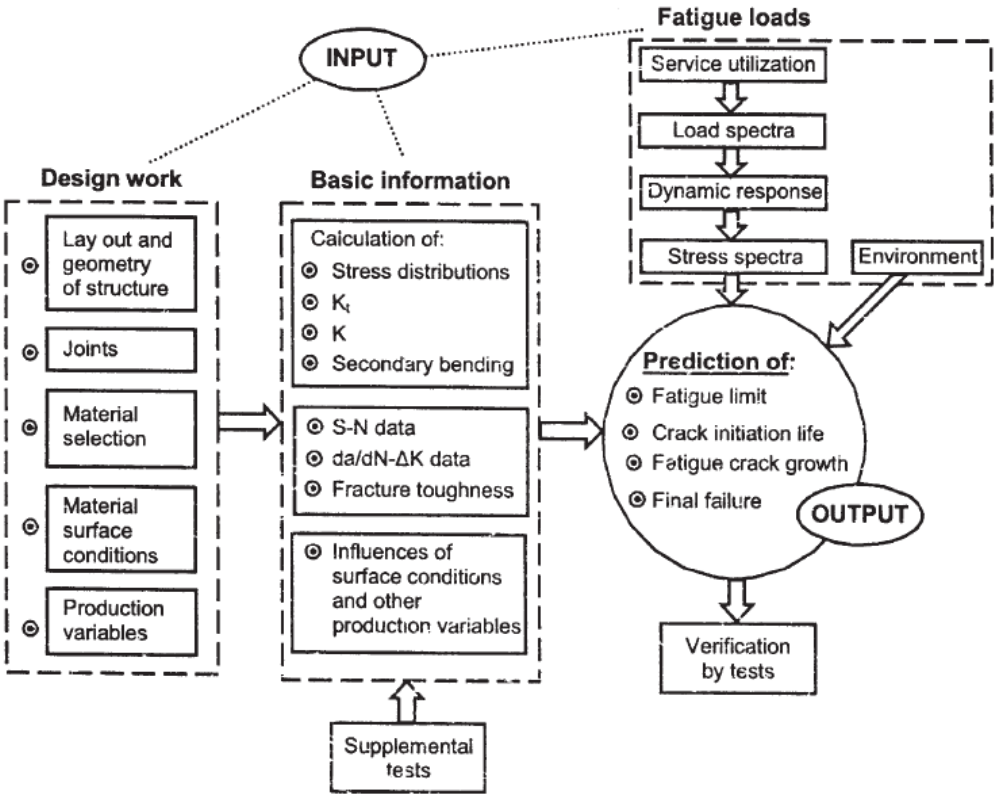


Figure 1 - Survey of the various aspects of fatigue of structures [1].

A well known fatigue failure is the Point Pleasant Bridge collapse which caused the loss of 46 lives, in 1972.



Figure 2 - Photograph of St. Mary's Bridge similar to the Point Pleasant Bridge [2].



Figure 3 - Photograph of Point Pleasant Bridge after collapse [2].

Bennett and Mindlin [3] conducted an investigation of the failure of the Point Pleasant Bridge and concluded that*:*

"1.The fracture in the lower limb of the eye of eyebar 330 was caused by the growth of a flaw to a critical size for fracture under normal working stress.

2. The initial flaw was due to stress corrosion cracking from the surface of the hole in the eye. There is some evidence that hydrogen sulfide was the reagent responsible for the stress-corrosion cracking. The final report indicates that the initial flaw was due to fatigue, stress-corrosion cracking and/or corrosion fatigue.

3. The composition and heat treatment of the eyebar produced steel with very low fracture toughness at the failure temperature.

4.The fracture resulted from a combination of factors; in absence of these, it probably would not have occurred: (a) the high hardness of the steel which rendered it susceptible to stress-corrosion cracking; (b) the close spacing of the components in the joint which made it impossible to apply paint to the most highly stressed region of the eye, yet provided a crevice in this region where water could collect; (c) the high design load of the eyebar chain, which resulted in a local stress at the inside of the eye greater than the yield strength of the steel; and (d) the low fracture toughness of the steel which permitted the initiation of complete fracture from the slowly propagation stress-corrosion crack when it had reached a depth of only 3.0 mm (Figure 4)."

More fractures in steel bridges and many other types of structures occurred since the failure of the Point Pleasant Bridge as a result of unsatisfactory design approaches, e.g. Figure 5. These fractures led to an increasing concern about the possibility of fatigue and brittle fractures in steel bridges.



Figure 4 - Photograph showing origin of failure in Point Pleasant Bridge [2].

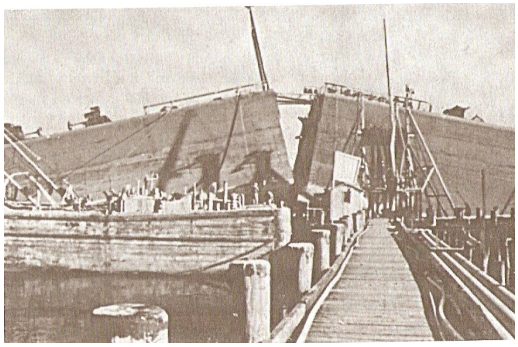


Figure 5 - Photograph of I.O.S. 3301 barge failure in 1972 [2].

Industrial sectors have developed fracture control plans for applications as different as arctic constructions or a space shuttle. Brittle fractures cannot be eliminated simply by using materials with improved notch toughness, the designer has an important responsibility for the safety and consistency of the structure. Fracture Mechanics can be used in design to prevent brittle fractures and fatigue failures of engineering structures.

1.2. Aims of the Present Thesis

The present master thesis is a contribution to a FCT - Fundação para a Ciência e Tecnologia (Portugal) research project on the behavior of metallic bridges for high speed trains. In the context of that project, there is a PhD thesis being prepared at FEUP by Carlos Albuquerque, that deals with advanced models for the evaluation of such structures, and uses as a case study the steel bridge being constructed for REFER at Alcácer do Sal, in Alentejo, Portugal.

This master thesis aims at characterizing the fatigue crack propagation behavior of the steel and of the welded connections of selected structural details of the above mentioned bridge, taken as critical. Therefore, the base material and the welded samples were provided by Teixeira Duarte SA, main contractor for this bridge. The specimens tested in the present thesis are therefore truly representative of this major engineering structure.

Figures 6 to 9 show several views of the Alcácer do Sal REFER Bridge, taken by the author of the present thesis during a visit on June 16, 2010.



Figure 6 - Image of the three arches of the Alcácer do Sal Bridge.



Figure 7- Alcácer do Sal Bridge: detail of the technical passageway under the viaduct.



Figure 8 - Metallic box girder used in the 3-span Alcácer do Sal Bridge.



Figure 9 - Double V weld: detail A of Figure 8.

2. Fatigue

Fatigue is a process of cumulative damage that is caused by repeated variable loads. The initiation and propagation of a crack occurs due to the accumulated damage of a number of load fluctuations in the plastic regions. Fracture of components occurs in many cases due to this fact. The fatigue crack initiation life, N_i, is the number of cycles necessary to initiate a fatigue crack. The number of cycles needed to propagate a fatigue crack to a critical size is called the fatigue crack propagation life, N_p. The total fatigue life, N_t, is defined as:

$$N_t = N_i + N_p \tag{1}$$

The boundary between fatigue crack initiation and propagation is not precisely defined, since it would require an explicit consensus on the minimum size of the flaw that constitutes a crack; such consensus does not exist.

Fatigue failure consists of three phases: initiation, propagation and final failure. It is hard to define the boundary between initiation and propagation. Usually it is assumed that one phase is prevailing and it is studied. Frequently in a defect free part the failure process is assumed as concerning the crack initiation. In large and complex structures it is more realistic to consider that defects already exist since fabrication, and determine how fast they can grow.

The life of such structures as aircraft, ships, bridges and off-shore drilling platforms is governed by the propagation of defects.

The two situations above roughly represent the two different philosophies of design.

In safe-life approach parts are designed for a finite service life during which no significant damage will occur. No defects are assumed to be present in the new structure and no inspections are required during the design life. After reaching the life limit the part is retired from service.

In damage tolerance design an initial flaw is assumed to exist in the structure from day 1- when it is manufactured or leaves the factory. In-service damage and damage that may occur during maintenance is also taken into account in evaluating the structure. The idea is to account for the assumed initial defects in such a way that they will be not allowed to reach critical size during the life of the component. Airframe components, for example, are being designed according to damage tolerance concept since the 1970´s.

Components designed on the basis of safe life concept are frequently observed to have appreciable remaining life after being discarded.

2.1. Fatigue Life Prediction Models

2.1.1. The S-N curve

An S-N curve, sometimes also called a Wohler curve, is obtained from fatigue tests at different stress levels. Figure 10 gives an example of such results for unnotched specimens of CrMo steel (SAE 4130). In these tests[1] the average stress is $S_m = 0$, and in consequence the stress ratio is $R = S_{min}/S_{max} = -1$. The variable in Figure 10 is the stress amplitude S_a. The stress amplitude is plotted in a logarithmic scale. The stress is usually represented in a linear or logarithmic scale. The log scale is preferred because it leads to an approximately linear relation of log S_a and log *N*. This linear relation can be written as:

$$S_a^k \cdot N = constant \tag{2}$$

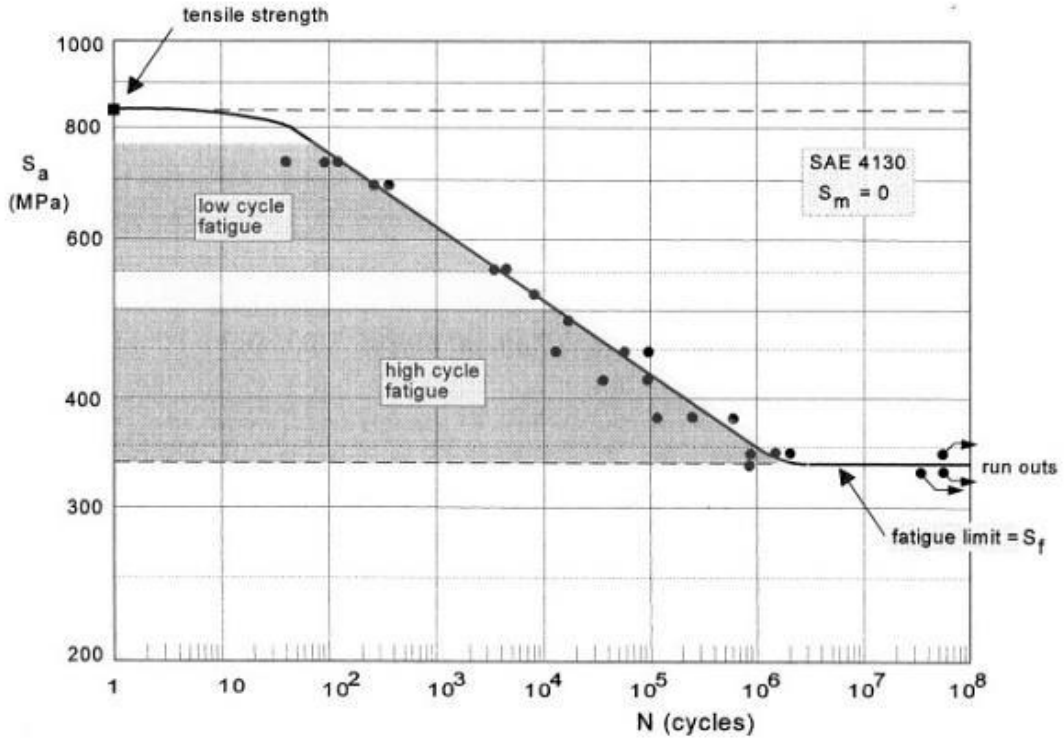


Figure 10 - Fatigue test results of unnotched specimens of a low alloy steel (SAE 4130) [1].

This relation is known as the Basquin equation. The slope of the linear part is equal to *1/k*. Some remarks concerning Figure 10 should be made:

I. Experiments for the same S_a do not all give the same fatigue life. Scatter between results of similar tests occurs.
II. The simple S-N data in Figure 10 require an expensive test program.

[1] A list of symbols is provided in the beginning of this thesis. In general, stress will be represented by σ; however, since 2.1 is mainly based in ref [1], the notation used in that book was kept in this section.

III. The lower asymptote is the fatigue limit S_f.

2.1.2. Damage Tolerance

When the crack growth phase covers nearly the whole fatigue life, safety factors on fatigue crack growth have to be considered. In welded structures, crack initiation is possible from weld defects, but also at the weld toe due to local profiles creating stress concentrations. These situations cannot be always avoided. Due to this fact, it could be needed to reflect on fatigue lives with an almost zero crack initiation phase, i.e. fatigue life which is almost equal to the crack growth period. In these cases, fatigue crack growth should be predicted.

Two situations can be defined: (i) the crack growth period until failure should be larger than the design life time of the structure because inspections for cracks in service are unwanted or not practicable, or (ii) the crack growth is accepted, but the occurrence of a complete failure is prevented by periodic inspections.

For example in aircraft structures crack growth is accepted and the damage tolerance requirements are specified in official airworthiness regulations; the same happens in other structures if inspections can be done in a trustworthy way and fatigue failures are not acceptable. Predictions of fatigue crack growth starts from an initial crack length a_0, which is normally associated with typical initial defects, until a final critical crack size a_c. The critical crack length at the end of the fatigue life depends of the critical condition considered. The stress intensity factor increases as the crack grows until the end of crack growth life. The critical crack length normally is reached when the maximum value of the stress intensity factor (K_{max}) is $K_{max} = K_c$ or $K_{max} = K_{Ic}$ (K_c and K_{Ic} are plane stress and plane strain fracture toughness respectively), depending on the state of stress. The crack growth life does not heavily depend on the final crack length because the crack growth rate is substantially large in the last part of the crack growth life which therefore covers a small part of the total life.

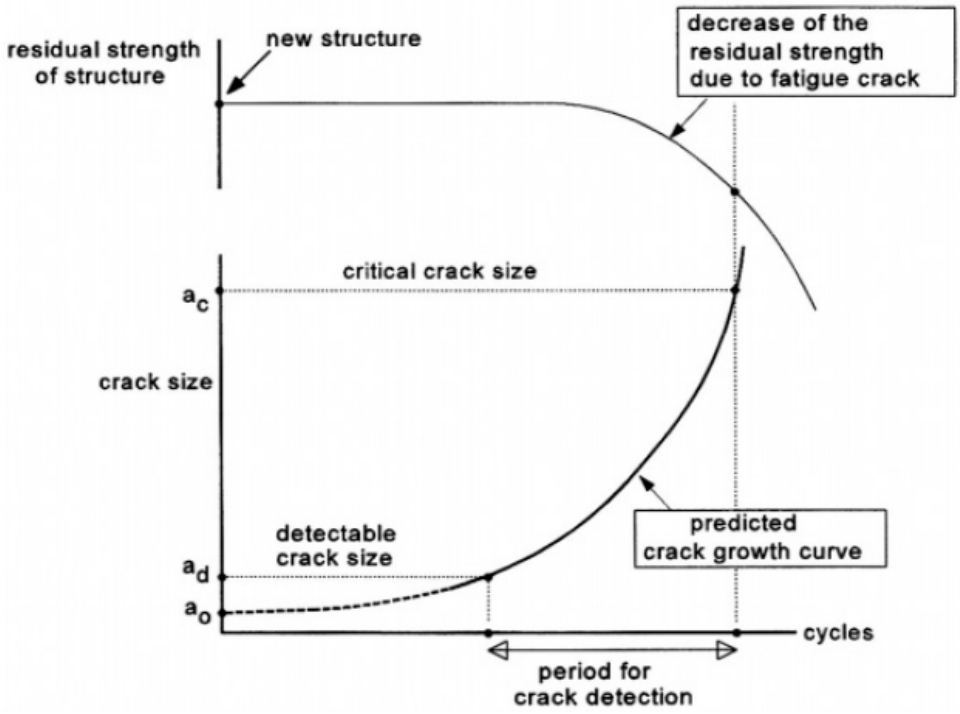


Figure 11 - Principle of safe life crack growth by periodic inspections [1].

The data required for using this model are (see Figure 11):

- the initial crack length a_0,
- the final crack length a_c,
- the crack growth prediction model,
- the crack growth data of the material, and
- the load spectrum.

The chosen initial length a_0 is a matter of concern. In a more conservative approach a large a_0 value should be chosen, but it must make sense. The size of possible defects should be considered. In constant amplitude (CA) - load spectrum crack growth prediction model is less critical than for variable amplitude (VA) -load situation. In the CA-loading case, prediction should give reasonably reliable results provided that stress intensity factor (K) solutions are available. Predictions on crack growth during VA-loading offer problems due to interaction effects and ignoring these effects should be expected to give a conservative prediction. The CA crack growth data used in the prediction are also subjected to uncertainties. When there are doubts about the severity of the load spectrum a safety factor should be applied on the stress amplitude or on the number of cycles in the load spectrum. Schijve [1] indicates that safety factor of 1,5 on stress is normally appropriate, which according to the Paris relation might correspond to a safety factor on number of cycles to failure in the order of 4 (calculated as $1{,}5^{3{,}5} = 4{,}13$). High safety factors values lead to insufficient crack growth life and the safety analysis must be reconsidered in order to obtain more feasible predictions. In some cases service simulations experiments have to be carried out to obtain more reliable

information. If the crack growth is accepted in the structure and no inspections are made, a profound analysis of all influence factors should be made. If there is the risk of a total failure of the structure, a large safety factor on the crack growth life needs to be used and the possibility of periodic inspections should be considered [1].

2.2. Factors Affecting Fatigue Performance

Parameters such as stress (load), geometry and proprieties of the component, and the external environment affect the performance of structural components. The stress parameters include state of stress, stress range, stress ratio, constant or variable loading, frequency, and maximum stress. The geometry and proprieties of the component include stress (strain) raisers, size, stress gradient, and metallurgical and mechanical proprieties of the base metal and weldments. The external environment parameters include temperature and aggressiveness of the environment.

2.2.1. Fatigue Loading

Structural components can be subjected to two types of load histories: constant amplitude (CA) loading (Figure 12) or variable amplitude loading (VA) (Figure 13). In the constant amplitude load case is possible to observe a mean stress, σ_{mean}; an alternating stress or stress amplitude, σ_{amp}; and a stress ratio, R, Figure 12. The stress range is the algebraic difference between the maximum stress, σ_{max}, and the minimum stress, σ_{min}, in the cycle

$$\Delta\sigma = \sigma_{max} - \sigma_{min} \tag{3}$$

The mean stress is the algebraic mean of $\sigma_{max}$and σ_{min} in the cycle

$$\sigma_{mean} = \frac{\sigma_{max} + \sigma_{min}}{2} \tag{4}$$

The alternating stress or stress amplitude is half the stress range in a cycle

$$\sigma_{amp} = \frac{\sigma_{max} - \sigma_{min}}{2} \tag{5}$$

The stress ratio R, represents the relative magnitude of the minimum and maximum stresses each cycle

$$R = \frac{\sigma_{min}}{\sigma_{max}} \tag{6}$$

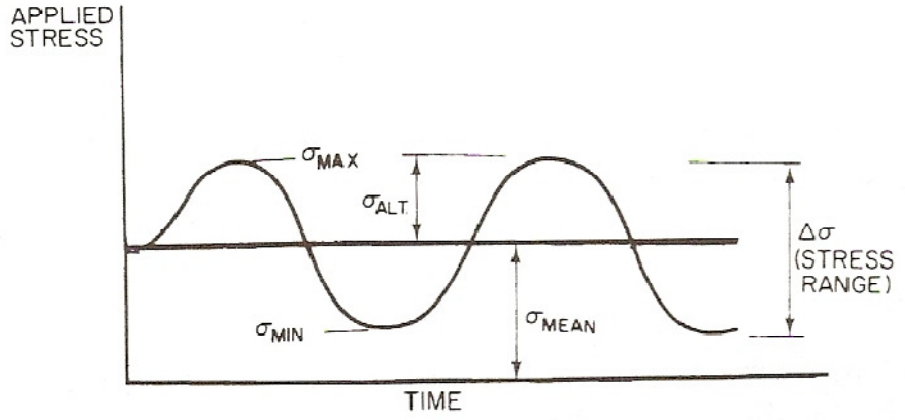


Figure 12 - Terminology in Constant-amplitude fatigue [2].

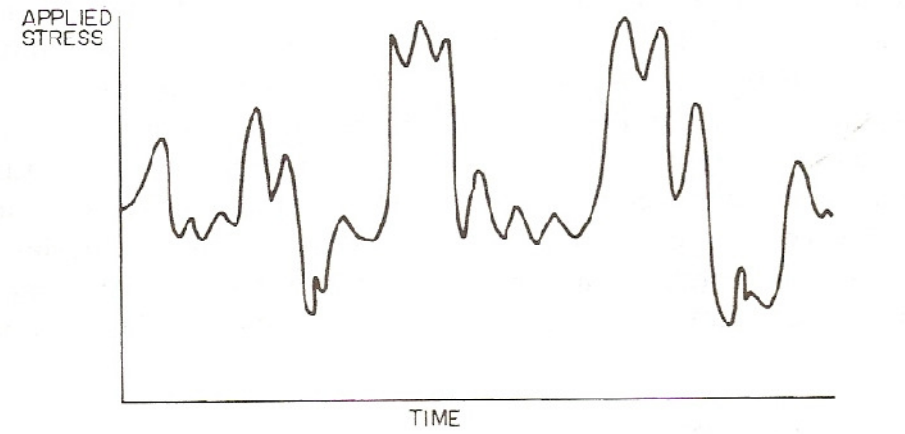


Figure 13 - Random-stress loading [2].

2.3. Fracture Behavior Regions or Regimes

Figure 14 shows the general regions of fracture that shows the increase of fracture toughness with the increase of temperature for typical structural steels.

Region I has an essentially brittle behavior regardless of the loading rate. Materials with this type of behavior should be avoided.

Region II shows an elastic-plastic behavior with increasing plastic zone sizes but unstable crack extension. In this case final fracture is rapid brittle fracture.

Region III has an elastic plastic behavior with large plastic zones and increasing amounts of ductile tearing followed by unstable mixed mode fast fracture, but only after considerable deformation. Stable crack growth would occur.

Region IV has a general yielding behavior, and specimens exhibit stable tearing at fracture.

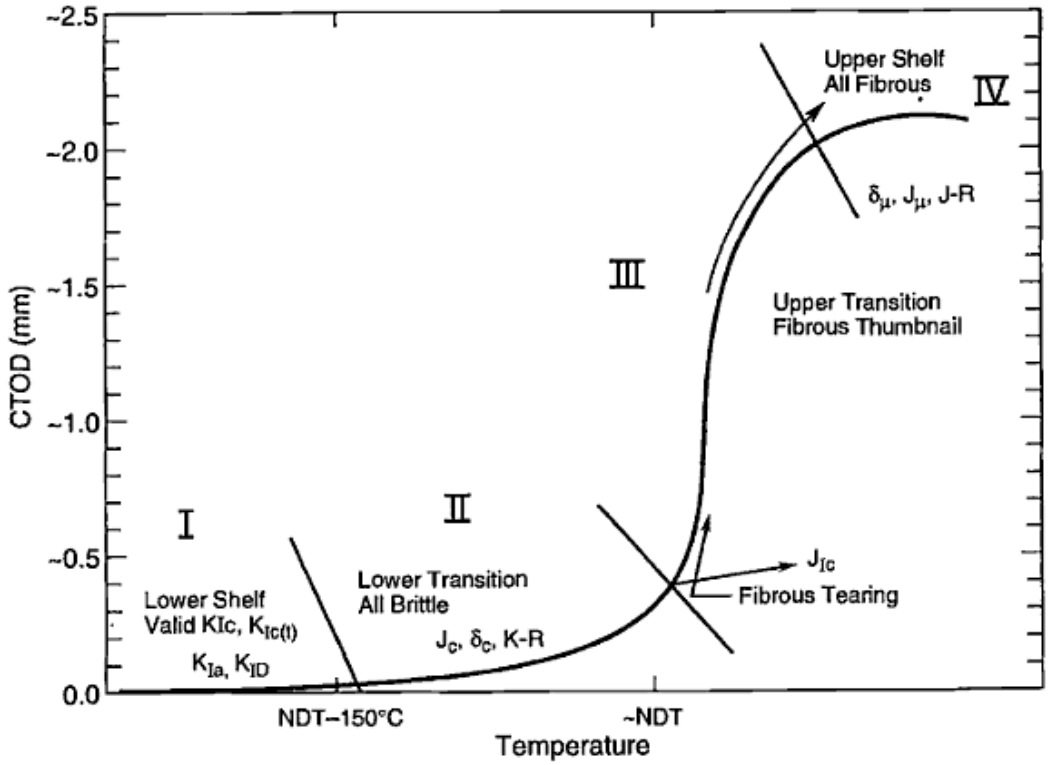


Figure 14 - General regions of fracture behavior for structural steels [2].

2.4. Stress Intensity Factor (SIF)

Stress Intensity Factor, K, is a parameter used in linear elastic fracture mechanics to describe stress state ("stress intensity") near the tip of a crack caused by a remote load or residual stresses. It is a theoretical concept applicable to a homogeneous elastic material and is useful for providing a failure criterion for brittle materials as well as for general application on many fatigue crack growth problems involving metallic materials. Stress intensity factors are function of load, crack size, and geometry. Three of the most common geometries are shown in Figure 15.

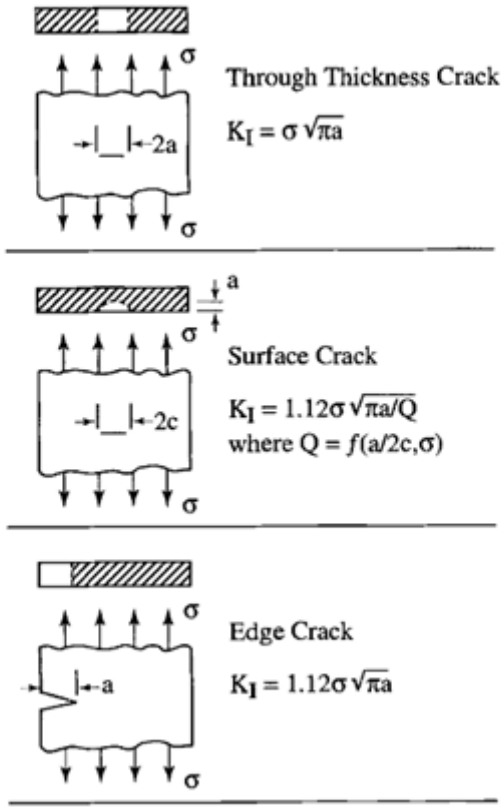


Figure 15 - K_I values for different crack geometries [2].

The value of the SIF is calculated in a cracked member as:

$$K_I = Y\sigma\sqrt{\pi a} \tag{7}$$

for a nominal stress σ, a geometric factor Y and a crack length a.

2.5. Crack Propagation Laws

There are various theories and laws that try to reproduce the behavior of the da/dN *vs*. ΔK curve. From these laws the best known, used and important one is the Paris Law. The Paris Law can be written as:

$$\frac{da}{dN} = C(\Delta K)^m \tag{8}$$

where C and m are taken as material properties and is known as Paris law fracture. The stress intensity factor range used in the da/dN *vs* ΔK is traditionally interpreted as:

$$\Delta K = \begin{cases} K_{max} - K_{min} & \text{for pure tensile loading } i.e.\ K_{min} \geq 0 \\ K_{max} - 0 & \text{for tension} - \text{compression type loading, } i.e.\ K_{min} < 0 \end{cases} \quad (9)$$

Since crack faces will close in compression and no singularity is expected at the tip, it is more logical to ignore the compressive part of the loading and just take the tensile range as damaging. Welded structures are exceptions to this generalization, however, because of the very wide range of values including high tensile residual stresses that may occur in weldments. It is then customary to use the full value of $K_{max} - K_{min}$ even if $K_{min} < 0$, ref. [4].

Paris equation (8) is a simple relation but is not capable of accounting for mean load effects, for threshold behavior for accelerated growth near K_c. More sophisticated relations have been proposed to reflect such factors. Forman equation

$$\frac{da}{dN} = \frac{C\Delta K^m}{(1-R)K_c - \Delta K} \quad (10)$$

is a popular one and identifies correctly fatigue crack propagation (FCP) response under combinations of high ΔK and ΔK_{mean} conditions, but it is sometimes difficult to apply since K_c is difficult to determine. Forman equation is reported to give good results with Al-Alloys and high strength steel but overestimates mild steel behavior. Major divergence may occur in predictions for CA-loading in the $R < 0$ range if the calculation is made with those Forman parameters determined for $R > 0$. As a general rule, though, predictions are conservative when "$R > 0$ parameters" are used.

The relation proposed Walker:

$$\frac{da}{dN} = C\left[\frac{\Delta K}{(1-R)^n}\right]^m \quad (11)$$

exhibits a particularly strong dependence upon R. the value of n should be determined from experimental data along with C and m; n=0.5 is a typical value used in literature.

$$\frac{da}{dN} = C(\Delta K - \Delta K_{th})^m \quad (12)$$

and

$$\frac{da}{dN} = C\left(\frac{\Delta K - \Delta K_{th}}{K_c - K_{max}}\right)^m \quad (13)$$

are other suggested relations reflecting the departures from power law behavior at high and low ΔK values. Figure 16 shows a typical fatigue crack propagation behavior.

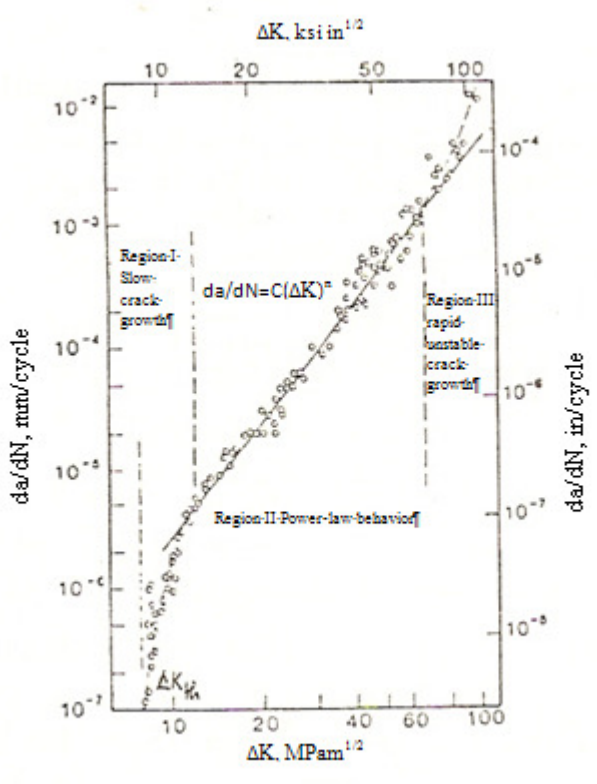


Figure 16 - Typical fatigue crack propagation behavior (A533B steel) [4].

All of the above cited relations are empirical and are not developed considering basic mechanisms of FCP. The differences among them are not large and none of them has general applicability. Each one may be found to be reasonably satisfactory in a limited region or for limited sets of data.

From these crack propagation laws the component fatigue life can be calculated by the integration between the initial crack value a_0 and the critical crack size a_c. For example for the Paris law:

$$\frac{da}{dN} = C(\Delta K)^m \tag{8}$$

with

$$\Delta K = Y\Delta\sigma\sqrt{\pi a} \tag{14}$$

Making the integration of the Equation 8

$$N = \int_{a_0}^{a_c} \frac{da}{C\left(Y\Delta\sigma\sqrt{\pi a}\right)} \tag{15}$$

which (for Y not changing within the limits of integration) will yield:

$$N = \frac{2}{(m-2)CY^m \pi^{m/2} \Delta\sigma^m} \left[\frac{1}{a_c^{\frac{m-2}{2}}} - \frac{1}{a_0^{\frac{m-2}{2}}} \right] \tag{16}$$

Note that $m \neq 2$ in this integration and a_0 and a_c denote the integration limits, namely the initial and final crack sizes. For $a_0 \ll a_c$ the computed fatigue life is not sensitive to the final crack length a_c but, instead, is strongly dependent on estimations of the starting crack size a_0. Thus, it becomes crucial to correctly determine a_0, which is the major problem in estimations of life combining the initiation as well as the propagation phases. The final size a_c, here, could be the critical size based on the fracture toughness of the material or a convenient length to determine the next inspection interval. Plastic collapse criterion may apply in the case of very ductile materials.

2.5.1. The Compact Tension Specimen (CTS)

The compact tension type of specimen is used for an experimental determination of fracture toughness, or of FCP crack laws. In fracture toughness testing, the first step is to define the main dimensions like thickness (B) depth or width (W), and crack length (a) as shown in Figure 17. In the case of plane strain fracture toughness, K_{Ic}, all dimensions are univocally related with B.

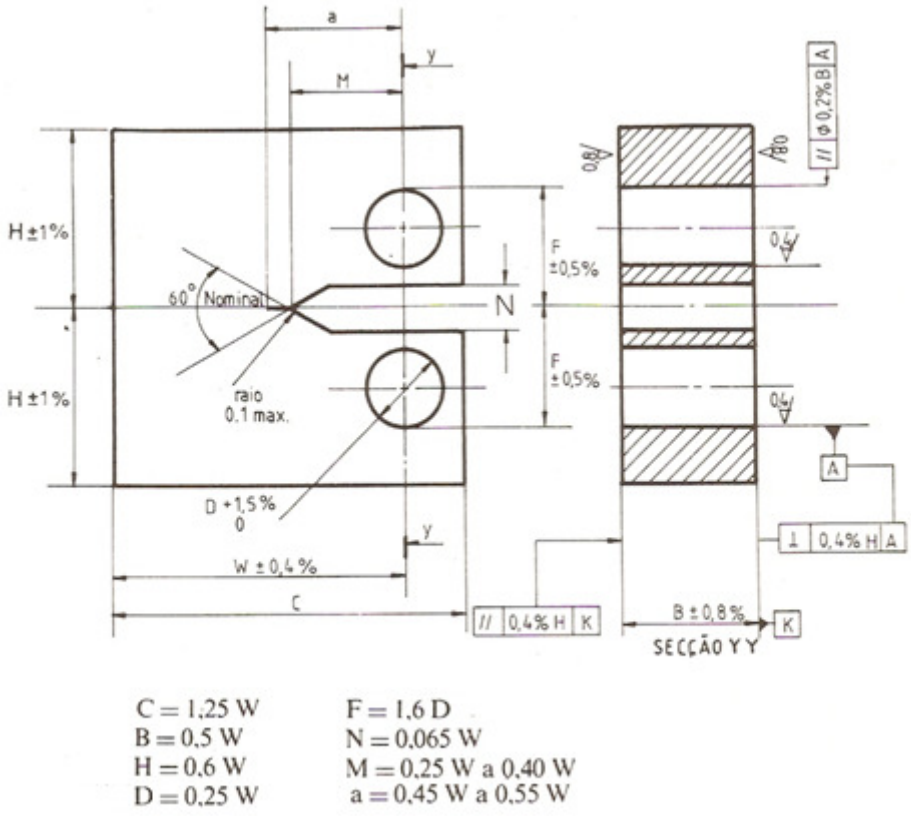


Figure 17 - Values of the CT specimen dimensions for K_{Ic} measurements, *e.g.* ASTM E399 [5].

The other specimen dimensions are length (C = L) and height (H) are of less importance, but still are prescribed in each test standard. Ideally the specimen thickness, B, should fulfill the given requirements such as the ones given below for K_{Ic} testing according to ASTM standard E399 [6]:

$$a = crack\ depth \geq 2{,}5\left(\frac{K_{Ic}}{\sigma_{ys}}\right)^2 \tag{17}$$

$$B = specimen\ thickness \geq 2{,}5\left(\frac{K_{Ic}}{\sigma_{ys}}\right)^2 \tag{18}$$

$$W = specimen\ width \geq 5{,}0\left(\frac{K_{Ic}}{\sigma_{ys}}\right)^2 \tag{19}$$

These requirements are hard to meet in most steels for welded structures. Therefore the plate thickness of interest, B, is usually adopted.

The maximum K_{Ic} that can be measured for a specimen of thicknes B is:

$$K_{Ic} = \sqrt{\frac{B}{2{,}5}}\sigma_{ys} \tag{20}$$

For K_{Ic} tests a load versus displacement should be obtained, and K_{Ic} is calculated for the minimum load where the preexisting fatigue crack begins to grow, and is equal to:

$$K = \frac{P}{BW^{1/2}} f(a/W) \tag{21}$$

where $f(a/W)$ is equal to:

$$f(a/W) = \frac{(2+\alpha)}{(1-\alpha)^{3/2}}(0.886 + 4.64\alpha - 13.32\alpha^2 + 14.72\alpha^3 - 5.6\alpha^4) \tag{22}$$

The present work will not concern toughness determination, and so above references to minimum specimen thickness necessary for a given K_{Ic} value are not relevant here. Nevertheless, the considerations above concerning thickness of interest B will be used in the selection of thickness for the present FCP CT specimen, which follow the ASTM E647 standard. Whilst planar dimensions follow the relationships given above for the E399 standard, the thickness may be chosen in a wider range of values.

For the experimental crack laws determination, crack length "a" versus number of cycles "N" curves should be obtained. Before the beginning test, a fatigue precrack needs to be made in the specimen.

3. Experimental

3.1. Material

Material similar to the one present in the real bridge in construction was provided by Teixeira Duarte SA. Some of the data provided is included here for the base and welded material.

The base material used was the steel grade S355NLZ15 according to EN 10025, EN10029 and EN 10163, with the chemical composition presented in Table 1.

Table 1 - Chemical composition of the S355NLZ15 steel (base material).

Steel grade	Item nº	C (%)	Si (%)	Mn (%)	P (%)	S (%)	Al (%)
S355NLZ15	2	0,14	0,28	1,23	0,013	0,004	0,027
	20	0,13	0,24	1,11	0,011	0,005	0,022

N (%)	Cr (%)	Cu (%)	Ni (%)	Ti (%)	V (%)	Nb (%)
0,007	0,008	0,31	0,29	0,016	0,044	0,001
0,007	0,006	0,25	0,27	0,013	0,043	0,001

Some mechanical proprieties were also given (Table 2).

Table 2 - Some mechanical proprieties of the base material.

R_{eh} (N/mm^2)	R_m (Nmm^2)	Elongation (%)	Charpy [J] at T= -50º
400	557	27,7	176
405	516	30,2	118

According to ISO E6947[2] standard PF stands for ascending vertical welding direction, and PC stands for horizontal welding. A set of welding procedure qualification (WPQ) certificates according to standard EN ISO 15614-1:2004 [3]were provided concerning PF and PC positions of welding for cored metal arc welding with active gas shield (according to ASME: flux cored arc welding). This process is given the reference 136 according to the standard EN ISO 4073:2004[4]. All certificates indicate 100ºC preheating

[2] Welding and allied processes -- Welding positions

[3] Specification and qualification of welding procedures for metallic materials -- Welding procedure test -- Part 1: Arc and gas welding of steels and arc welding of nickel and nickel alloys

[4] Welding and allied processes. Nomenclature of processes and reference numbers.

and an interpass temperature lower than 250ºC. Qualification certificates are available for thicknesses of 25 and 60 mm. The first (25 mm) corresponds to an approval range of thicknesses of 12,5 to 50 mm. The second (60 mm) corresponds to an approval range of thicknesses from 30 up to 120 mm.

The thickness of interest in the present work (original plates' thickness of 33 mm) is therefore covered by both WPQ procedure certificates for 25 or 60 mm.

It is therefore appropriate to present here a synthesis of the data available in the mentioned WPQ certificates. This is given as Table 3.

Table 3 - S355NL steel: welding process 136 WQP according to EN ISO 15614-1:2004.

Certificate; Position		Thickness [mm]	Rupture stress [MPa]	Charpy [J] at T= -50º		
				BM	HAZ	WM
08.L.1838	PF	25	525	67	75	80
08.L.1839	PC	25	555	154	173	96
08.L.1854	PC	60	533	143	133	71
08.L.2457	PC	25	555	140	55	34
08.L.2827	PC	60	528	69	83	75

3.1.1. Metallographic Study

A metallographic study was performed.

Samples were removed from a welded plate, subjected to the same welding parameters as weldments of the real bridge.

3.1.1.1. Samples

Two samples were extracted from a welded plate. The first sample was taken from the top of the welded plate as shown in Figure 18.

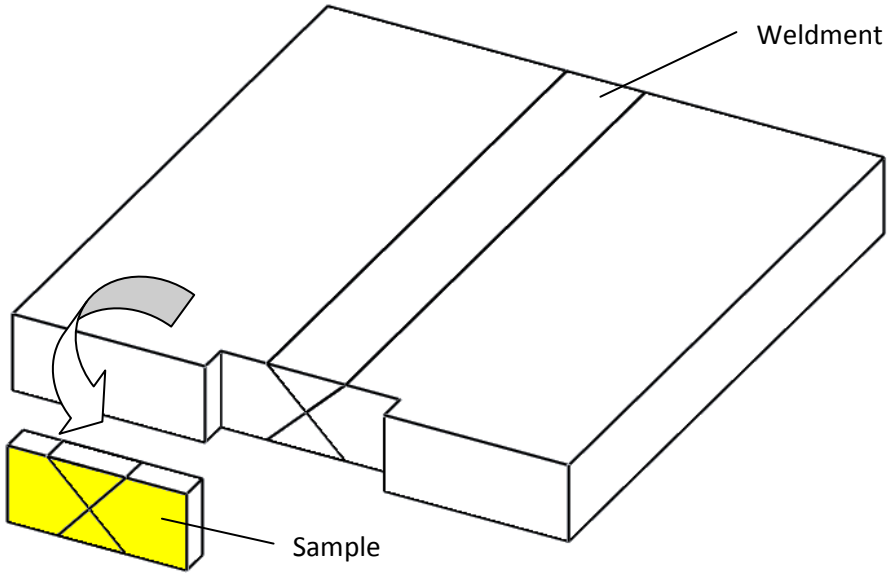


Figure 18 - Zone of the welded plate where the first sample was taken.

The second sample was taken from a zone distanced 100 mm away from the welded plate. Figure 19 shows the location of the second sample in the welded plate.

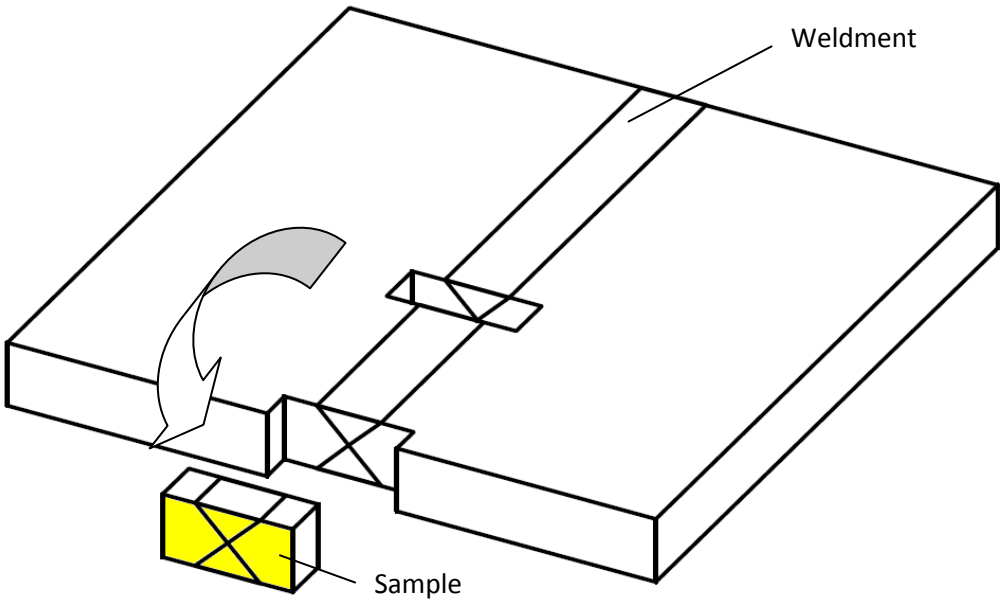


Figure 19 - Representation of the zone of the welded plate where the second sample was taken.

First Sample

Microstructures were acquired in different zones: transition between welded and base material; welded material; and base material. In Figure 20 the macrostructure of the

steel weld specimen is presented. In the macrostructure the different zones (Base Material - BM, Heat Affected Zone - HAZ, and Welded Material - WM) are identified.

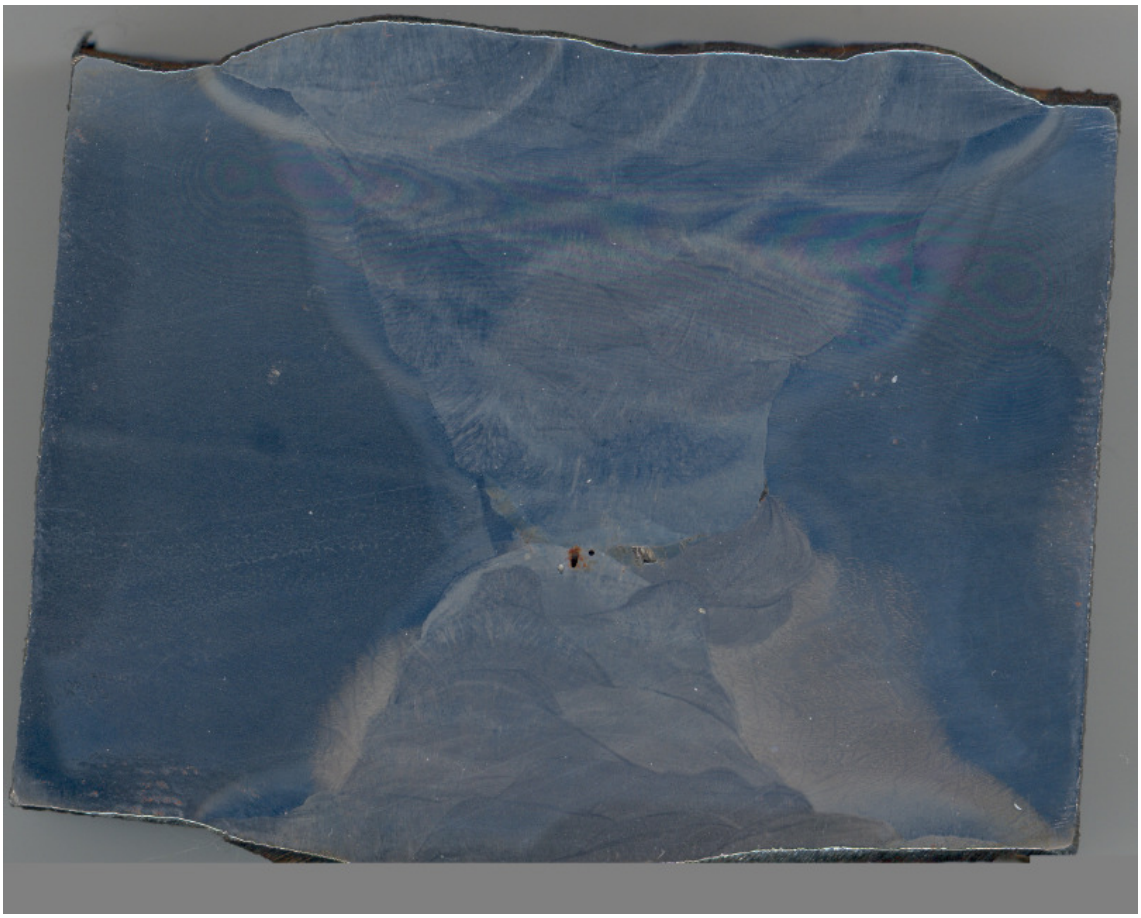


Figure 20 - Macrostructure of the welding (first sample).

As it can be seen in Figure 20, the first sample observed contained several defects, including various cracks. The presence of various cracks in this sample, is due to the sample location at one of the tops of the welded plate, where the welding process started. The cracks observed are probably related to insufficient pre-heating in this region, which is anyway a typical region for weld defects. Microstructures of some cracked zones are shown in Figures 21 and 22.



Figure 21 - Microstructure of two cracked zones ;above interface between weld metal (right) and base metal (left); below, inter-run zone.

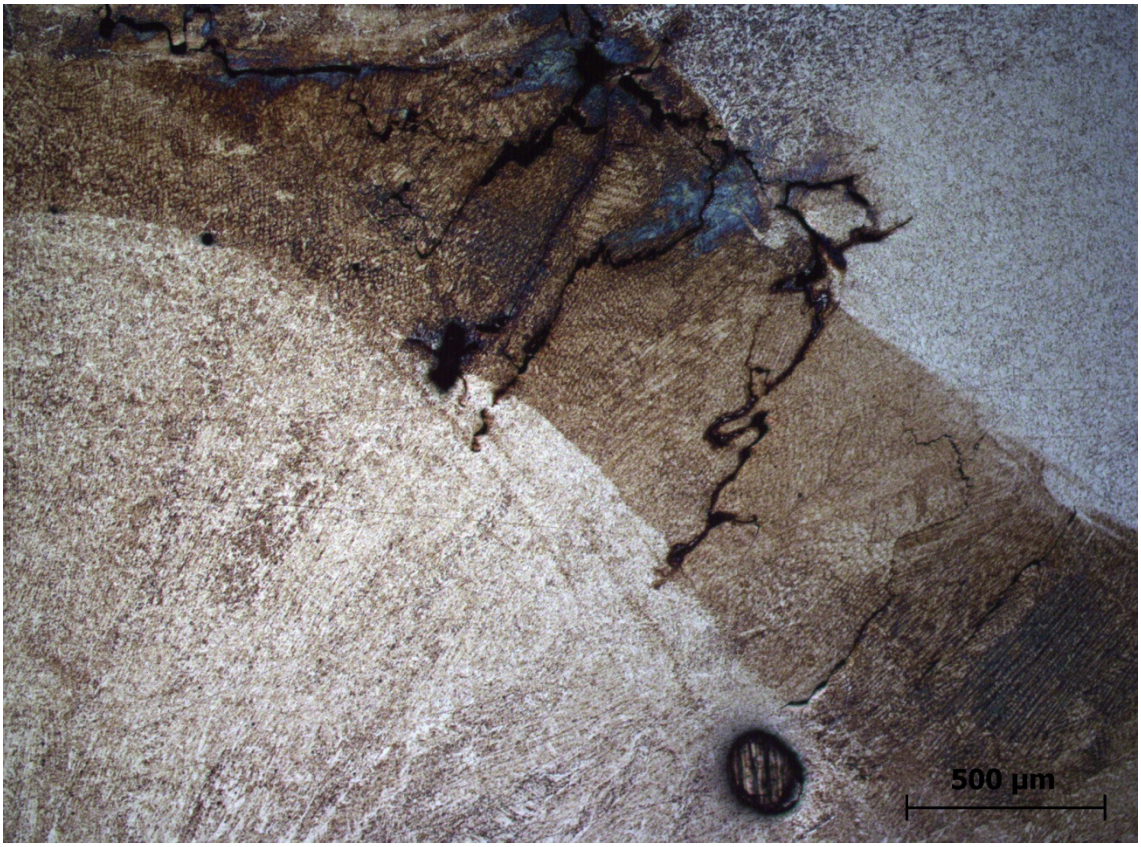


Figure 22 - Microstructure of cracked zone.

Vickers hardness values were measured near cracked zones (Figure 23), in order to analyze this damage and test the hypotheses mentioned above.

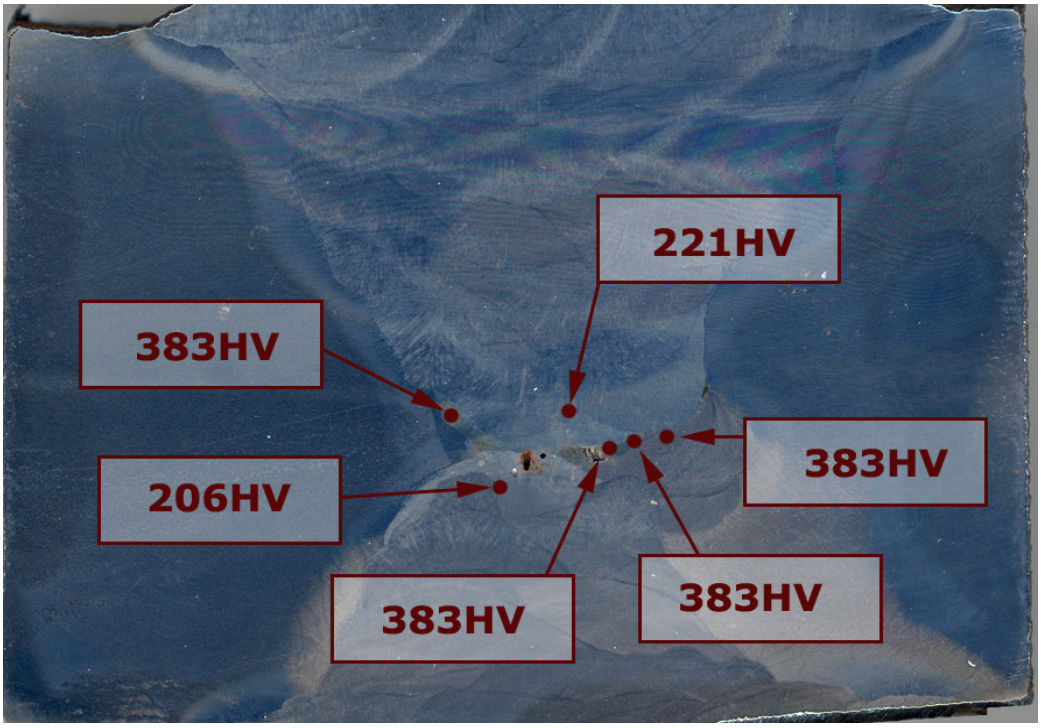


Figure 23 - Macrostructure of the steel weld with the respective hardness points measured (first sample).

High hardness values were measured near to the crack locations. In those zones martensitic areas probably exist (383 HV), suggesting that there was a lack of pre-heating in the beginning of the welding procedure.

This sample is not representative of the welding which is intended to be studied; hence a second sample was analyzed further away from the welding start point.

Second Sample

The macrostructure of the second sample is shown in Figure 24.

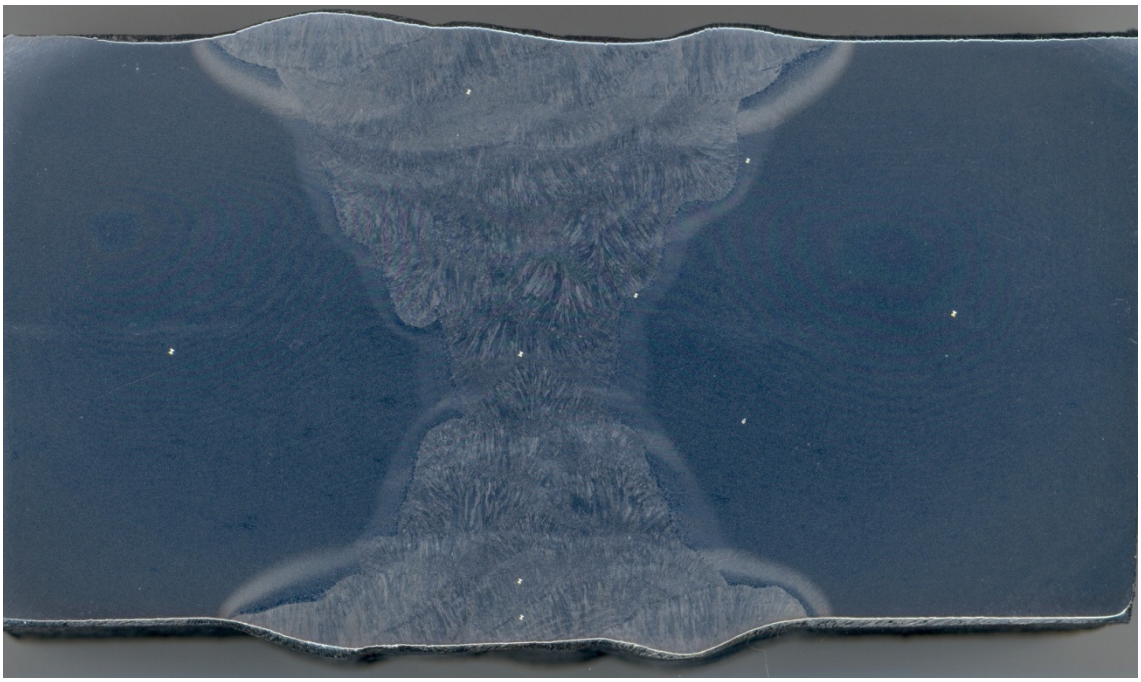
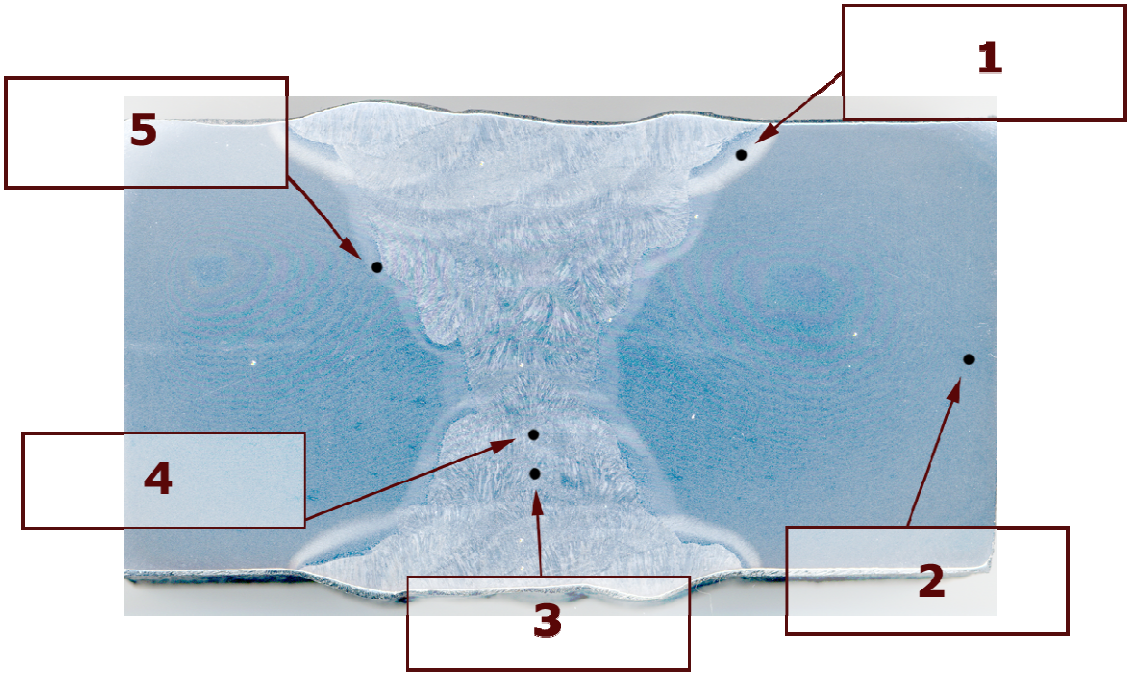


Figure 24 - Macrostructure of the welding (second sample).

In this second sample, and as expected, the welding cross section presents a nearly perfect structure, where it is possible to distinguish the three different zones of the welding (BM, HAZ, WM).Various pictures of microstructures of the studied welding were made in five different location as shown in Figure 25 (HAZ-1 and 5; WM-3 and 4; BM-2), to analyze the various microstructures.



nes from where the

Next, some hardness measurements were performed in various regions of the weld. Those measurements are represented in the Figure 26.

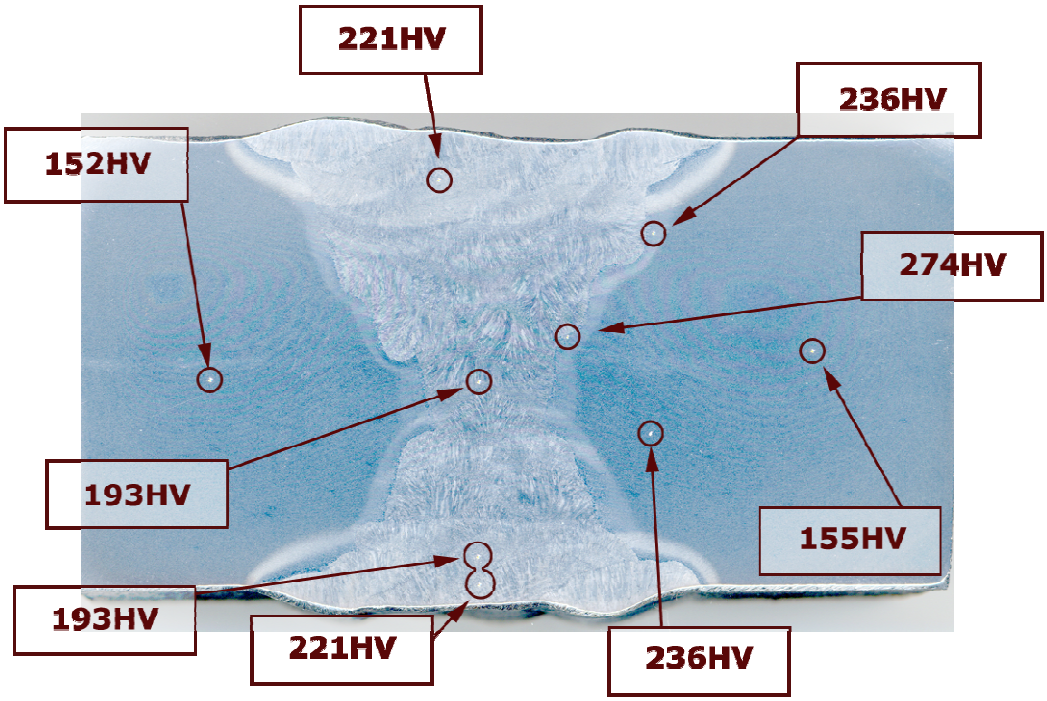


Figure 26 - Macrostructure of the steel weld with the respective hardness points measured (second sample).

The hardness measurements agree with the expectations from this steel type and welding procedure along the different zones of the welding (BM, HAZ, WM).

The microstructures of the various zones are shown in Figures 27 to 33.

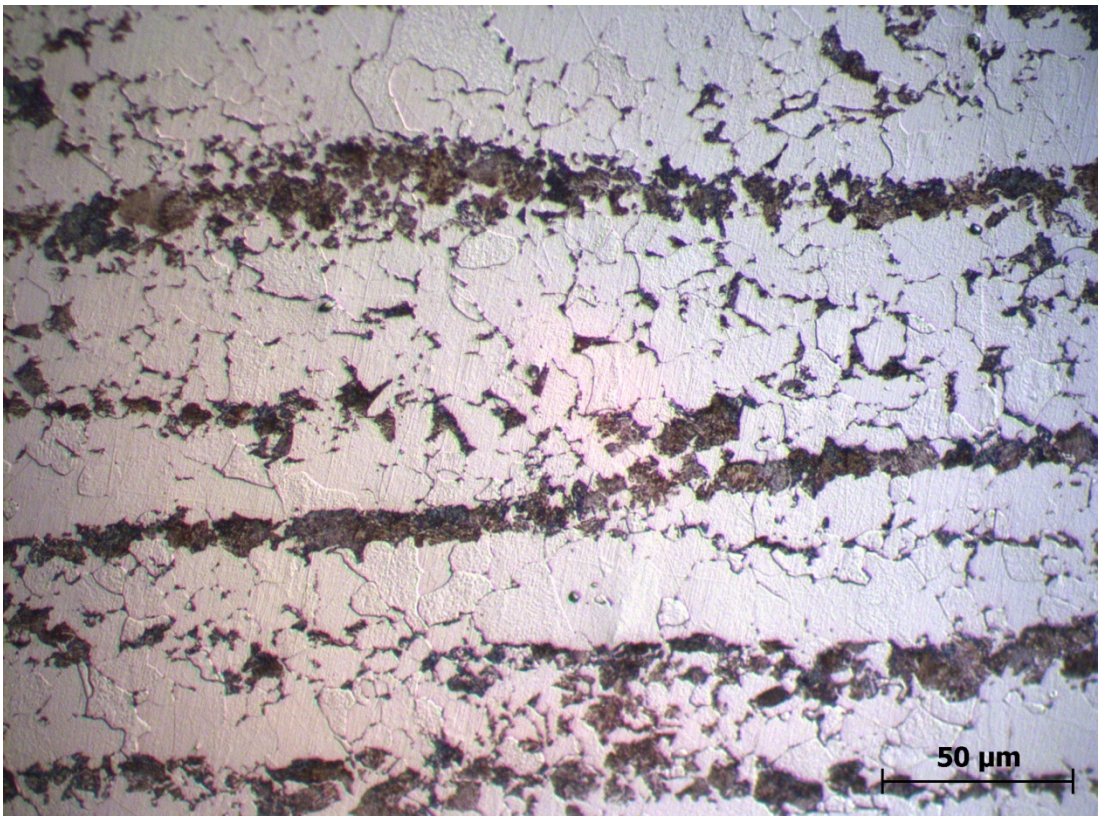


Figure 27 - Microstructure ferritic-perlitic of the Base Metal, zone 2 of Figure 25.

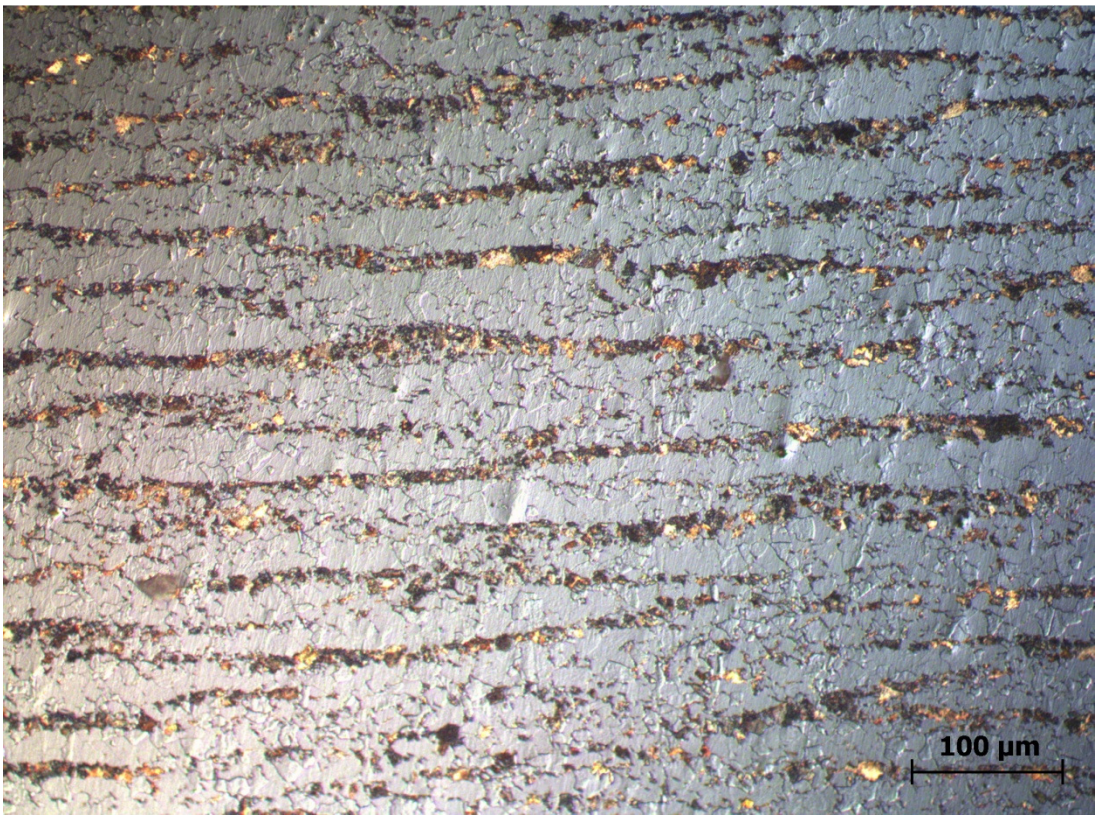


Figure 28 - Microstructure ferritic-perlitic of the Base Metal (DIC), zone 2 of Figure 25.

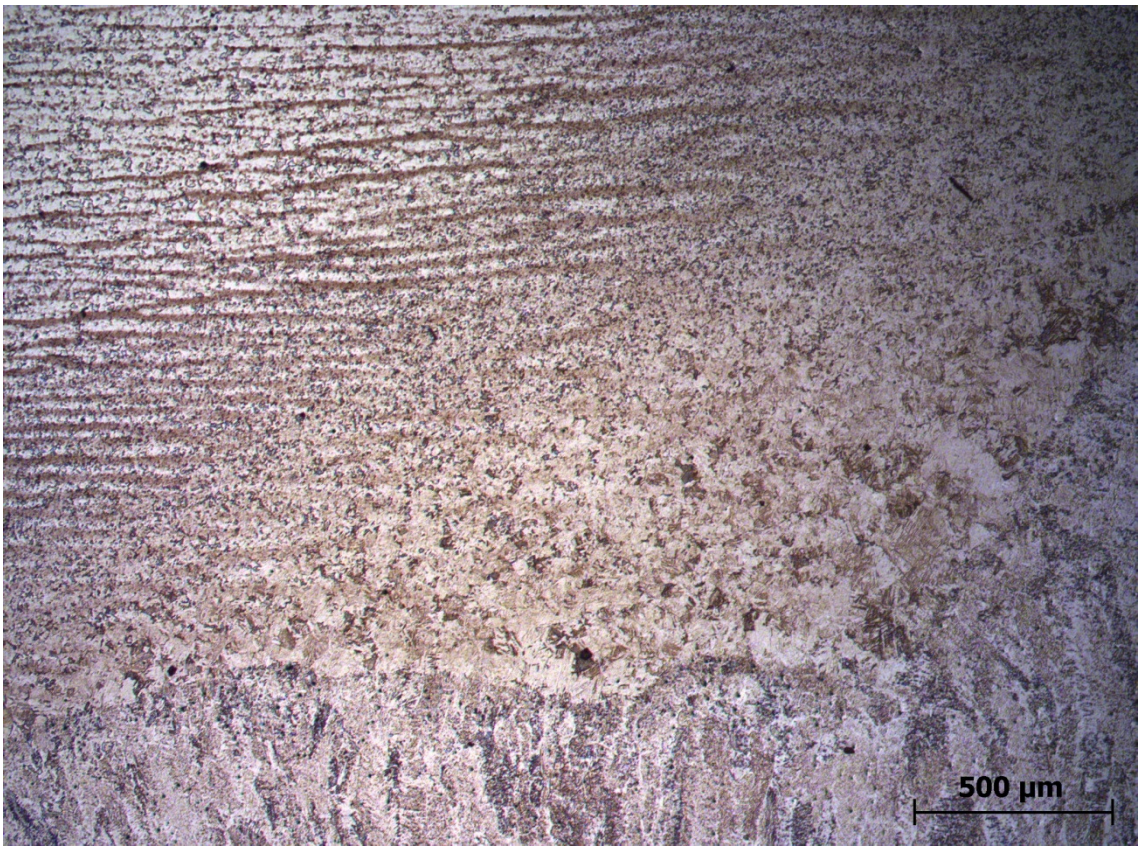


Figure 29 - Microstructure of the Heat Affected Zone material; zone 5 of Figure 25.

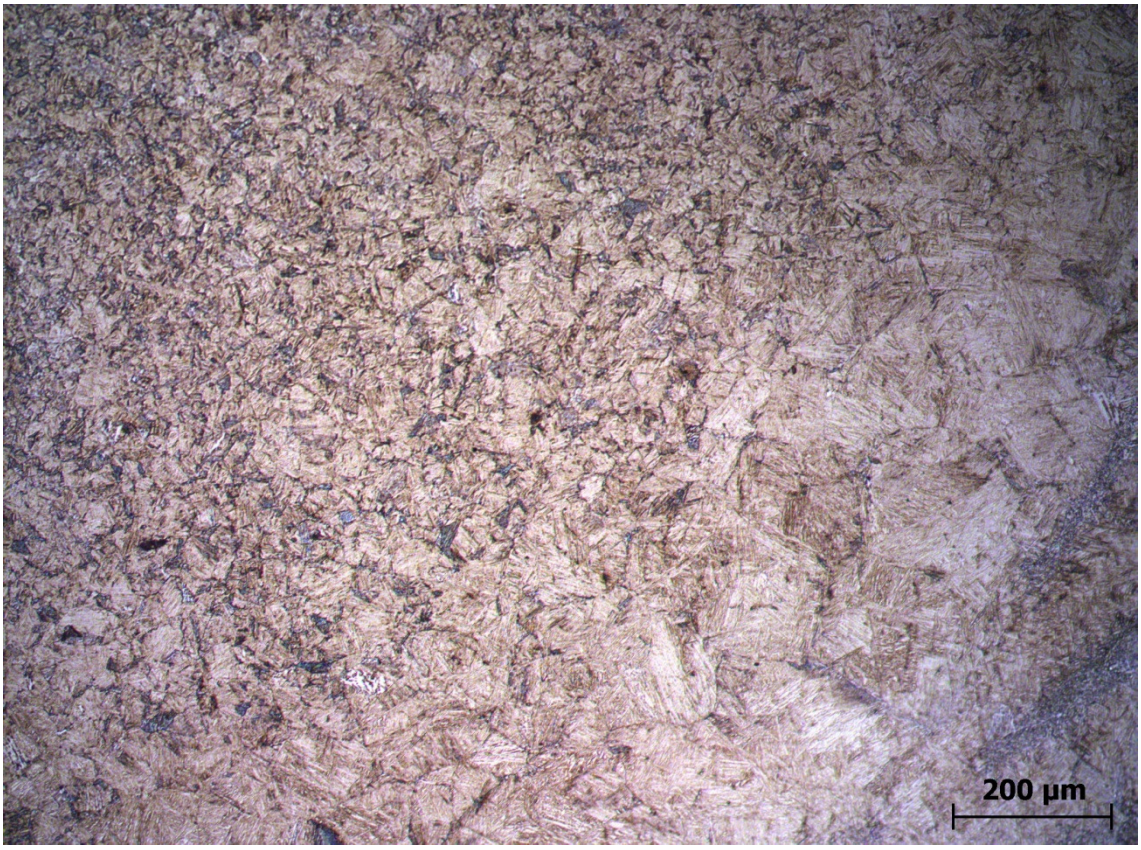


Figure 30 - Microstructure of the Heat Affected Zone material coarse grain zone, essentially bainitic; zone 1 of Figure 25.

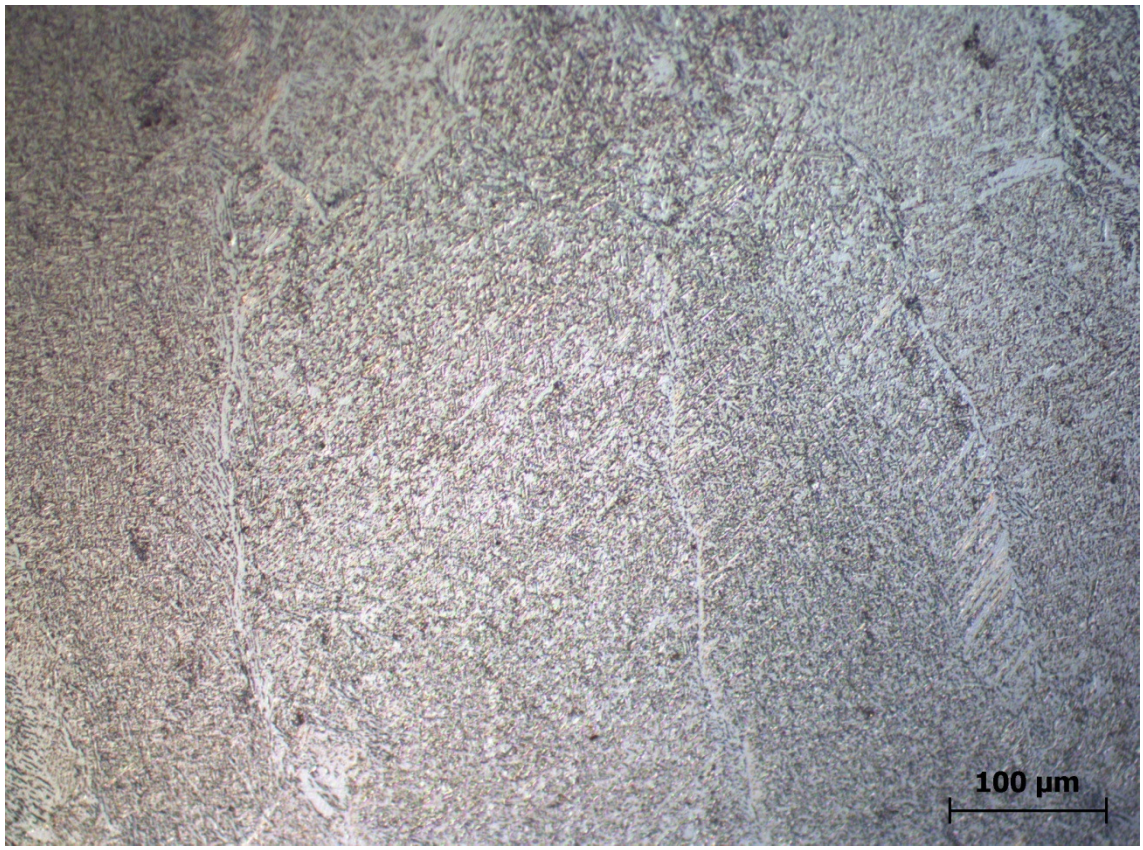


Figure 31 - Microstructure of the Welded material composed of acicular ferrite and proeuctectoid ferrite (boundary ferrite); zone 3 of Figure 25.

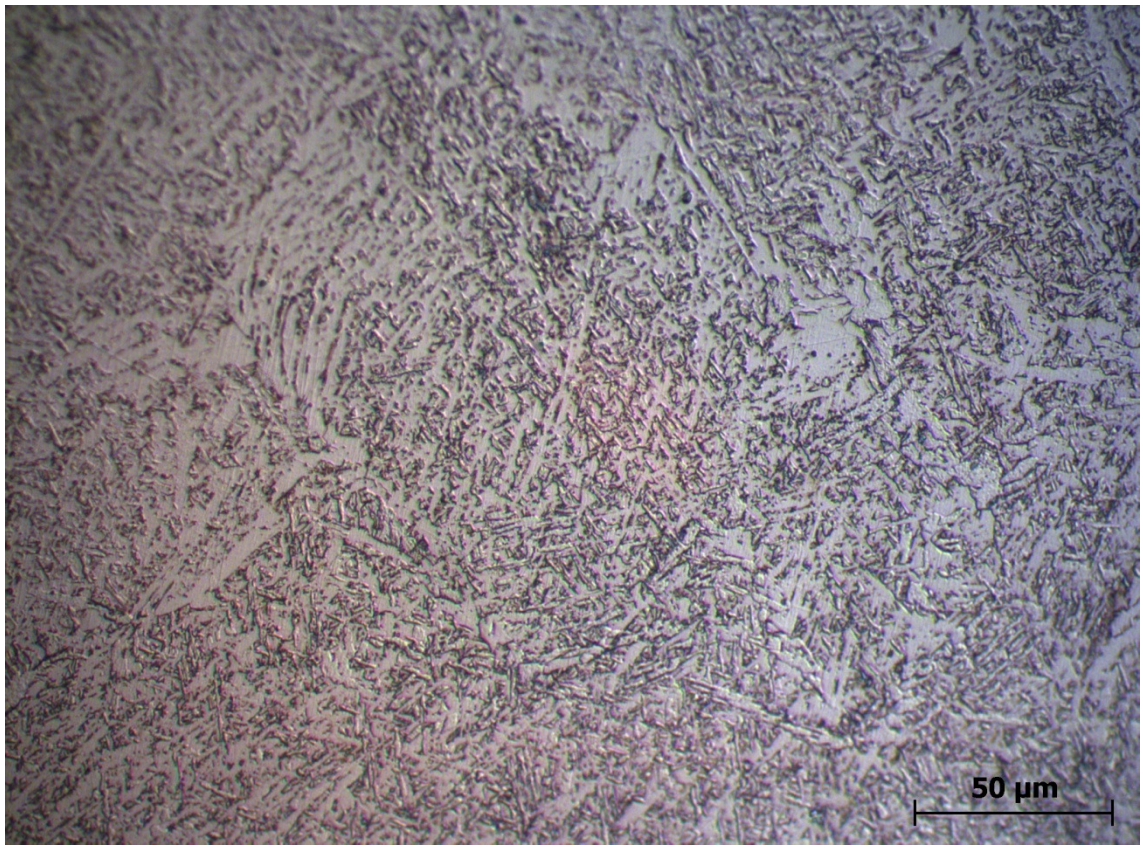


Figure 32 - Microstructure of the melded material: detail of Figure 30 showing acicular ferrite.

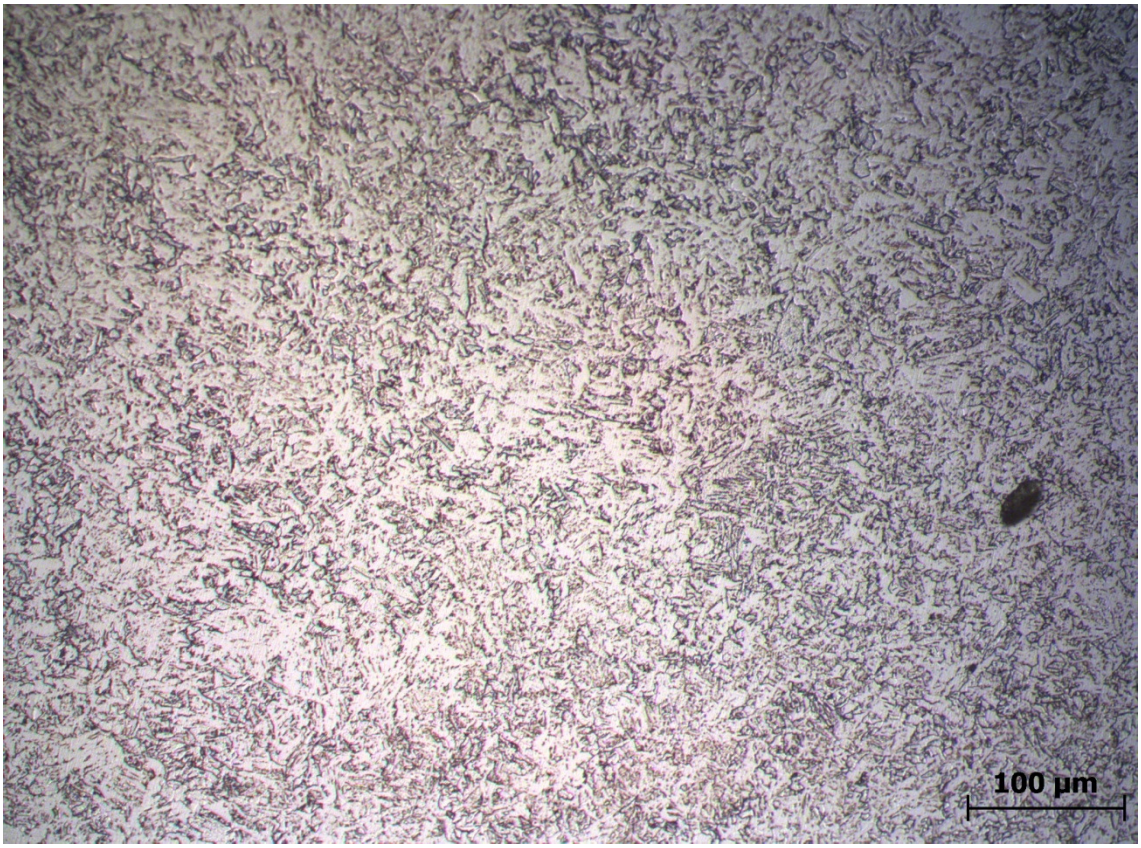


Figure 33 - Microstructure of the welded material: inter-run zone. Zone 4 of Figure 25.

The observed microstructures indicate the quality of the weld and are in conformity with what is expected for this type of steel and welding procedure. The base material presents a mostly ferritic structure (light zones in Figure 26), with some perlite (dark zones); this can be explained by the carbon percentage, since it is a hipoeutectoid steel ($\%C < 0{,}86$). The HAZ (Figure 30) shows a mainly bainitic structure near the fusion line with 274 HV. In the WM (Figure 31 to 33), two zones are observed:

i. solidification microstructure constituted by boundary proeuctectoid ferrite plus acicular ferrite (Figures 31 and 32);
ii. inter-run zone with a typical line annealed structure.

Vickers Hardness Test

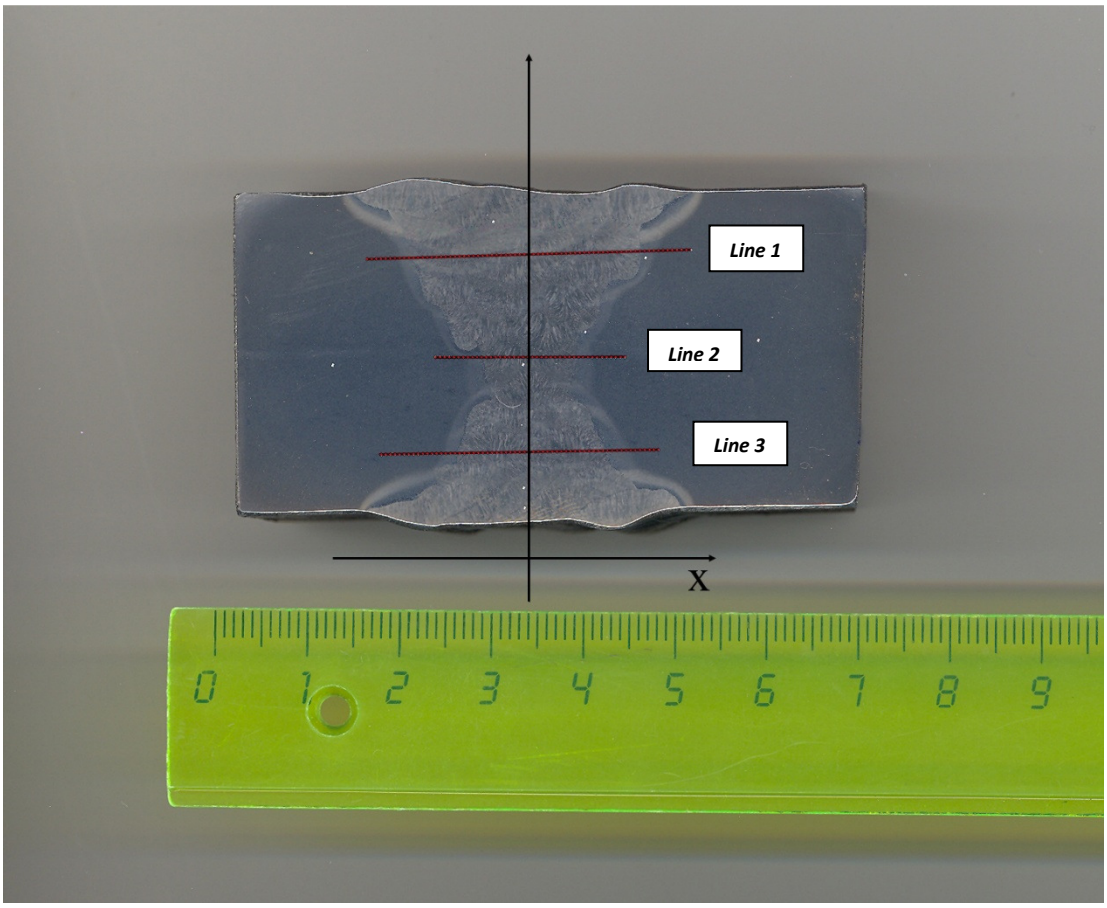


Figure 34 - Representation of the zones where the hardness measurements were carried out.

Three Vickers macrohardness filiations were carried out with a 5 kgf load. The measurements were made on the specimen along three longitudinal directions, close to the upper and lower surfaces (line 1 and 3 of Figure 34) and one in the central region, always with a 0.5 mm distance between consecutive measurements according with the ASTM E62 standard [7]. A macro photograph is shown in Figure 34 with the three lines of hardness measurements represented. As expected, for lines 1, 2 and 3 (Fig. 35, 36 and 37) the peak hardness values occur for the HAZ near the fusion line. The hardness of the base metal, given by the results obtained for line 2, varies between 170 and 180 HV.

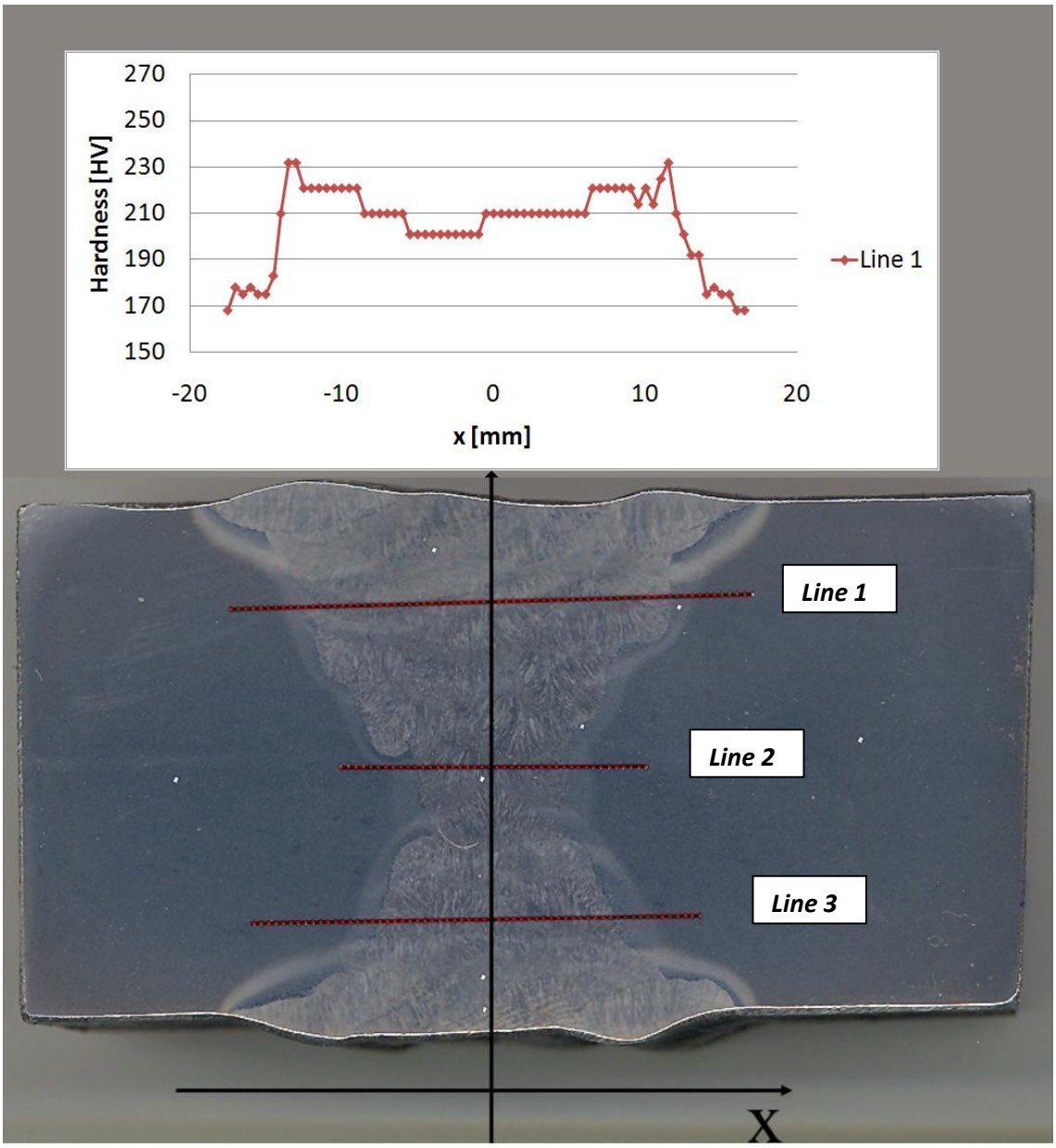


Figure 35 - Line 1 hardness measurements.

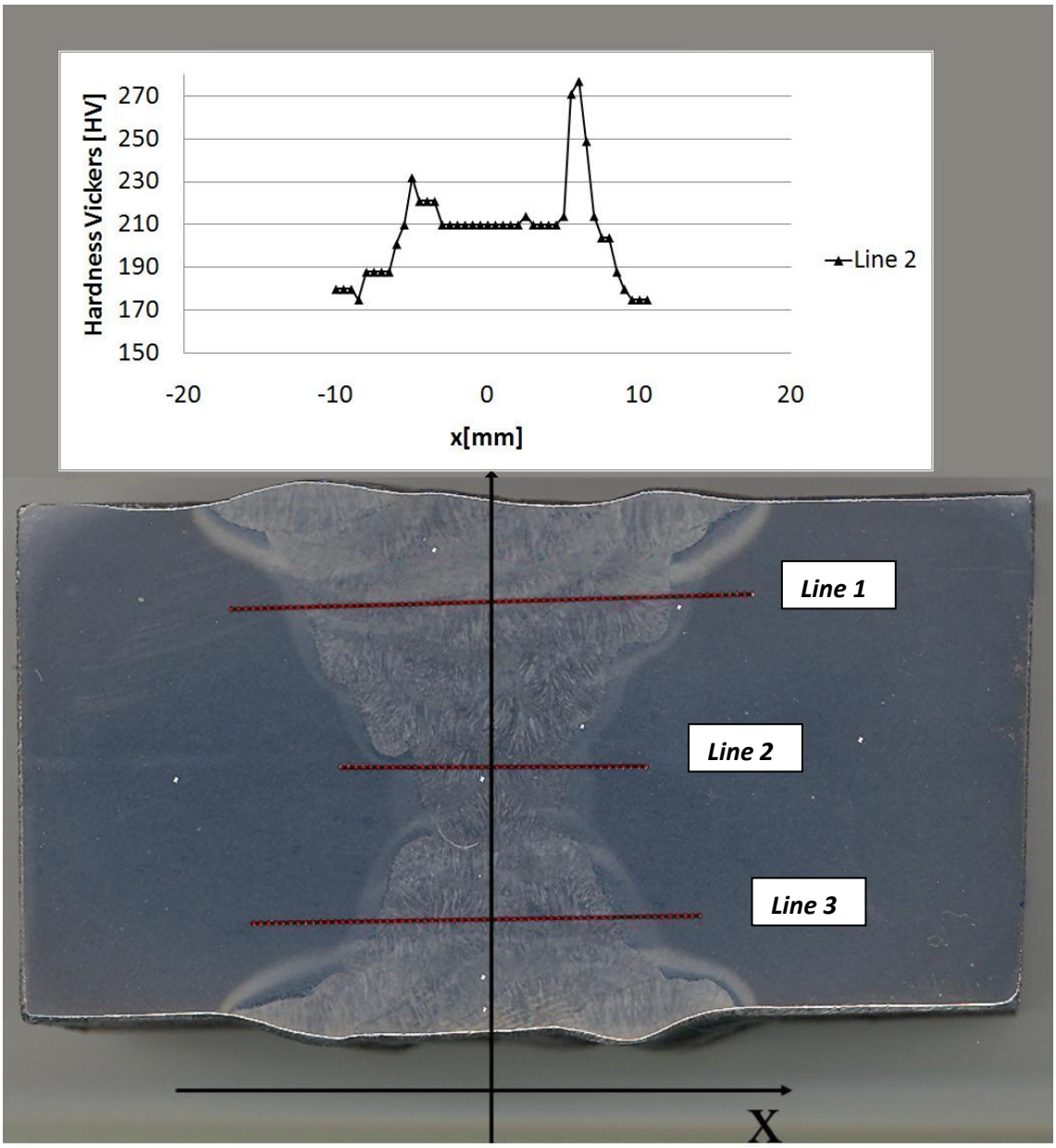


Figure 36 - Line 2 hardness measurements.

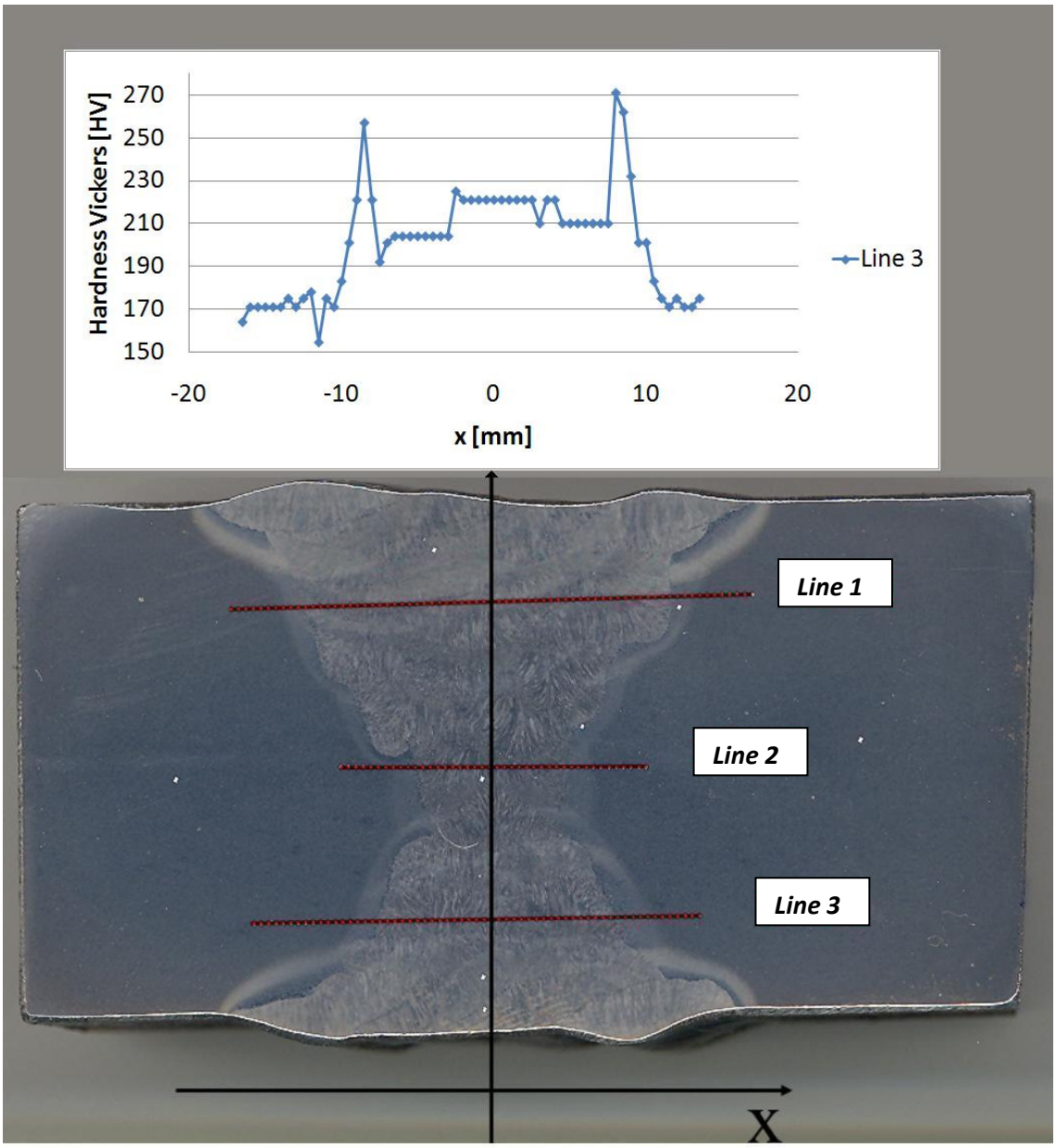


Figure 37 - Line 3 hardness measurements.

Figure 38 gives the complete set of hardness data, where it is possible to observe the increase of hardness in the HAZ where typically maximum values are reached. The hardness corresponding to the WM is lower than the HAZ hardness but higher than the BM hardness.

Some dispersion was found in BM hardness values: Figure 26 shows values of 152 – 155 HV, whereas in Figures 35 to 37 base metal hardness values are closer to 170 HV; this is attributed to experimental scatter.

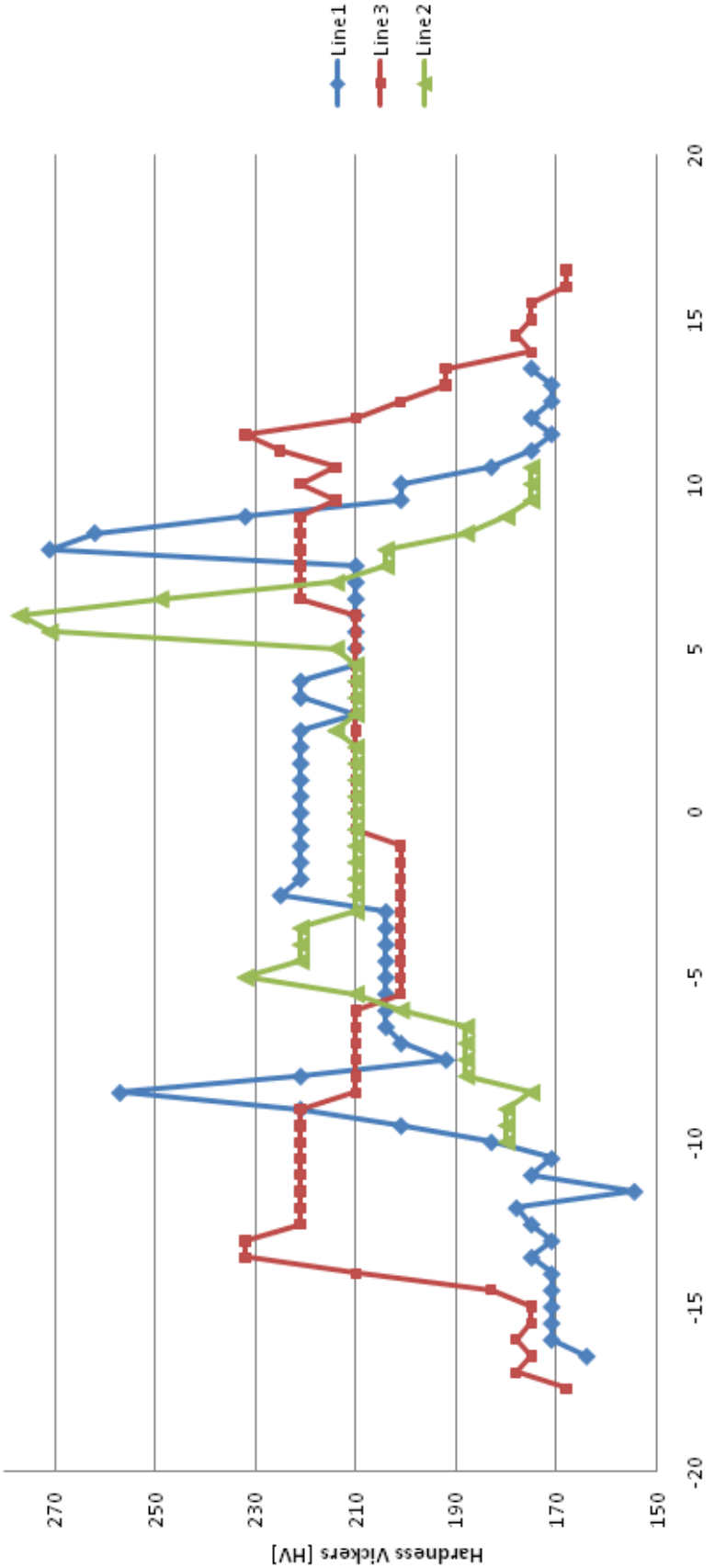


Figure 38 – Line 1, 2, 3 hardness measurements.

3.2. Calculation of the CT specimen dimensions

This section presents the preliminary study of the test programme to be performed, and is based on document ref. [8] prepared by Albuquerque. Once the decision to use CT specimens was taken, it was decided to use thickness (B) as close as possible to the thickness of structural parts and details of interest in the new REFER bridge at Alcácer do Sal. That thickness is B=33mm. Several paragraphs of this section 3.2. are directly reproduced from ref. [8].

3.2.1. Specimen dimensions

The dimensions of the test specimen of the present programme are shown in Figure 39.

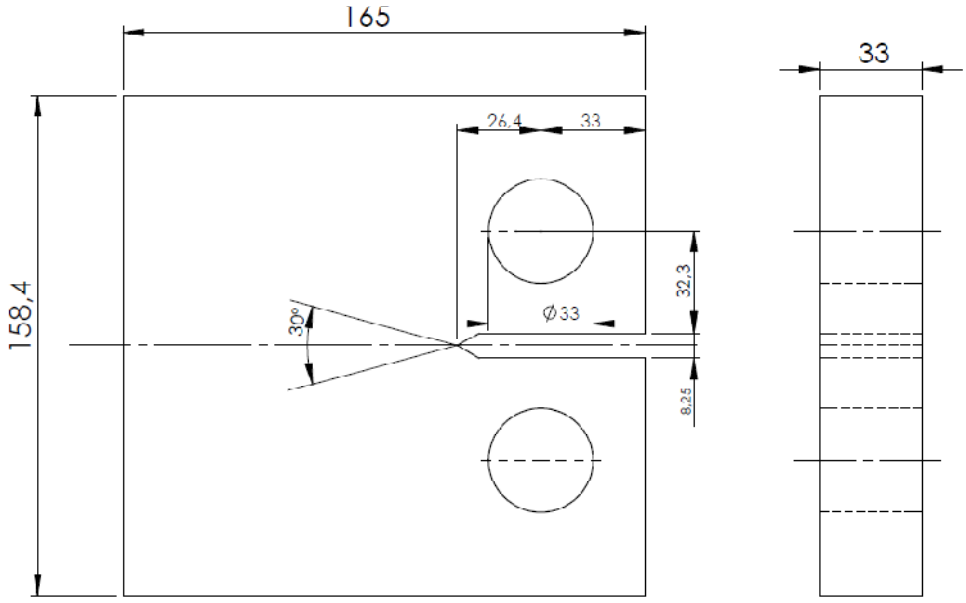
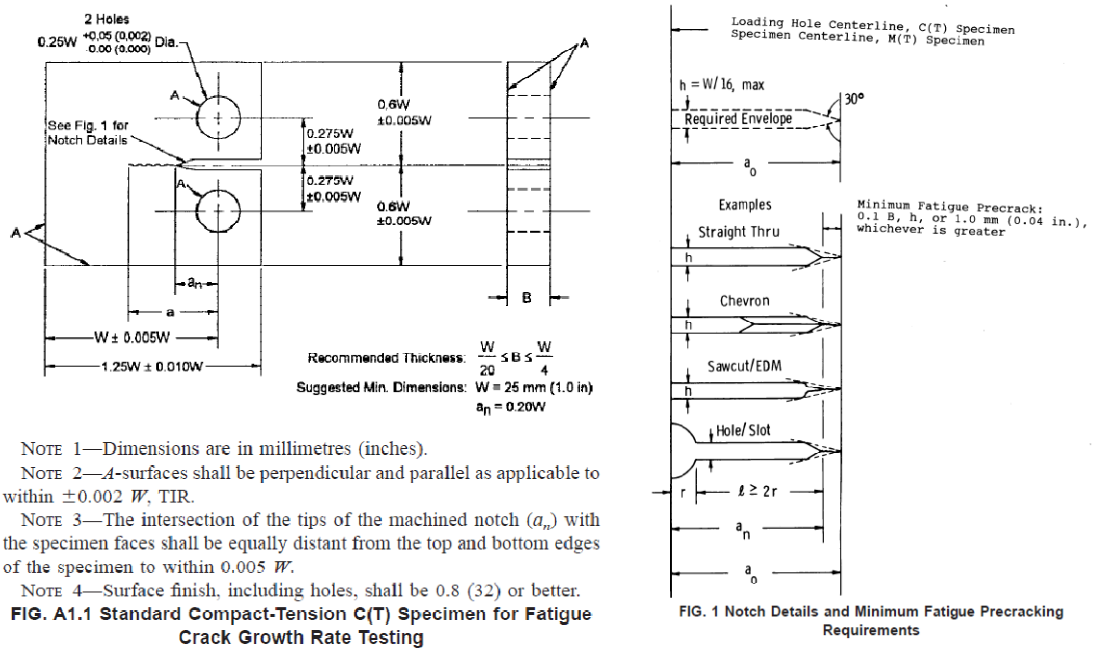


Figure 39 - Initially intended CT specimen dimensions.

As mentioned before the specimen thickness (B=33 mm) is equal to the thickness of some critical sections in the bridge of interest in this programme, the new railways steel bridge in Alcácer do Sal, currently being fabricated for REFER. Later on, in this report it will be stated that the actual thickness of the CT specimens tested was B=32 mm. This was due to the fact that the welded plates available presented some distortion and B=32 mm was the maximum thickness compatible with extracting flat specimens.

The remaining dimensions were defined in conformity with the ASTM E647 standard [9] (Figure 40).



NOTE 1—Dimensions are in millimetres (inches).
NOTE 2—*A*-surfaces shall be perpendicular and parallel as applicable to within ±0.002 *W*, TIR.
NOTE 3—The intersection of the tips of the machined notch (a_n) with the specimen faces shall be equally distant from the top and bottom edges of the specimen to within 0.005 *W*.
NOTE 4—Surface finish, including holes, shall be 0.8 (32) or better.

FIG. A1.1 Standard Compact-Tension C(T) Specimen for Fatigue Crack Growth Rate Testing

FIG. 1 Notch Details and Minimum Fatigue Precracking Requirements

Figure 40 - Dimensional relationships given by the ASTM E647 standard [9].

The length of the test specimen must be defined between:

$$W \leq 20 \cdot B = 660 \text{ mm} \tag{22}$$

$$W \geq 4 \cdot B = 132 \text{ mm} \tag{23}$$

The adopted was:

$$W = 132 \text{ mm} \tag{24}$$

To fulfill the minimum dimensions in order to use the minimum material possible.

CT specimen base:

$$D = 1{,}25 \cdot W = 1{,}25 \cdot 132 = 165 \text{ mm} \tag{25}$$

CT specimen height:

$$H = 1{,}2 \cdot W = 1{,}2 \cdot 132 = 158{,}4 \text{ mm} \tag{26}$$

Crack length before the fatigue precrack realization:

$$a_n = 0{,}2 \cdot W = 0{,}2 \cdot 132 = 26{,}4 \text{ mm} \tag{27}$$

Maximum height of the machined notch:

$$h = \frac{W}{16} = \frac{132}{16} = 8{,}25 \text{ mm} \tag{28}$$

the minimum fatigue precrack is:

$$\text{máx}\{0{,}1 \cdot B;\ h;\ 1\} = \text{máx}\{3{,}3;\ 8{,}25;\ 1\} = 8{,}25 \text{ mm} \tag{29}$$

The total length of the fatigue precrack is:

$$a = 26{,}4 + 8{,}25 = 34{,}65 \text{ mm} \quad (30)$$

3.2.2. Test loads and plastically deformed region ahead the crack

In agreement with [5], the fatigue threshold, for a mild steel , is between $\Delta K_{th} = 2 \text{ MPa}\sqrt{m}$ and $\Delta K_{th} = 8 \text{ MPa}\sqrt{m}$ (Table 4).

Table 4 - Fatigue threshold values [5]

Material	Resistência à tracção (MPa)	$R=K_{min}/K_{max}$	ΔK_{th} ($MPam^{1/2}$)
Low carbon steel (soft)	430	0,13	6,6
		0,35	5,2
		0,49	4,3
		0,64	3,2
		0,75	2,8
Steel A533B (low alloy steel for pressure vessels)	-	0,1	8
		0,3	5,7
		0,5	4,8
		0,7	3,1
		0,8	3,1
Steel A508 (medium carbon steel alloy)	606	0,1	6,7
		0,5	5,6
		0,7	3,1
Stainless steel 18/8	665	0	6
		0,33	5,9
		0,62	4,6
		0,74	4,1
Steel D6AC (high strength alloy steel)	1970	0,03	3,4

In agreement with [10], the fatigue threshold for steels assume the following approximate values given in Table 5:

Table 5 - Typical Fatigue threshold for modern steels [10].

R	ΔK_{th} [$\text{MPa}\sqrt{m}$]
0,1	4,7
0,4	2,7
0,7	2

The plastic zone ahead of the crack can be calculated as:

$$r_y = \frac{1}{2\pi} \cdot \left(\frac{K}{\sigma_{ced}}\right)^2 \tag{31}$$

The plastic zone ahead of the crack will be analyzed for the two extreme situations:

$\Delta K_{initial} = 2MPa\sqrt{m}$ e $\Delta K_{initial} = 8MPa\sqrt{m}$.

The expression that relates the stress intensity factor amplitude with the load amplitude is given by the ASTM E647 standard as shown in Equation 22.

$$K = \frac{P(2+\alpha)}{B\sqrt{W}(1-\alpha)^{3/2}}(0.886 + 4.64\alpha - 13.32\alpha^2 + 14.72\alpha^3 - 5.6\alpha^4) \tag{22}$$

Being :

$$\alpha = \frac{34{,}65}{132} = 0{,}2625 \tag{32}$$

and:

$$\Delta K_{th} = 2E6 = \frac{\Delta P}{0{,}033 \times \sqrt{0{,}132}} \cdot 5{,}093 \Leftrightarrow \Delta P = 4708{,}23\ N = 479{,}941\ kgf$$

Or alternatively,

$$\Delta K_{th} = 8E6 = \frac{\Delta P}{0{,}033 \times \sqrt{0{,}132}} \cdot 5{,}093 \Leftrightarrow \Delta P = 18832{,}90\ N = 1919{,}766\ kgf$$

For the situation of $\Delta K_{th} = 2\ MPa\sqrt{m}$ we have:

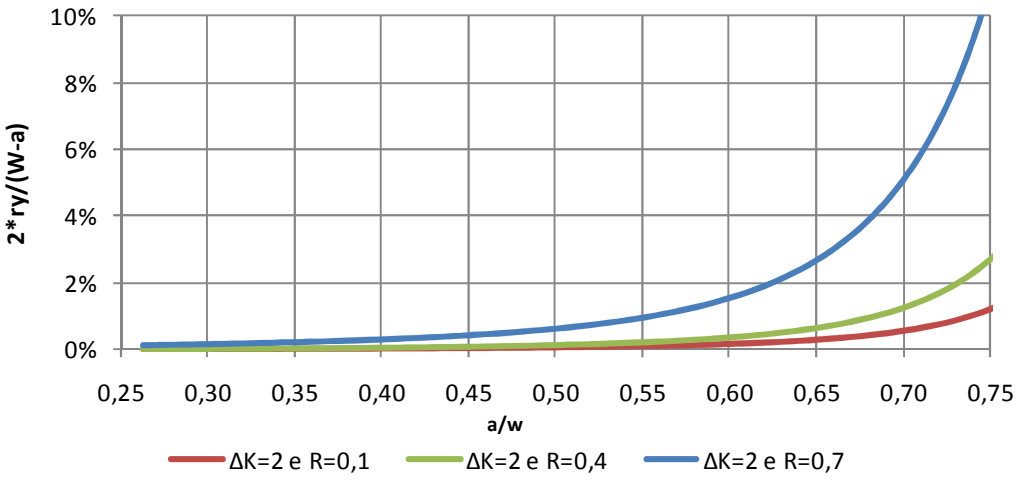


Figure 41 - Plastically deformed region ahead of the crack for $\Delta K_{th} = 2\ MPa\sqrt{m}$.

For the situation of $\Delta K_{th} = 8\ MPa\sqrt{m}$:

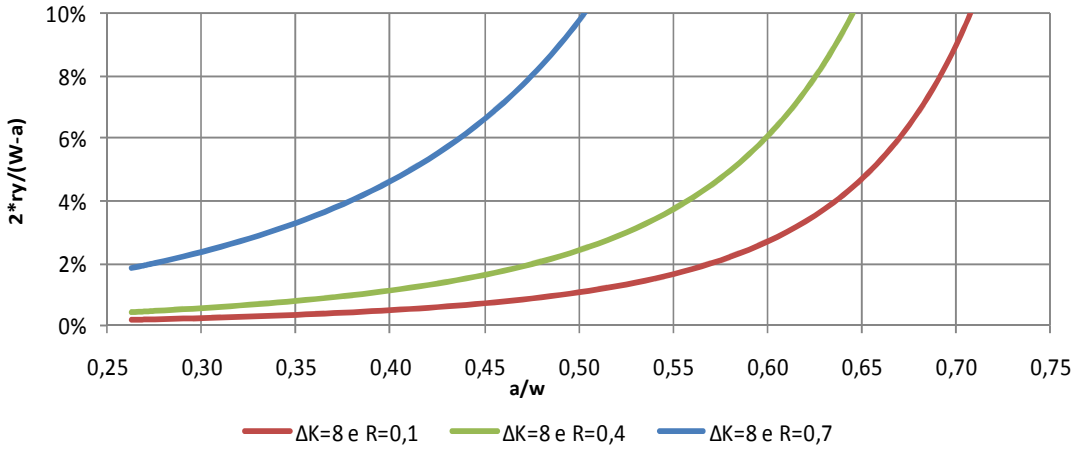


Figure 42 - Plastically deformed region ahead of the crack for $\Delta K_{th} = 8\ MPa\sqrt{m}$.

Finally is important to refer the maximum loads for each cases:

Table 6 - Maximum fatigue crack loads [10].

ΔK [$MPam^{1/2}$]	R	K_{max} [$MPam^{1/2}$]	P_{max} [N]	P_{max} [kgf]
2	0,1	2,22	5231	533
	0,4	3,33	7846	800
	0,7	6,67	15693	1600
8	0,1	8,89	20923	2133
	0,4	13,3	31385	3199
	0,7	26,7	62770	6399

3.3. Study of the notch geometry

The ASTM E647 standard specifies the requirements for the notch and minimum fatigue precrack.

For CT (compact tension) specimens the notch tip is at a distance of the loading hole centerline of $a_n = 0{,}2W$, and may be made by milling, electrical discharge machining (EDM) or other techniques. The notch plus the minimum fatigue precrack specified in the standard must be within a specified envelope characterized by a 30º angle at the tip of the fatigue precrack, as shown in Figure 43 [9].

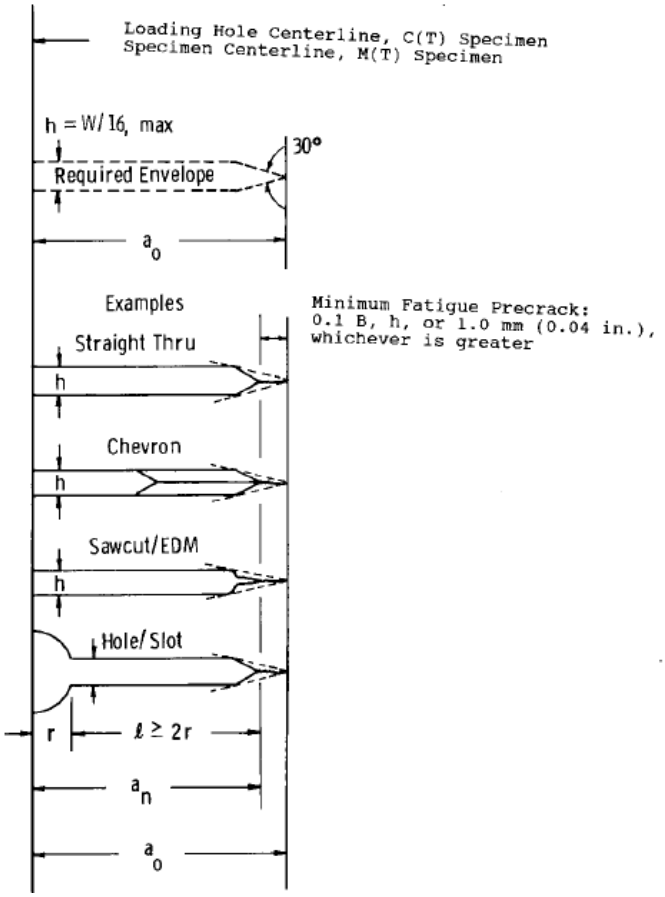


Figure 43 - Notch details and minimum fatigue precracking requirements, from [9].

It was intended to use a milling tool with a 30º angle (detail A of Figure 44), specifically manufactured for this project by the company "Irmãos Sás Ferramentas de Corte e Precisão". This solution did not work properly, and additional cutting edges were introduced in the flat surfaces of the milling tool (detail B of Figure 44). Unfortunately the tool broke shortly after starting the milling operations. Consideration was also given to using a milling tool with a 60º angle, but finally it was decided to use a notch with a circular tip made by milling. A wire-EDM straight notch was subsequently cut, to create conditions for the initiation of the fatigue precrack.

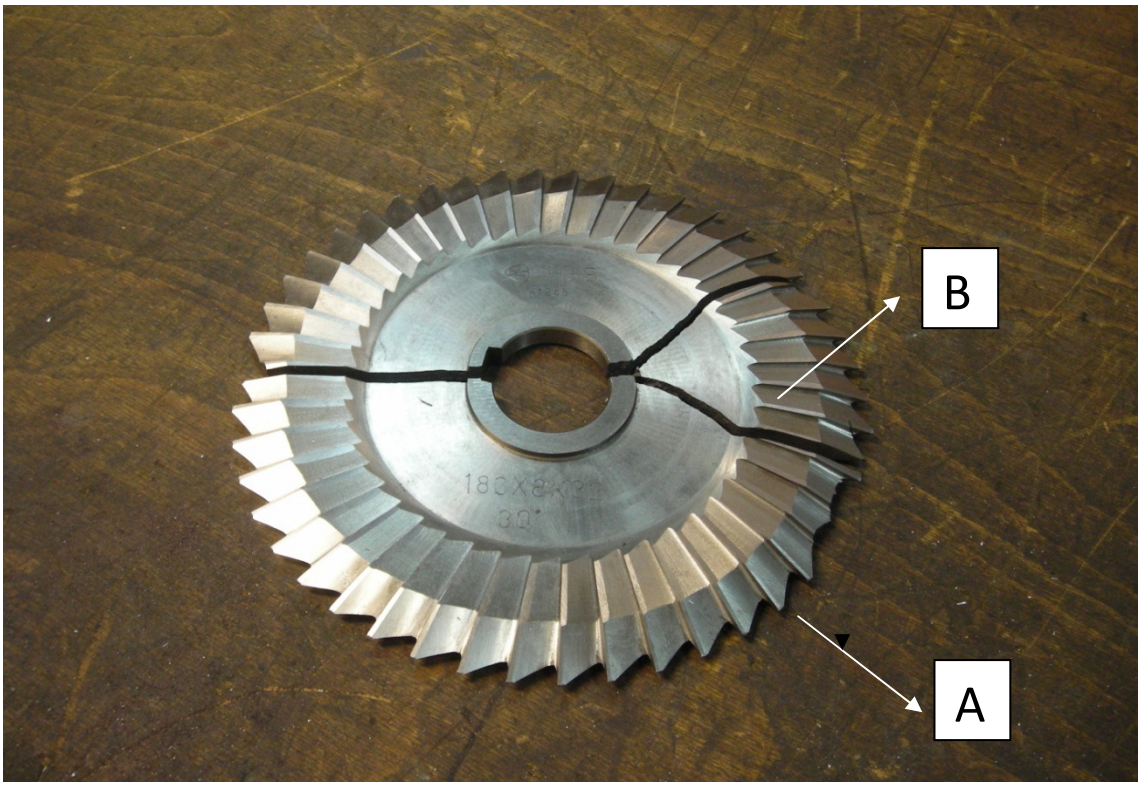


Figure 44 - Fractured 30º milling tool. The tool was firstly supplied as a disk finished with the 30º cutting tool.

Figures 45 to 47 show the notch geometries that were considered in the preliminary study and respective dimensions. The chosen geometry is presented in Figure 47. Annex A shows the clevis used.

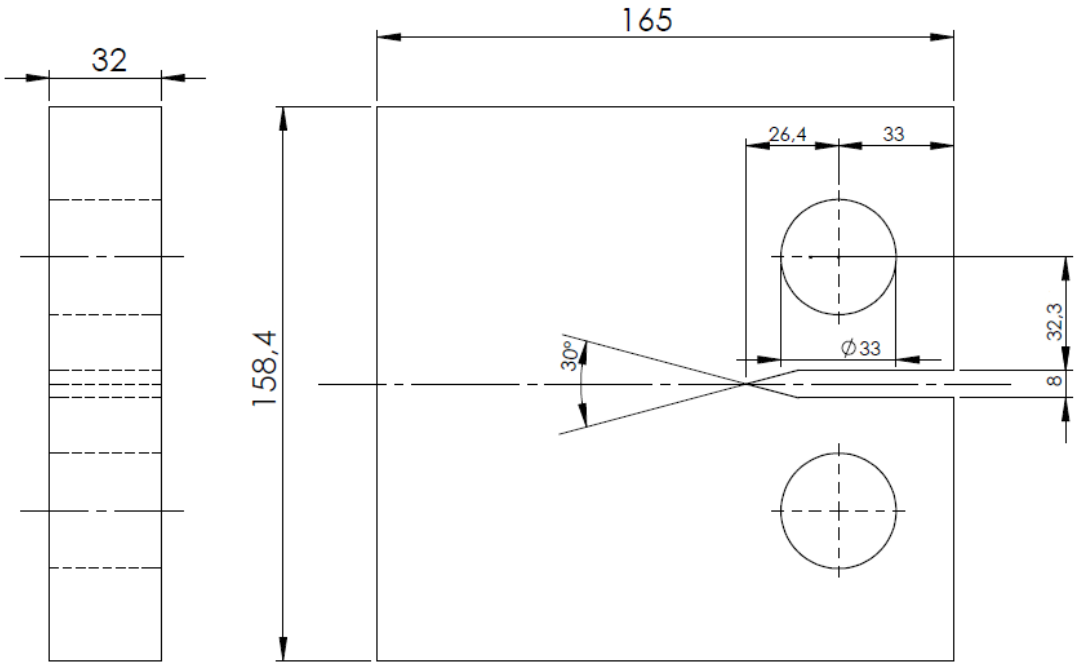


Figure 45 - Specimen dimensions with a 30º notch angle.

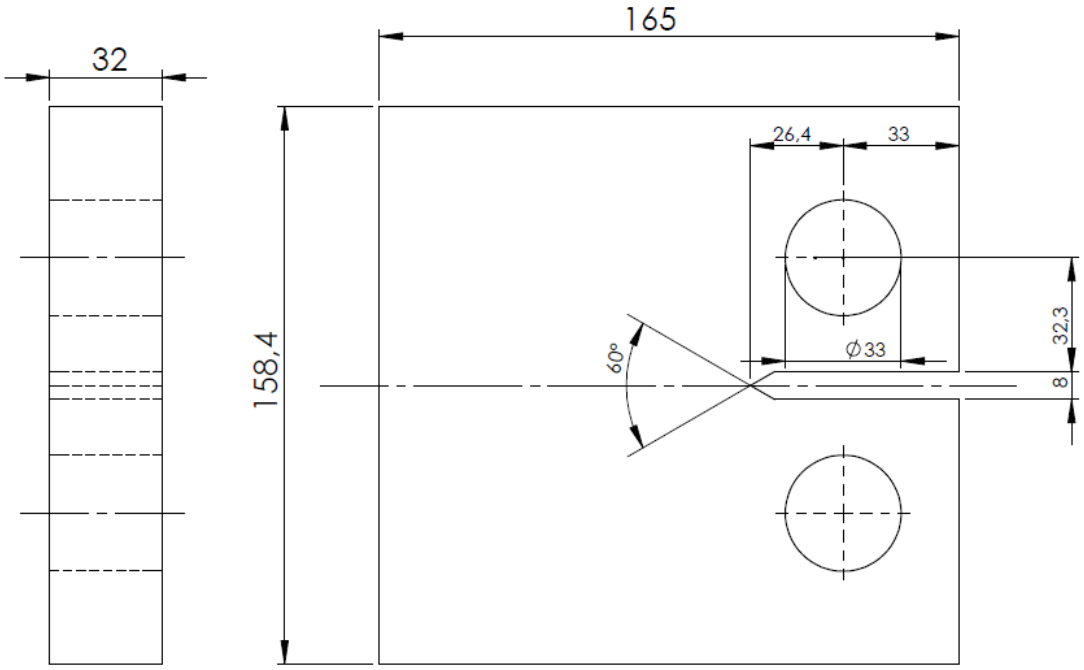
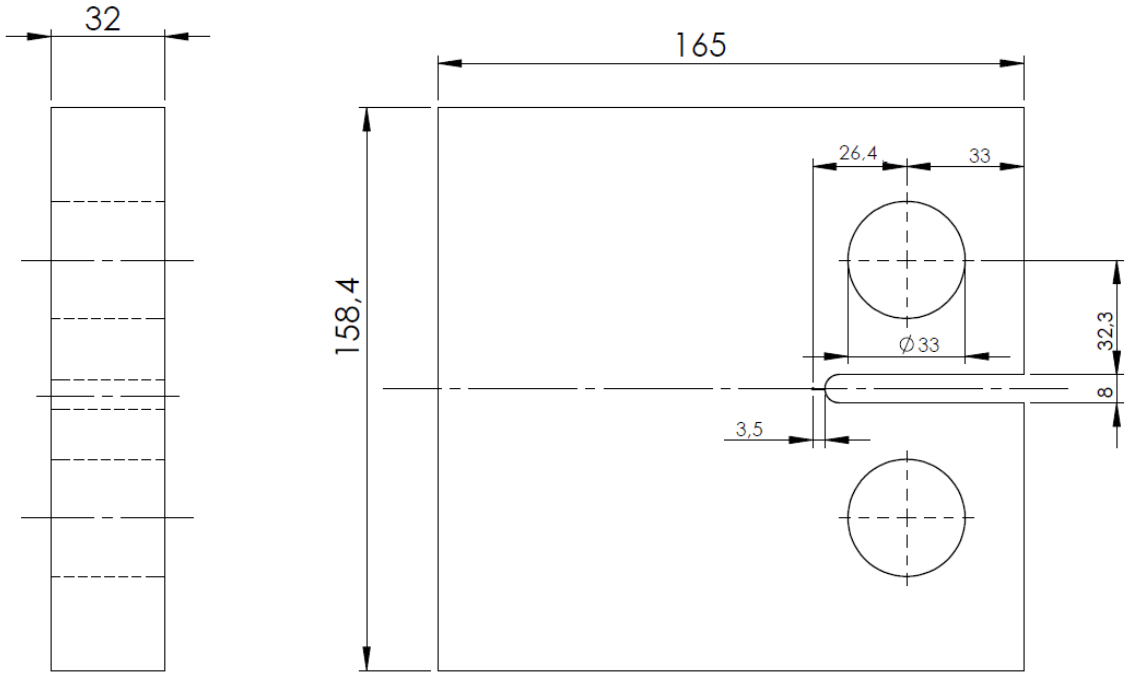
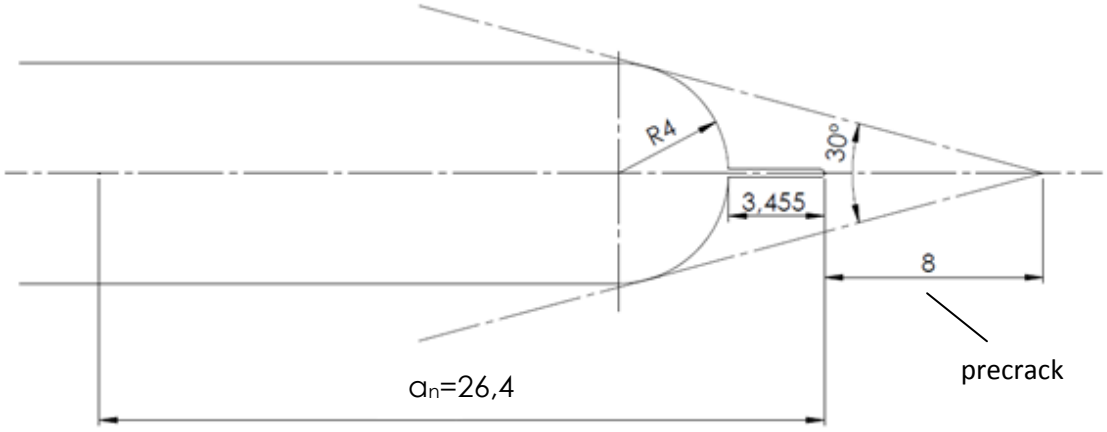


Figure 46 - CT Specimen dimensions with a 60º notch angle



a)



b)

Figure 47 – a) CT Specimen dimensions with a straight EDM notch angle. b) Detail of the EDM notch.

3.3.1. Determination of the Stress Concentration Factor (SCF)

Simulations were carried out using the Finite Element Method (FEM) with the purpose of notch tip stresses field determination and computation of the related stress concentration factors. Two of the previously mentioned geometries were selected for this purpose: the circular notch with EDM straight cut (Figure 47), and the V notch with an angle of 30º (Figure 47).

ABAQUS commercial software code was used and 3-D solid elements ref. C3D8R were selected. For the simulation of a CT specimen with EDM notch, 53930 hexagonal elements were used (Figure 48), whereas for the simulation of the V notch specimen 68864 hexagonal elements were used (Figure 49).

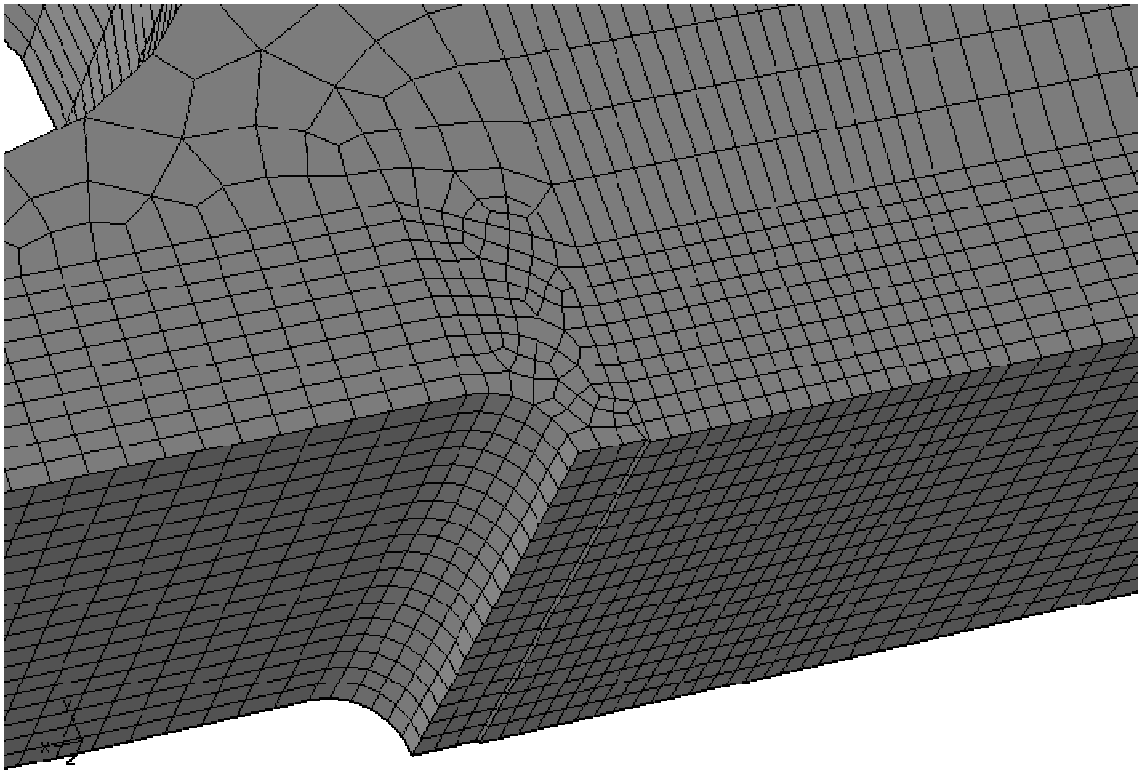


Figure 48 – Detail of the specimen with EDM notch. Meshed model using 53930 C3D8R elements (half model).

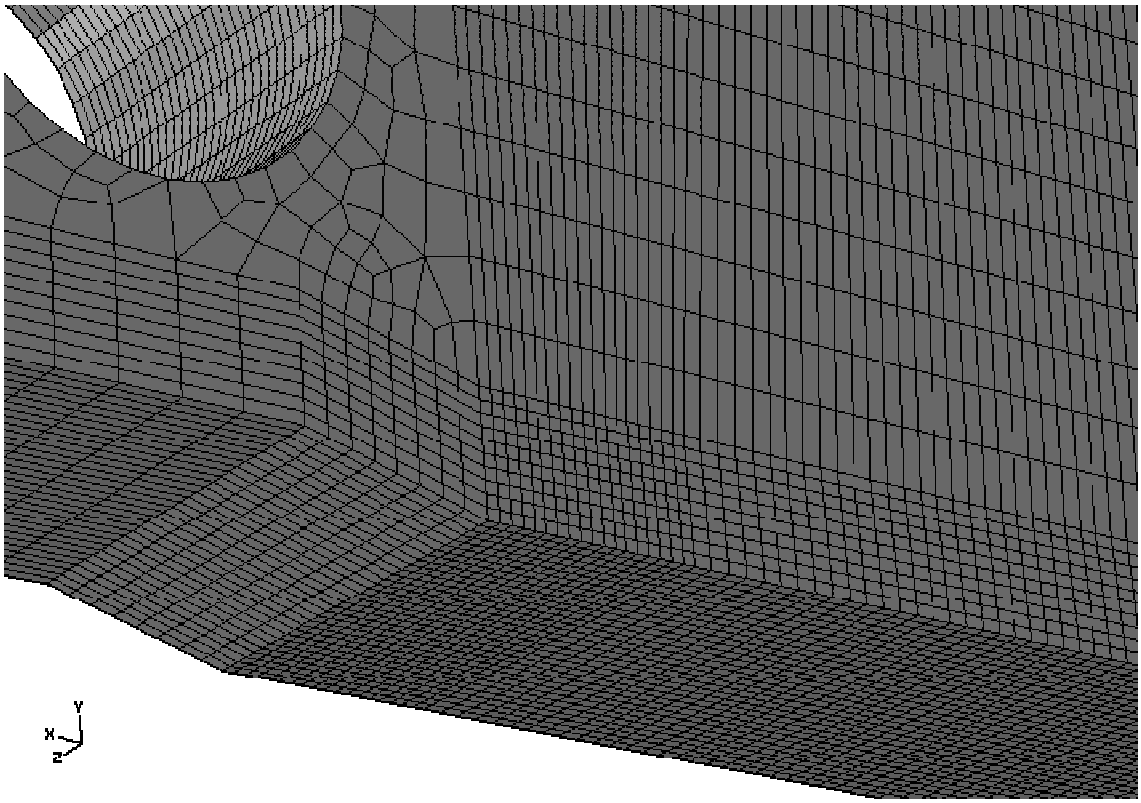


Figure 49 – Detail of the specimen with 30º . Meshed model using 68864 C3D8R elements (half model).

Figures 50 to 55 show stress maps ($\sigma_{xx}, \sigma_{yy}, \sigma_{zz}$), for both cases (Figures 50 to 52 concern EDM notch, whereas Figures 53 to 55 concern the 30º notch). A 50000 N load was applied on the center of the CT specimen hole.

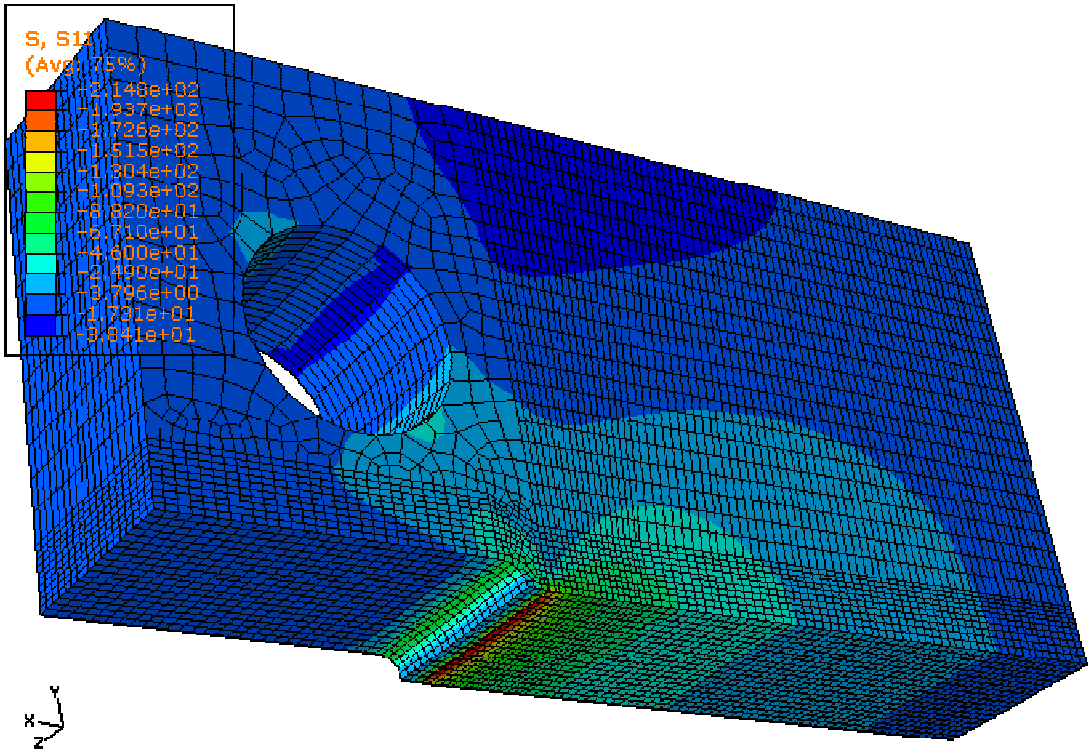


Figure 50 - σ_x values for a Compact Tension Specimen with an EDM notch.

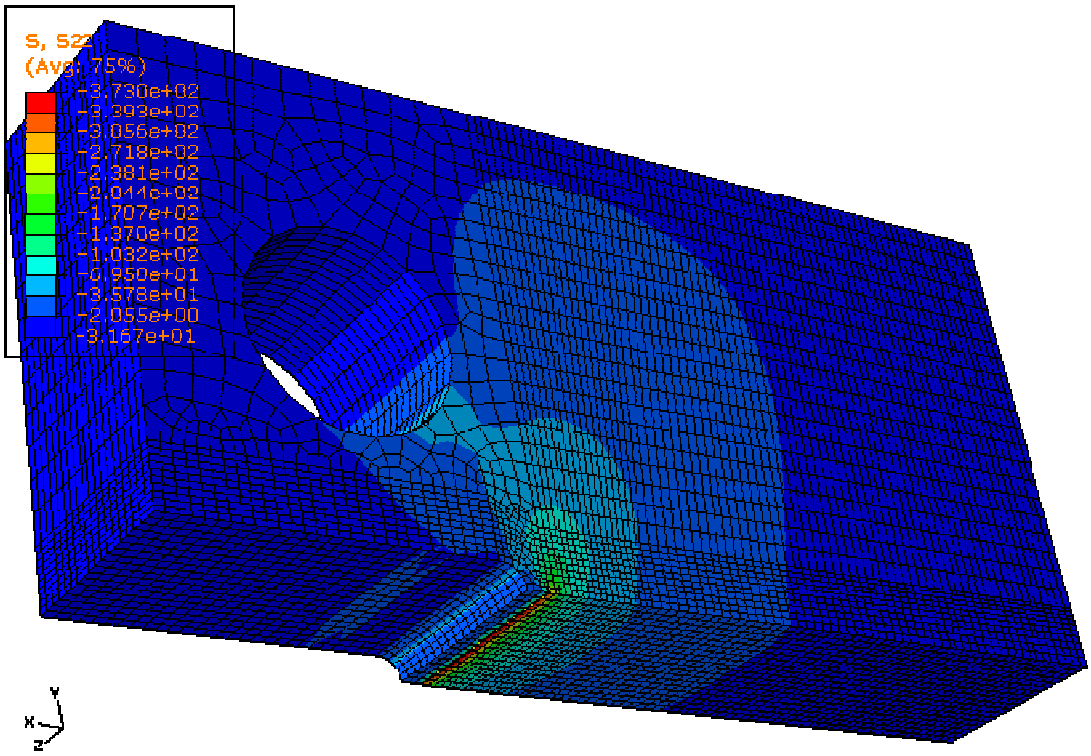


Figure 51 - σ_y values for a Compact Tension Specimen with an EDM notch.

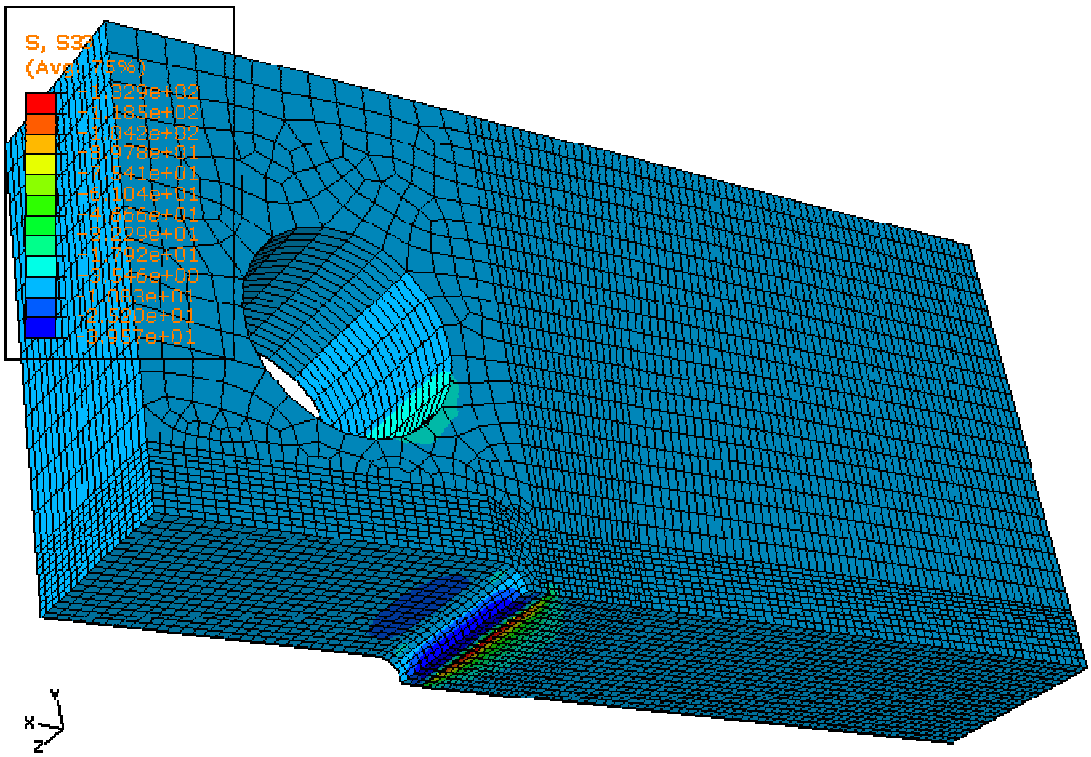


Figure 52 - σ_z values for a Compact Tension Specimen with an EDM notch.

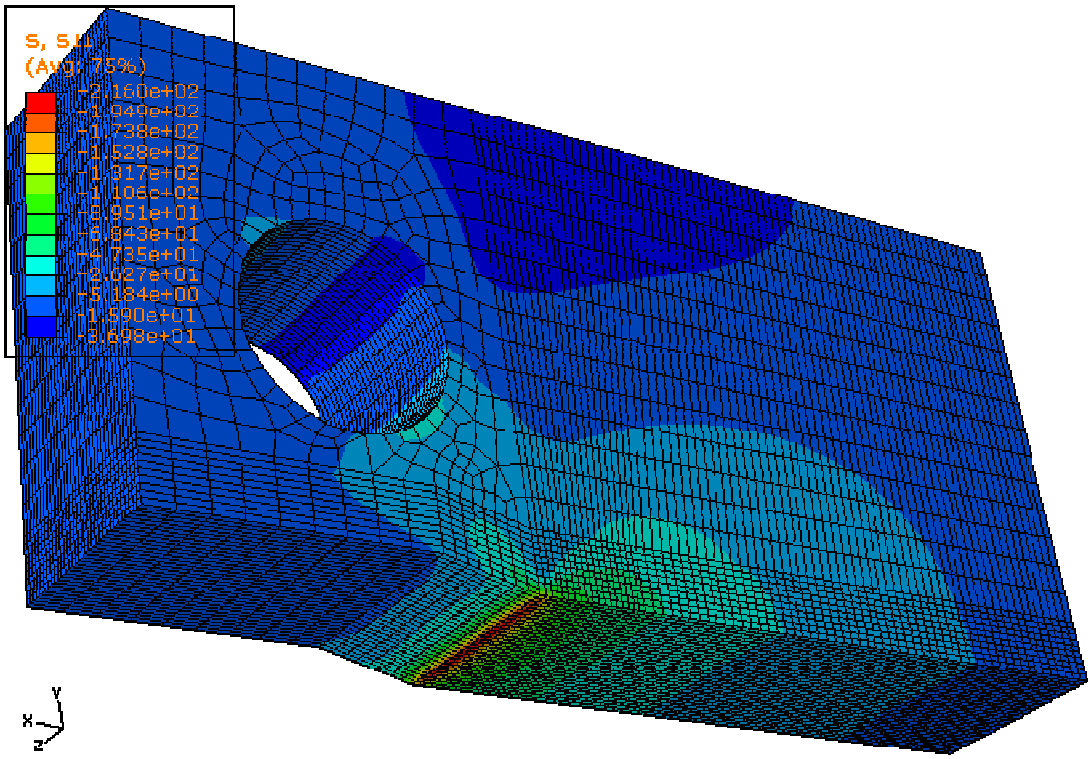


Figure 53 - σ_x values for a Compact Tension Specimen with a 30^o notch angle.

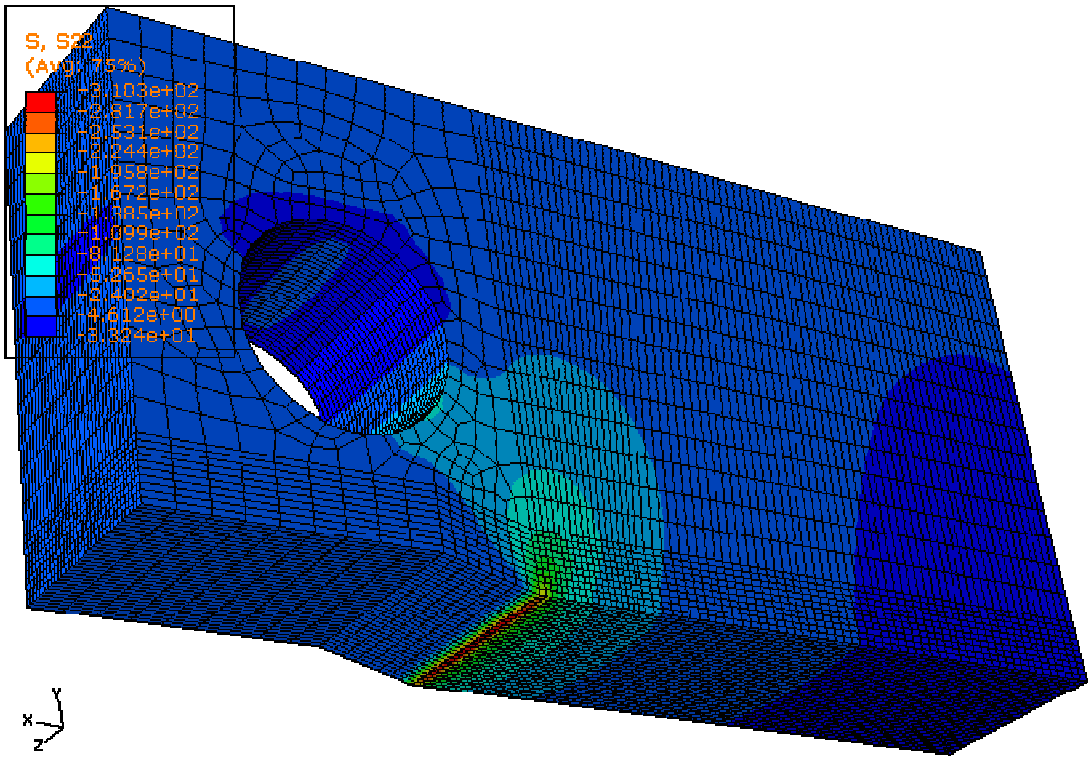


Figure 54 - σ_y values for a Compact Tension Specimen with a 30^o notch angle.

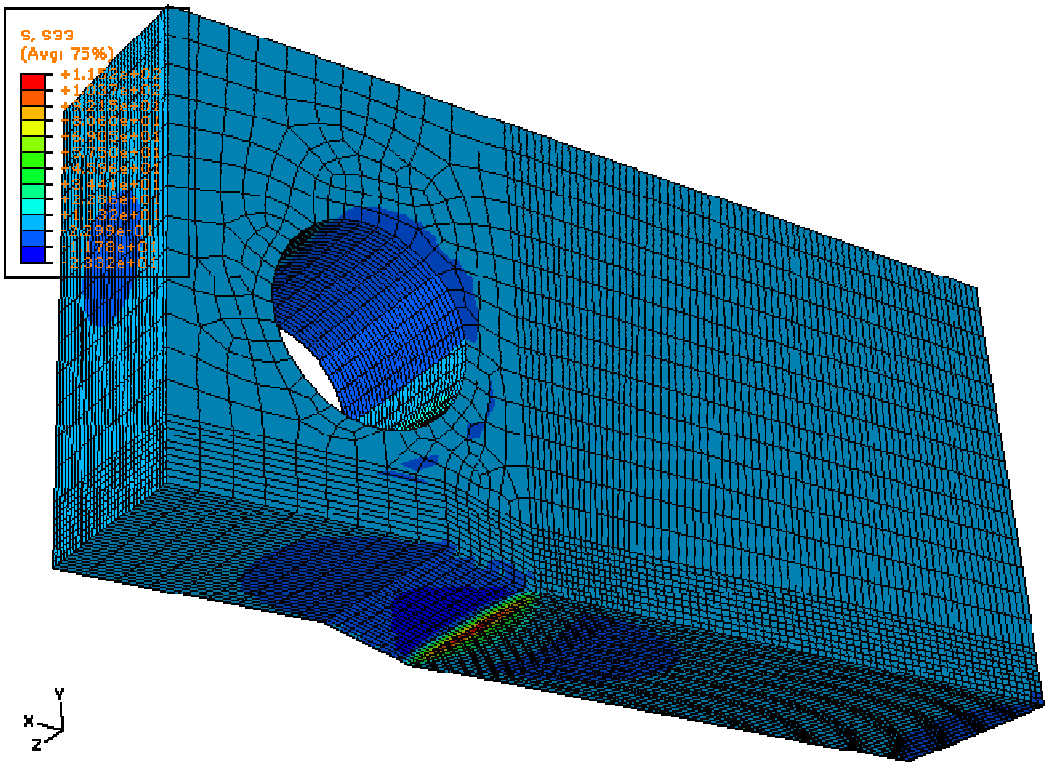


Figure 55 - σ_z values for a Compact Tension Specimen with a 30^o notch angle.

The nominal stress at the point of interest can be calculated using basic Strength of Materials considerations, see Figure 56.

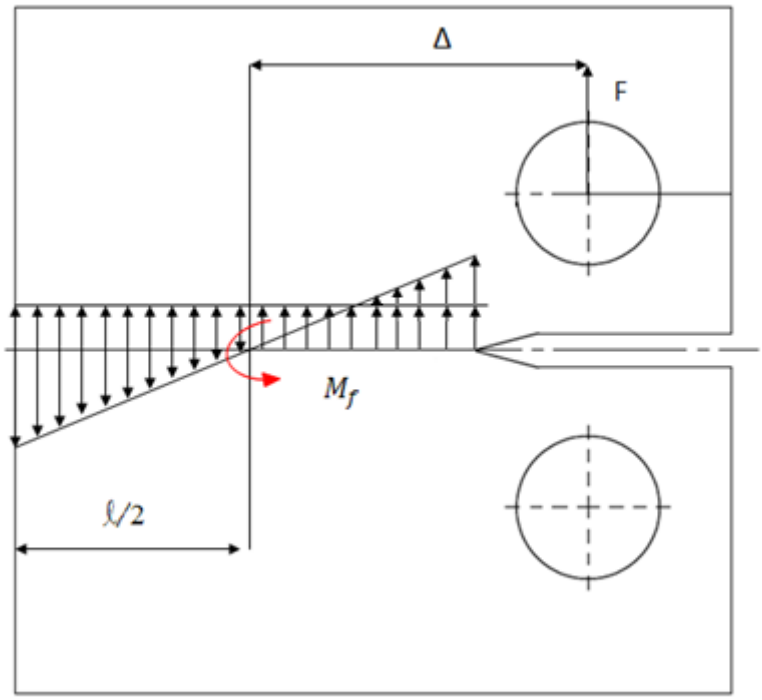


Figure 56 - Forces and moments applied in the specimen for the nominal stress calculation.

For both cases the related stress concentration factors were calculated considering a nominal stress equal to:

$$\sigma_{nom} = \frac{F}{A} + \frac{\frac{M_f.l}{2}}{B \cdot \frac{l^3}{12}} = \frac{F}{A} + \frac{\frac{F \cdot \Delta \cdot l}{2}}{B \cdot \frac{l^3}{12}} \tag{33}$$

$$= \frac{50000}{(132 - 26{,}4) \cdot 32} + \frac{\frac{50000 \cdot (132 - \frac{132 - 26{,}4}{2}) \cdot (132 - 26{,}4)}{2}}{\frac{32 \cdot (132 - 26{,}4)^3}{12}} = 81{,}38\ MPa$$

$$SCF = \frac{\sigma}{\sigma_{nom}} \tag{34}$$

where σ is the y direction stress at the tip of the notch given by FEM.

For EDM notch,

$$SCF_{EDM} = 4{,}58$$

For the 30º notch,

$$SCF_{30^\circ} = 3{,}80$$

As it can be seen in Figures 50 to 55 the stress values in the notch tip for the notch made by EDM are higher than the stress values obtained with a notch angle of 30º. Since the nominal stress is equal in both cases, this happens because the stress concentration factor in the case of the notch made by EDM is higher than with a 30º notch. Within the precision of the numerical model used, these results indicate that the adopted solution (EDM notch) is more favorable to fatigue crack initiation than the solution initially planned (30º notch). The use of an EDM notch is therefore favorable because what is intended with the notch is just to facilitate fatigue crack initiation.

It should be noted that theoretically the stress concentration of the V notch should be higher than the stress concentration of an EDM notch, since in the second case there is a notch tip radius of curvature, albeit very small. The calculations presented above are however approximations, which could be improved with an even more refined mesh, this was not persuade, since in practice no perfect V notches may be made, and there is always some bluntness at the V tip.

3.3.2. Stress Intensity Factor values as a function of crack length

ABAQUS 3D and 2D models were made using the dimensions of the Compact Tension Specimen (CTS) that will be used for the tests. The 3D and 2D finite element method (FEM) was used for stress intensity factor determination. The values obtained by FEM are compared with the results provided by the ASTM E647 standard. The applied load for the comparison of the results was $P = 50000\,N$. The ASTM E647 analytical solution for the stress intensity factor is given by the formula already mentioned before:

$$K = \frac{P(2+\alpha)}{B\sqrt{W}(1-\alpha)^{3/2}}(0.886 + 4.64\alpha - 13.32\alpha^2 + 14.72\alpha^3 - 5.6\alpha^4) \qquad (22)$$

where $= a/W$; expression valid for $a/W \geq 0.2$

The 2D ABAQUS model mesh was designed using a two-dimensional quadrilateral element (CPS4R) composed of 1376 elements. The mesh in the crack zone was more refined because this is the more important region for the present study, where the stresses are higher due to the stress concentration introduced by the notch. Using ABAQUS, K_I for given crack length is calculated using the relation $J = K^2/E$ as applicable in plane stress situations, relevant for the 2D analysis. A range of a/W values were used to calculate K_I. Values calculated with the present FEM 2D analysis are shown in Figure 57.

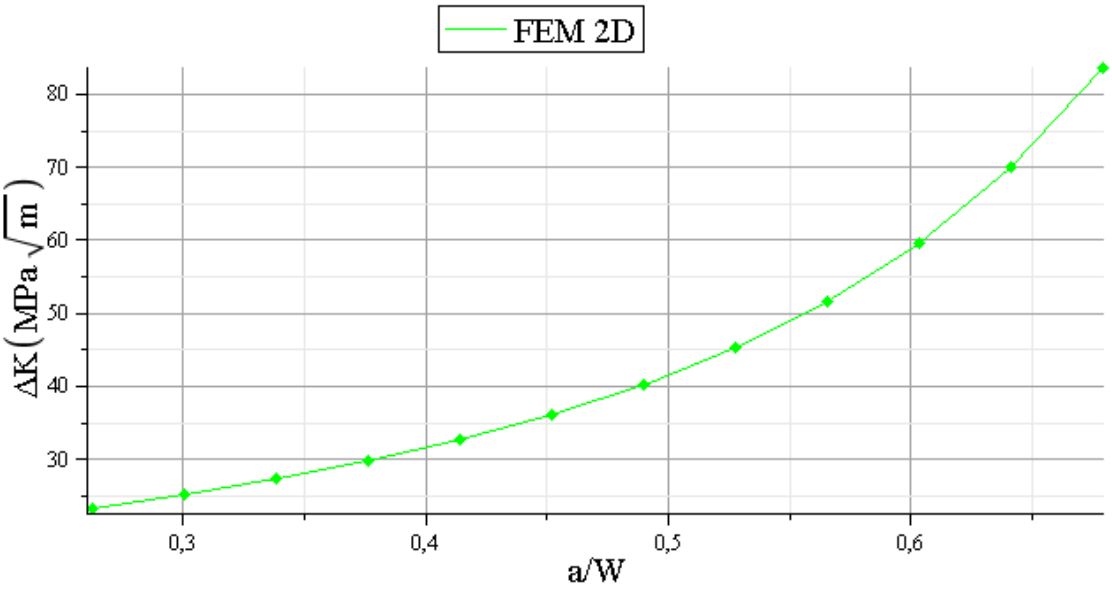


Figure 57 - Stress intensity factor values for different values of a/W using FEM 2D.

The 3D ABAQUS model mesh was designed using a tridimensional hexagonal element (C3D8R) composed of 68864 elements in this case of *a/W=0,2625*. For the other *a/W* values the number of elements was slightly higher. The mesh in the crack zone was again more refined because as stated before this is the more important region. Using ABAQUS, K_I for given crack length is calculated as an average of *J* values values along the thickness using the relation $J = K^2 \cdot (1 - \nu^2)/E$ as applicable to plane strain stuations (corresponding to thick material, a condition that may only approximately satisfied with the present case). The *J* value was calculated as:

$$J = \left(\sum_{1}^{i} J_i \right) \Big/ i \tag{35}$$

where *i* is equal to the number of nodes along the thickness used. A representation of the *K* values along the thickness is shown in Figure 58.

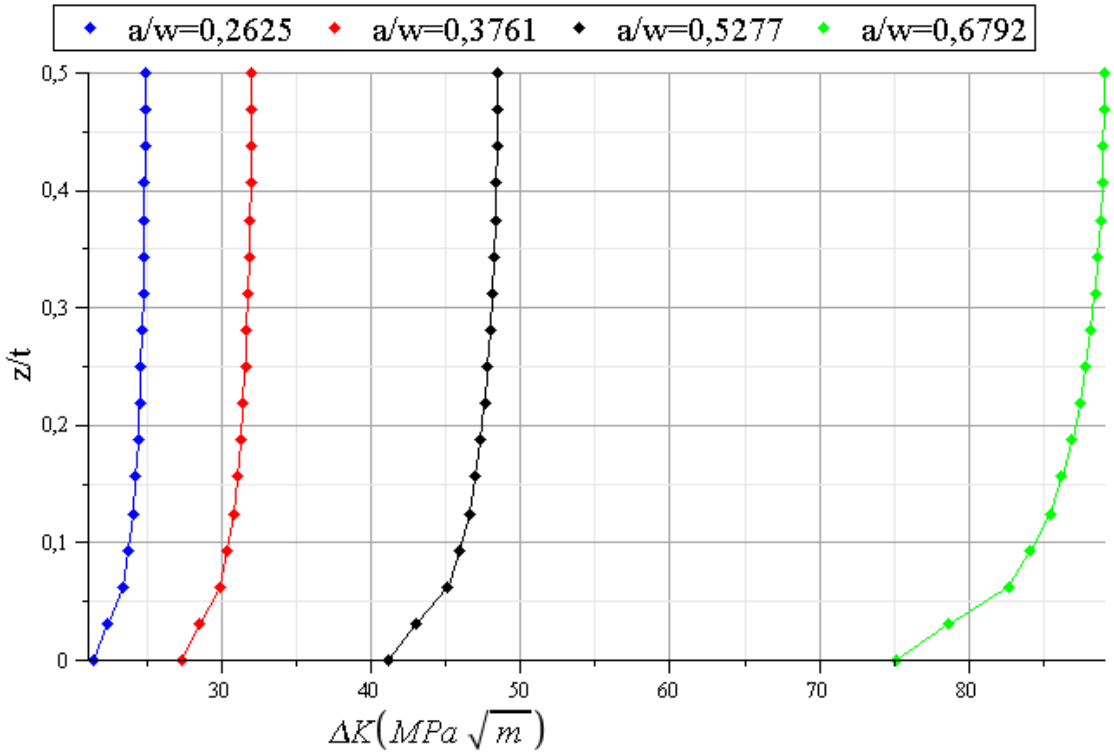


Figure 58 – K values along the thickness for different values of *a/W*.

A comparison of the maximum and minimum values obtained by FEM 3D with the average results was made and it is shown in Figure 59. The maximum values correspond to the half thickness of the specimen and the minimum values to the free surfaces.

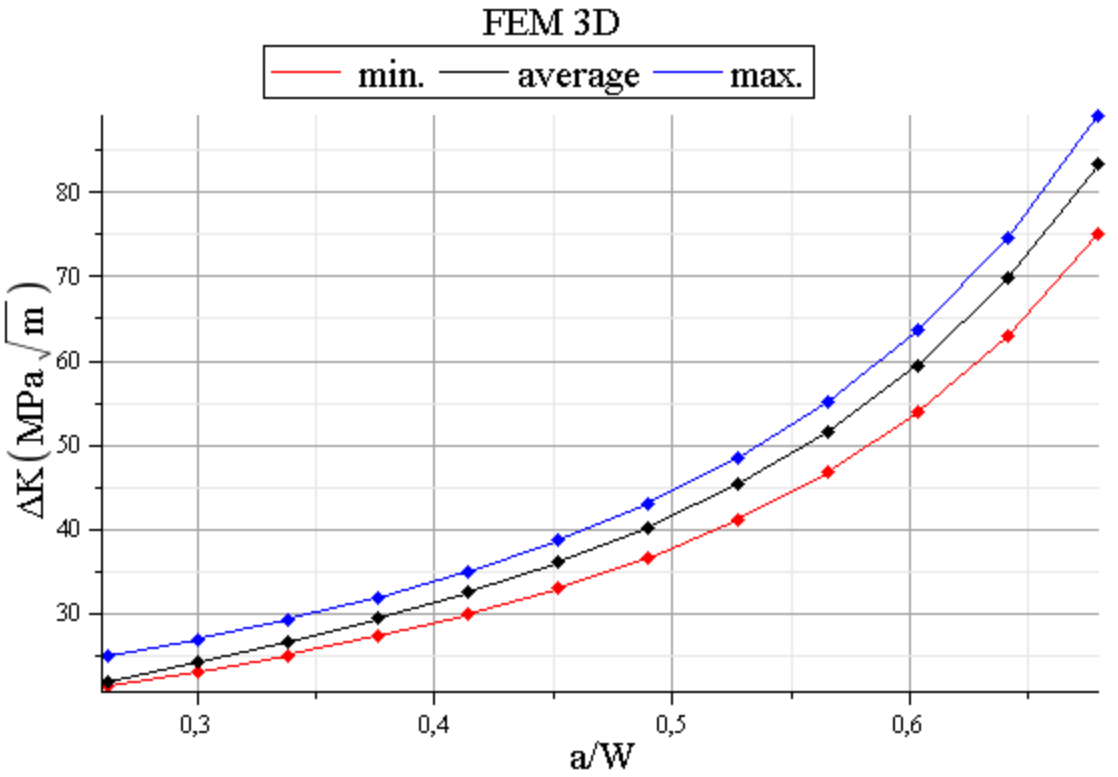


Figure 59 - Stress intensity factor maximum, minimum and average values for different values of a/W using FEM 3D.

Figure 60 shows the results obtained comparing ASTM E647 equation and the present FEM 3D and 2D analysis.

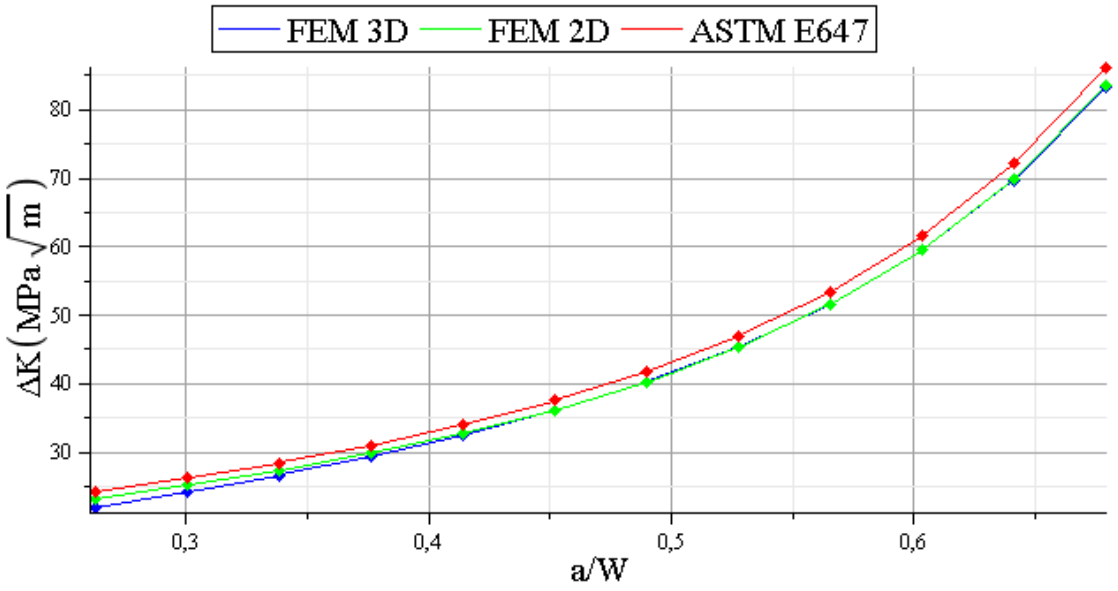


Figure 60 - Comparison of stress intensity factor values for different values of a/W.

As it can be seen in Figures 60 and 61 the solutions obtained using the ASTM E647 standard and using the results provided by FEM 3D are close (difference less than 4%) for *a/W* greater than 0,45, but the agreement is poorer for *a/W* smaller than 0,45 reaching 11% for *a/W* approximately equal to 0,25. The values calculated from the FEM 2D analysis are closer to the ASTM E647 standard than the values obtained from the FEM 3D analysis (difference is almost 0% for *a/W* values higher than 0,45). This happens, because the ASTM E647 standard is a 2D solution calculated considering Plane Stress conditions. Difference [%] relates finite element results with the results found in the ASTM E647 standard, and it is defined as,

$$Difference[\%] = \frac{result - reference\ value}{reference\ value} \times 100 \tag{36}$$

The variation of K_I trough the thickness, as captured by 3D analyses maybe one reason for the differences between the 3D analysis and ASTM E647 standard values, and because of that it was decided to analyze the dependence of K_I as a function of z/t.

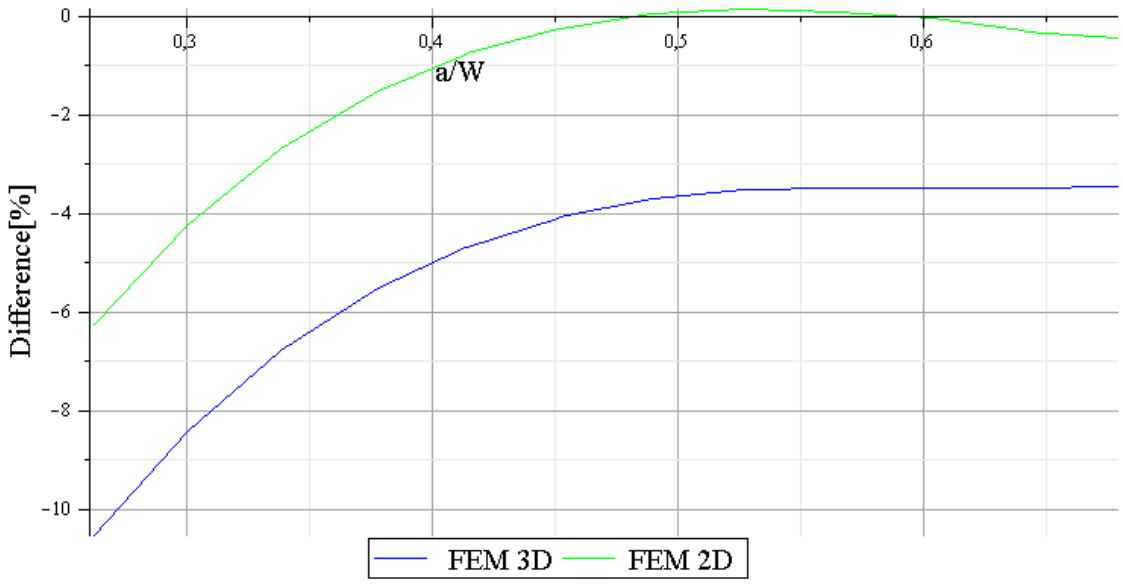


Figure 61 - Error committed using FEM compared with the ASTM E647 standard.

3.3.3. Stress intensity factor through thickness (a/W=0,23)

As the test specimen thickness is value of B = t = 32 mm, considerable variations of the stress intensity factor value along the thickness are expected. Simulations were carried out for three different configurations of the test specimen that were possible, according to the ASTM E647 standard, notch angle of 30º, notch angle of 60º, and EDM notch (i.e., semi circular notch type of very small radius).

3.3.3.1. Notch angle of 30°

In this case a Compact tension specimen, Figure 45, with $a/W = 0{,}2324$ and a notch angle of 30º was analysed. ASTM E647 standard present stress intensity factors solutions for the same geometry. The geometry was defined with the values presented in Figure 45. The ABAQUS simulation was made with the mesh represented in Figure 49.

Figure 62 presents a detail of the less refined mesh showing the σ_y stress distribution in the load direction when a remote load of 50000 N is applied.

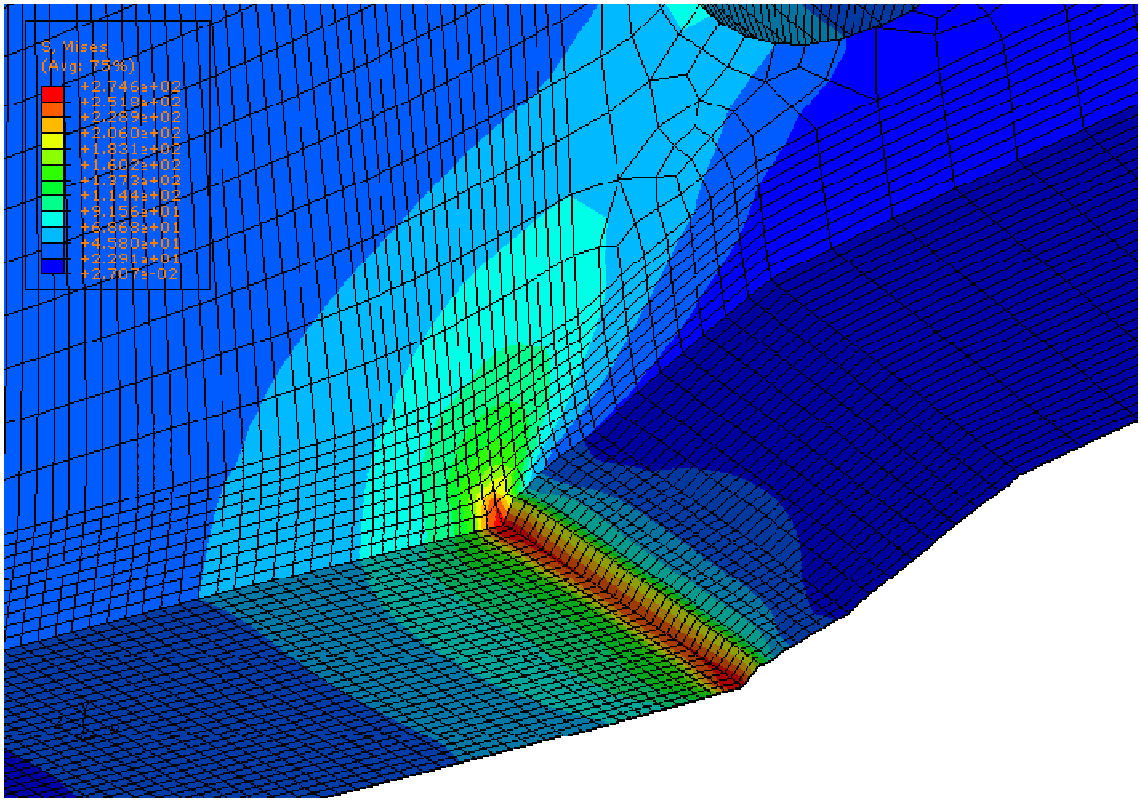


Figure 62 - Detail of less refined mesh for 30º notch angle for a/W=0,23.

Table 7 and 8 show the values of non-dimensional stress intensity factor along the thickness for the different meshes used. Difference [%] for two meshes used relates finite element three-dimensional results with the results found in the literature, and it is calculated using Equation 36.

Table 7 - Non-dimensional 3D FEM SIF along the thickness, 45942 elements mesh for a/W=0,23.

Node layer	z/t	$K/\sigma\sqrt{\pi a}$	ASTM E647	Difference [%]
1 (Free surface)	0,00000	2,846	2,903	2,0
2	0,03125	2,973		-2,4
3	0,06250	3,108		-7,1
4	0,09375	3,154		-8,6
5	0,12500	3,195		-10,0
6	0,15625	3,219		-10,9
7	0,18750	3,240		-11,6
8	0,21875	3,255		-12,1
9	0,25000	3,268		-12,5
10	0,28125	3,277		-12,9
11	0,31250	3,285		-13,1
12	0,34375	3,291		-13,4
13	0,37500	3,296		-13,5
14	0,40625	3,300		-13,7
15	0,43750	3,303		-13,7
16	0,46875	3,304		-13,8
17 (Half thickness)	0,50000	3,305		-13,8

Table 8 - Non-dimensional 3D FEM SIF along the thickness, 68704 elements mesh a/W=0,23.

Node layer	z/t	$K/\sigma\sqrt{\pi a}$	ASTM E647	Difference [%]
1 (Free surface)	0,00000	2,847	2,903	2,0
2	0,03125	2,970		-2,3
3	0,06250	3,106		-7,0
4	0,09375	3,153		-8,6
5	0,12500	3,193		-10,0
6	0,15625	3,217		-10,8
7	0,18750	3,238		-11,5
8	0,21875	3,253		-12,0
9	0,25000	3,266		-12,5
10	0,28125	3,276		-12,8
11	0,31250	3,284		-13,1
12	0,34375	3,290		-13,3
13	0,37500	3,295		-13,5
14	0,40625	3,298		-13,6
15	0,43750	3,301		-13,7
16	0,46875	3,302		-13,7
17 (Half thickness)	0,50000	3,303		-13,8

A comparative plot of the percent differences between ASTM E647 and three-dimensional finite element as a function of z/t for both meshes is presented in Figure 63. In this case the use of a more refined mesh is useless; the difference with respect to the reference solution is similar for both meshes.

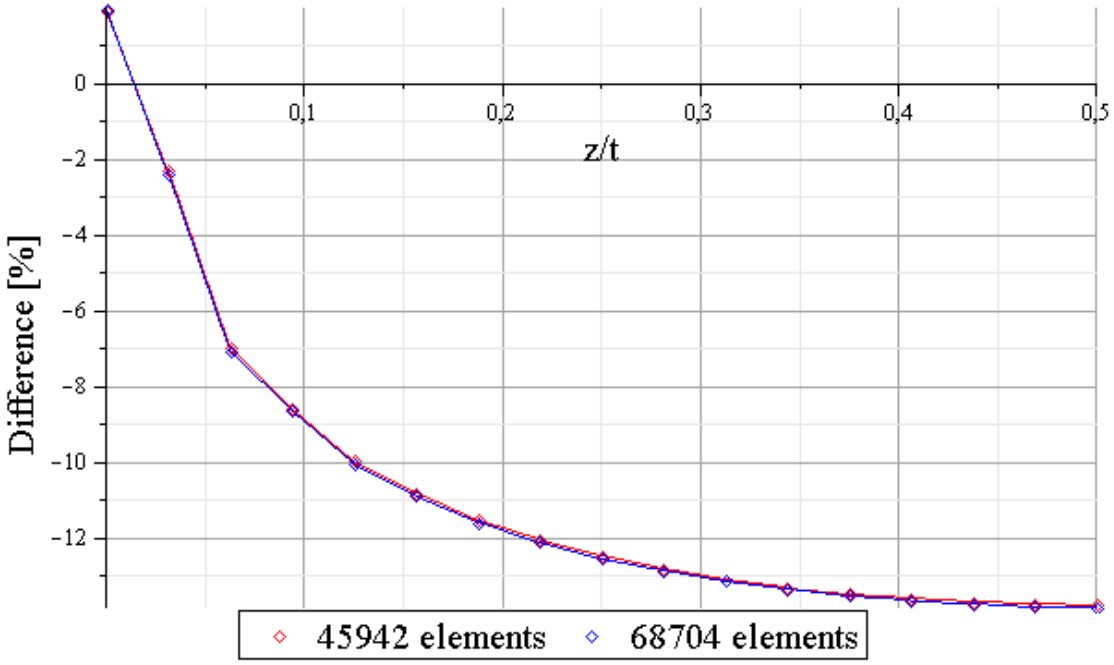


Figure 63 - Comparative plot of the % differences between ASTM E647 and FEM as a function of the coordinate z/t for both meshes for a/W=0,23.

Using the three results of SIF for each element, and according to Fig. 64, an average value of SIF is calculated:

$$K_{average} = \frac{K_A + 4K_B + K_C}{6} \tag{37}$$

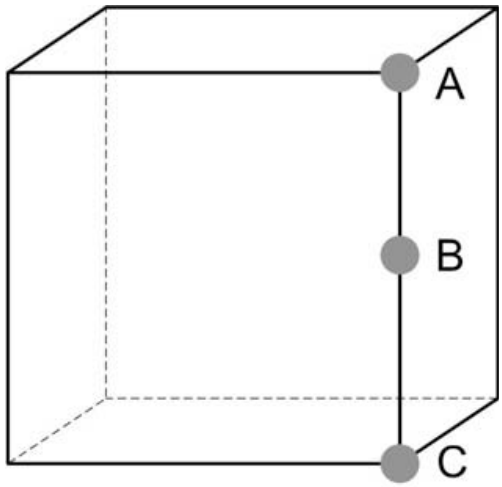


Figure 64 - Nodes for calculating the average stress intensity factor for an element.

Table 9 - 3D FEM $K/\sigma\sqrt{\pi a}$, 68704 elements mesh for a/W=0,23.

Element layer	$K/\sigma\sqrt{\pi a}$	ASTM E647	Difference [%]
1	2,974	2,903	-2,4
2	3,153		-8,6
3	3,218		-10,8
4	3,254		-12,1
5	3,277		-12,9
6	3,291		-13,4
7	3,300		-13,7
8	3,304		-13,8

Table 9 presents values of non-dimensional stress intensity factor in each element along the thickness at the crack tip for the 68704 elements mesh. Layer 1 contains elements on the surface; External nodes layer is averaged with the other subsequent layers. Stress intensity factors obtained using the three-dimensional finite element analyses are compared ASTM E647 standard results.

3.3.3.2. Notch angle of 60°

In this case a Compact tension specimen, Figure 46, with $a/W = 0{,}2324$ and a notch angle of 60º was analysed. ASTM E647 standard present stress intensity factors solutions for the same geometry but with a notch angle of 30º. The geometry was defined with the values presented in Figure 46. For the ABAQUS simulation the following model was used, Figure 65.

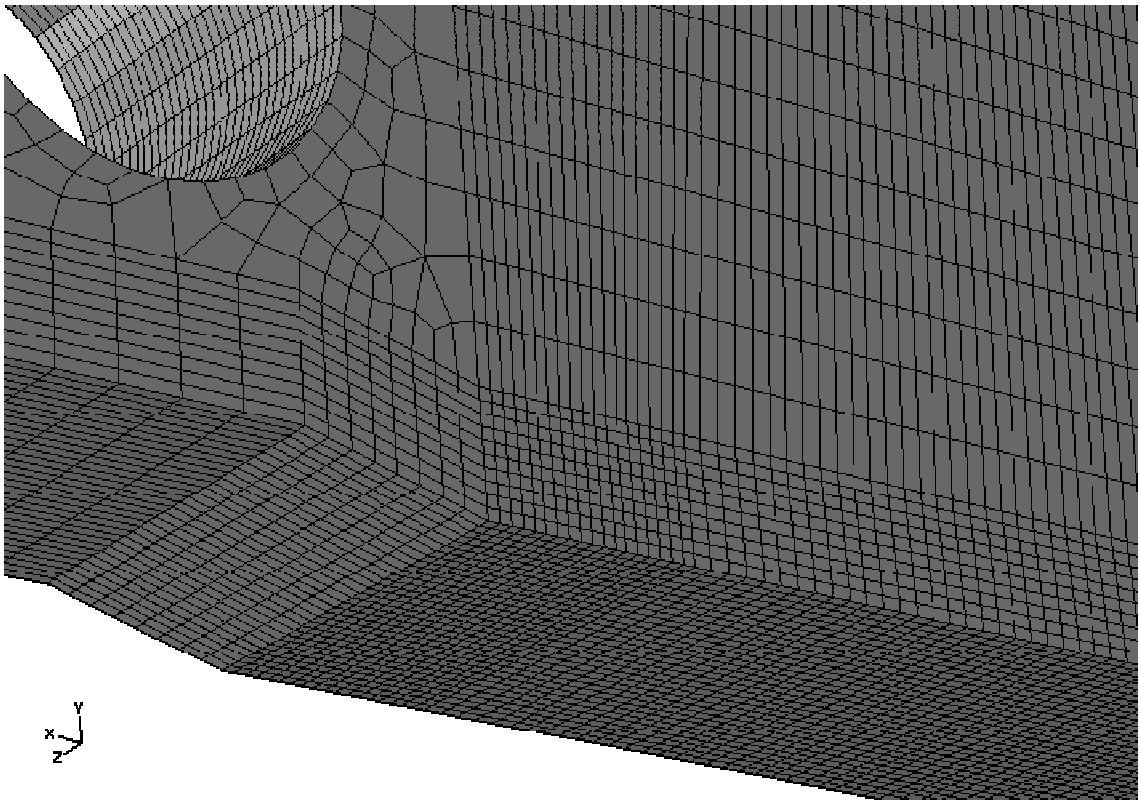


Figure 65- Detail of meshed model using C3D8R elements (half model).

Figure 66 presents a detail of less refined mesh showing the σ_y stress distribution in the load direction when a remote load of 50000 N is applied.

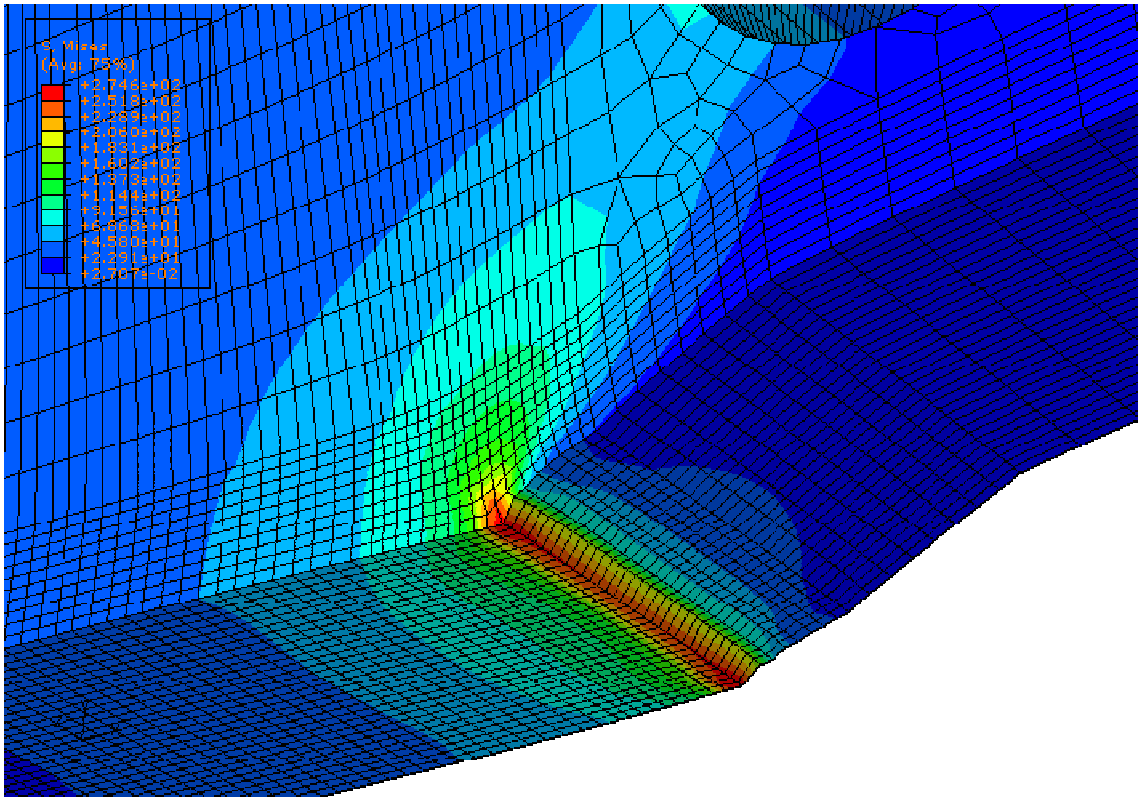


Figure 66 - Detail of the less refined mesh for a 60^{o} notch angle for a/W=0,23 .

Table 10 and 11 show the values of non-dimensional stress intensity factor along the thickness for the different meshes used. Difference [%] for two meshes used relates finite element three-dimensional results with the results found in the literature, and it is calculated using Equation 36.

Table 10 - Non-dimensional 3D FEM SIF along the thickness, 78946 elements mesh for a/W=0,23.

Node layer	z/t	$K/\sigma\sqrt{\pi a}$	ASTM E647	Difference [%]
1 (Free surface)	0,00000	2,856	2,903	1,6
2	0,03125	2,983		-2,7
3	0,06250	3,119		-7,4
4	0,09375	3,164		-9,0
5	0,12500	3,205		-10,4
6	0,15625	3,230		-11,2
7	0,18750	3,251		-12,0
8	0,21875	3,265		-12,5
9	0,25000	3,278		-12,9
10	0,28125	3,288		-13,3
11	0,31250	3,296		-13,5
12	0,34375	3,303		-13,8
13	0,37500	3,308		-13,9
14	0,40625	3,312		-14,1
15	0,43750	3,314		-14,2
16	0,46875	3,316		-14,2
17 (Half thickness)	0,50000	3,317		-14,2

Table 11 - Non-dimensional 3D FEM SIF along the thickness, 44608 elements mesh for a/W=0,23.

Node layer	z/t	$K/\sigma\sqrt{\pi a}$	ASTM E647	Difference [%]
1 (Free surface)	0,00000	2,858	2,903	1,6
2	0,03125	2,981		-2,7
3	0,06250	3,116		-7,3
4	0,09375	3,163		-8,9
5	0,12500	3,203		-10,3
6	0,15625	3,228		-11,2
7	0,18750	3,249		-11,9
8	0,21875	3,264		-12,4
9	0,25000	3,277		-12,9
10	0,28125	3,287		-13,2
11	0,31250	3,295		-13,5
12	0,34375	3,301		-13,7
13	0,37500	3,306		-13,9
14	0,40625	3,310		-14,0
15	0,43750	3,313		-14,1
16	0,46875	3,314		-14,2
17 (Half thickness)	0,50000	3,315		-14,2

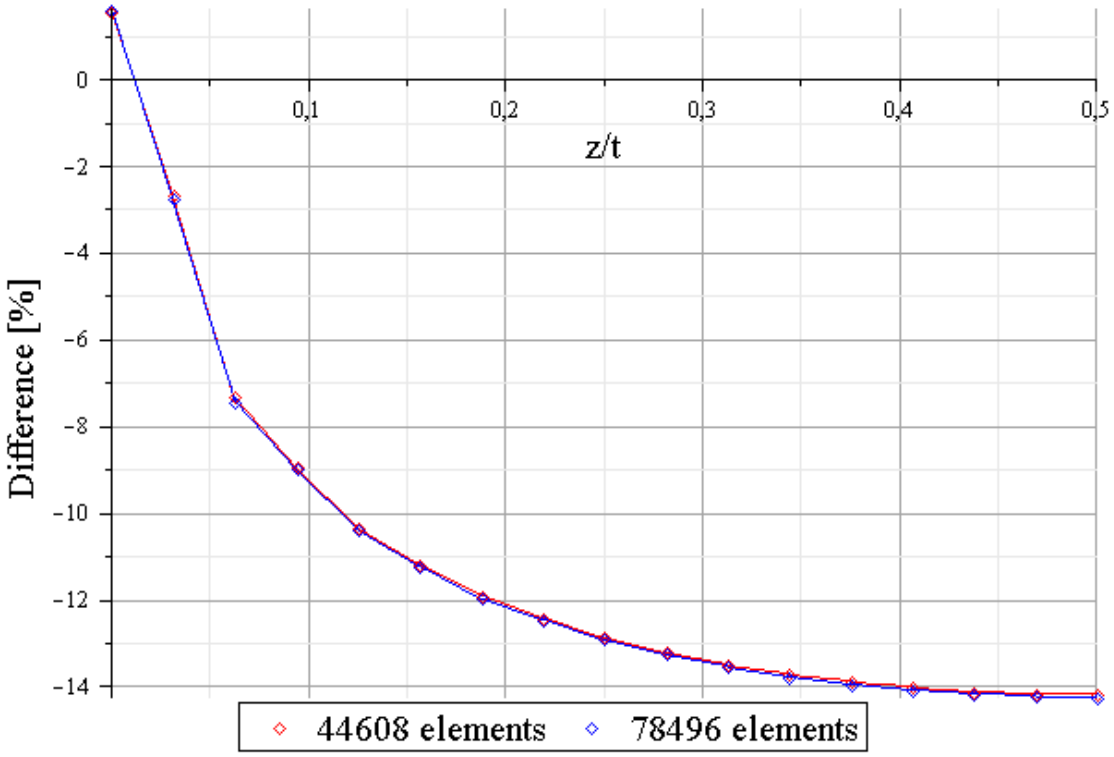


Figure 67 - Comparative plot of the % differences between ASTM E647 and FEM as a function of the coordinate z/t for both meshes for a/W=0,23.

Figure 67 shows comparative plot of the percent differences between ASTM E647 and three-dimensional finite element as a function of z/t for the different meshes used.

Table 12 - 3D FEM $K/\sigma\sqrt{\pi a}$, 78496 elements mesh for a/W=0,23.

Element layer	$K/\sigma\sqrt{\pi a}$	ASTM E647	Difference [%]
1	2,985	2,903	-2,8
2	3,164		-9,0
3	3,229		-11,2
4	3,265		-12,4
5	3,288		-13,2
6	3,303		-13,8
7	3,312		-14,1
8	3,316		-14,2

Table 12 presents values of non-dimensional stress intensity factor in each element along the thickness at a crack tip for the 78496 elements mesh. The K values for each element were calculated using Equation 27. Layer 1 contains elements on the surface; External nodes layer is averaged with the other subsequent layers. Stress intensity factors obtained using the three-dimensional finite element analyses are compared ASTM E647 standard results.

3.3.3.3. EDM notch

In this case a Compact tension specimen, Figure 47, with $a/W = 0{,}2324$ and a straight EDM notch was analyzed. ASTM E647 standard present stress intensity factors solutions for the same geometry. The geometry was defined with the values presented in Figure 47.

The ABAQUS simulation was made with the mesh represented in Figure 48.

Figure 68 presents a detail of less refined mesh showing the σ_y stress distribution in the load direction when a remote load of 50000 N is applied.

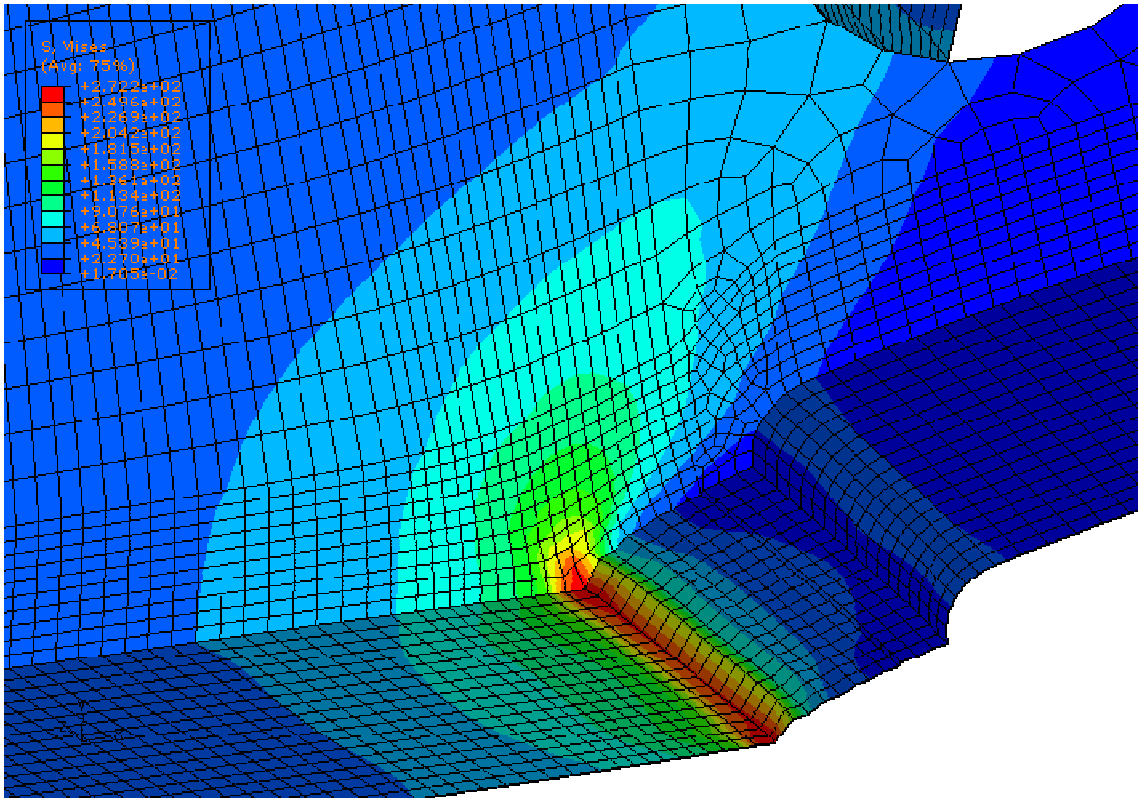


Figure 68 - Detail of less refined mesh for an EDM notch for a/W=0,23.

Table 13 and 14 show the values of non-dimensional stress intensity factor along the thickness for the different meshes used. Difference [%] for two meshes used relates finite element three-dimensional results with the results found in the literature, and it is calculated using Equation 36.

Table 13 - Non-dimensional 3D FEM SIF along the thickness, 29988 elements mesh for a/W=0,23.

Node layer	z/t	$K/\sigma\sqrt{\pi a}$	ASTM E647	Difference [%]
1 (Free surface)	0,00000	2,924	2,903	-0,7
2	0,03125	3,051		-5,1
3	0,06250	3,183		-9,6
4	0,09375	3,222		-11,0
5	0,12500	3,255		-12,1
6	0,15625	3,271		-12,7
7	0,18750	3,285		-13,1
8	0,21875	3,292		-13,4
9	0,25000	3,296		-13,5
10	0,28125	3,296		-13,5
11	0,31250	3,292		-13,4
12	0,34375	3,290		-13,3
13	0,37500	3,295		-13,5
14	0,40625	3,298		-13,6
15	0,43750	3,301		-13,7
16	0,46875	3,303		-13,7
17 (Half thickness)	0,50000	3,303		-13,8

Table 14 - Non-dimensional 3D FEM SIF along the thickness, 53930 elements mesh for a/W=0,23.

Node layer	z/t	$K/\sigma\sqrt{\pi a}$	ASTM E647	Difference [%]
1 (Free surface)	0,00000	2,922	2,903	-0,6
2	0,03125	3,051		-5,1
3	0,06250	3,181		-9,6
4	0,09375	3,220		-10,9
5	0,12500	3,254		-12,1
6	0,15625	3,271		-12,7
7	0,18750	3,286		-13,2
8	0,21875	3,293		-13,4
9	0,25000	3,299		-13,6
10	0,28125	3,299		-13,6
11	0,31250	3,299		-13,6
12	0,34375	3,291		-13,4
13	0,37500	3,296		-13,5
14	0,40625	3,300		-13,7
15	0,43750	3,303		-13,7
16	0,46875	3,304		-13,8
17 (Half thickness)	0,50000	3,305		-13,8

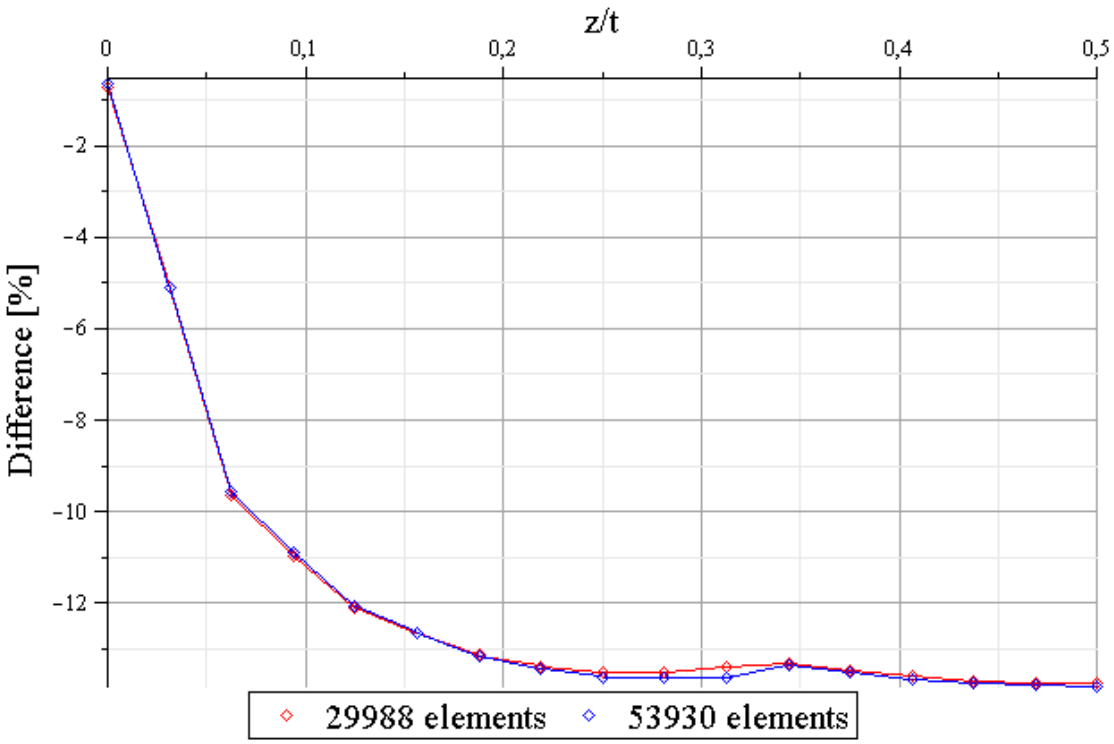


Figure 69 - Comparative plot of the % differences between ASTM E647 and FEM as a function of the coordinate z/t for both meshes for a/W=0,23.

Figure 69 shows comparative plot of the percent differences between ASTM E647 and three-dimensional finite element as a function of z/t for the different meshes used.

Table 15 - 3D FEM $K/\sigma\sqrt{\pi a}$, 53730 elements mesh for a/W=0,23.

Element layer	$K/\sigma\sqrt{\pi a}$	ASTM E647	Difference [%]
1	3,051	2,903	-5,1
2	3,219		-10,9
3	3,270		-12,6
4	3,293		-13,4
5	3,299		-13,6
6	3,293		-13,4
7	3,300		-13,7
8	3,304		-13,8

Table 15 presents values of non-dimensional stress intensity factor in each element along the thickness at a crack tip for the 53730 elements mesh. The K values for each element were calculated using Equation 27. Layer 1 contains elements on the surface; External nodes layer is averaged with the other subsequent layers. Stress intensity factors obtained using the three-dimensional finite element analyses are compared ASTM E647 standard results.

As we can conclude from the study of the three geometries (EDM, 60º and 30º) the value of the SIF is higher in the specimen half thickness than in the free surfaces. Thus the notch geometry does not have influence in the SIF values. With these results, a longer fatigue crack length is expected to be observed in the specimen half thickness. A fatigue crack front with a nail format should be observed.

3.4. Fatigue crack growth testing

This section presents the main work carried out in this thesis. Annex B gives a summary of resources used.

3.4.1. Specimen Preparation

Specimens were cut from welded plates according to the scheme of Figure 70, where WM stand for weld metal and HAZ for heat affected zone. Base Material (BM) specimens were machined from an unwelded plate. Welding was carried out parallel to the rolling direction. Although in Figure 70 WM specimens are presented, these were not tested in the context of the present thesis, but will be used later in the continuation of this work.

3.4.1.1. Polishing

Polishing was made in order to facilitate the crack tip length measurement during the tests. Firstly, the sample was polished using a sandpaper of 320, and then other of 800. Lastly alumina was used to give the sample a mirror surface that allows an easier observation of the crack tip.

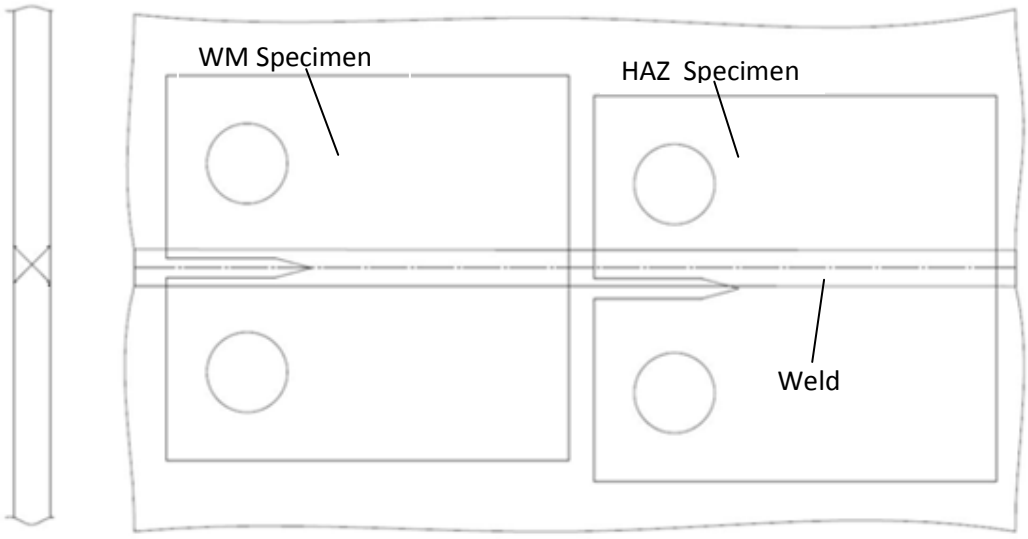


Figure 70- Representation of the position of the weld in the tested specimens.

3.4.1.2. Precracking

The ASTM E647 standard state that before test initiation the specimen needs a minimum fatigue precrack equal to 0,1B, h or 1mm, whichever is greater (Figure 43). The ASTM E647 standard does not specifies a maximum fatigue crack initiation load, thus in order to obtain an approximation to the fatigue crack initiation load, an approximation presented in the British COD tests standard BS5762:1979 [11] was used. The expression suggested by this standard for the maximum crack initiation load is such that:

$$K_f = 0{,}63\sigma_y B^{\frac{1}{2}} \tag{38}$$

$$K_f = 45{,}08\ \text{MPa}\sqrt{\text{m}}$$

This value suggests a maximum fatigue crack initiation around 120kN, but to ensure that little plastic deformation occurred at the notch tip, an initial fatigue load of 80 kN was chosen. After this, the test was initiated and after initiation was detected, the fatigue crack growth was measured at adequate intervals. Test load was gradually reduced as the fatigue crack advanced in agreement with the ASTM E647 standard, when the minimum fatigue precrack was obtained, the value of ΔK is a little higher than the ΔK_{th} of the material which is unknown. Figure 71 shows the precracking sequence used for the first test specimen.

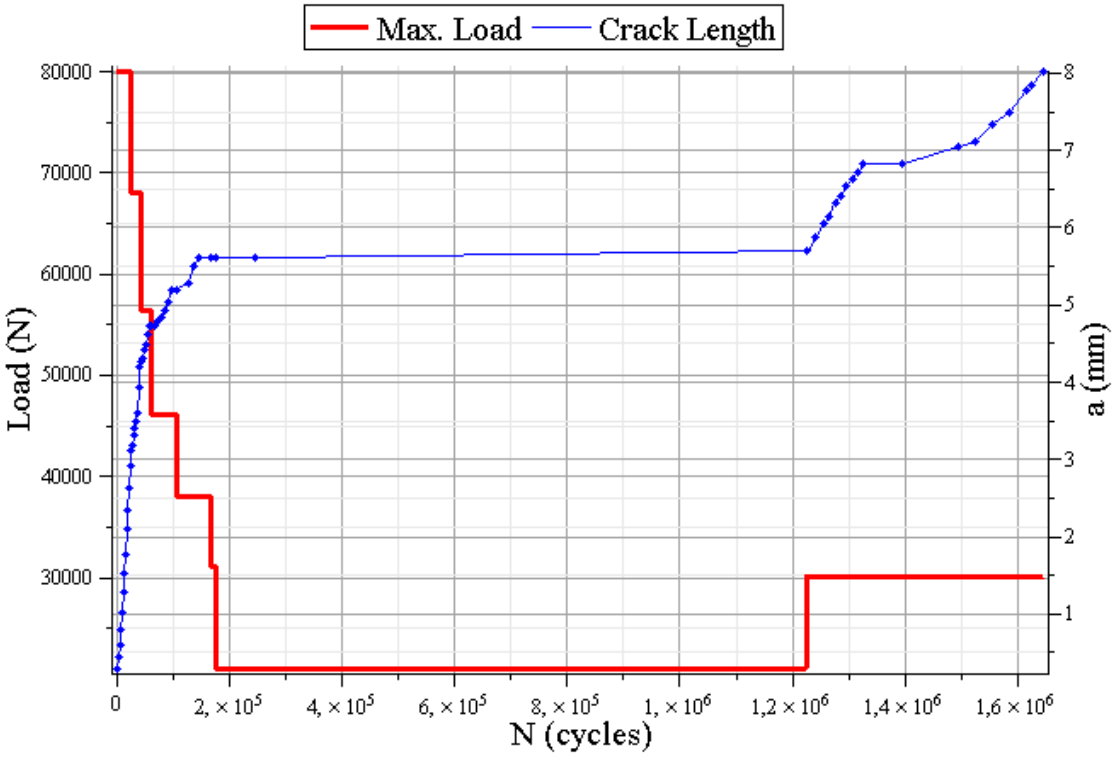


Figure 71 - Precracking sequence used in the first test specimen (MB, R=0,1, precrack measured from the tip of the EDM notch);a measured from EDM notch.

3.5. Results

The purpose of these tests is the determination of the Paris law constants $da/dN = (C) \cdot (\Delta K)^m$ where *a* is the crack length and *N* is the number of cycles, *C* and *m* are the constants. As mentioned before, before the actual fatigue crack growth test the realization of a fatigue precrack of specified minimum size is necessary. During the test the fatigue crack growth was measured for both of the test specimen sides (a_1 and a_2). These measurements were made with the aid of a travelling microscope of 20x magnification (Figure 72), located on both side of the testing machine, a MTS servo-hydraulic machine of 250 kN capacity, see Figure 73.



Figure 72 - PEAK microscope, to be mounted on a travelling device incorporating a Mitutoyo digital ruler.

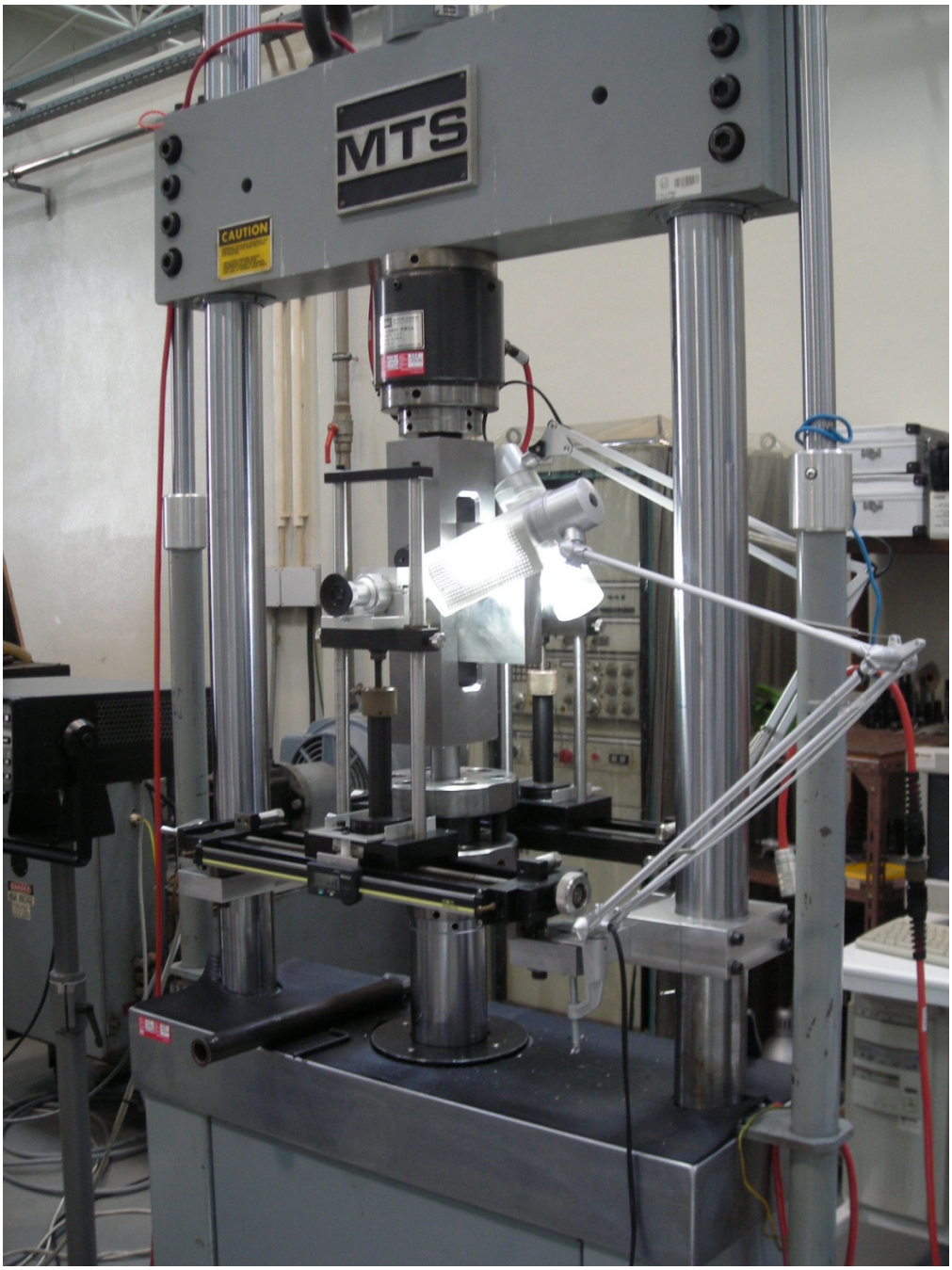


Figure 73 - MTS machine used for the tests and traveling microscopes (one on each side of the specimen).

3.5.1. BM specimen tested with R=0,1

According to ASTM standard E647, the precrack shall consist of a natural fatigue crack with some minimum length defined by a refired envelope centered at the tip of precrack (see Figure 43 and 47b) The first test specimen to be tested was a BM specimen loaded with an R value ($R = min.load/max.load$) equal to 0,1. The test began with an a value (average fatigue crack length) equal to 35,2 mm, a_1=34,42 mm and a_2=35,97 mm. 1466000 cycles were necessary to obtain these values of crack length in order to

fulfill the minimum fatigue crack requirements. Precracking procedure is the one already shown in Figure 71. The test of this specimen was made with a 16 Hz frequency, a maximum load of 30 kN with a 27 kN amplitude ($\Delta P = 27$ kN). The data obtained from the experimental activity are represented in Figure 74.

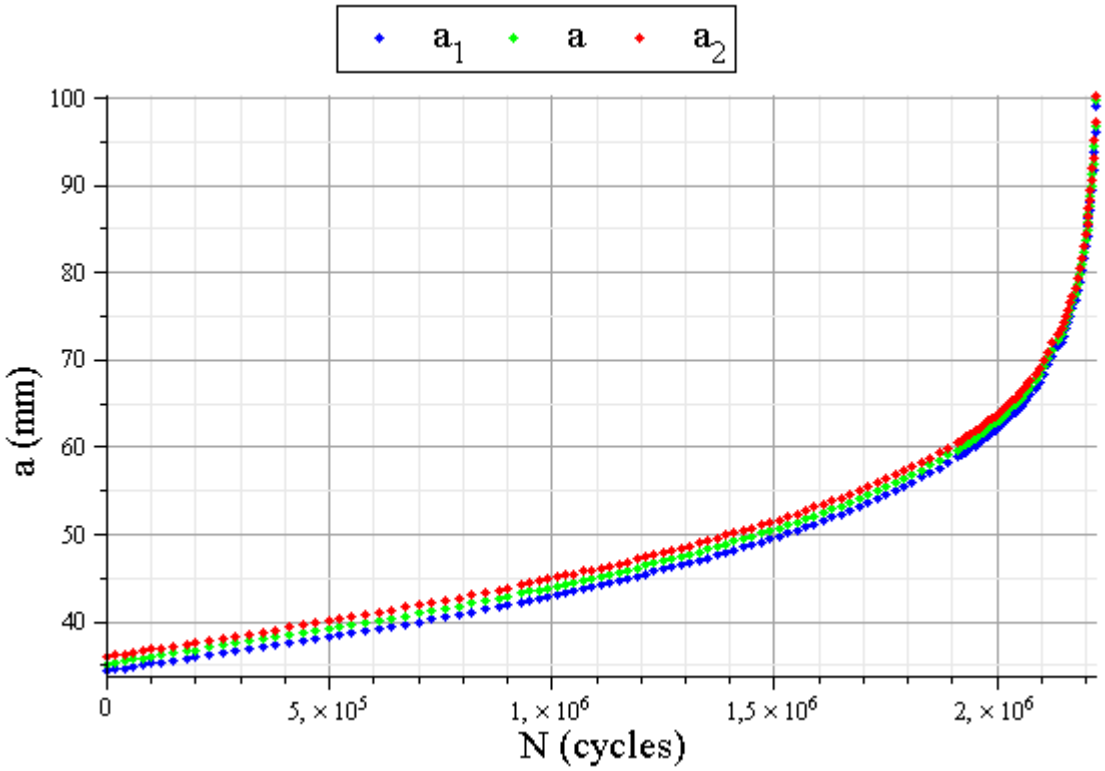


Figure 74- a *vs.* N data results obtained from measurements of the test specimen fatigue crack (BM, R=0,1).

In Figure 74 it is shown that the last crack length measurements correspond to a very large crack length increment per cycle, and this was associated to visible plastic deformation at the crack tip and large displacement of the loading pins. Similar considerations were used to end the tests of all the other specimens. (see Figures 81, 88 and 95).

With the obtained data results the constants of the Paris Law were calculated using two methods: Secant Method (SM) and the Polynomial Method (PM) with seven points; the corresponding software codes are given as Annexe A. Plots of $\log(\mathrm{da/dN})$ $vs.\log(\Delta K)$ obtained with the secant method and the software Excel and using the Matlab with basis on the ASTM E647 standard codes are shown in Figures 75 and 76 respectively. Using the secant method and the Excel software the resulting equation is, with a in mm and ΔK in MPa $\sqrt{\mathrm{mm}}$:

$$\frac{\mathrm{da}}{\mathrm{dN}} = (6{,}52 \times 10^{-15}) \cdot (\Delta K)^{3{,}48} \qquad (39)$$

which is undistinguishable from the result obtained using the Matlab software.

Figure 77 shows the results obtained using the PM method, programmed in Matlab.

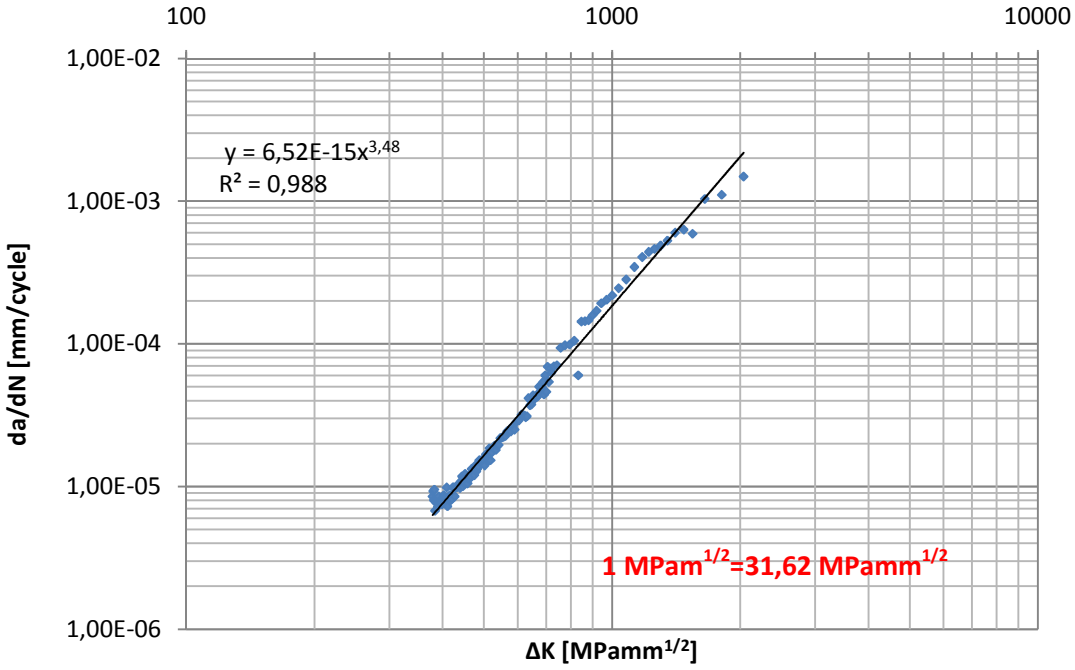


Figure 75 - da/dN *vs.* K data results using the Excel (SM, BM, R=0,1).

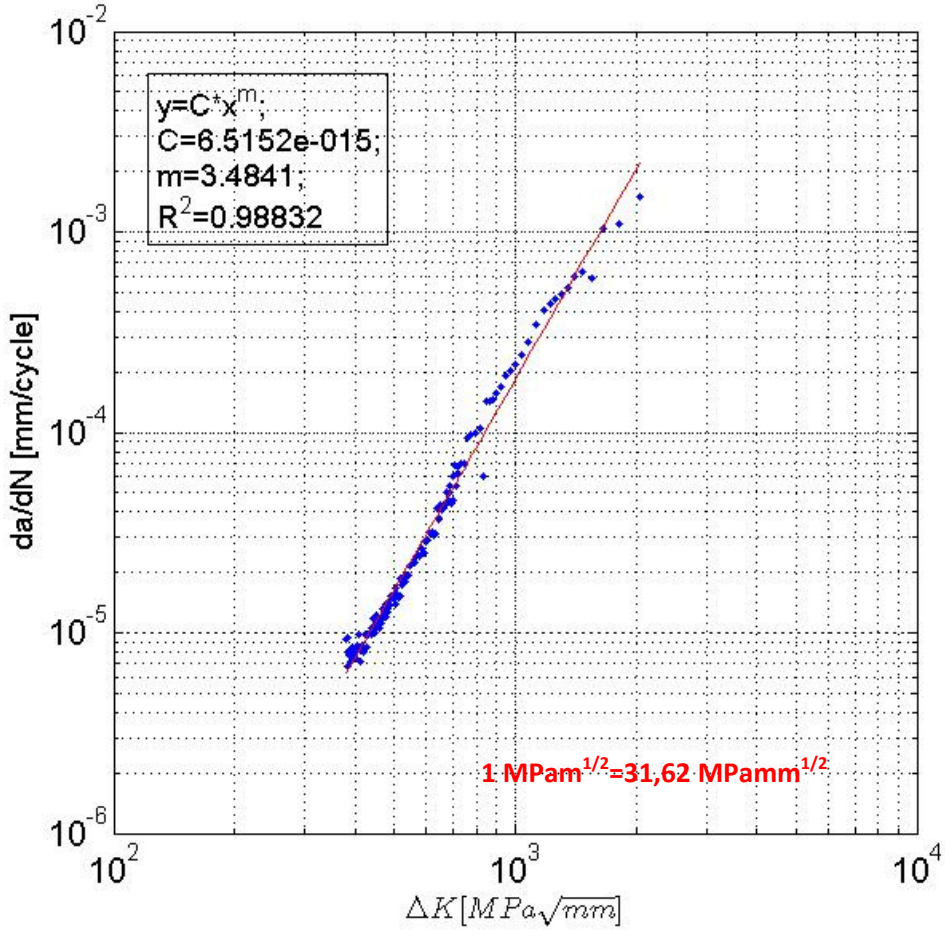


Figure 76 - da/dN *vs.* Δ K data results using the Matlab (SM, BM, R=0,1).

The Paris law obtained using the second method (PM) was:

$$\frac{da}{dN} = (3{,}38 \times 10^{-15}) \cdot (\Delta K)^{3{,}5884} \qquad (40)$$

The values obtained are close to the values calculated using the first method.

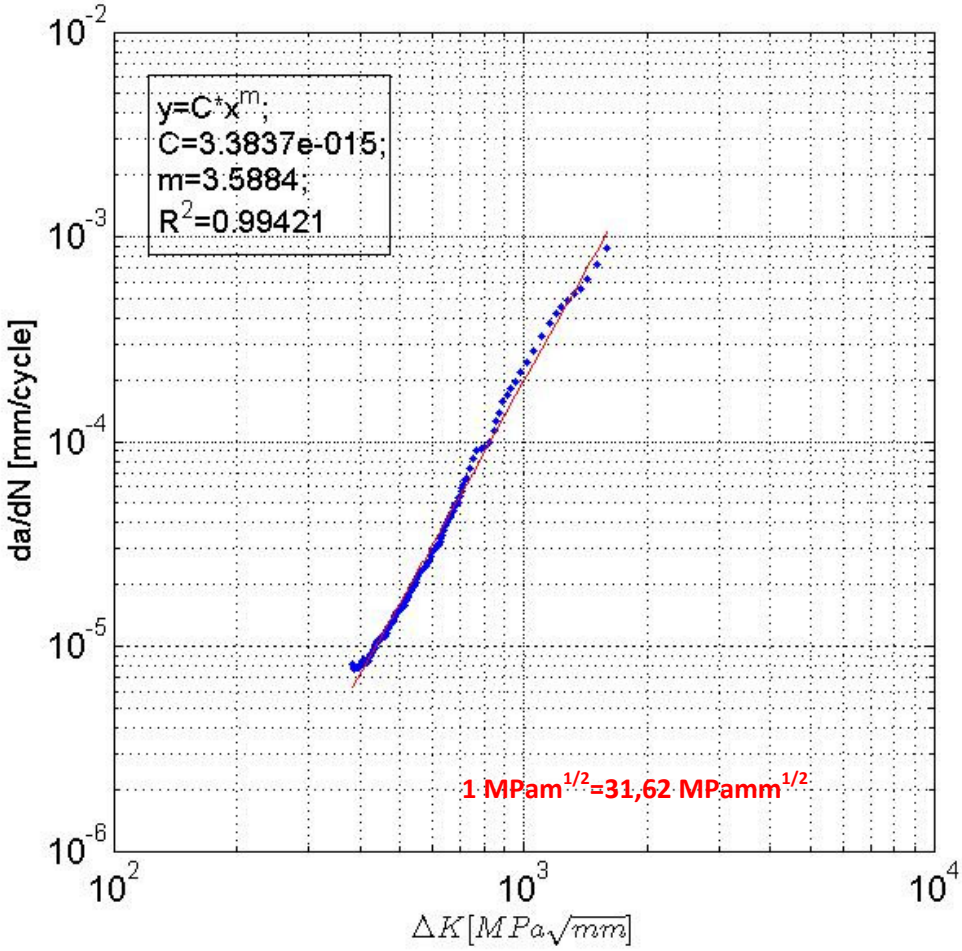


Figure 77 - da/dN *vs.* Δ K data results using the Matlab (PM, BM, R=0,1).

In order to verify the quality of the approximation made using the calculated Paris Laws using the 1st and 2nd (SM and PM) methods, N *vs.* a experimental results were compared with the N *vs.* a values obtained integrating the Paris laws curves, Figure 78. It is noted that the agreement between experimental test data and the prediction based upon the Paris law is very good.

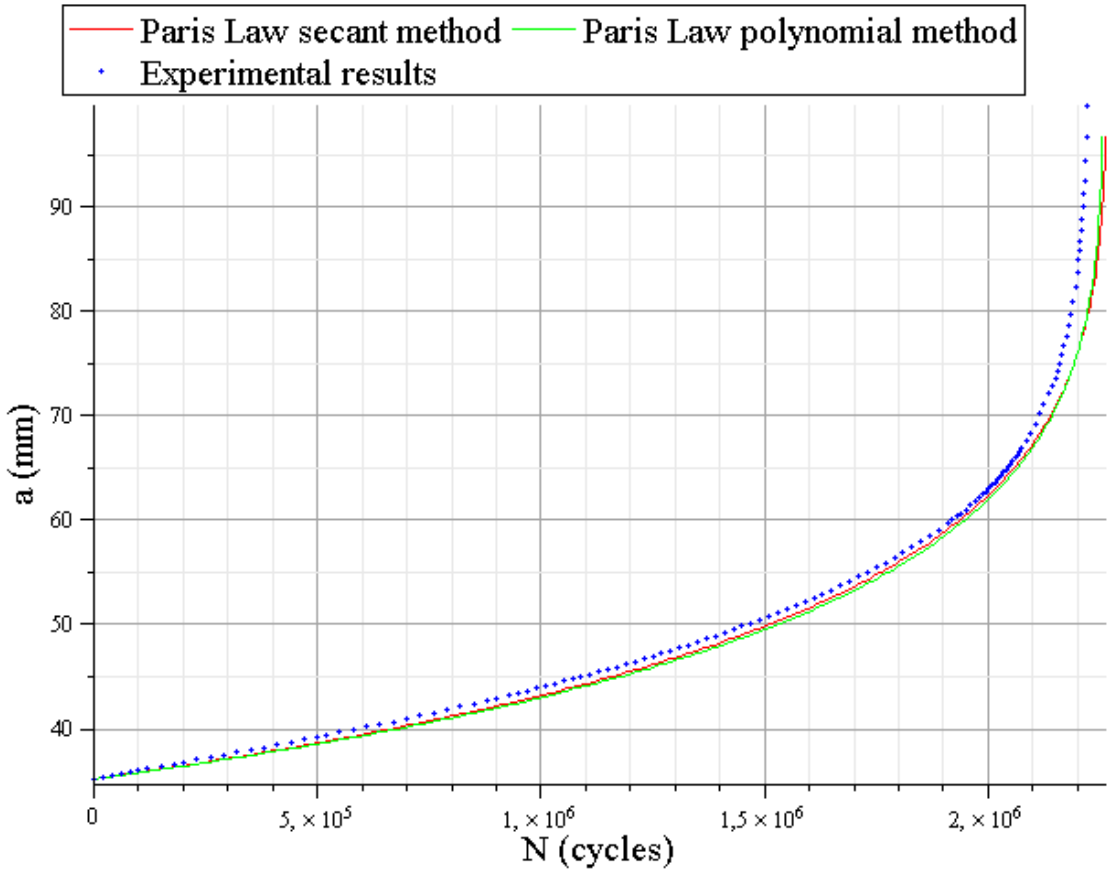


Figure 78 - Comparative plot of the experimental results with the calculated Paris laws (BM R=0,1).

The final aspect of the fatigue test specimen can be observed in Figure 79. As it can be seen, and from FEM analyses previously presented, the crack front presents a geometry similar to a "nail" with the crack length being bigger in the half thickness and a little smaller in free surfaces. This is related to the fact that the stress intensity factor is higher in the half thickness then for the free surfaces.

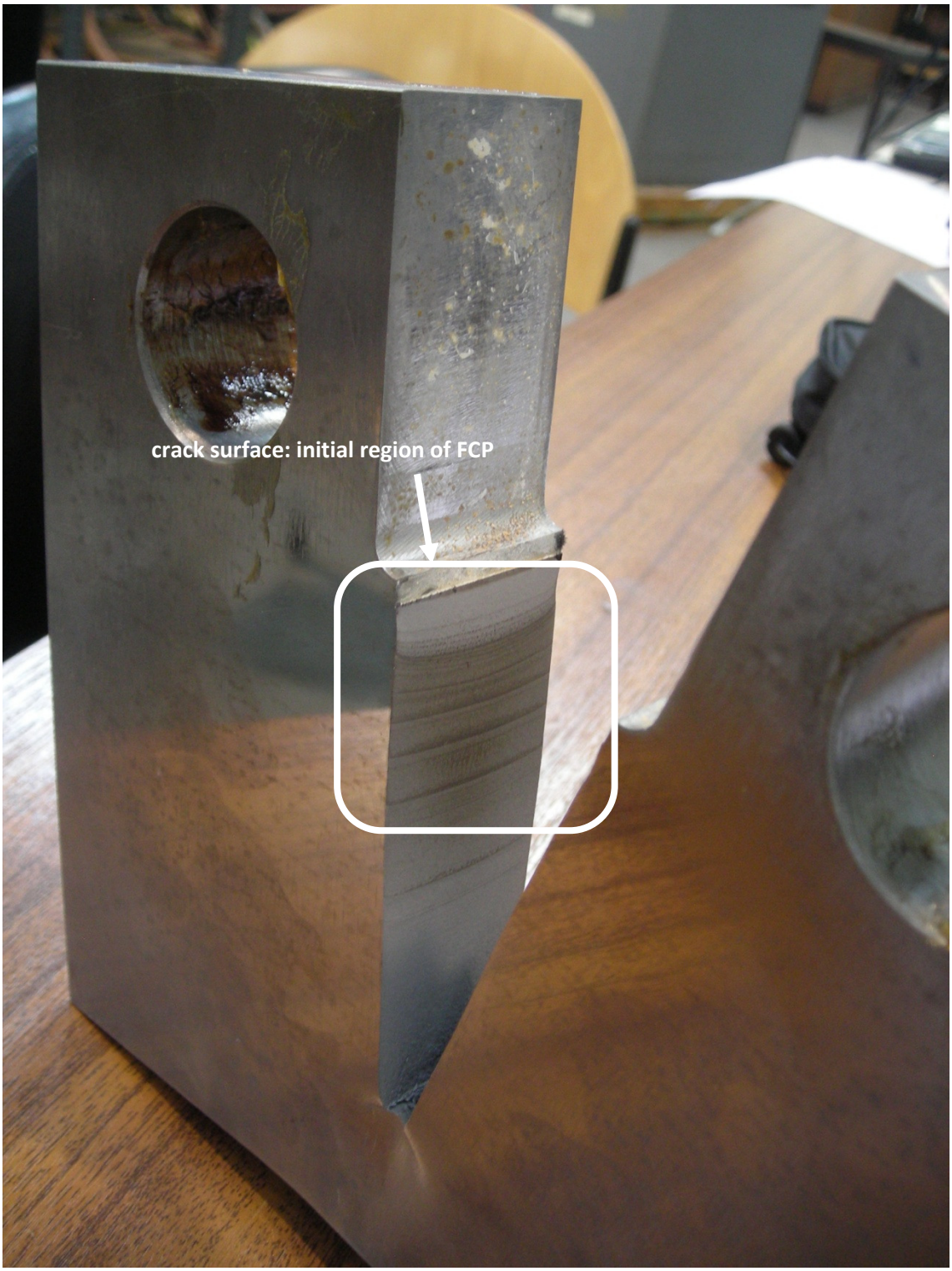


Figure 79 - Specimen Picture in the end of the test (BM R=0,1).

3.5.2. BM specimen tested with R=0,4

The specimen to be tested was a BM specimen loaded with an R value equal to 0,4. The test began with an a value equal to 34,43 mm, a_1=34,66 mm and a_2=34,19 mm. 313000 cycles were necessary to obtain these values of crack length in order to fulfill

the minimum fatigue crack requirements. Precracking procedure for this test specimen is shown in Figure 80.

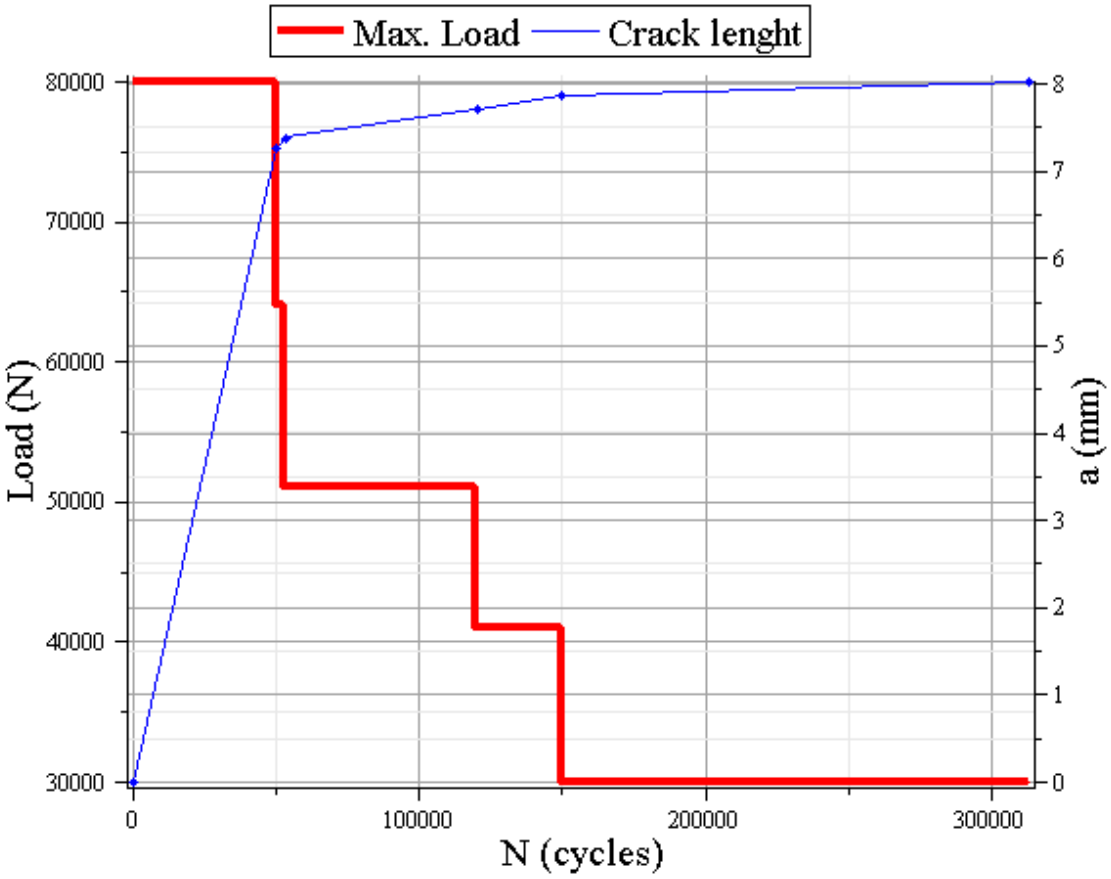


Figure 80 - Precracking sequence used in the MB R=0,4 test specimen; a measured from the EDM notch.

The test of this specimen was made with a 18 Hz frequency, a maximum load of 30 kN with a 18 kN amplitude ($\Delta P = 18$ kN). The data obtained from the experimental activity is represented in Figure 81.

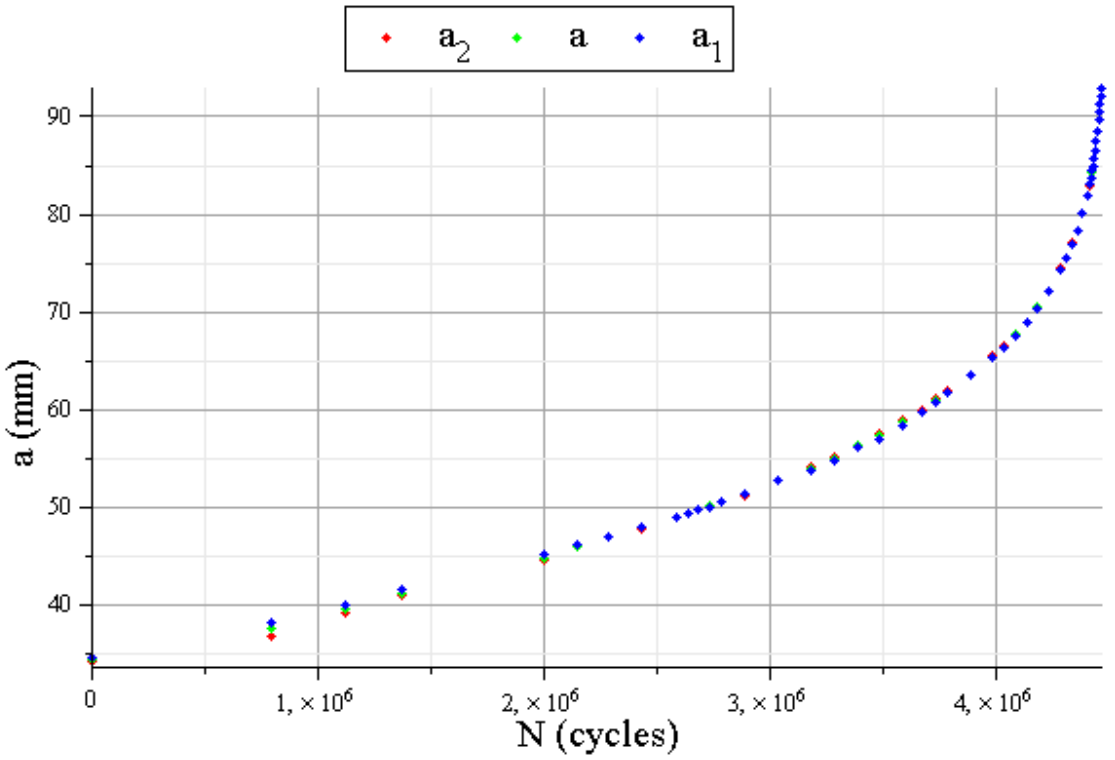


Figure 81 - N *vs*. a data results obtained from measurements of the test specimen fatigue crack (BM, R=0,4).

With the obtained data results the respective Paris Law was calculated. Again, log (da/dN) $vs.$ log (ΔK) plots were obtained using three procedures: SM calculated using the software Excel (Figure 82), SM with basis on the ASTM standard code and Matlab (Figure 83), and PM method using Matlab (Figure 84).

Using the secant method and the Excel software the resulting equation is:

$$\frac{da}{dN} = (9{,}929 \times 10^{-14}) \cdot (\Delta K)^{3{,}136} \qquad (41)$$

which is undistinguishable from the result obtained using SM method and the Matlab software.

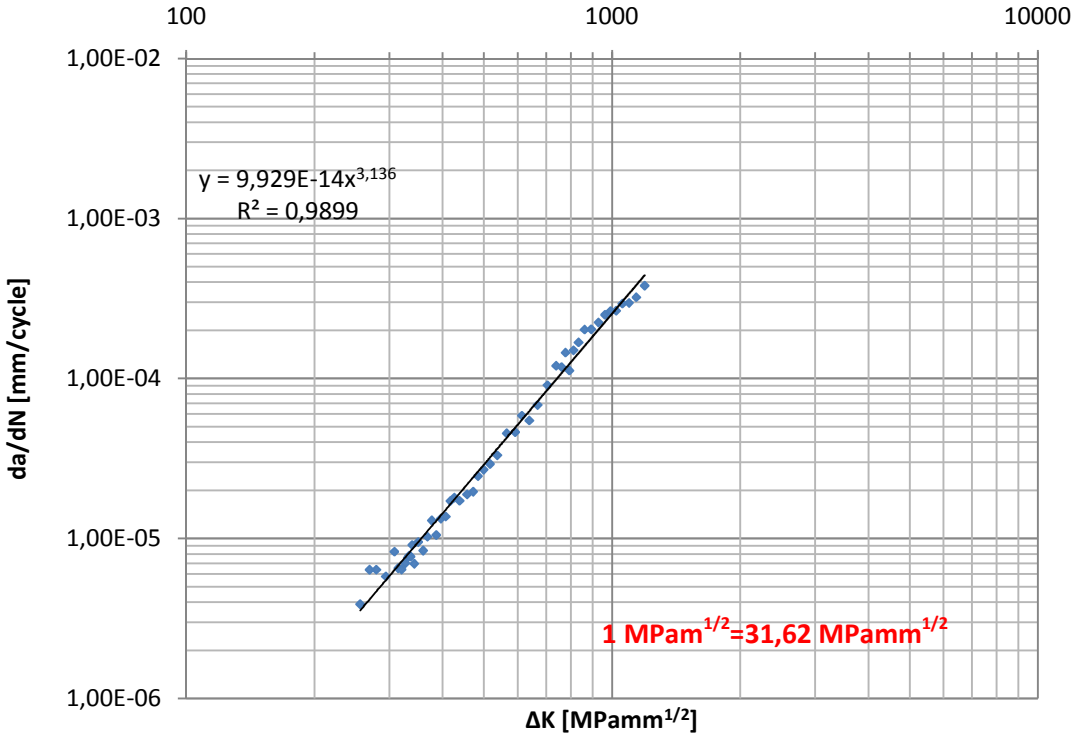


Figure 82 - da/dN *vs*. Δ K data results using the Excel (SM, BM R=0,4).

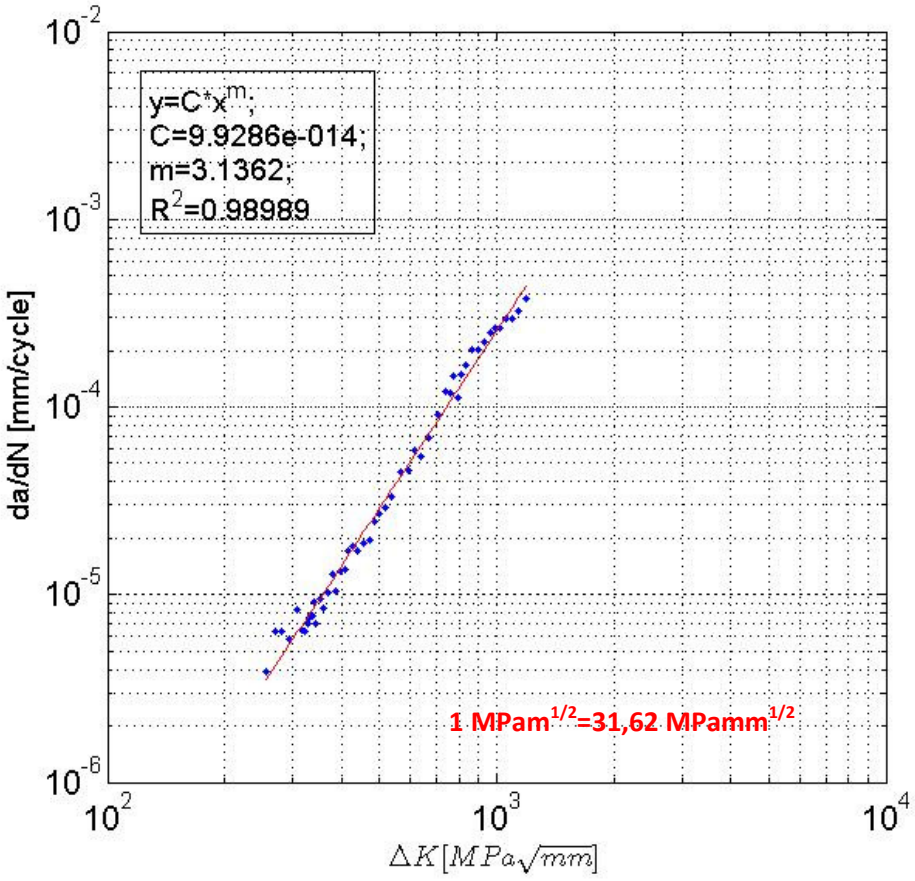


Figure 83 - da/dN *vs*. Δ K data results using the Matlab (SM, BM R=0,4).

The Paris law obtained using the PM was:

$$\frac{da}{dN} = (4{,}5931 \times 10^{-14}) \cdot (\Delta K)^{3{,}2608} \qquad (42)$$

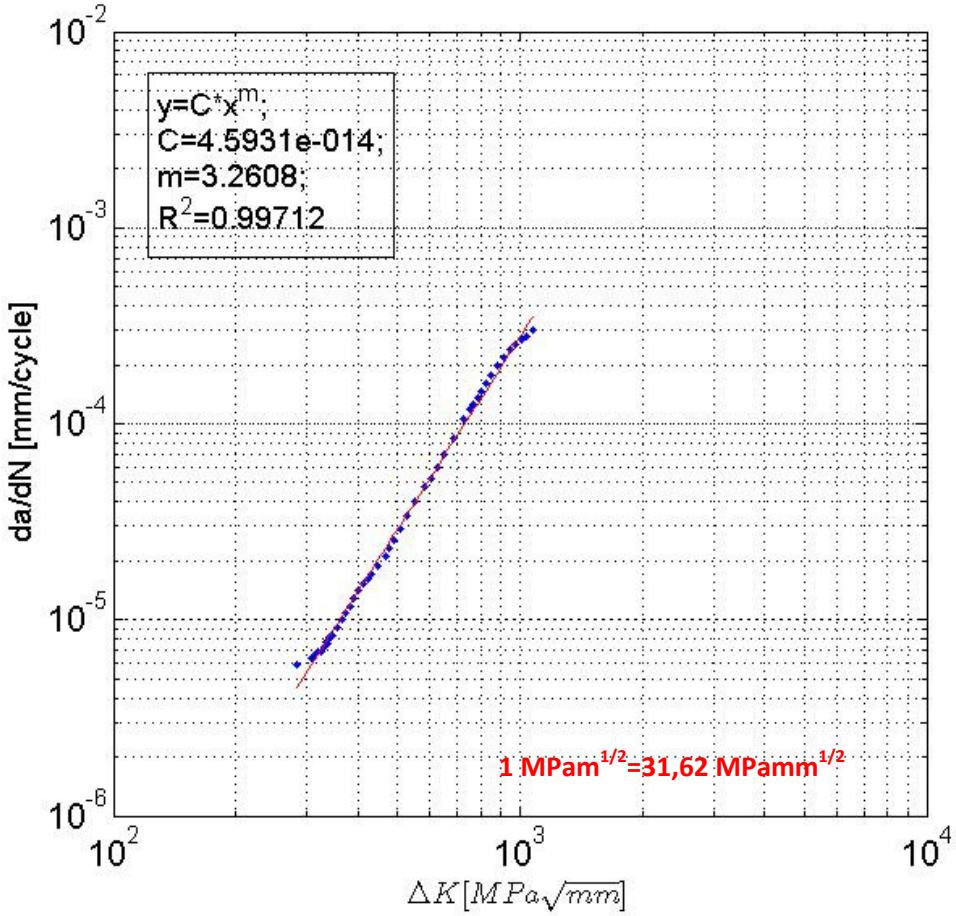


Figure 84 - da/dN *vs.* Δ K data results using the Matlab (PM, BM R=0,4).

In order to verify the quality of the approximation made using the calculated Paris Laws using the 1st and 2nd (SM and PM) methods, N *vs.* a experimental results were compared with the N *vs.* a values obtained integrating the Paris laws curves, Figure 85.

Though the agreement with the calculated Paris law is good, it is not as good as the agreement obtained with the first test specimen (see Figure 78). This occurs probably because the number of points measured were far less than in the first test specimen. The quality of the approximation using the SM is better than the quality of the approximation calculated with the PM.

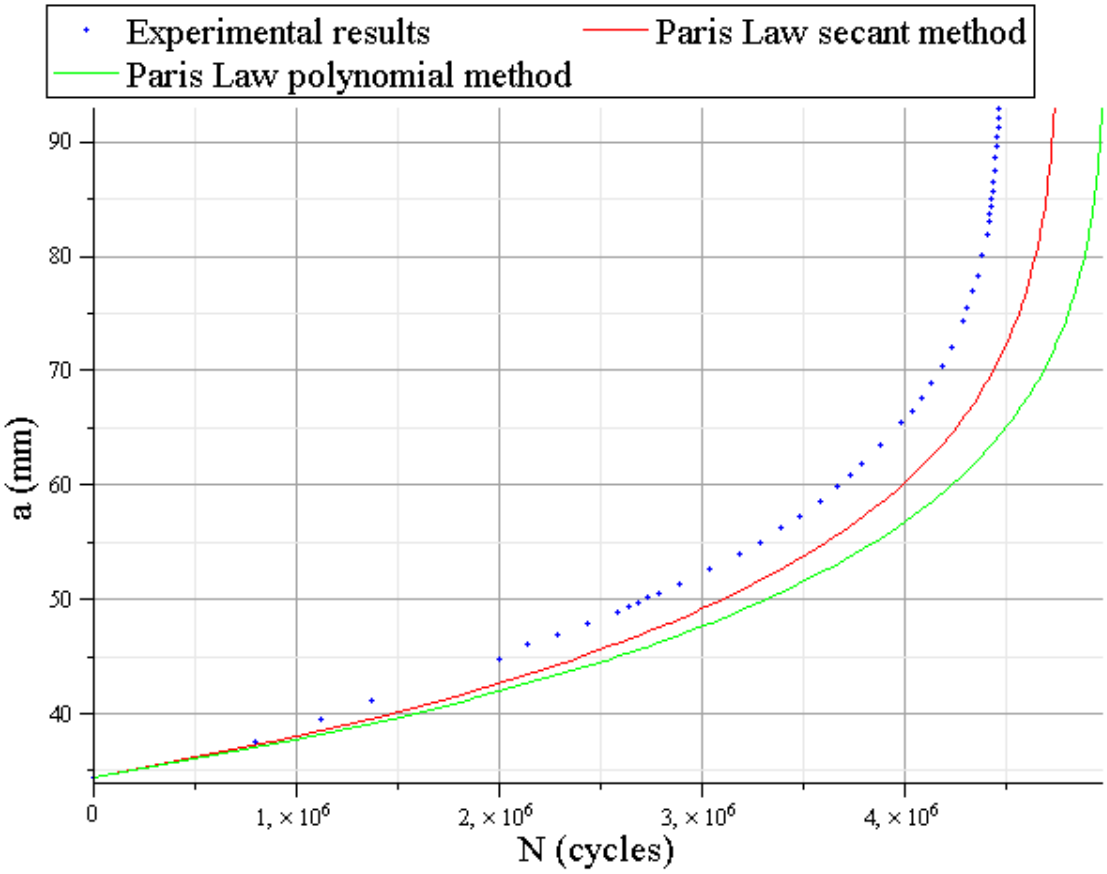


Figure 85 - Comparative plot of the experimental results with the calculated Paris laws (BM R=0,4).

The final aspect of the fatigue test specimen can be observed in Figure 86[5]. As it can be seen the fatigue crack front presents the expected "nail" geometry, with the crack length being bigger in the half thickness and a little smaller in the free surfaces. This is associated to the higher stress intensity factor in the half thickness. The appearance of the crack front is similar to the one observed for the BM test specimen tested with R=0,1.

[5] Unfortunately during the separation of the tested specimen in two halves, a manual saw and vise clamp were used, and during the operation the fracture surfaces were slightly damaged, as can be seen in Figure 87.

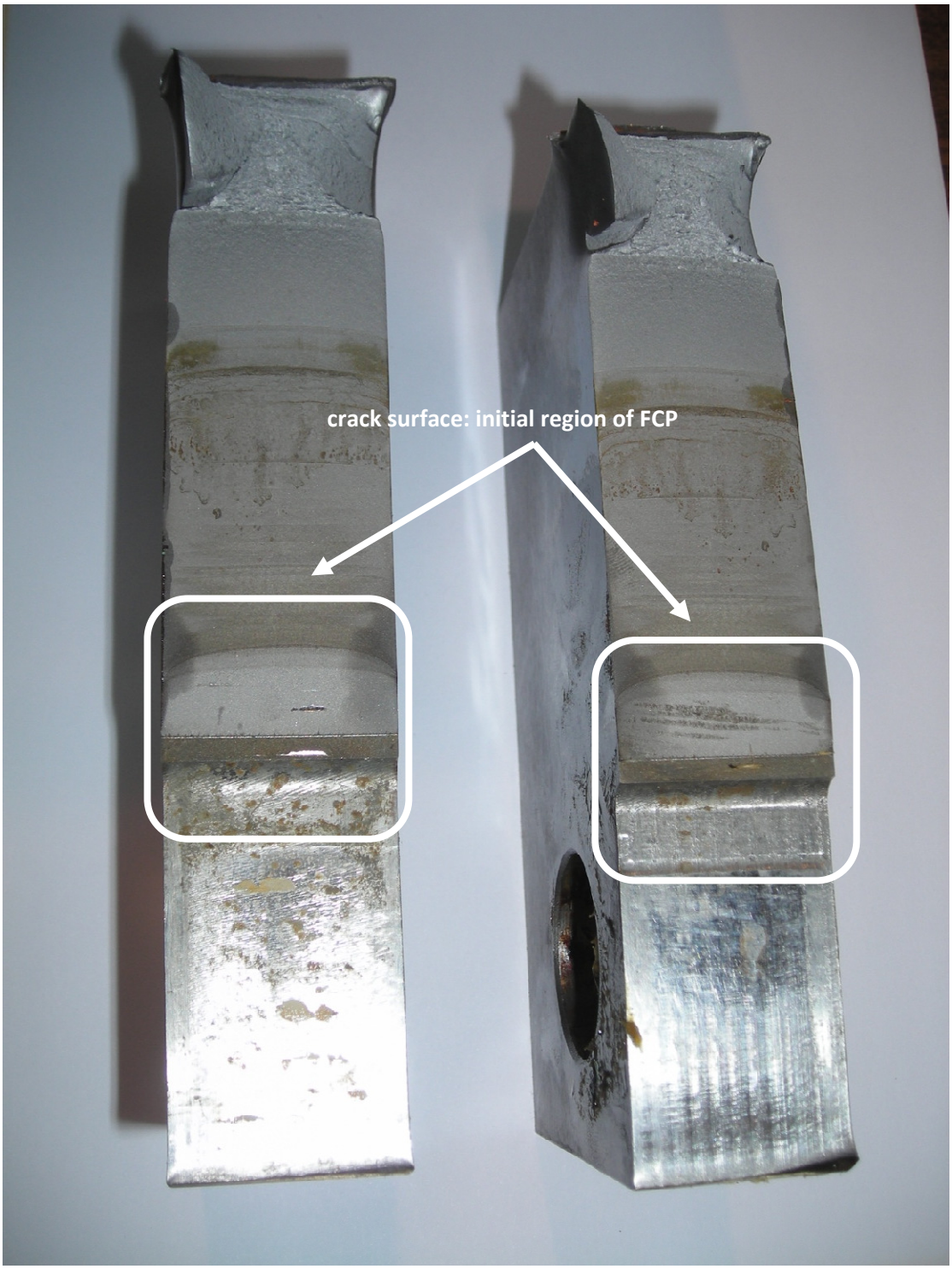


Figure 86 – Fracture surfaces in the end of the test (BM R=0,4).

3.5.3. BM specimen tested with R=0,7

A BM specimen was loaded with an R value equal to 0,7. The test began with an a value equal to 34,75 mm, a_1=34,80 mm and a_2=34,70 mm. 200000 cycles were necessary to obtain these values of crack length in order to fulfill the minimum fatigue crack requirements. Precracking procedure for this test specimen is shown in Figure 87.

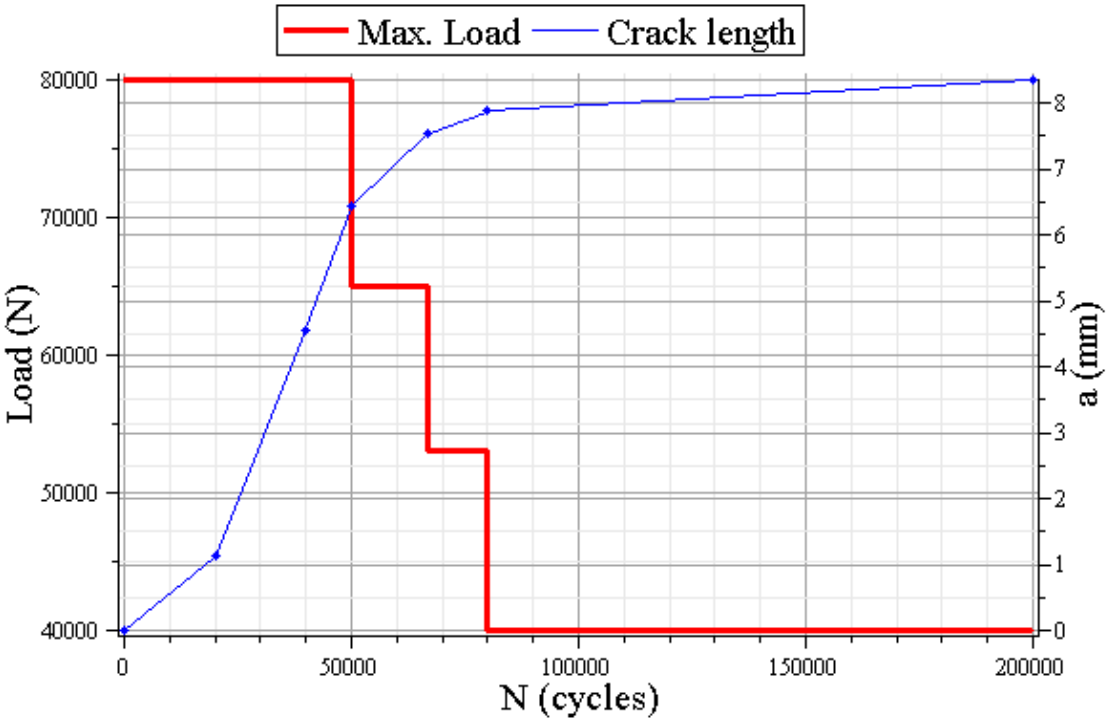


Figure 87 - Precracking sequence used in the BM R=0,7 test specimen; a measured from EDM notch.

The test of this specimen was made with a 16 Hz frequency, a maximum load of 40 kN with a 12 kN amplitude ($\Delta P = 12$ kN). The data obtained from the experimental activity is represented in Figure 88.

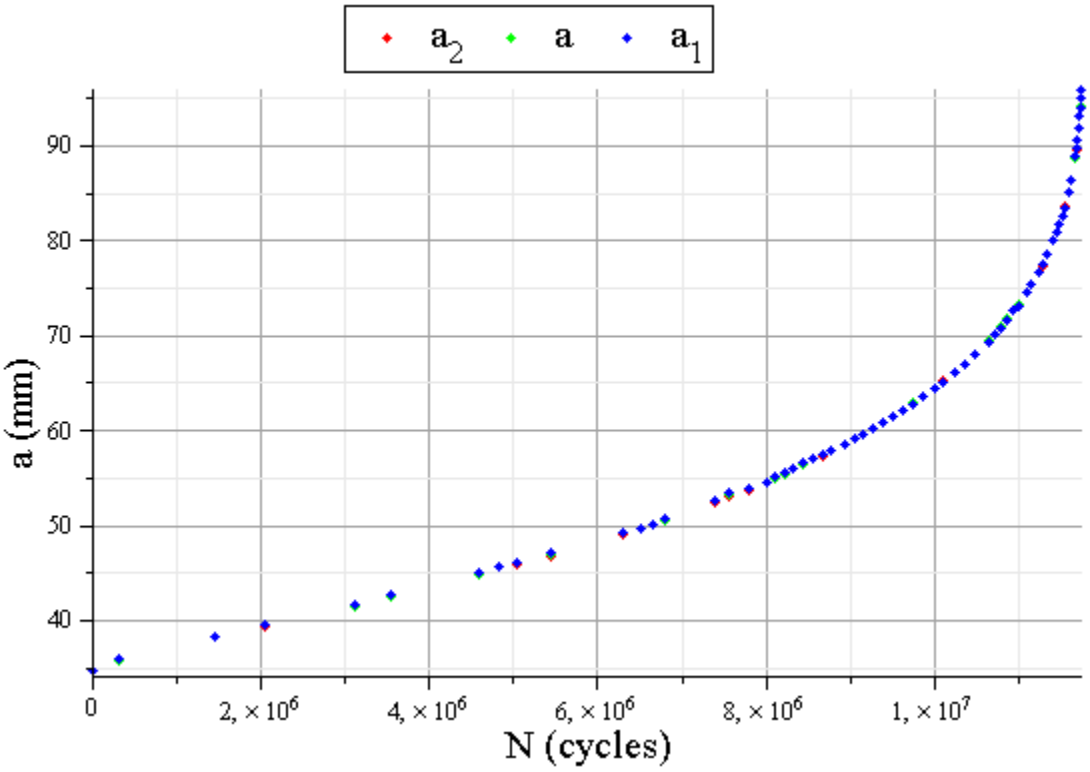


Figure 88- N *vs*. a data results obtained from measurements of the test specimen fatigue crack (BM R=0,7).

With the obtained data results the respective Paris Law was calculated.

Again, $\log(\mathrm{da/dN})$ *vs* $\log(\Delta K)$ plots were obtained using three procedures: SM calculated using the software Excel (Figure 89), SM with basis on the ASTM standard code and Matlab (Figure 90), and PM method using Matlab (Figure 91).

Using the secant method and the Excel software the resulting equation is:

$$\frac{da}{dN} = (3{,}468 \times 10^{-13}) \cdot (\Delta K)^{2{,}949} \qquad (43)$$

which is undistinguishable from the result obtained using the Matlab software.

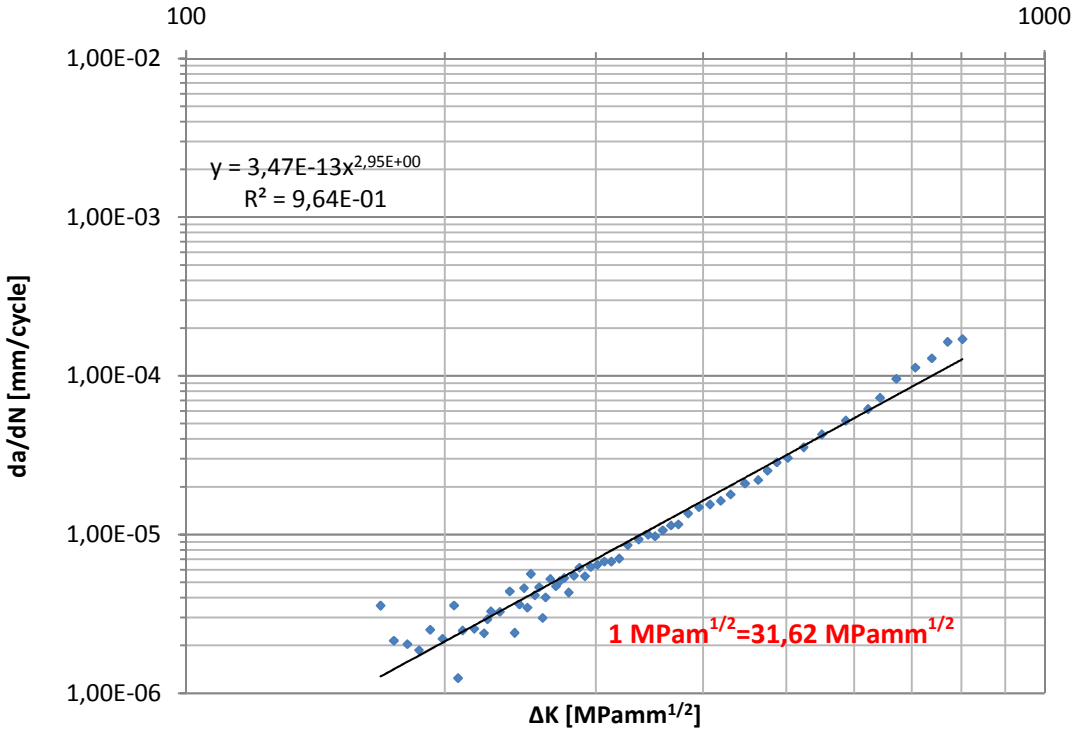


Figure 89 - da/dN *vs*. Δ K data results using the Excel (SM, BM R=0,7).

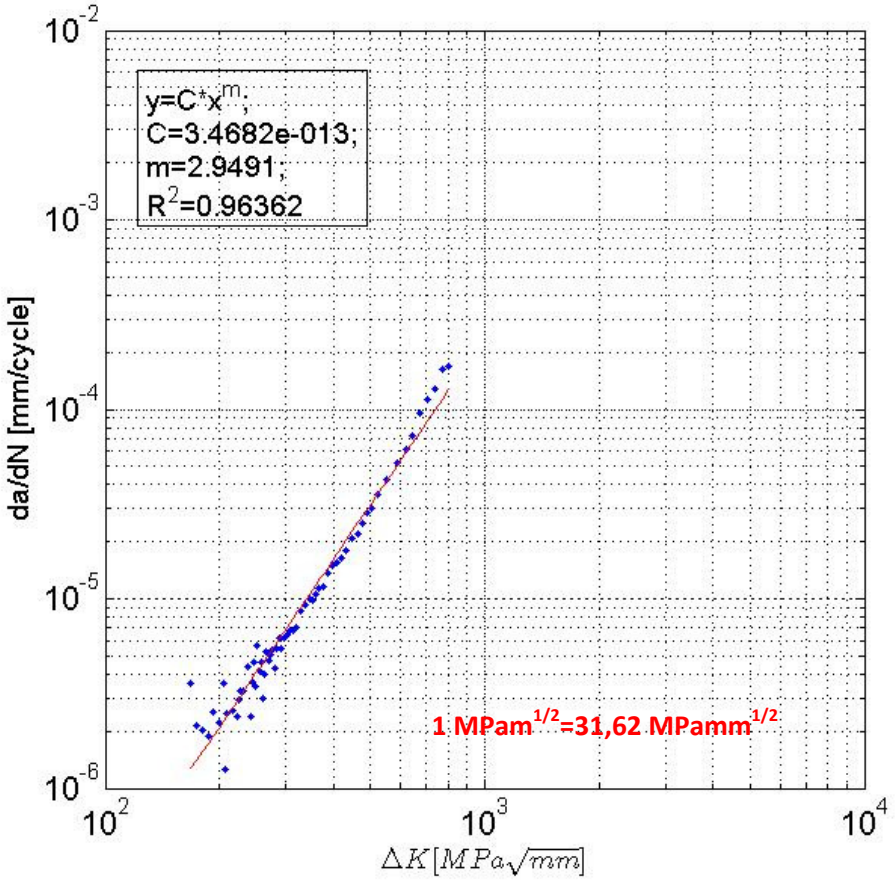


Figure 90 - da/dN *vs*. Δ K data results using the Matlab (SM, BM R=0,7).

The Paris law obtained using the PM was:

$$\frac{da}{dN} = (2{,}304 \times 10^{-14}) \cdot (\Delta K)^{3{,}0172} \qquad (44)$$

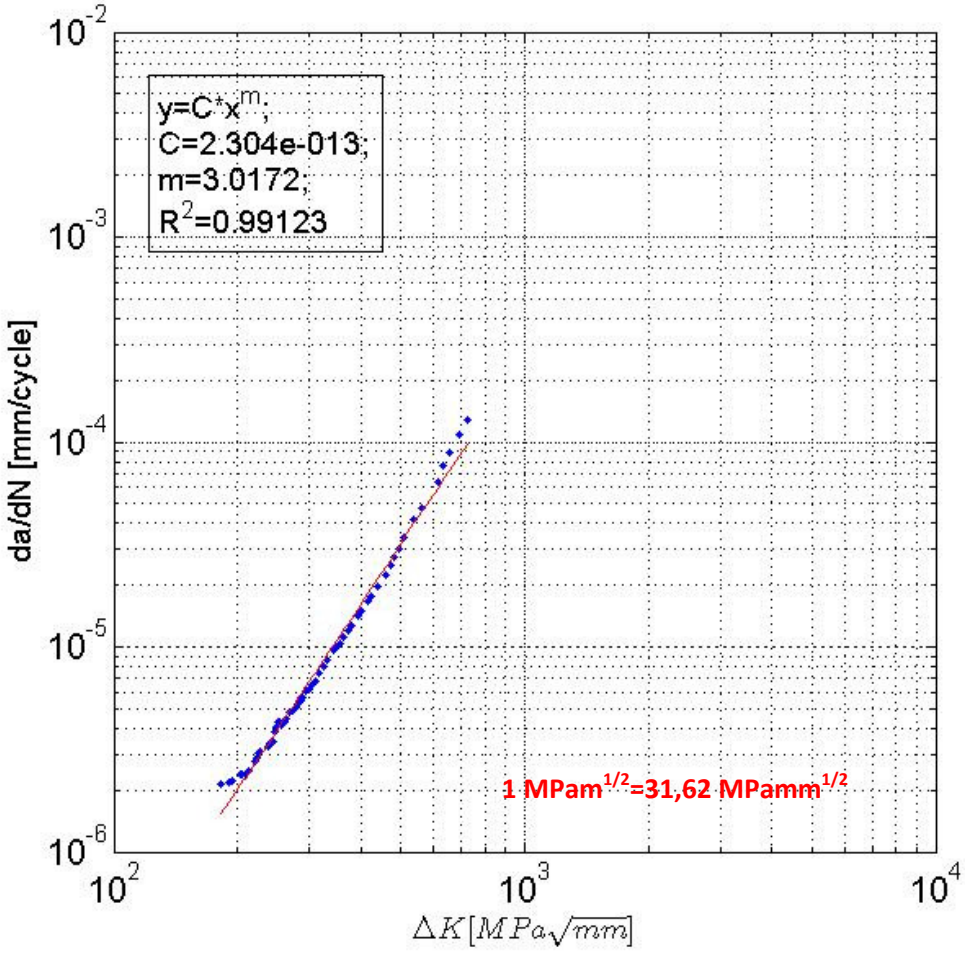


Figure 91 - da/dN *vs.* Δ K data results using the Matlab (PM, BM R=0,7).

The quality of the agreement of the experimental N *vs.* a with the integration of the calculated Paris laws is similar to the agreement obtained for the MB specimen tested with R=0,4 (see Figure 92). The quality of the approximation using the SM is better than the quality of the approximation calculated with the PM.

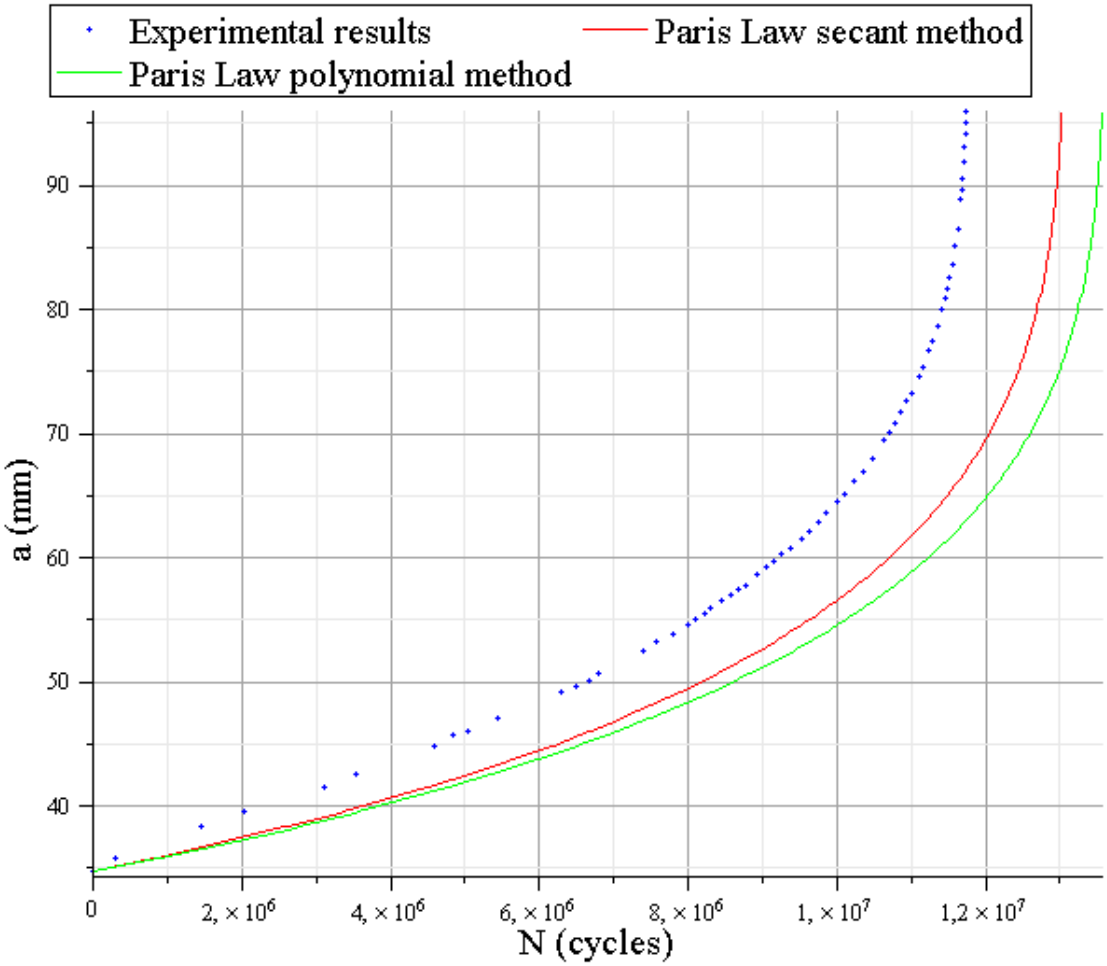


Figure 92- Comparative plot of the experimental results with the calculated Paris laws (BM R=0,7).

The final aspect of the fatigue test specimen can be observed in Figure 93. As it can be seen the fatigue crack front presents the expected "nail" geometry, as expected, that is similar to the surfaces obtained for the BM with R=0,1 and R=0,4 test specimens.

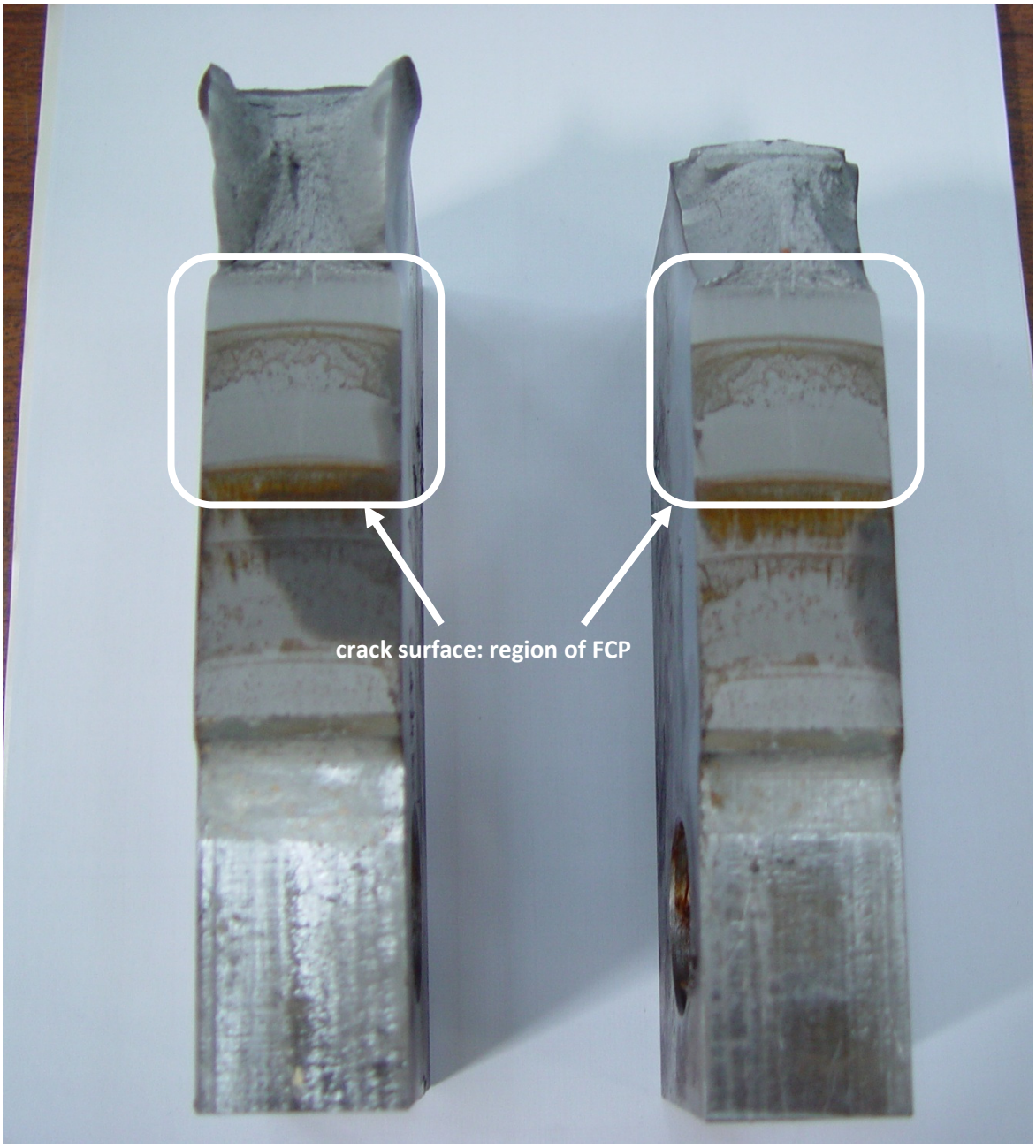


Figure 93 - Fracture surfaces in the end of the test (BM R=0,7).

3.5.4. HAZ specimen tested with R=0,1

The HAZ specimen was tested with a R = 0,1. The test began with an average crack length value equal to 34,88 mm, a_1=34,03 mm and a_2=35,72 mm. 2445000 cycles were necessary to obtain these values of fatigue crack length in order to fulfill the minimum fatigue precrack requirements. The test of this specimen was made at a 10 Hz frequency. The precracking procedure of this specimen is shown in Figure 94.

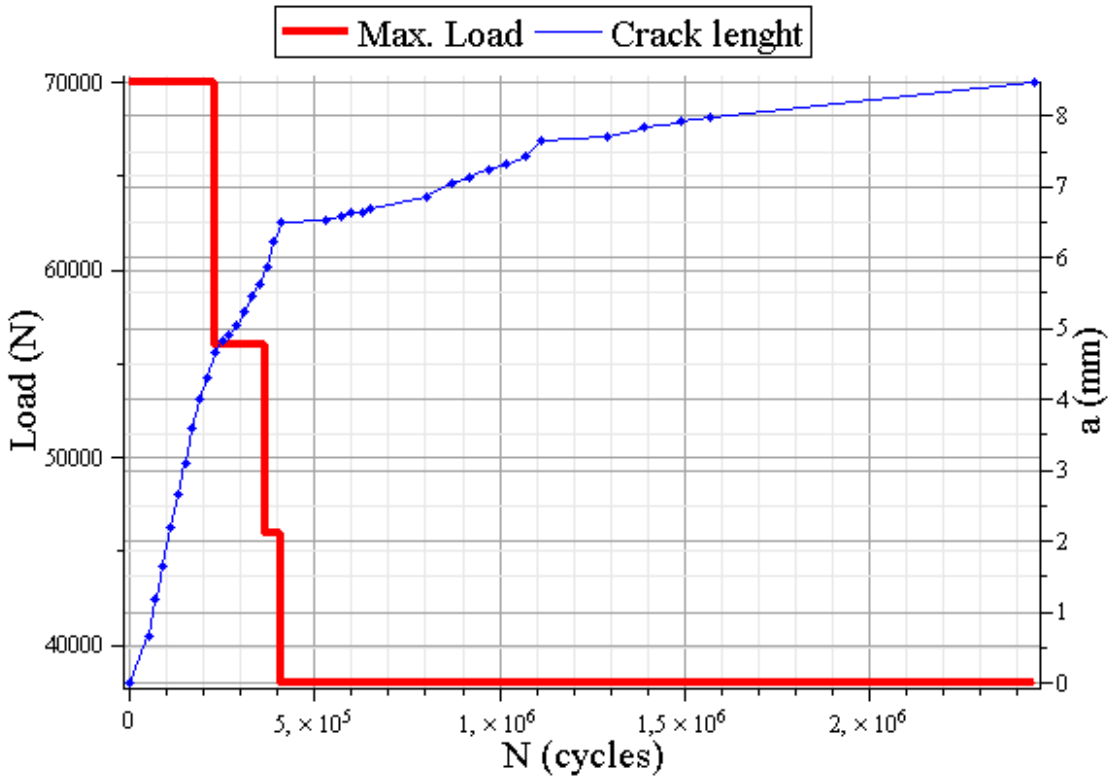


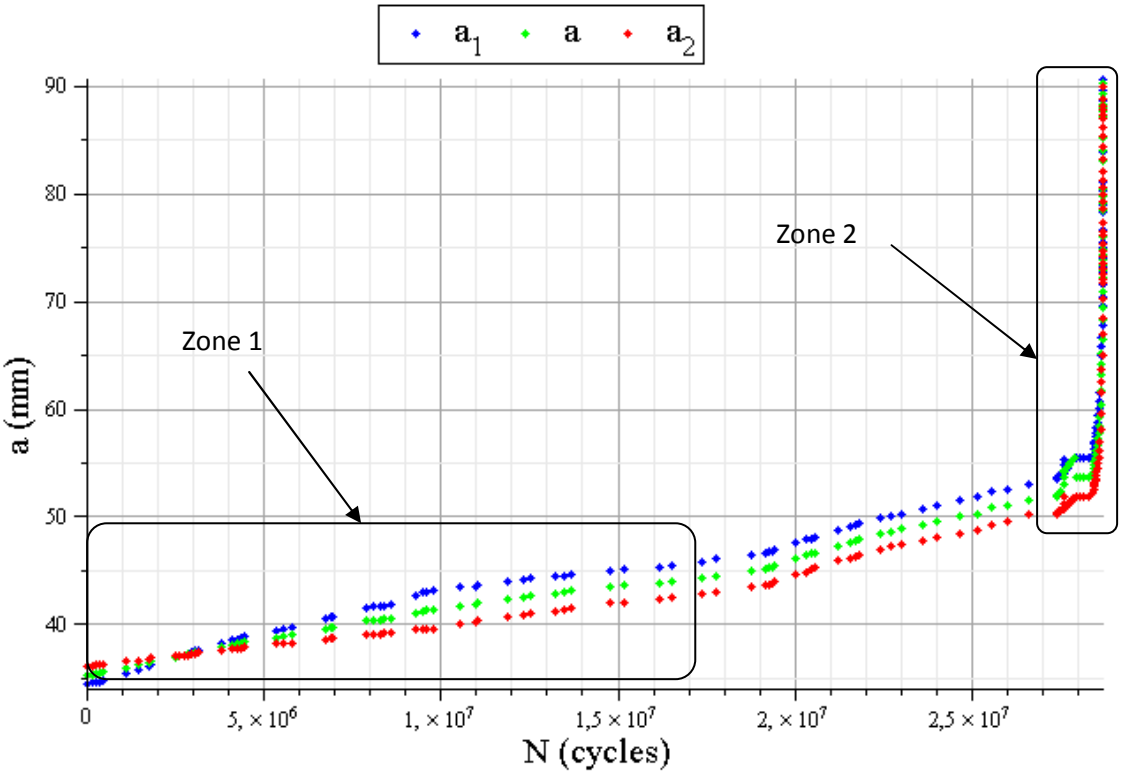
Figure 94 - Precracking sequence used in the HAZ R=0,1 test specimen; a measured from EDM notch.

During the tests several problems occurred as an unexpected slowdown of the crack growth rate, which led to consecutive fatigue test load increases in order to raise the ΔK_I values and increase the fatigue crack growth rate. Several weeks were spent with this test specimen due to this unexpected crack growth rate, see Table 16.

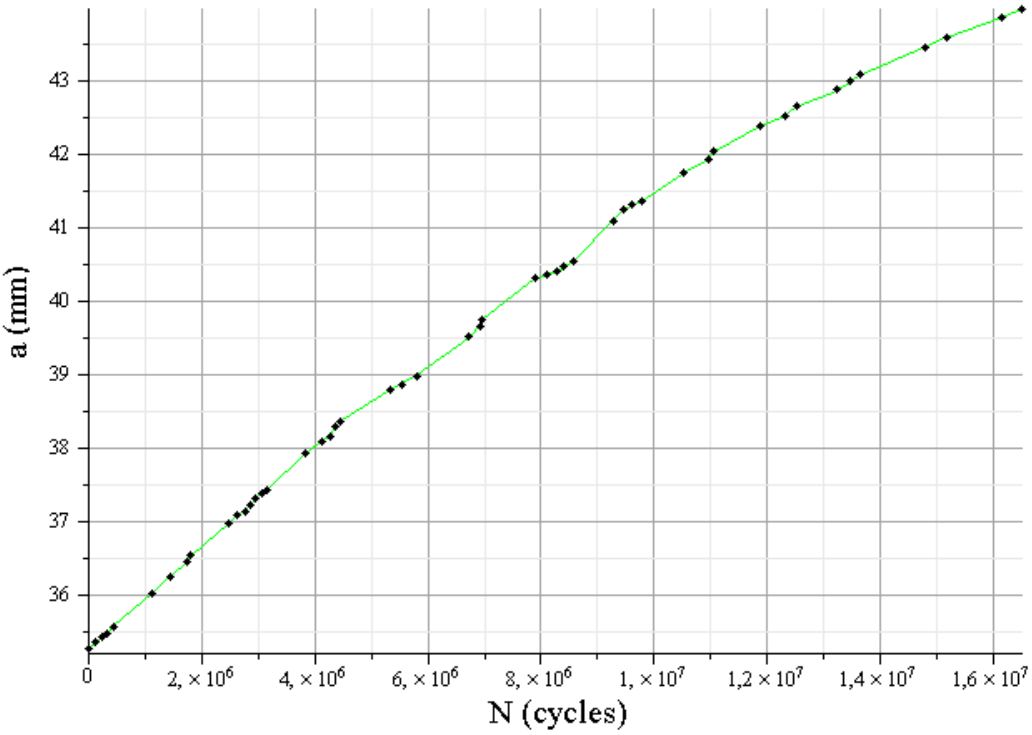
Table 16 - Load variation during the test.

a (mm)	P max (N)	P min (N)
34,49 < a <45,10	38000	3800
45,10 < a < 51,58	50000	5000
51,58 < a < 53,73	70000	7000
53,73 < a < 90,09	80000	8000

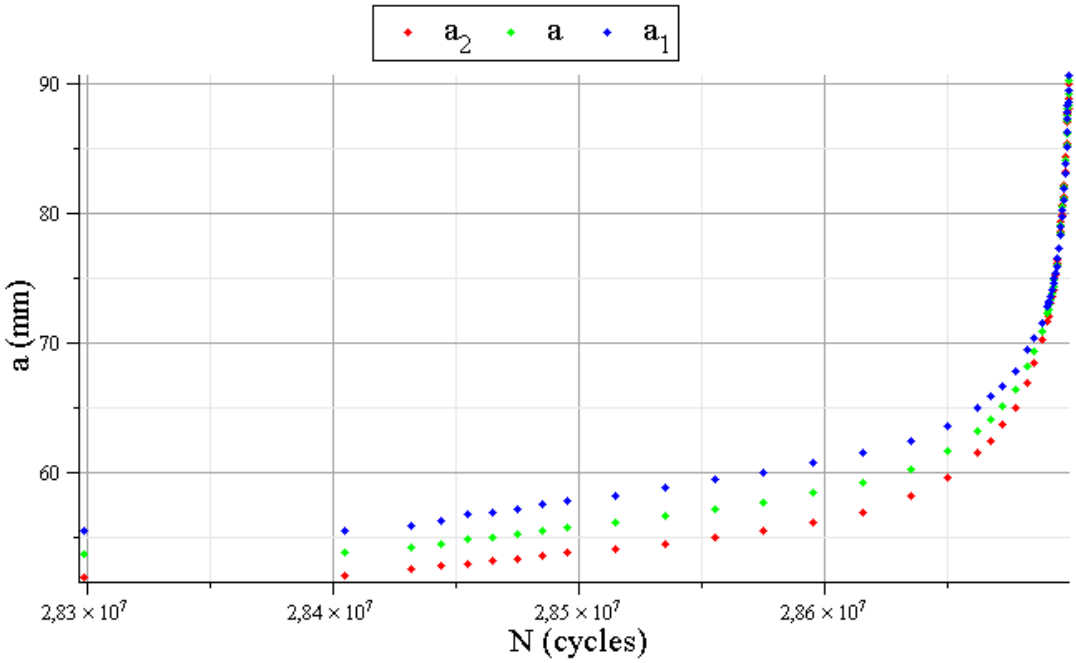
Also during this test a threaded pin tool that made the connection between the machine load cell and fixtures of grips broke, situation that caused further delay of the test. A new tool was ordered in “Autoconceptus” in order to replace the broken tool. Finally the experimental data results obtained are presented in Figure 95.


a1
a
a2
Zone 1
Zone 2
a (mm)
N (cycles)
90
80
70
60
50
40
0
5, × 10^6
1, × 10^7
1,5 × 10^7
2, × 10^7
2,5 × 10^7

a)


a (mm)
N (cycles)
43
42
41
40
39
38
37
36
0
2, × 10^6
4, × 10^6
6, × 10^6
8, × 10^6
1, × 10^7
1,2 × 10^7
1,4 × 10^7
1,6 × 10^7

b)



c)

Figure 95

a) a *vs.* N data results obtained from measurements of the test specimen fatigue crack (HAZ R=0,1);

b) Zoom plot of the zone 1 data results obtained from measurements of the test specimen fatigue crack (HAZ R=0,1).

c) Zoom plot of the zone 2 data results obtained from measurements of the test specimen fatigue crack (HAZ R=0,1).

From the experimental data the respective points in the da/dN *vs* ΔK were obtained (Figure 96).

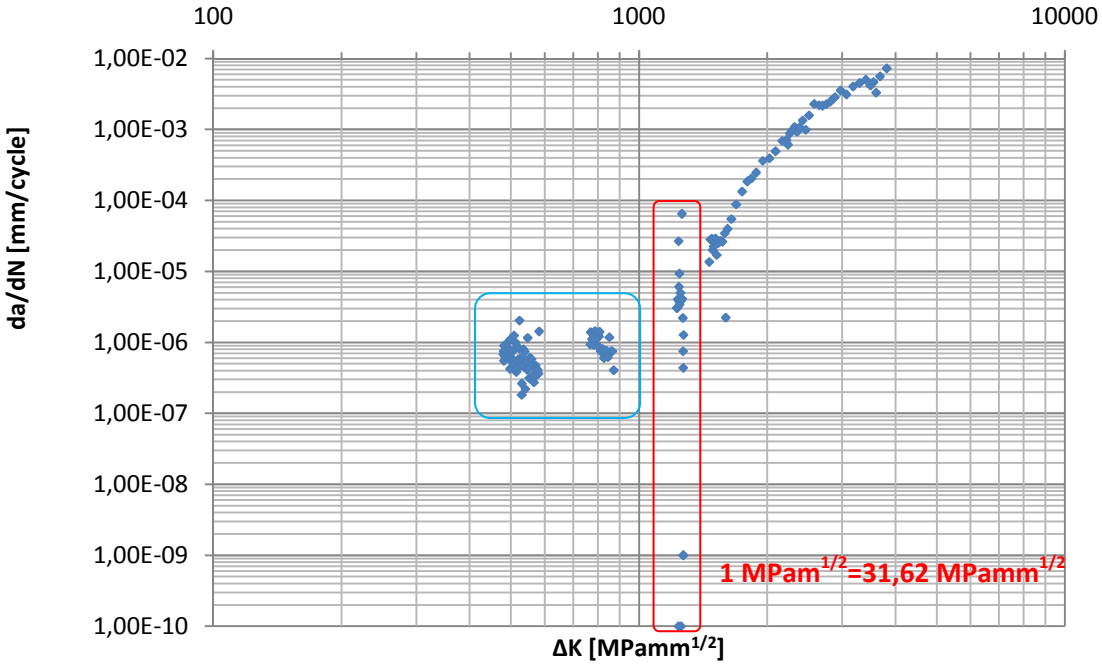


Figure - 96 da/dN *vs*. K data results (SM, HAZ R=0,1).

Distances in the horizontal axis without data correspond to moments where the load amplitude was increased, in order to get propagation and increase the crack growth rate. The data points marked in red in Figure 96 should not be considered relevant, since they were associated to the moment where the previously mentioned rupture of a grip element took place.

It should be mentioned that the ΔK values associated to the blue rectangle of Figure 96 are calculated on the assumption that cracks are through cracks. *Post mortem* it was identified that the crack was not a through crack, as will be seen later (Figure 100). Therefore the data corresponding to the blue region should be taken as approximate and not rigorous. Paris law determination was made with basis on the data results above 1400 MPamm$^{1/2}$. The respective Paris law can now be obtained from the experimental data. Using the secant method and the Excel software the resulting equation is:

$$\frac{da}{dN} = (9{,}969 \times 10^{-26}) \cdot (\Delta K)^{6{,}47} \qquad (45)$$

which is undistinguishable from the result obtained using the Matlab software.

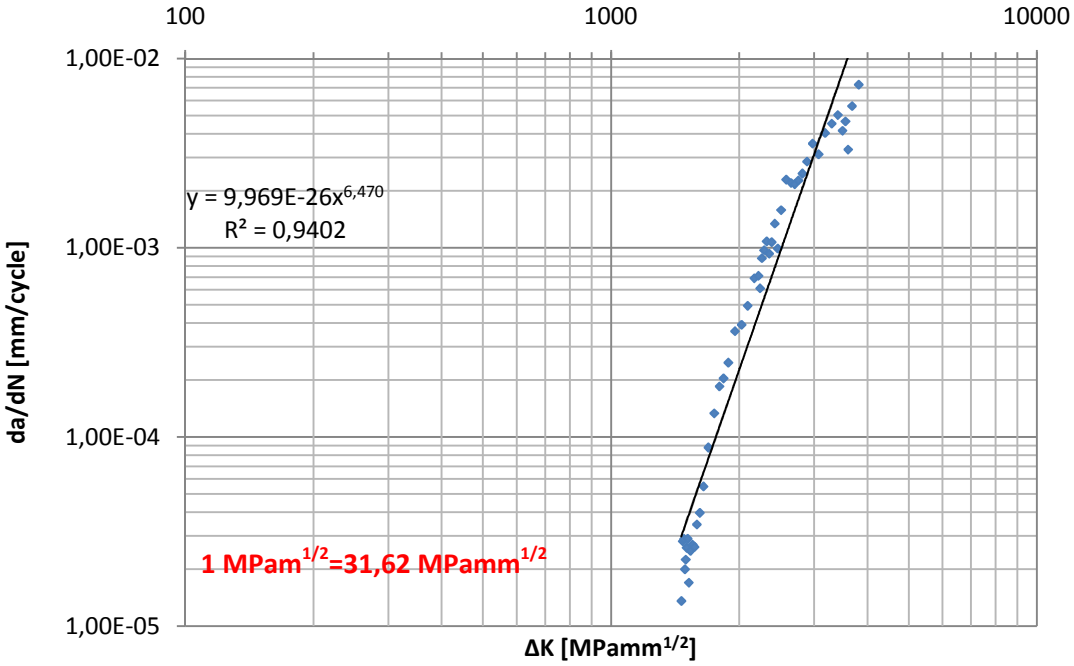


Figure 97 - da/dN *vs*. Δ K data results using the Excel (SM, HAZ R=0,1).

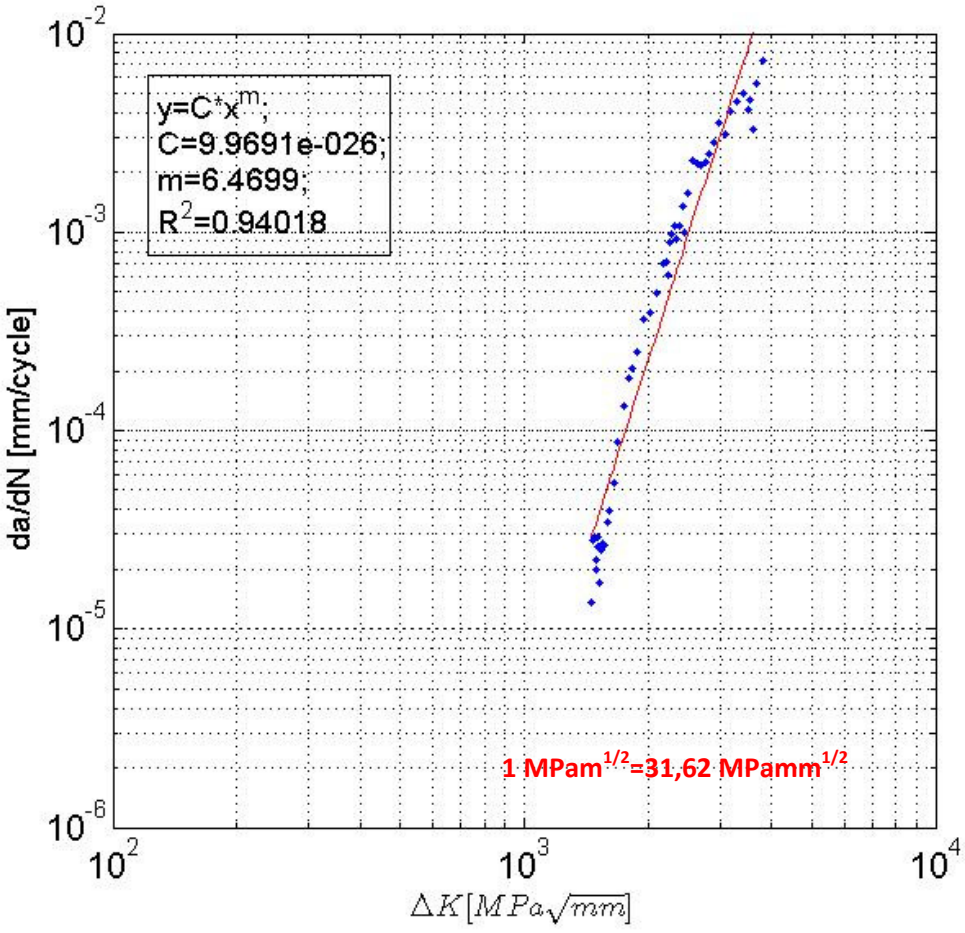


Figure 98 - da/dN *vs*. Δ K data results using the Matlab (SM, HAZ R=0,1).

The Paris Law calculated using the PM is:

$$\frac{da}{dN} = (2{,}9269 \times 10^{-26}) \cdot (\Delta K)^{6{,}6445} \qquad (46)$$

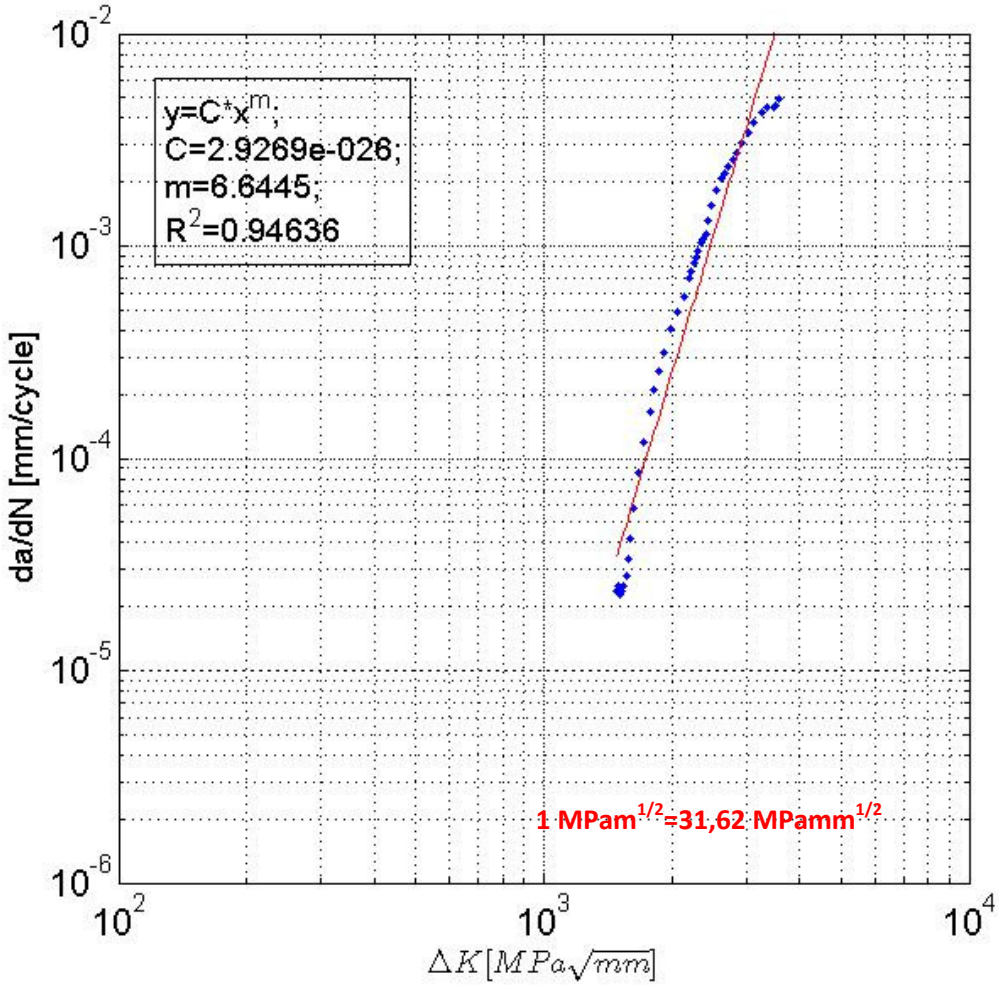


Figure 99 - da/dN *vs.* Δ K data results using the Matlab (PM, HAZ R=0,1).

After the end of the test the specimen was half cut for the crack surface observation and once again a surprising and unexpected fracture surface was observed, see Figure 100.

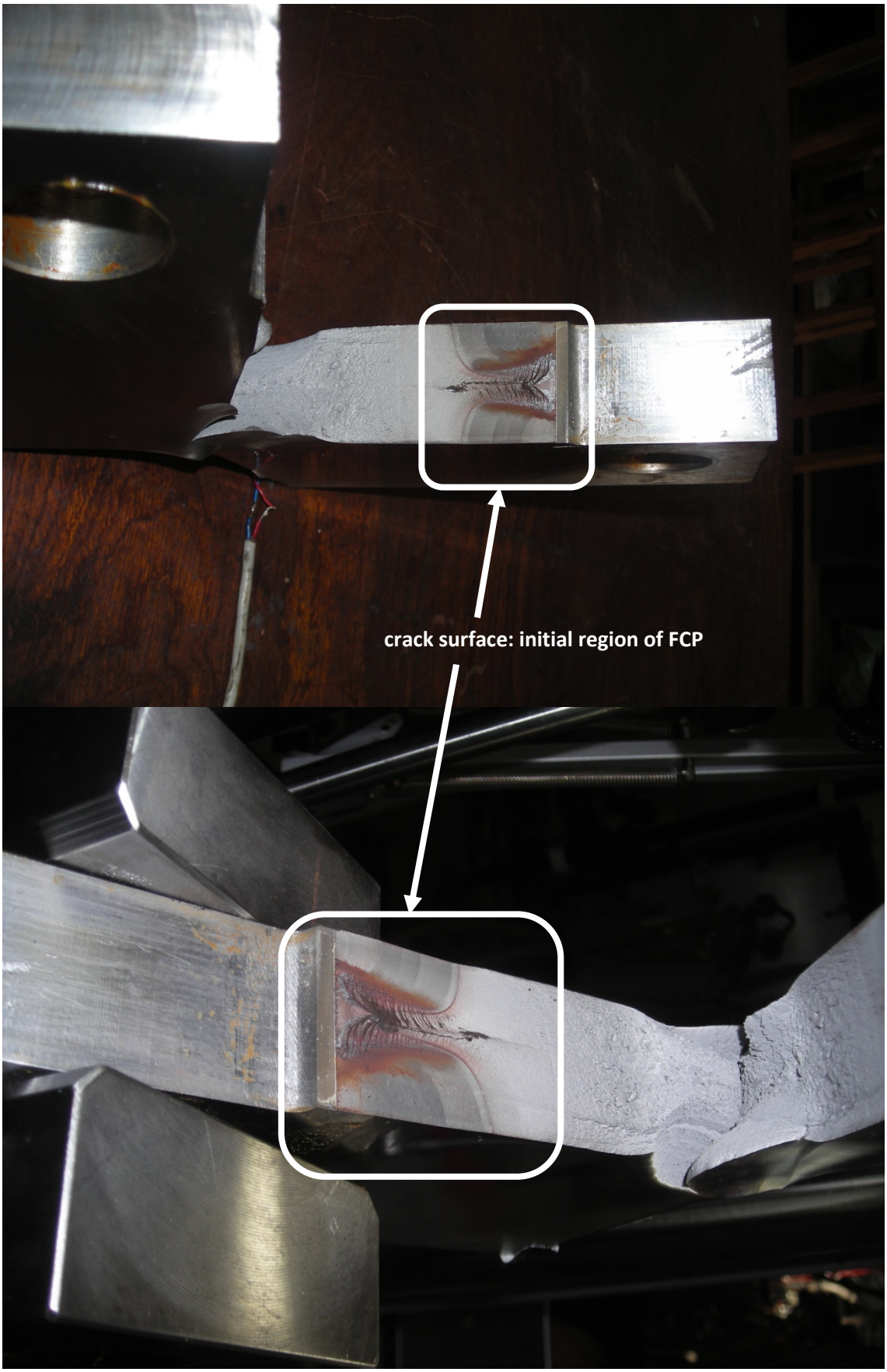


Figure 100 - Specimen Picture in the end of the test (HAZ R=0,1).

The crack front surface is expected to have a "nail" format (the same as BM in Figure 79) and to be longer in the specimen half thickness due to higher stress intensity factor values, but from the analysis of the crack front surface we can unexpectedly see that the crack length are bigger in the specimen free surface than at half thickness. The observation of the surface suggests that the central zone of the weld is subjected during loading to compressive residual stresses only, and in the lateral areas of the weld to tensile stresses. The compressive stresses retard or stops crack propagation, whereas tensile stresses are associated to crack growth. The delay in the crack growth in the central area causes retardation in the crack growth in the other areas which made the test even slower. The stresses in the specimen half thickness grow when the crack length grows in the free surfaces and seems to be ruptured when the stresses get too big in the specimen's central region (mid-thickness).

Numerical simulations of this situation were carried out by FEM 3D. The purpose was to determine the stress values on the free surfaces of the specimen for the two cases represented in the Figure 101 and to try to explain the unexpected slowing down of the crack propagation rate very well documented in Figure 95, where c) consists of a zoom of the initial region of propagation. This Figure represents schematically two moments of the crack propagation that led to the actual fracture surfaces photographed in Figure 100. In the left diagram, the situation corresponding to a visible fatigue crack with tip at point A is shown, whereas the right diagram shows a subsequent moment where the visible crack tip is at point B.

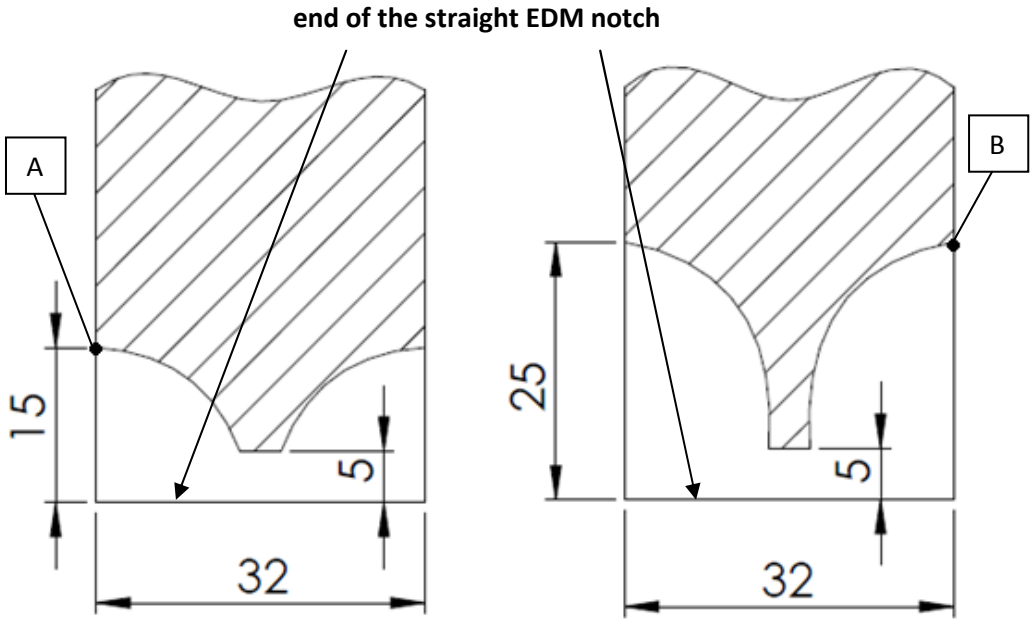


Figure 101 - Representation of the two cases in study (a_1=a_2=15 mm and a_1=a_2=25 mm).

Figure 101 indicates the boundary conditions used along the specimen plane of symmetry, where the crack grows. The white part was modeled in the FEM 3D mesh as cracked area whereas the hatched area corresponds to the uncracked ligament. The preparation of the 3D model and mesh for this peculiar shaped cracked area was very simplified due to the availability of the 3D models of the CT specimen, discussed earlier in this report. Figures 102 and 103 show the stress maps in the y direction for both cases.

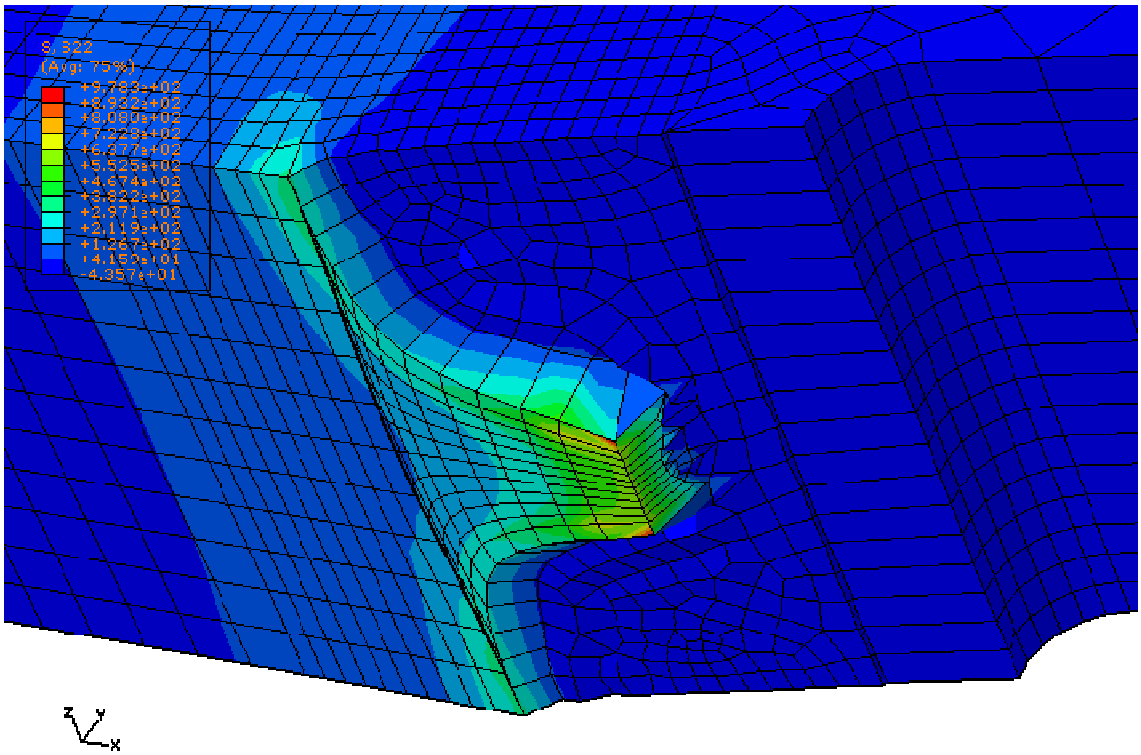


Figure 102 - σ_y values for a_1=a_2=15 mm (using 22938 elements of type C3D8R).

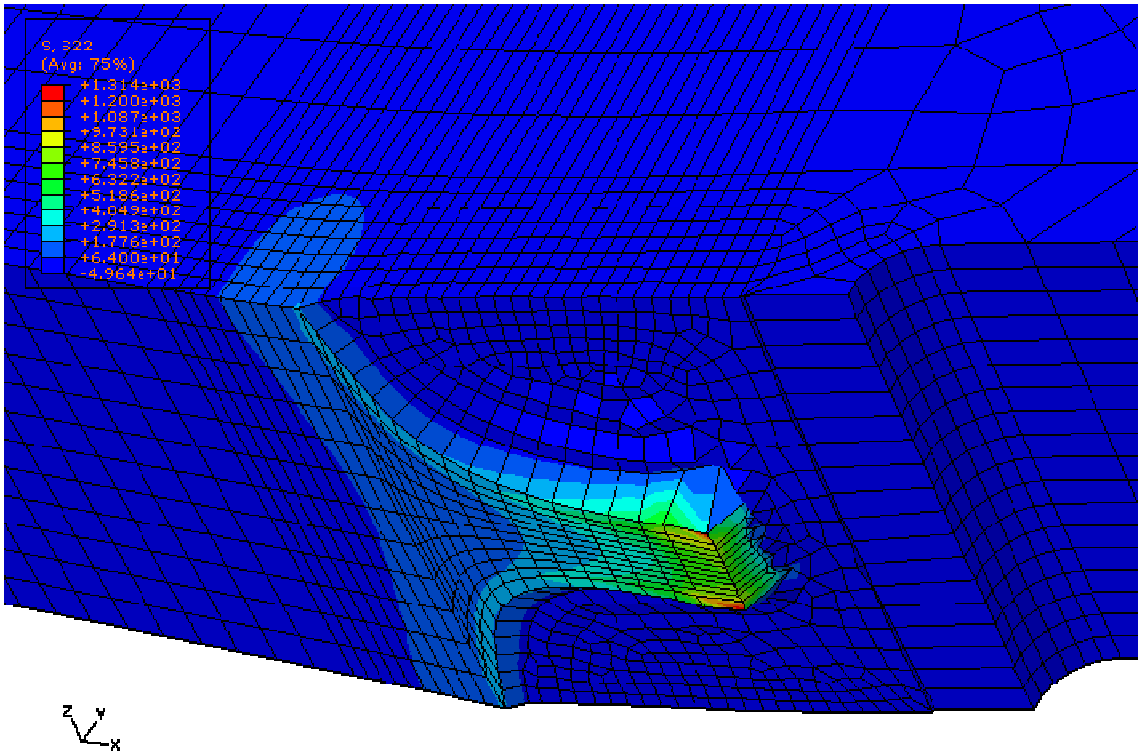


Figure 103 - σ_y values for a_1=a_2=25 mm (using 27558 elements of type C3D8R).

Table 17 shows the stress values in the points A and B.

Table 17 - Stress values in the y direction for points A and B.

Point	Stress in the y direction (MPa)
A	317
B	189

As it can be observed from Figures 102 and 103, the stress values obtained using the 3D FEM on the tip of the visible cracks for the two situations considered in the model are lower for the longer crack (Point B) than for the shorter crack (Point A). This peculiar situation may justify the slowing down in the crack propagation rate observed in the early stages of the FCP test of this HAZ specimen, see Figure 95.

3.5.5. Fatigue crack propagation threshold values

With the data obtained, fatigue crack propagation threshold (ΔK_{th}) values were calculated for all the four test specimens tested. According to the ASTM E647 standard, ΔK_{th} values correspond to a da/dN value of $10^{-7} mm/cycle$. The ΔK_{th} values were obtained extrapolating the Paris law previously presented. Table 18 gives the data obtained.

Table 18 – Fatigue crack propagation threshold values obtained from the experimental tests.

Specimen	$\Delta K_{th}(MPa\sqrt{m})$
MB R=0,1	3,82
MB R=0,4	2,78
MB R=0,7	2,34
HAZ R=0,1	19,47
HAZ R=0,1 effective	1,52

As it can be seen from Table 18 the ΔK_{th} values decrease with increasing R values. Their magnitude follows expected trend mentioned in earlier section of this dissertation (see Tables 4 and 5, refs. [5, 10]), as presented by Albuquerque in [8].

3.5.6. Summary of FCP laws abtained

Figure 104 presents a summary of the fatigue crack propagation laws obtained in the tests presented above. This figure shows that fatigue crack propagation rates for base metal specimens, tested with R=0,1 are lower than FCP rates for base material specimens tested at R=0,4 and R=0,7. It is observed that there is almost no difference between results for R=0,4 and R=0,7. Reasons for the behavior of the HAZ specimen are discussed in the next section.

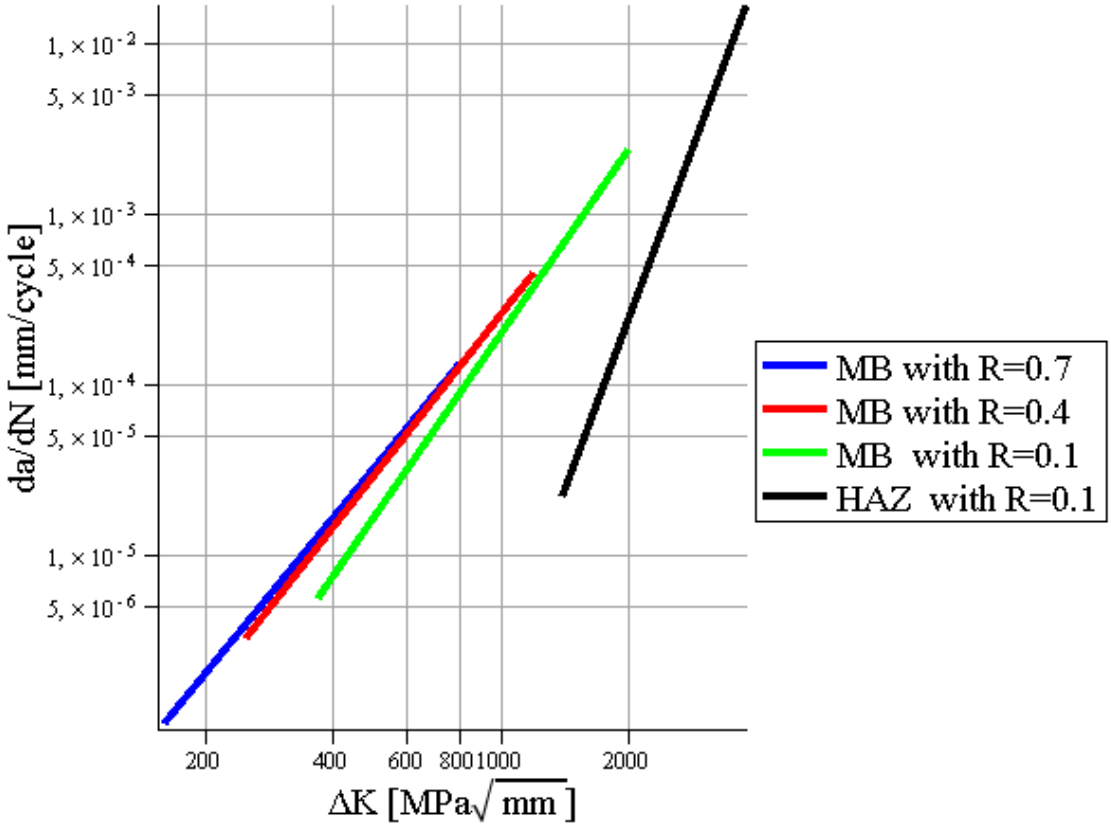


Figure 104 - da/dN vs. ΔK summary of FCP laws obtained in the tests.

4. Discussion. Crack Closure Effects

4.1. Crack Closure Assessment for HAZ Specimen

A study of possible reasons the unexpected fatigue crack growth rates of the HAZ specimen tested with R=0,1 was made. A simple procedure was followed consisting of using a strain gauge in the back face of the test specimen in order to measure the back face strain (see Figure 105). This is a procedure for identifying crack closure in fatigue crack crack propagation tests. This effect may be related to residual stress states, *e.g*. Beghini and Bertini [12].

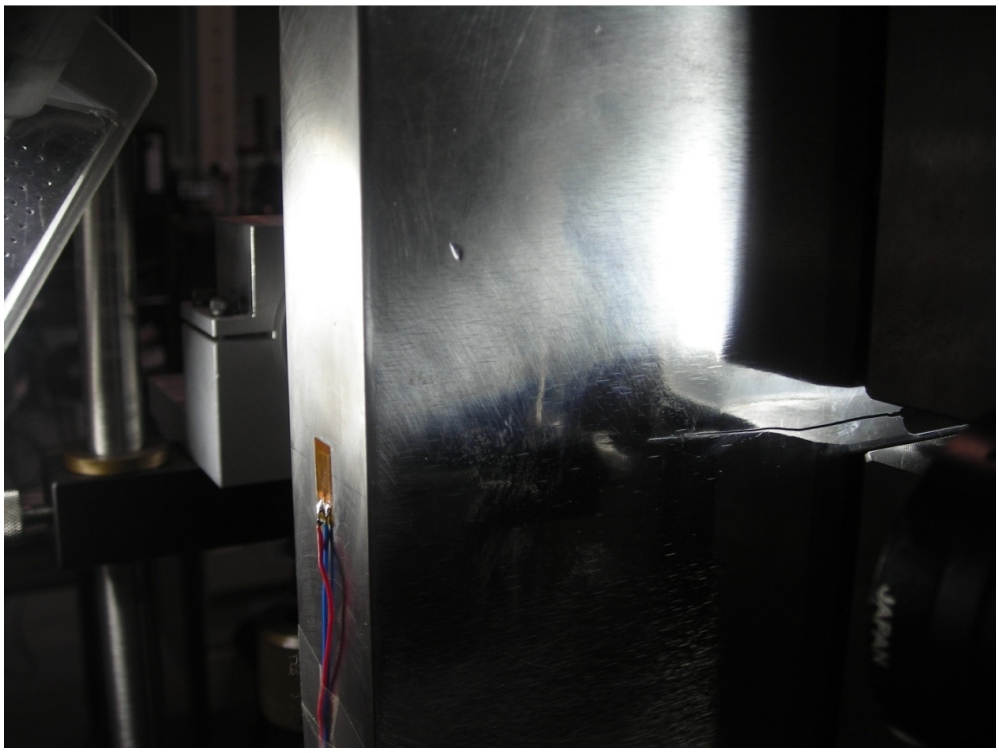


Figure 105 - Back face strain gauge used.

If there are residual stresses in the test specimen two different slopes should be seen in the Force *vs*. strain plot. The Force *vs.* strain plot was obtained using a "Spider8" data acquisition system (Figure 106).

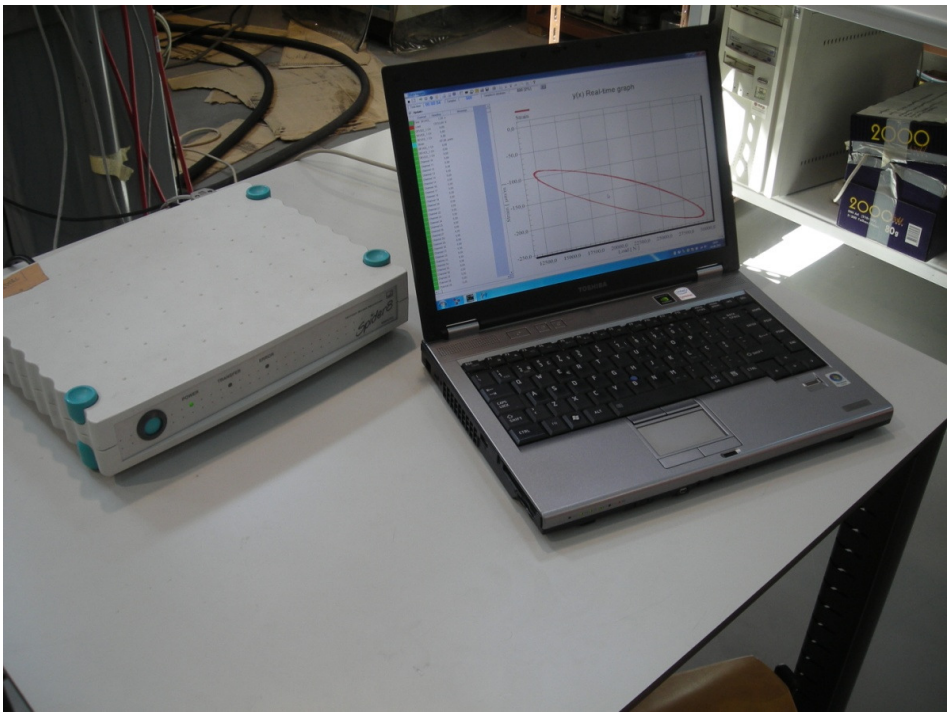


Figure 106 - Data acquisition system used to obtain the Force vs strain graphic.

The turning point in the graphic reveals approximately the effect of the residual stresses in the specimen behavior. Only the final linear portion of the Force *vs* strain plot corresponds to an open crack. Before this, although external loading is applied, the crack faces are closed under the influence of compressive residual stresses. G.O. Rading [13] refers that the residual stress field present in the uncracked ligament of roughly similar CT specimen is as shown in Figure 107. This shape of residual stress distribution in CT specimens including weldments parallel to the crack is also described in a variety of other papers, see *e.g.* [14,15,16,17]

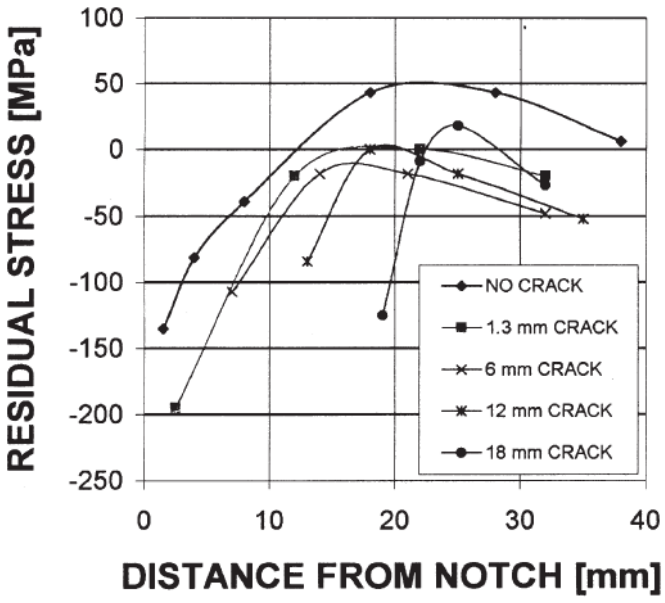


Figure 107 - Redistribution of residual stress with crack length [13].

The crack growth rate slowdown can be explained with the presence of compressive residual stresses just ahead of the crack front. The residual stresses in the crack front do not exhibit a linear variation, fact that may explain the observed variation in the crack growth rates. During the crack growth the compressive stresses in the fatigue crack front are closing it, implying that his growth slows down, through the crack closure phenomenon. The measured values in the back face strain are shown in Figures 108 to 111.

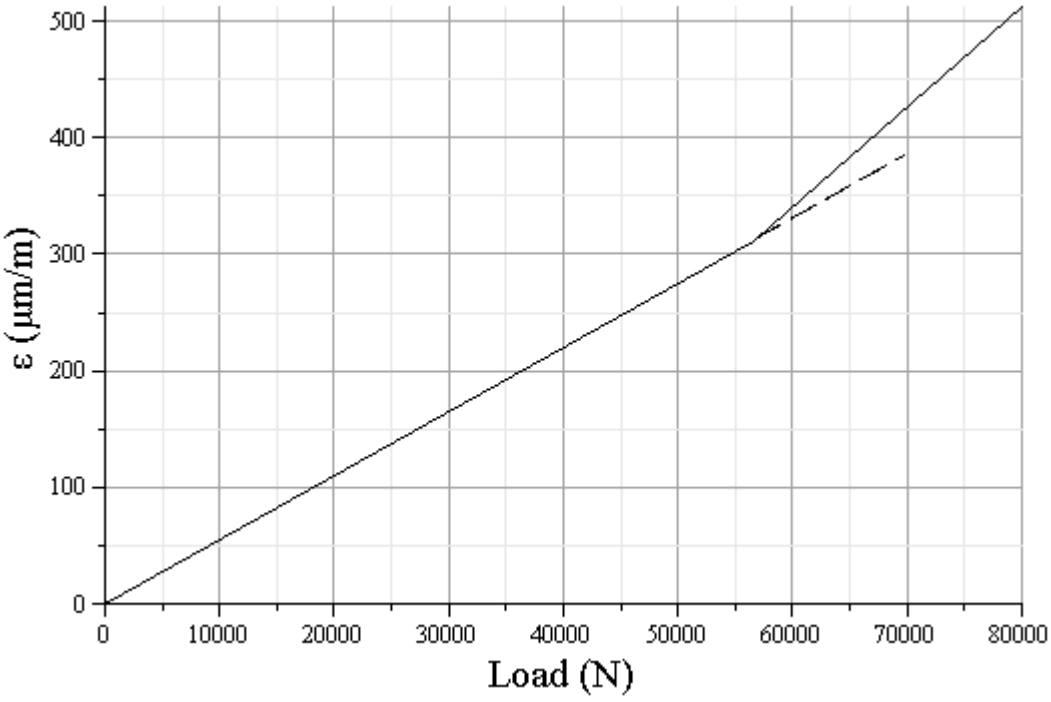


Figure 108 - Back face strain *vs.* force applied in the HAZ test specimen for a=58,46 mm.

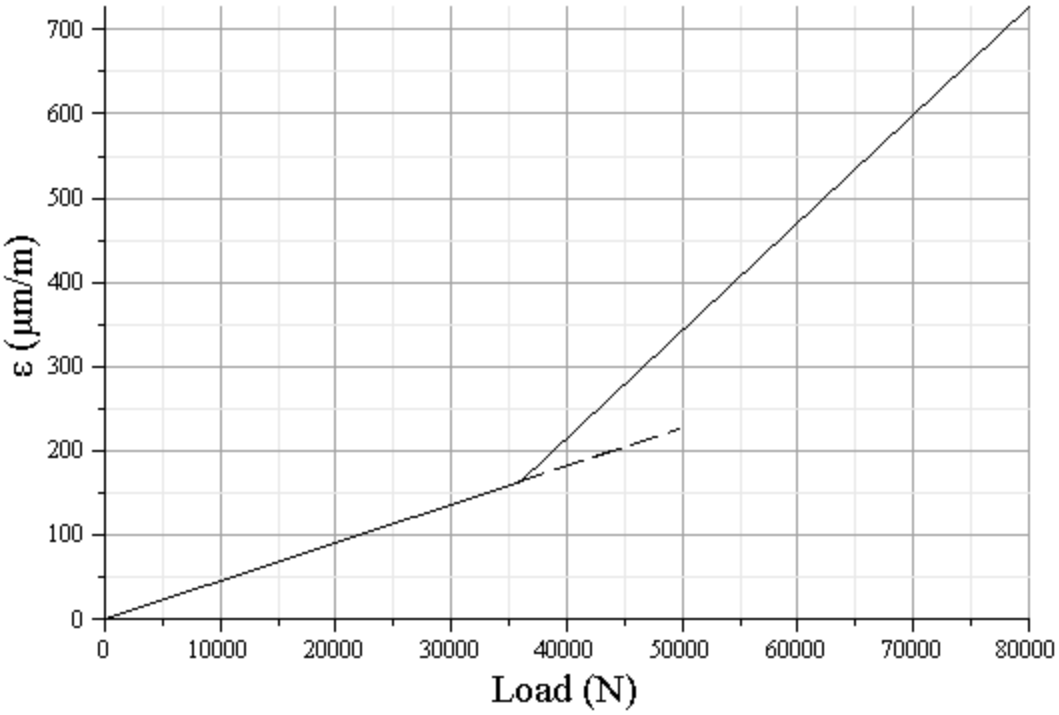


Figure 109 - Back face strain *vs.* force applied in the HAZ test specimen for a=64,19 mm.

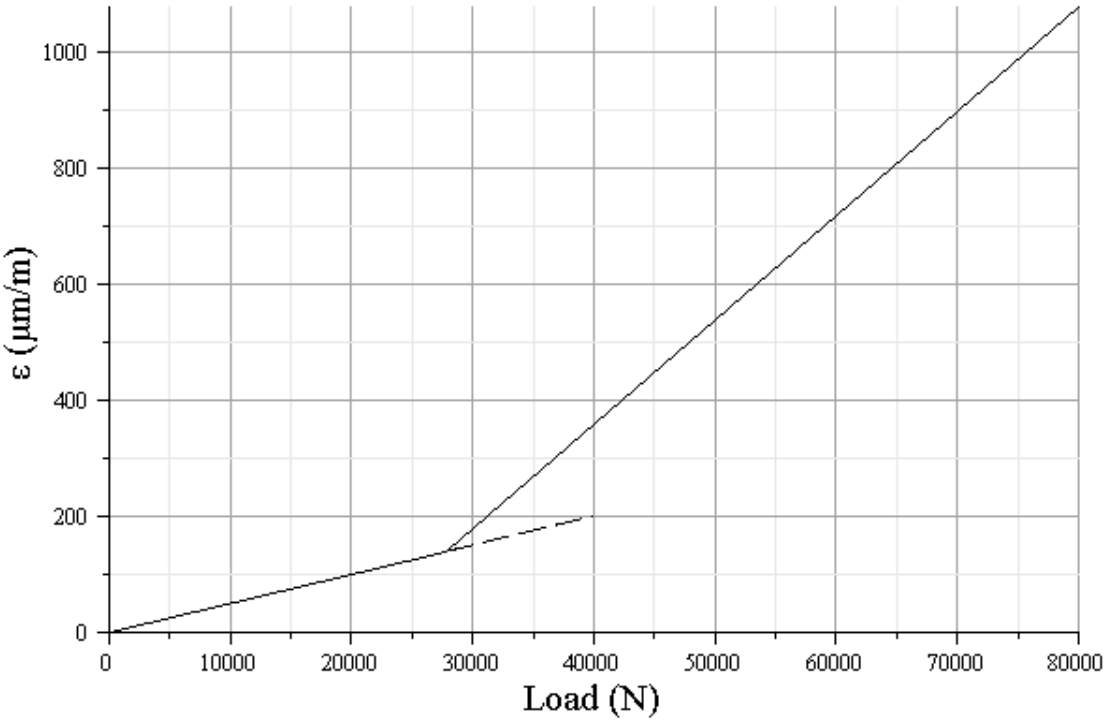


Figure 110 - Back face strain *vs.* force applied in the HAZ test specimen for a=69,43 mm.

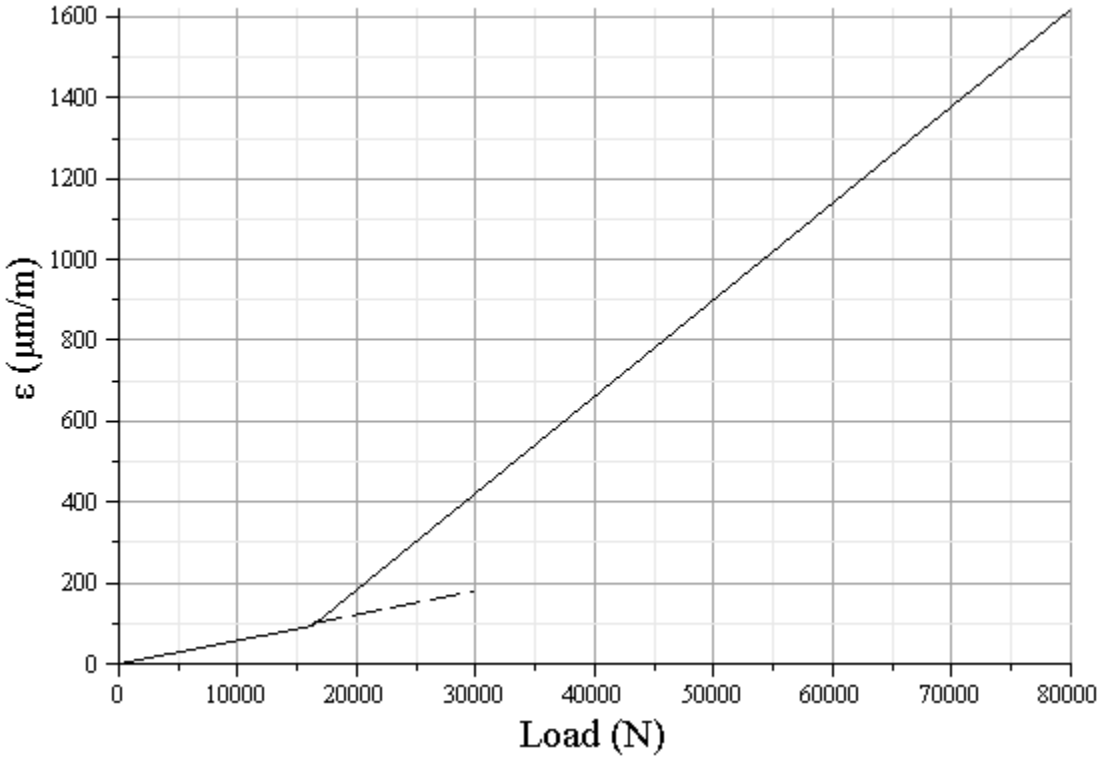


Figure 111 - Back face strain *vs.* force applied in the HAZ test specimen for a=76,58 mm.

The respective values of the load in the fatigue crack front are shown in Table 19.

Table 19 - - Crack closure load values at the fatigue crack front (HAZ R=0,1).

Crack length a (mm)	Crack opening loads (N)	% of max. load
58,46	56738	70,9
64,19	35781	44,7
69,43	27829	34,8
76,58	16318	20,4

Figure 112 shows the inflection point as a function of a/W for the HAZ specimen. It is recalled that these tests consisted of monotonic loading of the specimens starting at zero load. This Figure shows that the closure effect is reduced at higher crack lengths.

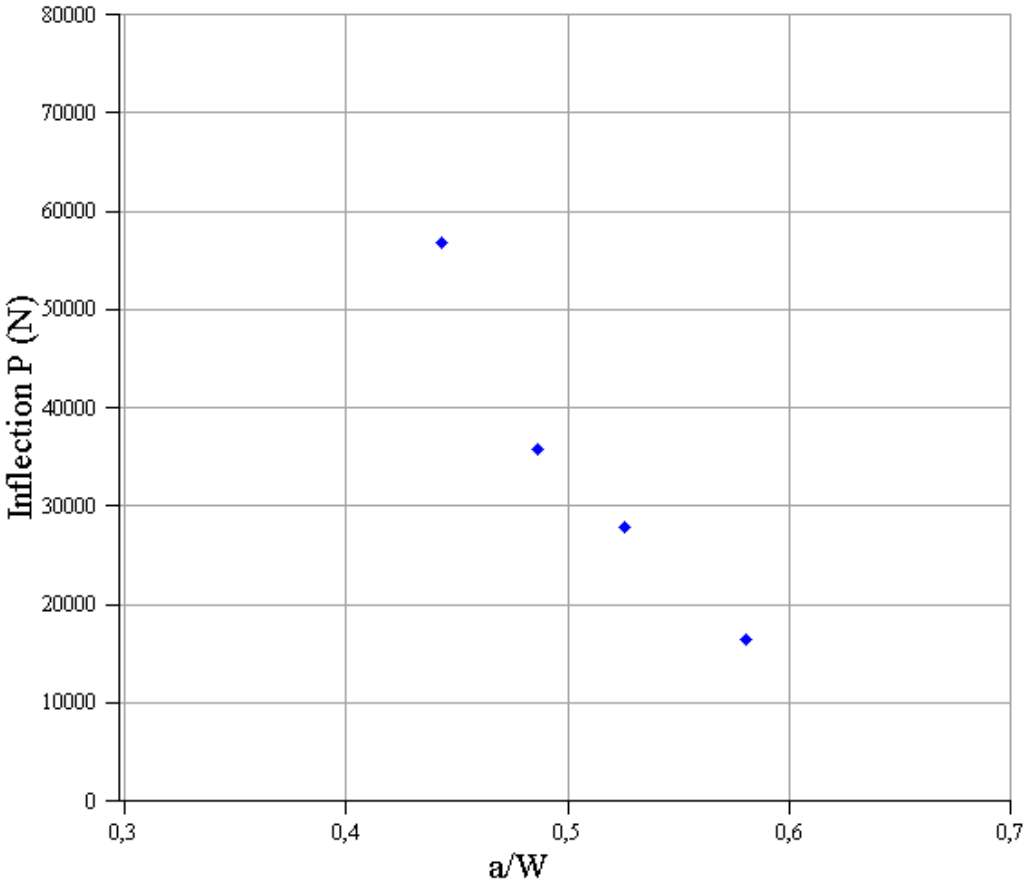


Figure 112 - Crack opening loads infection points (HAZ R=0,1).

Measurements of the back face strain were also made in real time during the cyclic loading with constant amplitude corresponding to the fatigue test conditions. An example of the plots obtained from these measurements is shown in Figure 113.

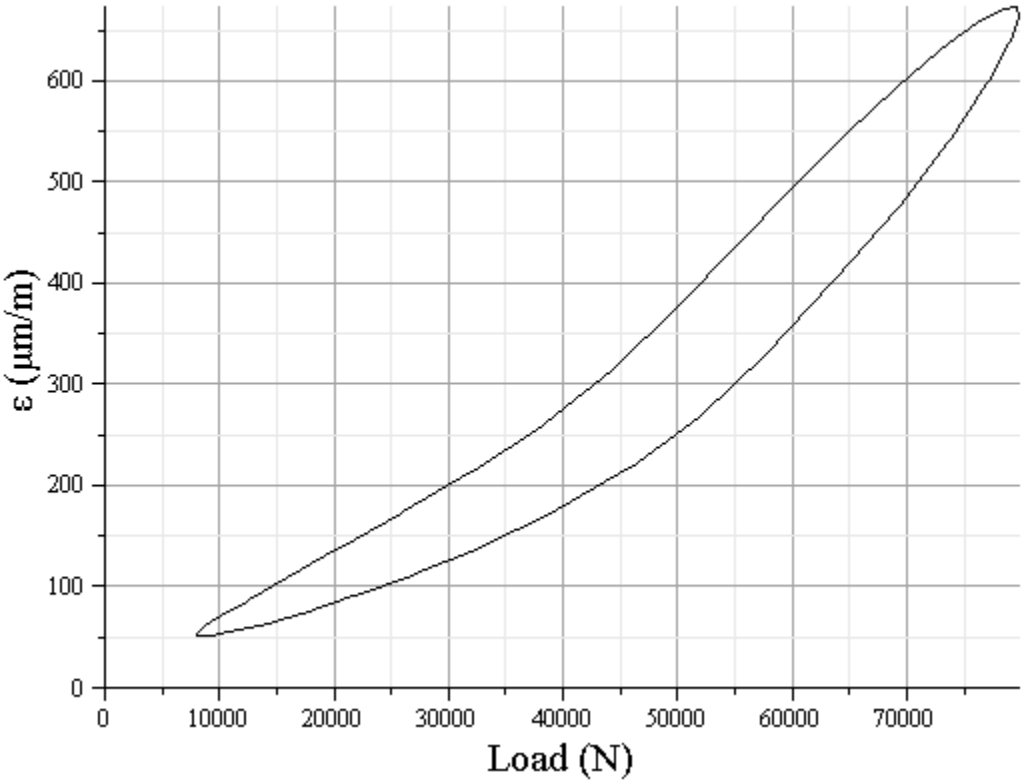


Figure 113 - Back face strain *vs.* force applied in the HAZ test specimen for a=64,19 mm, under cyclic load.

In Figure 113 the presence of two different slopes with a turning point can be observed. This behavior is similar to the behavior found in the previous measurements under monotonic load reported in Figures 108 to 111. The strain gauge hysteresis caused by the cyclic load applied makes the slope turn point observation more difficult and approximate. The other measurements made are shown in Annex C.

Using the effective ΔK values that were obtained from the Force *vs*. strain plots we can get a new da/dN *vs* ΔK plot without the effect of the residual stresses. The effective ΔK can be calculated as:

$$K_{eff} = K_{ext} + K_{res} \tag{47}$$

$$\Delta K_{eff} = K_{eff}^{max} - K_{eff}^{min} \tag{48}$$

$$R_{eff} = \frac{K_{eff}^{min}}{K_{eff}^{max}} \tag{49}$$

Equation 37 is valid only when the crack is not fully open.

When the crack is fully closed $K_{min} = 0$.

Then for this case (crack fully closed) comes considering R ≈ 0 :

$$\Delta K_{eff} = K_{ext}^{max} + K_{res} \tag{50}$$

In our case, relevant K_{res} is negative as indicated *e.g.* in Rading [13], and therefore ΔK_{eff} is lower than ΔK nominal.

The corrected da/dN *vs* ΔK_{eff} plot is shown in Figure 114.

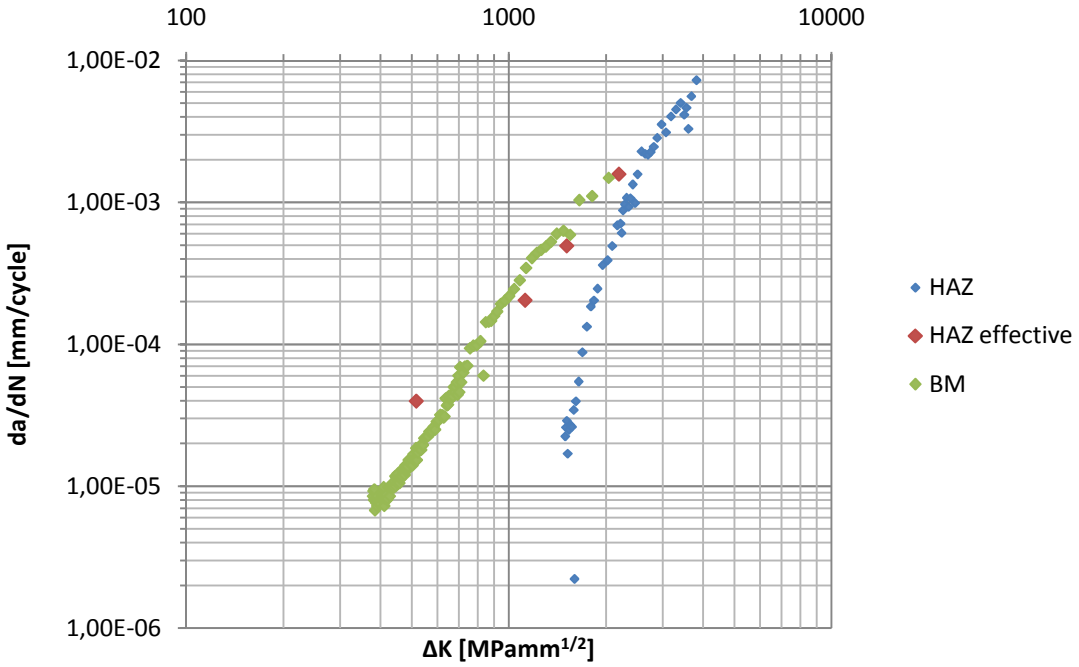


Figure 114 - da/dN *vs*. ΔK_{eff} data results using the Matlab with MB, HAZ and HAZ effective R=0,1 (SM).

Figure 114 shows the raw da/dN *vs.* ΔK data, and the suggested da/dN *vs*. ΔK_{eff} curve, based on the approximate crack closure study presented above.

From Figure 114 we can observe that HAZ da/dN *vs* ΔK experimental data, when corrected with the residual stresses effects measured with the back face strain gauge, is roughly similar to the BM test results obtained. A new corrected Paris law can be calculated for the HAZ effective data results:

$$\frac{da}{dN} = (6 \times 10^{-12}) \cdot (\Delta K)^{2,5106} \qquad (51)$$

The residual stresses are taken into consideration in the da/dN *vs* ΔK data obtained in the HAZ, the data points are in the same region as the BM.

Similar behaviors were found in the literature.

Figures 115 and 116 show some of the experimental results found by Y.Kitsunai [14] (Figure 115) and by Beghini and Bertini [12] (Figure 116) that reveals some of the *crack closure* effects presented in this thesis, with the respective corrections. It is noticed that the behaviors presented by these authors were found in the work described in the present thesis.

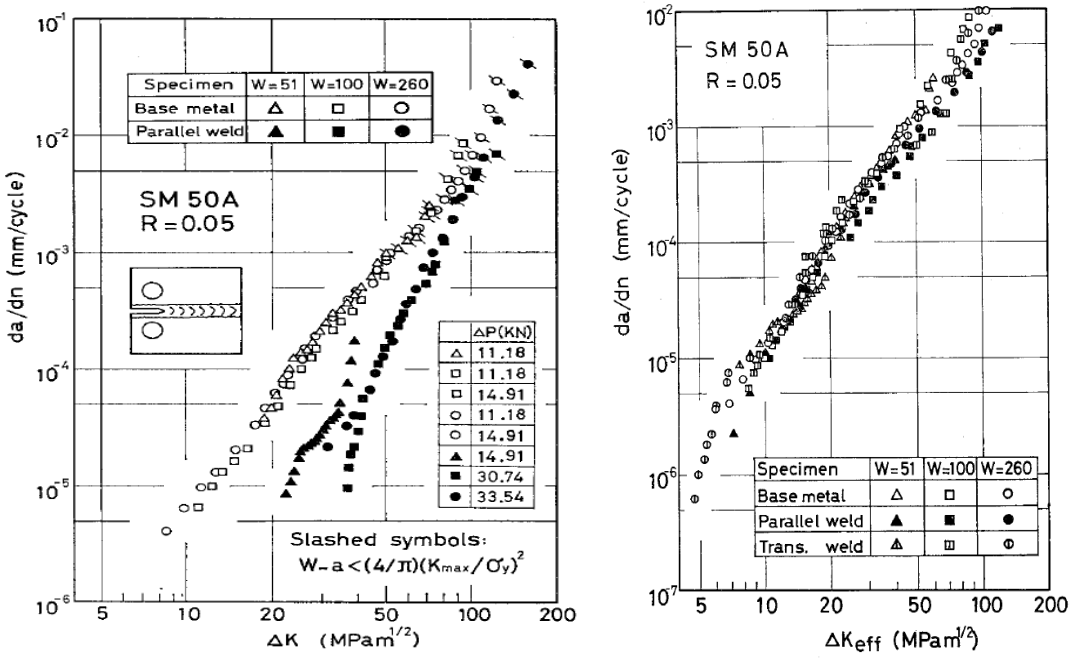


Figure 115 – Fatigue crack growth results correlated using the effective stress intensity factor range.[14]

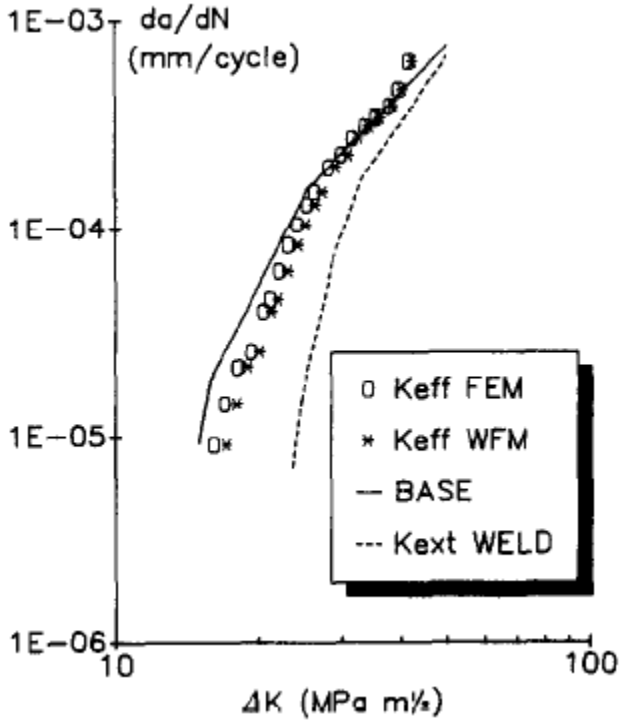


Figure 116 - Fatigue crack growth rates as a function of external and effective SIF [12].

4.2. Crack Closure Assessment for Base Metal

During the test of the base metal specimen loaded at R=0,4 a study of possible crack closure was made. The same procedure as followed for the HAZ specimen was carried out and the results are shown in Figures 117 to 123. It should be explained that Figures 111 to 114 were obtained interrupting the fatigue test at several (four) different values of crack length, and recording the strain vs. force corresponding to a monotonic application of load starting from the unloaded condition. This means that the crack opening loads estimated correspond to approximately $R \approx 0$, *i.e.* they are directely comparable with the opening loads for the HAZ test carried out at R=0,1.

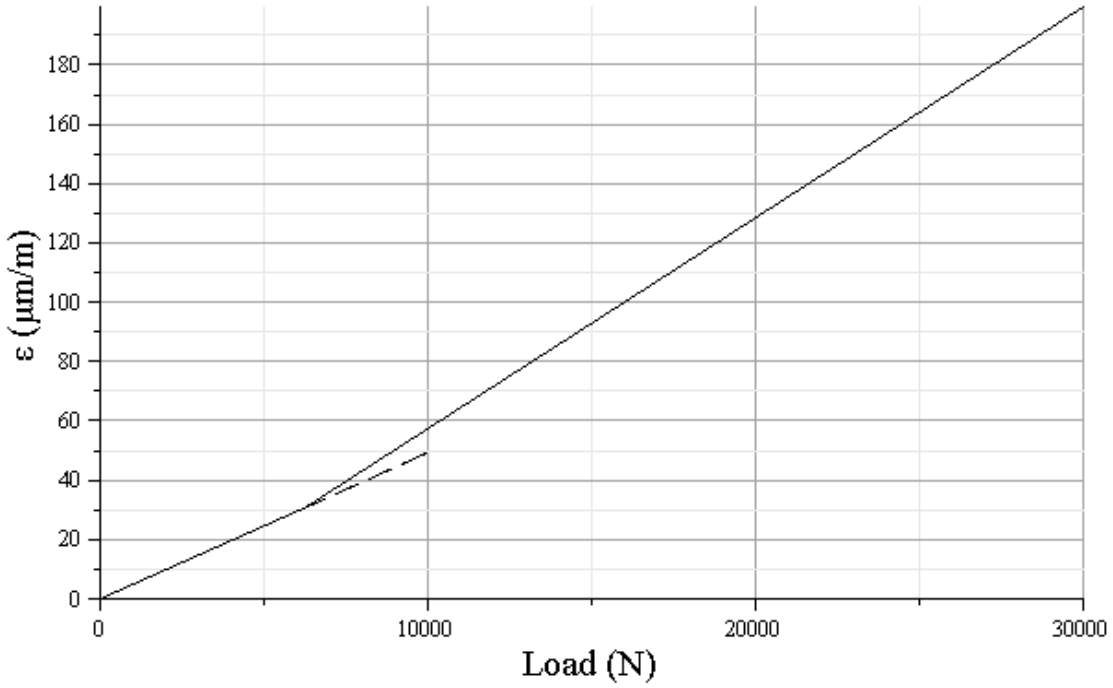


Figure 117 - Back face strain *vs.* force applied in the test specimen for a=47,91 mm (BM specimen R=0,4).

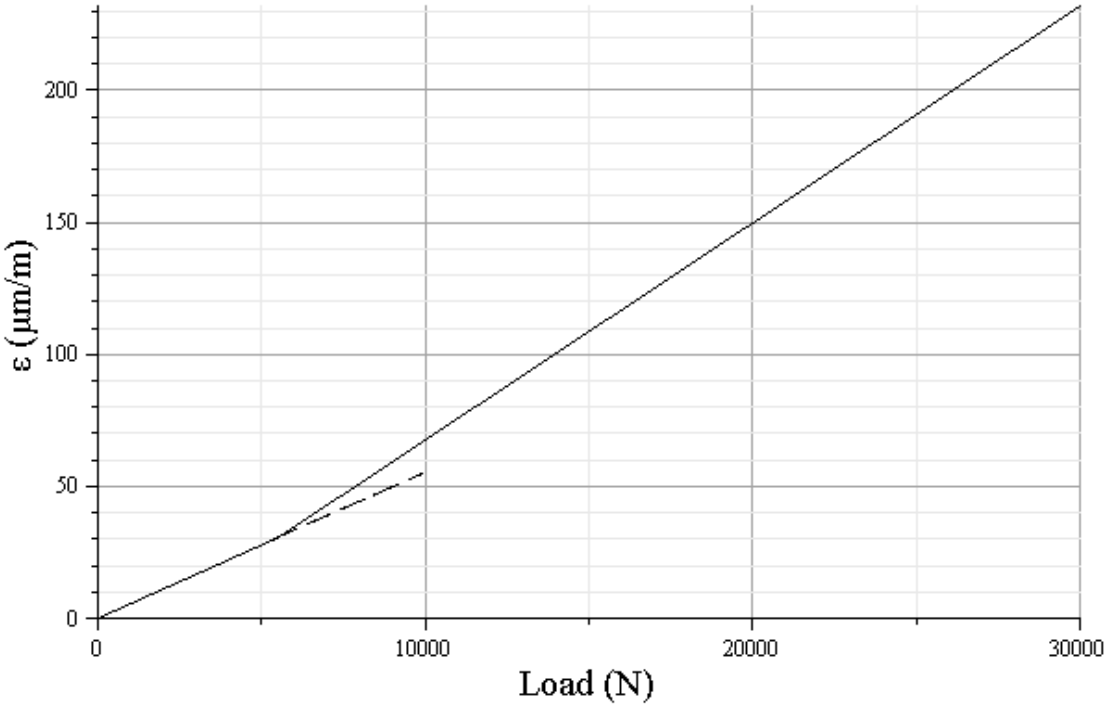


Figure 118 - Back face strain *vs*. force applied in the test specimen for a=51,27 mm (BM specimen R=0,4).

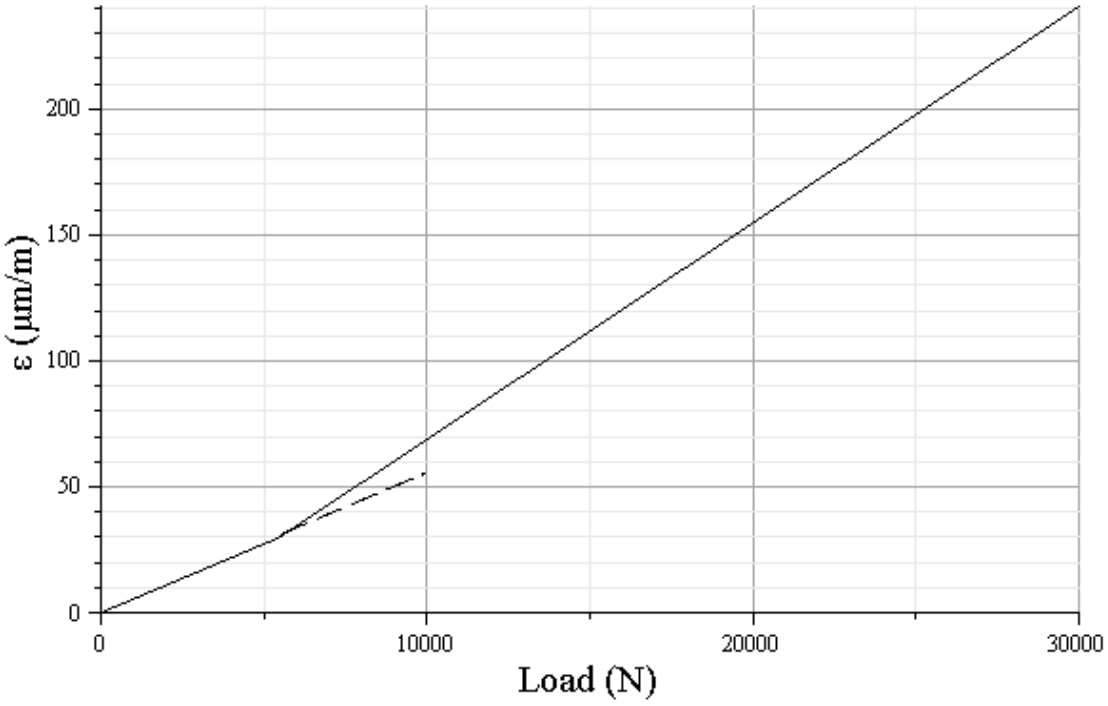


Figure 119 - Back face strain *vs.* force applied in the test specimen for a=52,69 mm (BM specimen R=0,4).

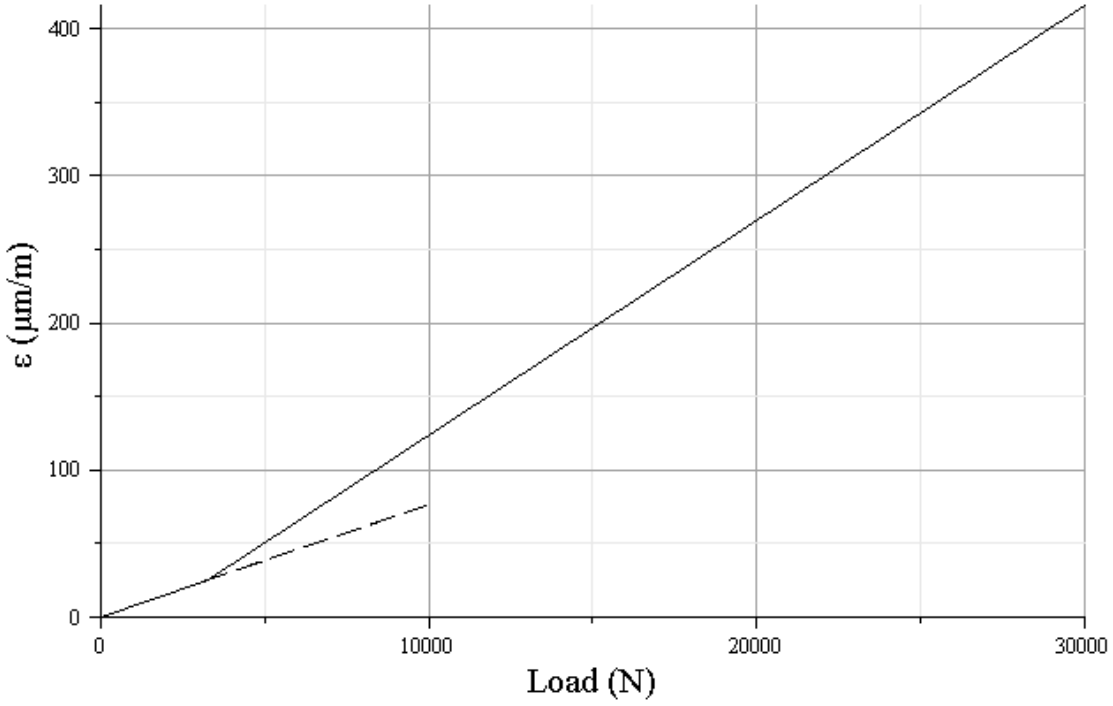


Figure 120 - Back face strain *vs.* force applied in the test specimen for a=65,43 mm (BM specimen R=0,4).

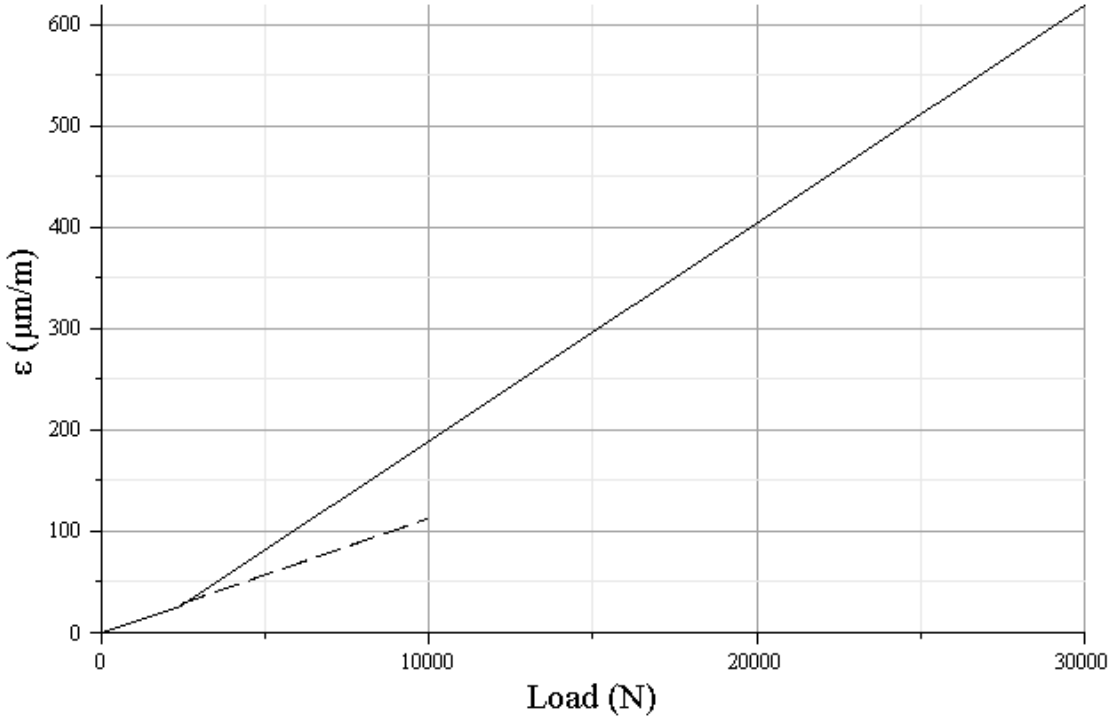


Figure 121 - Back face strain *vs.* force applied in the test specimen for a=74,37 mm (BM specimen R=0,4).

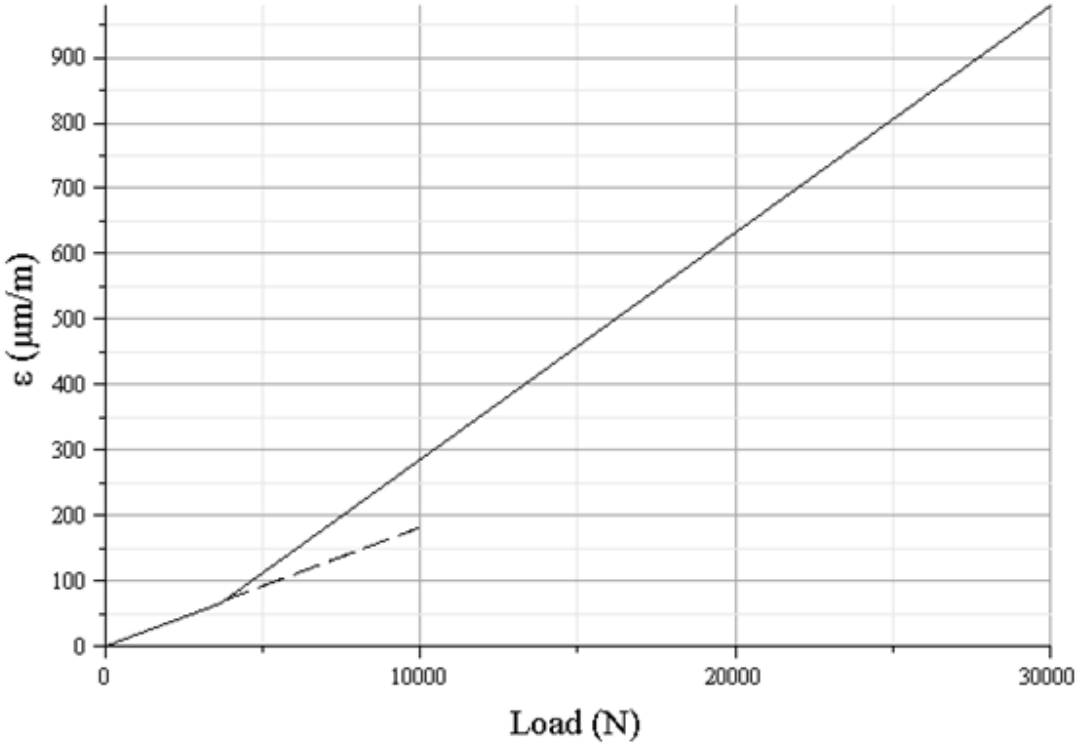


Figure 122 - Back face strain *vs.* force applied in the test specimen for a=84,39 mm (BM specimen R=0,4).

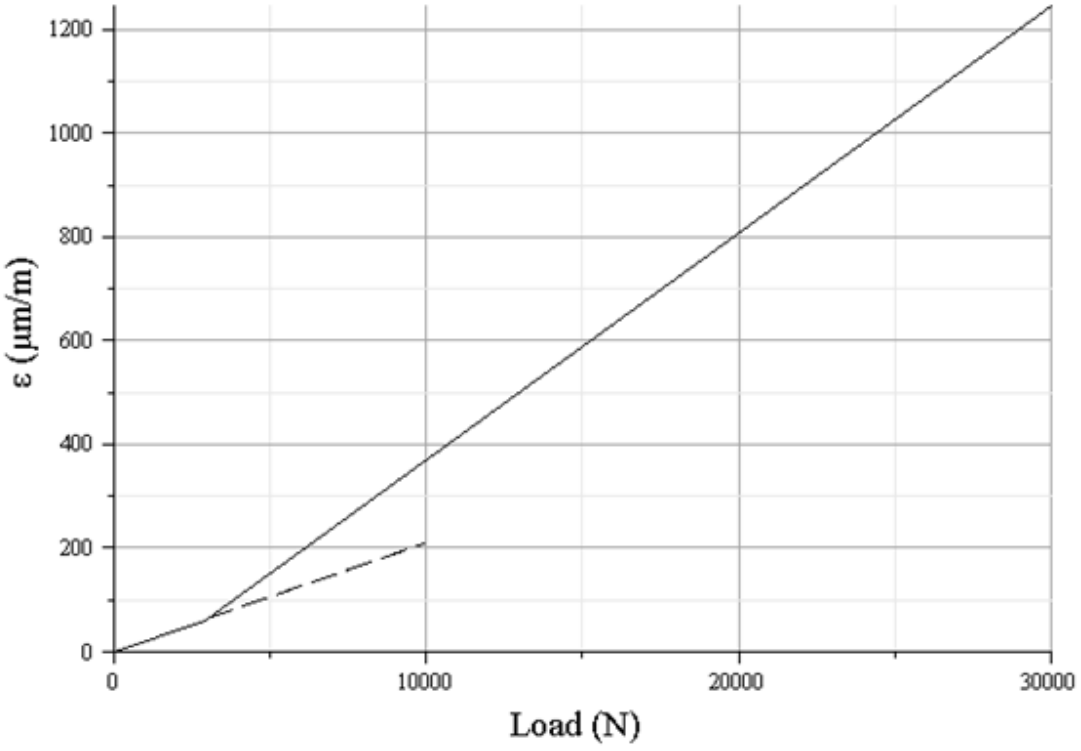


Figure 123 - Back face strain *vs.* force applied in the test specimen for a=87,55 mm (BM specimen R=0,4).

Table 20 shows the values of crack opening load as a function of crack length.

Table 20 - Crack closure load values at the fatigue crack front (BM R=0,4).

Crack length a (mm)	Crack opening load (N)	% of max. load
47,91	6115	20,4
51,27	5351	17,8
52,69	5549	18,5
65,43	3140	10,5
74,37	2471	8,2
84,39	3732	12,0
87,55	2983	10,0

As it can be seen from the values measured, though crack closure effects still exist, their values are far lower than the ones measured in the HAZ specimen tested, as it should be expected. In Figure 124 the inflection points corresponding to monotonic loading are shown. Although there is a tendency for decreasing load at inflection point as a function of crack length, it is noticed that values are approximately stable for higher a/W values and in general very small.

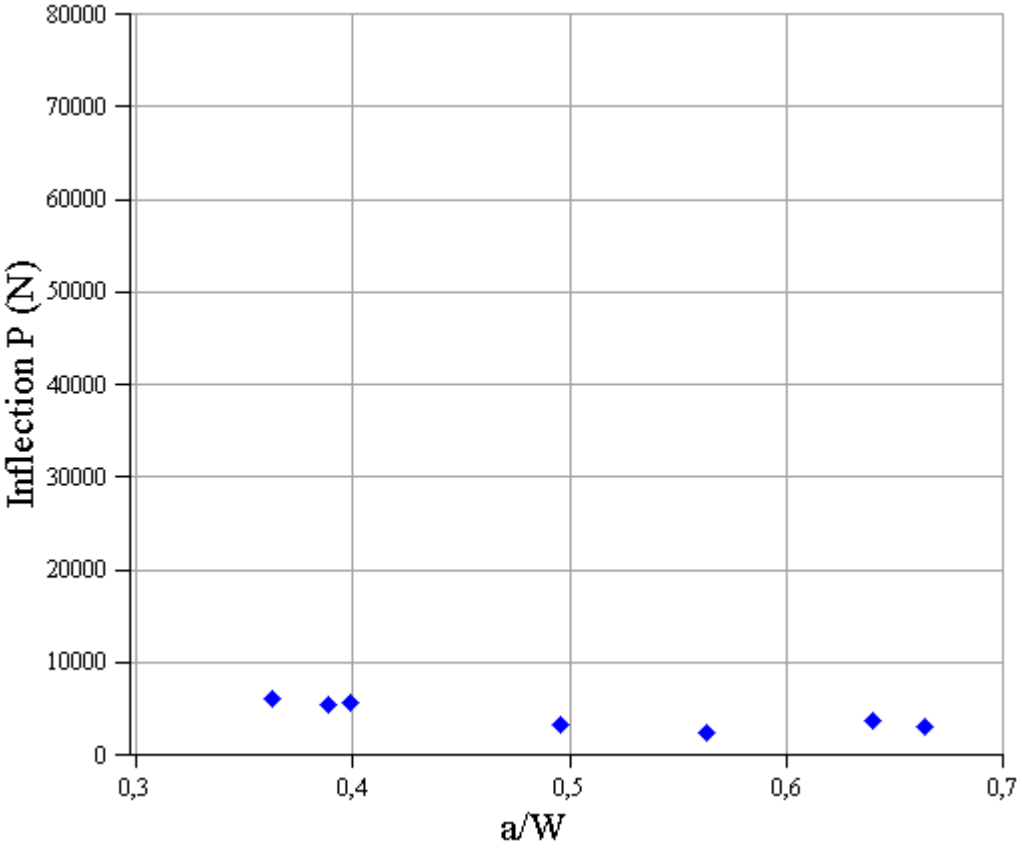


Figure 124 - Crack opening loads inflection points (MB R=0,4).

It is understood that closure effects may be due to a variety of mechanisms, such as plasticity effects, fracture surfaces mismatches, residual stresses and others, and in particular depend upon R ratio, see *e.g.* [1, 2].

It is noted that during the FCP test of the BM specimen at R=0,4 some real time records of load *vs.* strain were also made, see Figure 125.

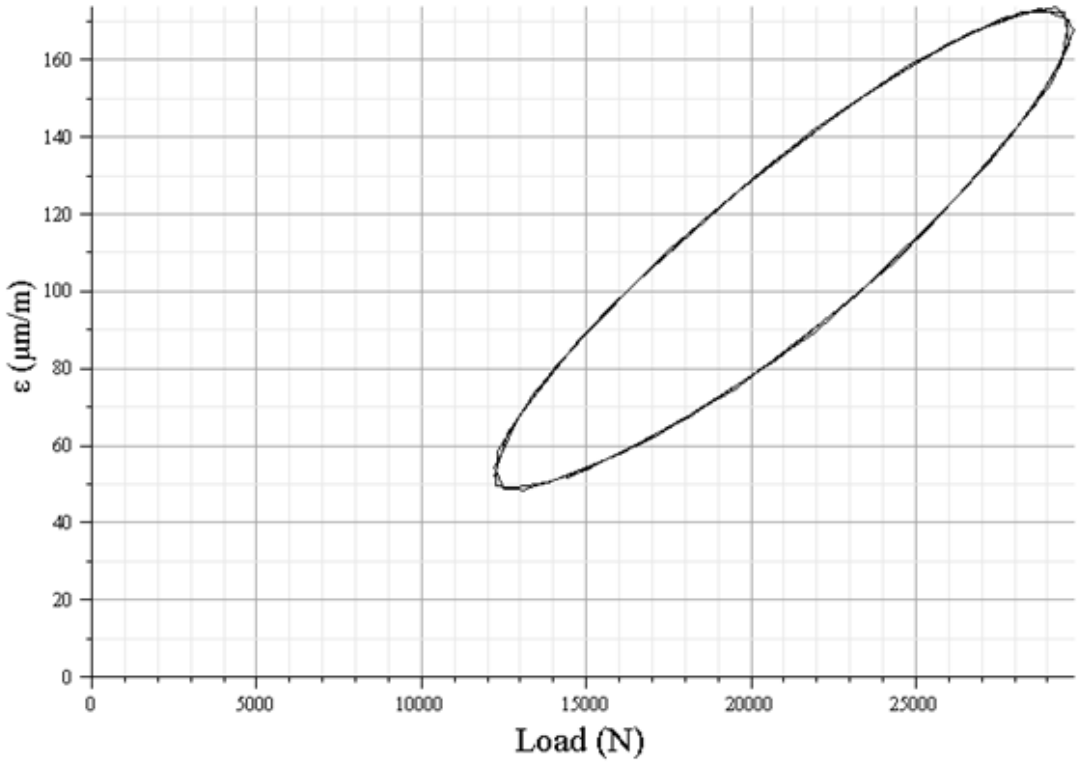


Figure 125 - Back face strain *vs.* force applied in the test specimen for a=47,91 mm (BM specimen R=0,4, under cyclic load).

Figure 125 shows clearly that no crack closure effect is observed, since the axes of the represented curve are a straight line, *i.e.* the curve is an ellipse corresponding to the strain gauge hysteresis. This should be compared with real time measurement carried out for the HAZ specimen tested at R=0,1 shown in Figure 112, which clearly reveals the crack closure effect. Other measurements are shown in Annex C.

Using the effective ΔK values that were obtained from the Force *vs*. strain plots we can get a new da/dN *vs.* ΔK plot without the effect of the residual stresses. The effective ΔK for this case (crack fully open at minimum load) comes:

$$\Delta K_{eff} = \Delta K_{ext} \tag{52}$$

The da/dN *vs* ΔK_{eff} plot is shown in Figure 126.

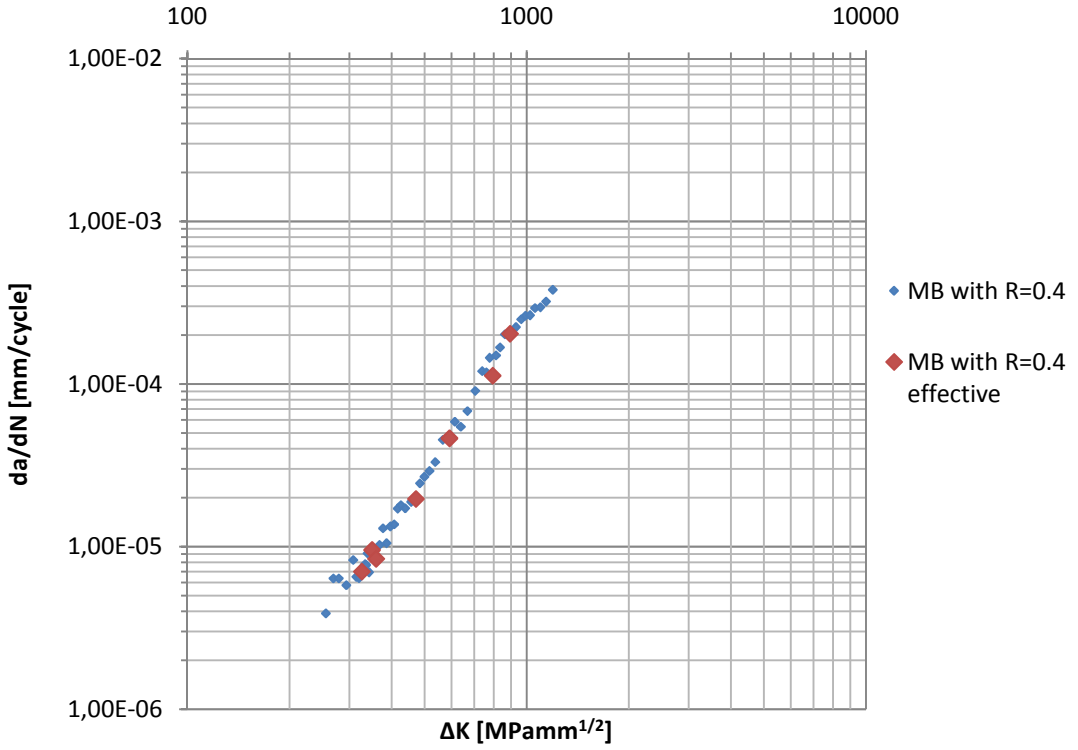


Figure 126 - da/dN *vs*. Δ K_{eff} data results using the Matlab with MB and MB effective R=0,4 (SM).

Figure 126 shows the raw da/dN *vs.* ΔK data, and the suggested da/dN *vs*. ΔK_{eff} curve, based on the approximate crack closure study presented above.

From Figure 126 we can observe that MB da/dN *vs.* ΔK experimental data, when corrected with the residual stresses effects measured with the back face strain gauge, is equal to the BM test results obtained.

Conclusions

- Microstructures of samples of welded plates were analyzed and are in conformity with what is expected for this steel type and welding procedure. The base material presents a mostly ferritic structure with some perlite.

- Vickers hardness measurements were carried out and agree with the expectations for this steel type and welding procedure. Peak hardness values were found as expected in the fusion line on the HAZ.

- BM hardness values in the range of 150-180 HV were measured, showing some experimental scatter.

- A comparison of 2D and 3D FEM models of the CT specimen was made, and the stress intensity factor calibration was compared with the solution given in the ASTM E647 standard. The study made clear the dependency of K with depth along thickness, for a given crack length.

- Base material CT specimens were tested for fatigue crack propagation at R=0,1, R=0,4 and R=0,7. As expected, for R=0,1 crack growth rate is smaller than for other R values.

- Base material fatigue crack propagation rates at R=0,4 and R=0,7 present considerable overlap.

- The expected crack front geometry ("nail" like shape) was found in the fracture surfaces of all three BM specimens tested.

- One HAZ specimen was tested and its exceptionally slow visible crack propagation rate was justified by compressive residual stresses.

- The peculiar shape of the initial stage of fatigue crack growth in the HAZ was discussed on the basis of FEM 3D model.

- HAZ specimen presents considerably lower FCP rates than base metal specimen tested at the same R value (R=0,1).

- Approximate crack closure effect was measured using back face strain. Consideration of these closure loads made it possible to estimate ΔK_{eff} for the HAZ test.

- FCP rates for HAZ tested at R=0,1 are approximately similar to FCP rates for base metal, when ΔK_{eff} is used.

Suggestion for Future Works

Future work will include FCP tests of HAZ (R=0,4 and 0,7) and WM (R=0,1, 0,4 and 0,7).

Residual stress in HAZ and WM specimens should be measured, in order to completely clarify the reasons for the slow FCP measured in the HAZ specimen tested at R=0.1. Since the effects measured are dependent upon position through the thickness, surface residual stress measurements are in this case useless, and there is a need for full field measurement in the complete fracture surface.

An analysis of the fracture surfaces on electron microscopy (service provided by CEMUP) should be made particularly in cases where less common behaviors were found.

References

1. Schijve, Jaap, Fatigue of Structures and Materials. 2001, Kluwer Academic Publishers.
2. Barsom, John M. and Rolfe, Stanley T., Fracture and Fatigue Control in Structures, 1999, 3rd edition, Butterworth Heinemann and ASTM
3. Bennet, J. A. and Mindlin, H., Metallurgical aspects of the failure of point peasent bridge, *Journal of Testing and Evaluation*, March 1973, pp. 152-161.
4. Vardar, Oktem, Fracture Mechanics. 1988, Bogaziçi University.
5. Branco, C.A.G. de M., Fernandes, A.A., de Castro, P.M.S.T., Fadiga de Estruturas Soldadas. 2ª ed. Manuais Universitários. 1999, Lisboa: Fundação Calouste Gulbenkian.
6. ASTM E399, Standard test method for Plane-Strain Toughness of Materials. 1997, West Conshohocken: American Society for Testing and Materials.
7. ASTM E62, Standard test method for Vickers Hardness of Metallic Materials. 1997, West Conshohocken: American Society for Testing and Materials.
8. Albuquerque, Carlos, Cálculos justificativos das dimensões dos provetes e das cargas a aplicar no ensaio de taxa de propagação de fenda, FEUP, internal working document.
9. ASTM E647, Standard test method for measurement of fatigue crack growth rates. 1995, West Conshohocken: American Society for Testing and Materials.
10. Kühn, B., *et al*., Assessment of Existing Steel Structures: Recommendations for Estimation of Remaining Fatigue Life; Background documents in support to the implementation, harmonization and further development of the Eurocodes, EUR 23252 EN, ISSN 1018-5593, Luxembourg: Office for Official Publications of the European Communities
11. BS 5762:1979, Methods for crack opening displacement (COD) testing.
12. M. Beghini and L. Bertini, Fatigue crack propagation through residual stress fields with closure phenomena, *Engineering Fracture Mechanic,s* vol.36, (3), pp.379-387, 1990.
13. Rading, G.O., An evaluation of residual stress distribuition in welded compact tension specimens using neutron difraction, *Journal of Strain Analysis*, vol.40, (2), pp.211-216, 2004.
14. Kitsunai, Y., 'Effect of specimen size and configuration on fatigue crack growth behavior of mild steel butt welded joints', *Journal of the Society of Materials Science, Japan*, vol.32, no.354, 1983, pp.304-309
15. Kitsunai Y., *et al*, 'Prediction of fatigue crack growth lives in high strength steel weldments under low temperature', Research Report of the Research Institute of Industrial Safety RIIS-RR-87, 1987
16. Kitsunai, Y., Tanaka, M., Yoshihisa, E., 'Influence of residual stresses and loading frequencies on corrosion fatigue crack growth behavior of weldments', *Metallurgical and Materials Transactions A*, vol.29A, April 1999, pp.1289-1298
17. Andersen, Michael R., 'Fatigue crack initiation and growth in ship structures', PhD Thesis, Technical University of Denmark, 1998

Annex A

Clevis design

Supplied by Carlos Albuquerque.

In agreement with the ASTM E 647 standard:

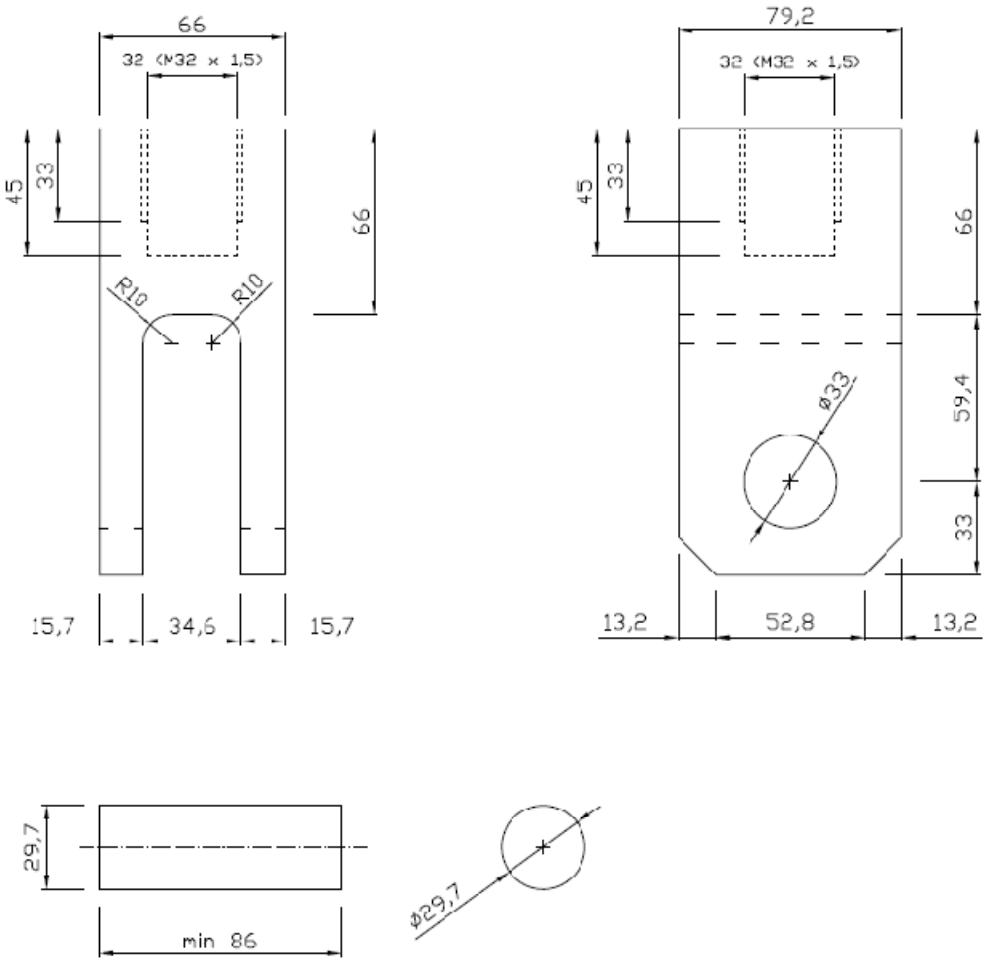


Figure 127 – Clevis design.

Annex B

Resources used

An incomplete list of resources used in this work is as follows:

250kN MTS servo-hydraulic machine:

- BM specimen, R=0.1. Start date: April 13; end date: April 27.
- HAZ specimen, R=0.1. Start date: April 28, end date: June 4.
- BM specimen, R=0.4. Start date June 7, end date: June 17.
- BM specimen, R=0.7. Start date: June 17, end date: July 7.

External supplies:

- Machining of 35 CT specimens: INEGI.
- Milling tool, Irmãos Sás Ferramentas de Corte e Precisão.
- EDM initial notch for 35 CT specimens: Autoconceptus.
- Repair and re-threading of clevis using orbital EDM; machining of new threaded pins for clevis: Autoconceptus.
- EDM complete cut of a BM specimen and of an HAZ specimen, intended for future residual stress measurements and analyses: Autoconceptus.

Annex C

Spider 8 dynamic measurements

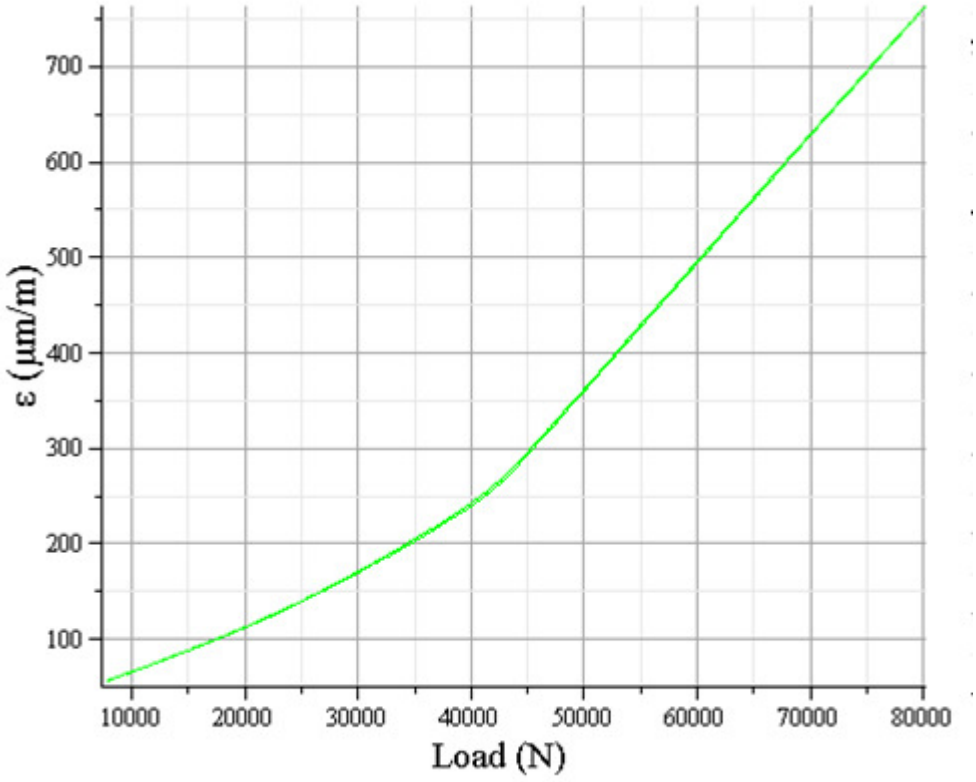


Figure 128 – Force *vs.* strain plot under dynamic load with a=64,19 mm with 1HZ frequency (HAZ R=0,1).

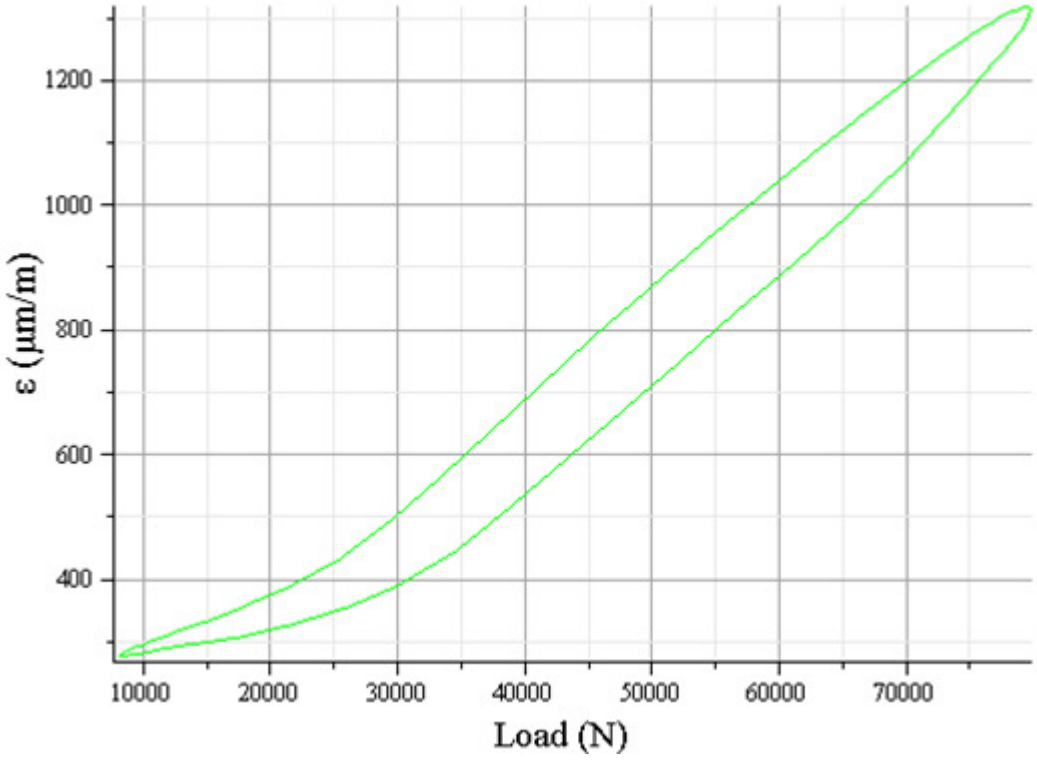


Figure 129- Force *vs.* strain plot under dynamic load with a=69,43 mm with 16 HZ frequency (HAZ R=0,1).

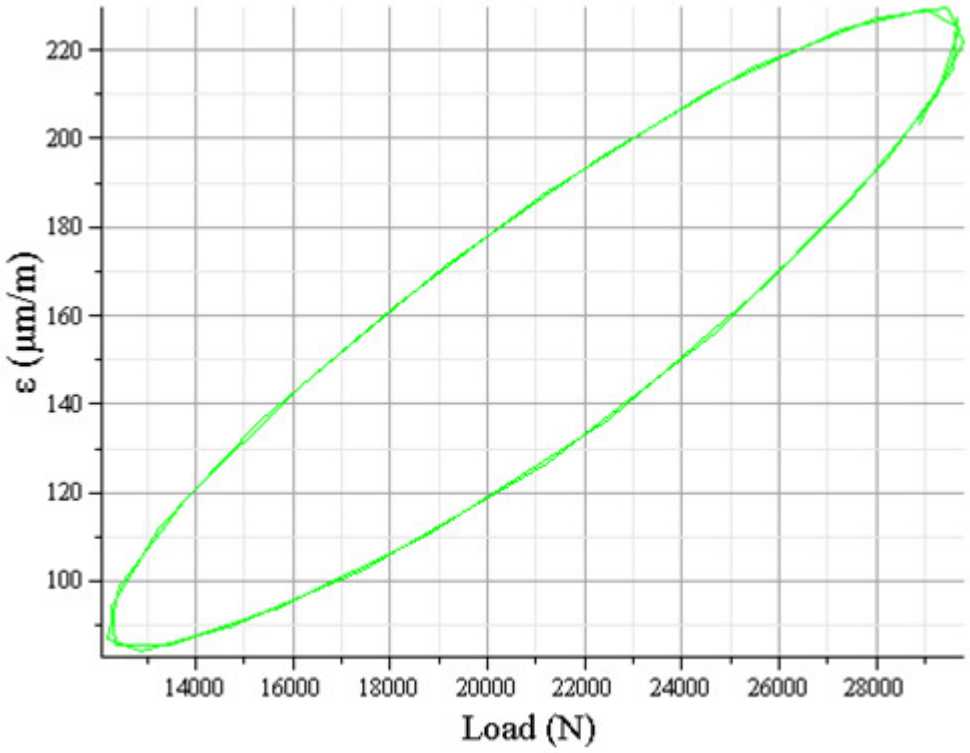


Figure 130 - Back face strain *vs.* force applied in the test specimen for a=51,27 mm (BM specimen R=0,4, under cyclic load).

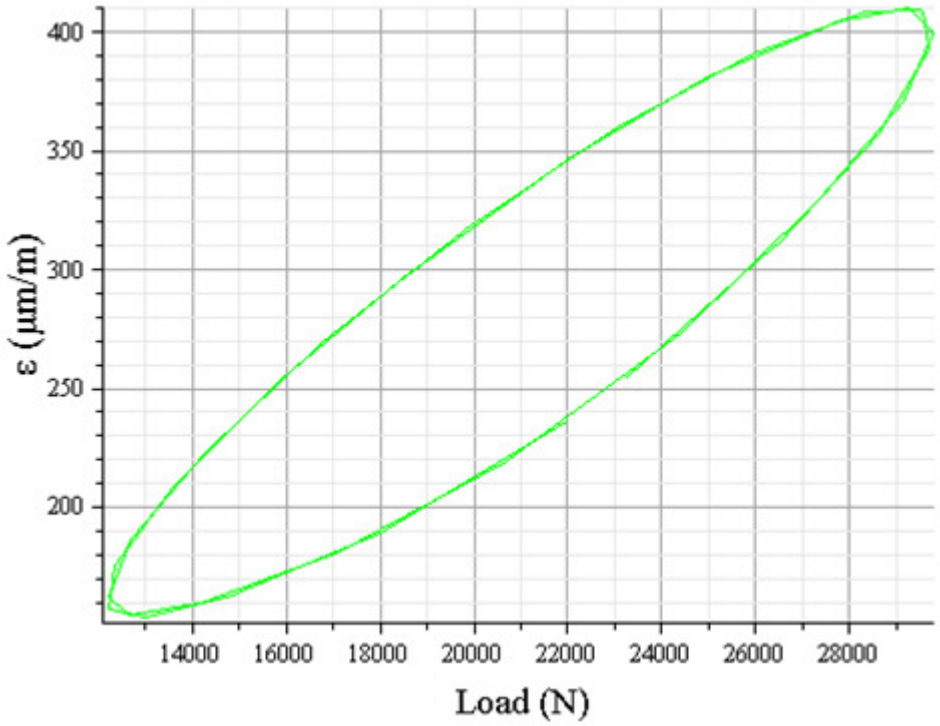


Figure 131 - Back face strain *vs.* force applied in the test specimen for a=52,69 mm (BM specimen R=0,4, under cyclic load).

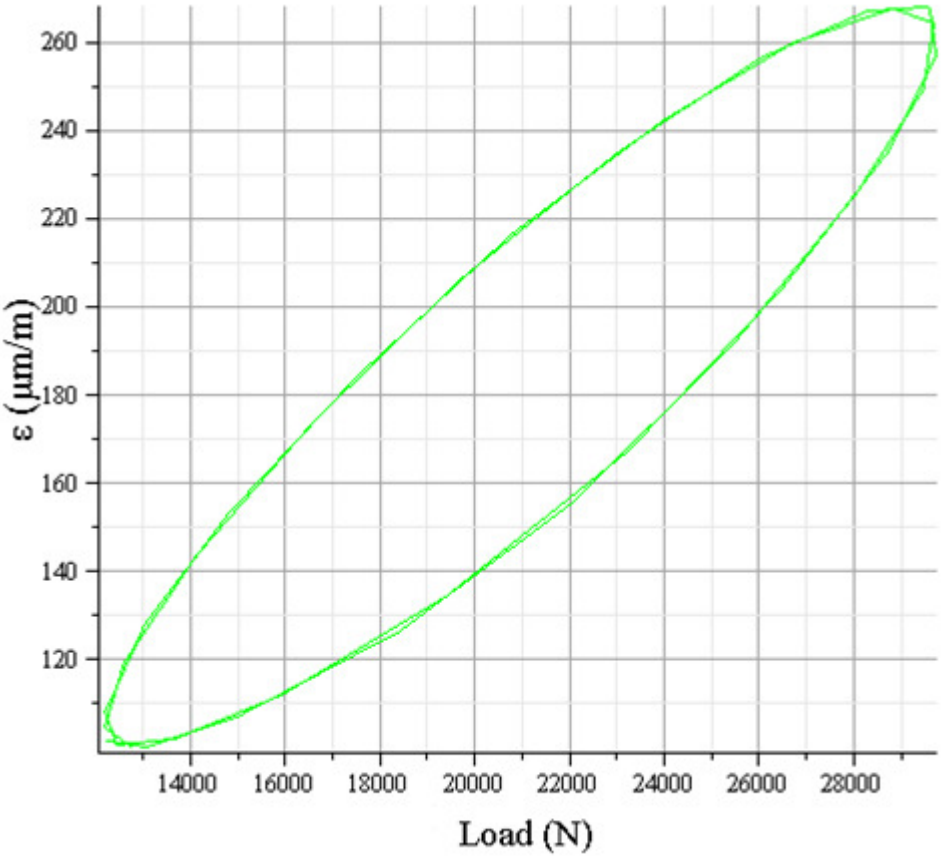


Figure 132 - Back face strain *vs.* force applied in the test specimen for a=65,43 mm (BM specimen R=0,4, under cyclic load).

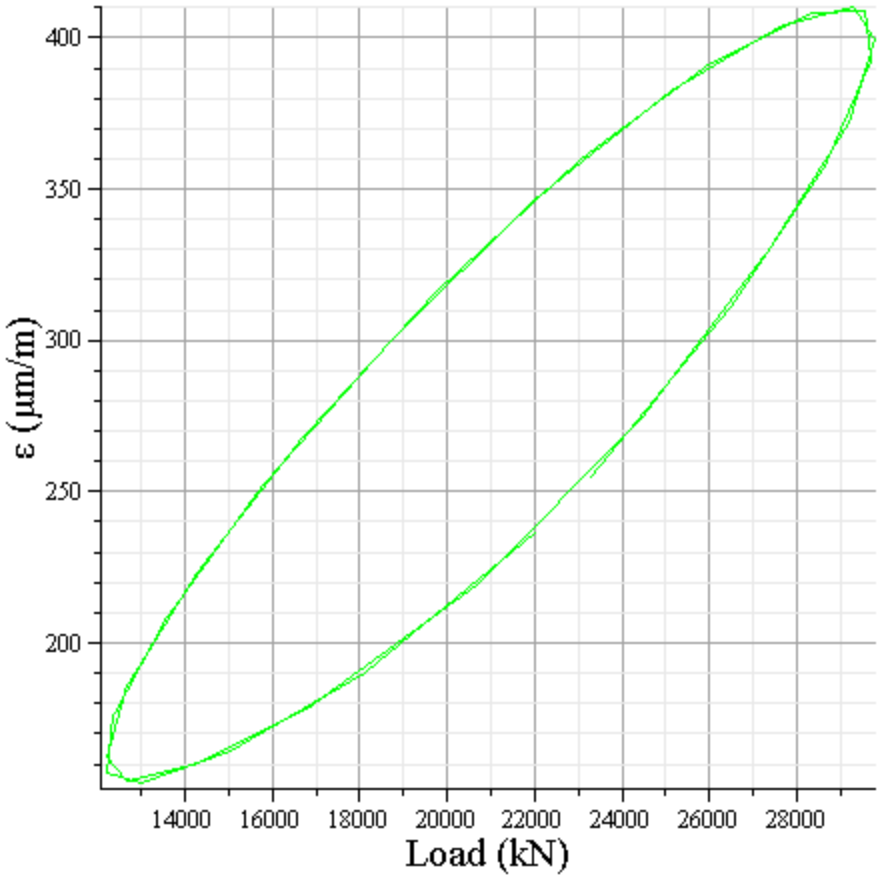


Figure 133 - Back face strain *vs.* force applied in the test specimen for a=74,37 mm (BM specimen R=0,4, under cyclic load).

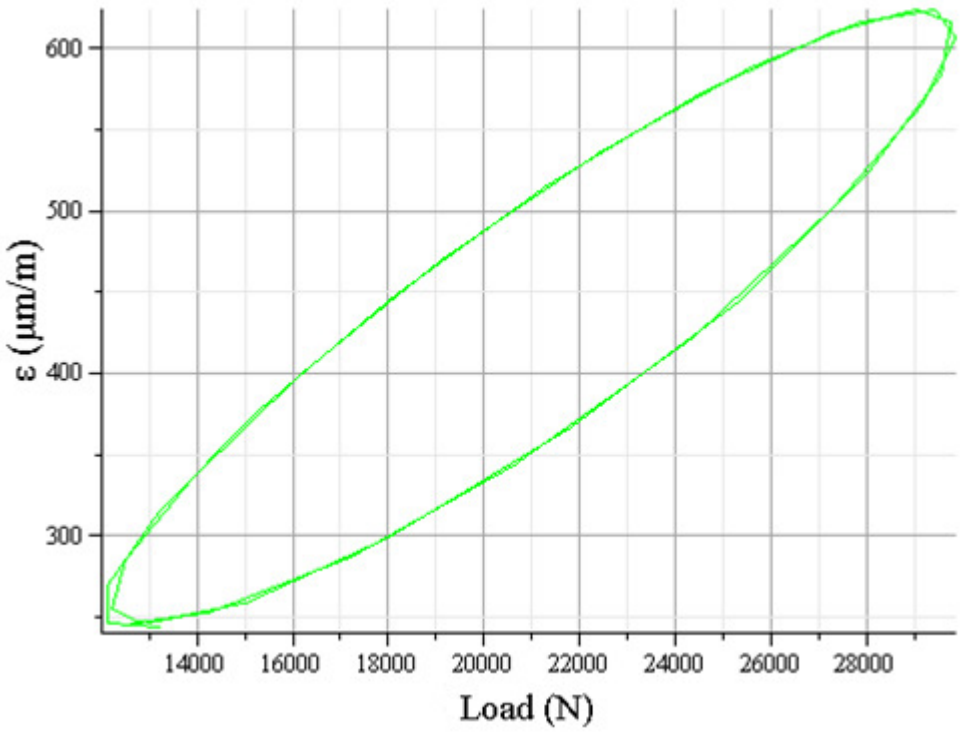


Figure 134- Back face strain *vs.* force applied in the test specimen for a=84,39 mm (BM specimen R=0,4, under cyclic load).

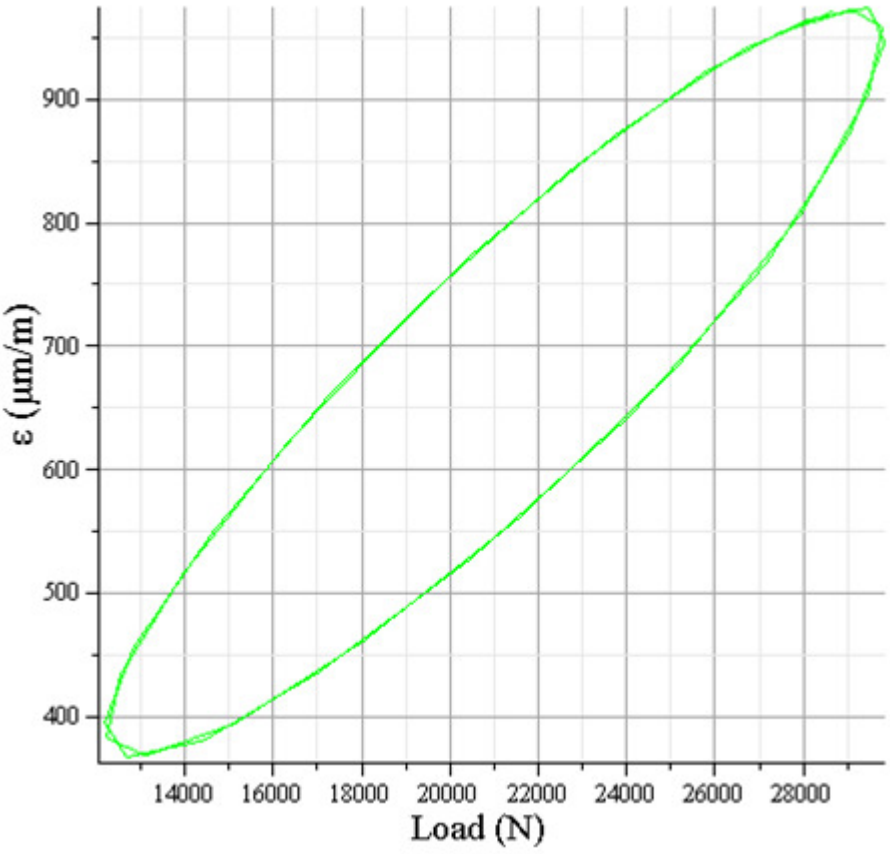


Figure 135 - Back face strain *vs.* force applied in the test specimen for a=87,55 mm (BM specimen R=0,4, under cyclic load).